

**Advanced Signal Processing for  
Fiber-Optic Communication Systems  
Scaling Capacity Beyond 100 Tb/s**

Kohki Shibahara

Graduate School of Informatics,

Kyoto University

September 2017



# Preface

Started from the first attempt to exploit light as a means to transmit information by Alexander Graham Bell in 1880 (known as “photophone”), a number of considerable improvements have contributed to developments in communication networks. The intensive research on networks over optical fiber cables was driven by the invention of light emitting by stimulated radiation (LASER) in the early 1960s, and by the low-loss optical fiber concept in 1966. By the beginning of 1980, fiber-optic networks was introduced in UK, the US, and Japan with the system capacity up to 100 Mb/s. Over the last three decades, the system capacity using single-mode fiber (SMF) has increased by six orders of magnitude due to the technological breakthroughs in electronics/optoelectronics and signal processing techniques including electrical time division multiplexing, wavelength division multiplexing in conjunction with optical amplification, and digital coherent transmission. However, recent theoretical studies pointed out that the existing SMF-based fiber-optic systems cannot support the system capacity beyond 100 Tb/s per fiber. Currently, the information capacity resources of SMF-based fiber-optic systems are exhausted at an astonishingly rapid rate, and the *capacity crunch* might be coming in sight by the mid-2020s. A new multiplexing technologies with spatially-structured fibers may offer solutions against the capacity limit. This approach — known as spatial division multiplexing (SDM) — has attracted considerable attention worldwide from the late 2000s, although developments in both SDM signal transmission and SDM devices are still open issues for practical applications of SDM transmission systems. On the other hand, from the standpoint of industrial market maturity, a cost-effective solution to enhance the system capacity until the capacity crunch is to continuously exploit transmission technologies on SMF-based fiber-optic systems.

This thesis proposes some novel schemes based on statistical and/or signal processing approaches with the aim to enhance system capacity and transmission reach over both conventional SMFs and SDM fibers. A brief review regarding signal processing schemes to

understand the fundamentals of optical signal transmission is provided in Chapter 2. In Chapter 3,  $n$ -wavelength-interleaving (WI) transmission is proposed to mitigate the impact of polarization dependent loss. Experimental results show that  $n$ -WI transmission enables the outage probability to be reduced by utilizing statistical averaging effects among optical channels with different frequency. Chapter 4 proposes a transmission based on multiple-input multiple-output (MIMO) signal processing to improve the robustness against optical filtering imposed by multiple crossings of optical nodes. It is shown through numerical simulations that this scheme is particularly suitable for a super-channel transmission beyond 100 Gb/s comprising multiple subcarriers (SCs), and allows a super-channel to pass through a larger number of optical filters. Chapter 5 deals with fiber nonlinearity based on optical and signal approaches. In the first part, the system performance improvement is revealed by considering the combined use of optical and signal approaches. Second part proposes a novel polarization crosstalk canceler based on independent component analysis approach. Performance comparison to remove polarization crosstalk is conducted among conventional and proposed methods in signal transmission with different modulation formats. Also discussed are its advantages when applied prior to other receiver-side signal processing schemes. A novel inter-carrier interference canceling scheme is proposed in Chapter 6 which allows a *dense* transmission by multiplexing multiple SCs tightly in the frequency domain. The proposed inter-carrier interference cancellation technique utilizes the architecture of the advanced nonlinear MIMO signal processing and coding schemes. The chapter demonstrates the improvement in spectral efficiency through both numerical simulation and signal transmission experiments. Chapter 7 is intended to provide brief review of recent progress in SDM transmission, and discussion about the remaining challenges to be addressed. From signal processing perspective, it is revealed that two physical phenomena are considered to be dominant restriction factors for SDM transmission reach extension. Succeedingly, Chapter 8 newly proposes three MIMO signal processing schemes to offer solutions against issues discussed in Chapter 7. One aims to reduce the computational complexity in a MIMO equalization scheme, which contributes to the world's longest transmission demonstration of MIMO-SDM signals, the rest to improve optical MIMO-SDM signal performance under non-unitary channel. Each performance of the proposed schemes is independently evaluated in different MIMO-SDM transmission experiments.

# Acknowledgements

At the outset I would like to express my profound gratitude to my supervisor, Professor Masahiro Morikura, for the continuous discussions regarding every detail of the entire thesis. His fruitful suggestions, comments, and encouragement extraordinarily contributed to completing this work.

I am also deeply grateful to Professor Eiji Oki and Professor Ken Umeno of Graduate School of Informatics, Kyoto University for their constructive and insightful comments. The improvement of this thesis was significantly attributed to their invaluable supports.

I am greatly indebted to Dr. Ryutaro Kawamura, Head of NTT Network Innovation Laboratories, and Dr. Yutaka Miyamoto, Senior Distinguished Researcher, Director of Innovative Photonic Network Center, Group Leader of the Lightwave Signal Processing Research Group, for providing me the persistent help and supports including laboratory facilities and the great opportunity to complete this work.

I would like to appreciate the members of my research group, the Lightwave Signal Processing Research Group in NTT Network Innovation Laboratories, Dr. Takayuki Mizuno, Mr. Hiroto Kawakami, Mr. Takayuki Kobayashi, Dr. Fukutaro Hamaoka, Mr. Akira Isoda, and Mr. Masanori Nakamura.

I also would like to thank to the members of my previous research group, the Photonic Processing Systems Research Group in NTT Network Innovation Laboratories, Mr. Mitsunori Fukutoku, Dr. Shingo Kawai, Dr. Kunihiro Mori, Mr. Mitsuki Kawahara, and Mr. Akira Masuda.

Lastly I owe my deepest gratitude to family, my wife Yumi and my daughter Mio, who always supported me with heartwarming encouragement.

# Contents

Preface	i
Acknowledgements	iii
Abbreviations	xxiii
Chapter 1 Introduction	1
1.1 Growth of Today's Network Traffic . . . . .	1
1.2 Evolutions of Optical Communication Systems from a Historical Perspective	3
1.2.1 The Beginning of Optical Communication Systems . . . . .	3
1.2.2 The Evolutions Towards Terabit-Capacity Systems . . . . .	4
1.3 The Capacity Limit in Optical Fibers . . . . .	7
1.4 Space Division Multiplexing as a New Transmission Technology . . . . .	8
1.5 Contributions of This Thesis . . . . .	10
1.5.1 Fundamentals of Advanced Signal Processing . . . . .	11
1.5.2 PDL Penalty Reduction by Wavelength-Interleaving Transmission . .	11
1.5.3 Filtering-Tolerant Transmission for Super-Channel Beyond 100 Gb/s	12
1.5.4 Fiber Nonlinearity Mitigation/Compensation Based on Optical and Digital Approaches . . . . .	12
1.5.5 Multi-Stage SIC for Spectrally-Efficient Super-Nyquist Transmission	13
1.5.6 State-Of-The-Art Space Division Multiplexing Transmission and Challenges . . . . .	14
1.5.7 Space Division Multiplexing Transmission using Multicore and/or Multimode fiber . . . . .	14
Chapter 2 Fundamentals of Advanced Signal Processing	15

---

2.1	Overview . . . . .	15
2.2	Waveform Evolution in Optical Fibers . . . . .	15
2.2.1	Nonlinear Schrödinger Equation . . . . .	16
2.2.2	Digital Back-Propagation . . . . .	17
2.3	Performance Metric in Optical Signal Transmission . . . . .	20
2.3.1	Optical Signal-to-Noise Ratio . . . . .	20
2.3.2	Bit Error Rate and Relations with $Q$ -factor . . . . .	22
2.4	Adaptive Filtering Techniques . . . . .	24
2.4.1	Classical Wiener Filter Theory . . . . .	25
2.4.2	Adaptive Filtering Based on the Stochastic Gradient: LMS Algorithm . . . . .	27
2.4.3	Adaptive MIMO Equalization in PDM Systems . . . . .	28
2.4.3.1	LMS-based Adaptive MIMO Equalization . . . . .	29
2.4.3.2	CMA-based Adaptive MIMO Equalization . . . . .	30
Chapter 3	PDL Penalty Reduction by Wavelength-Interleaving Transmission . . . . .	32
3.1	Overview . . . . .	32
3.2	$n$ -Wavelength-Interleaving Transmission . . . . .	33
3.3	Experimental Setup and Results . . . . .	34
3.4	Analysis by Extreme Value Statistics . . . . .	35
3.5	Numerical Simulation . . . . .	38
3.6	Summary . . . . .	40
Chapter 4	Filtering-Tolerant Transmission for Super-Channel Beyond 100 Gb/s . . . . .	41
4.1	Overview . . . . .	41
4.2	Proposed Method: WHT-Spreading . . . . .	43
4.3	Analysis of the WHT Spreading . . . . .	45
4.3.1	System Model . . . . .	45
4.3.2	$Q$ -factor Characteristics . . . . .	46
4.4	Numerical Simulation . . . . .	48
4.4.1	Simulation Setup . . . . .	48
4.4.2	Simulation Results . . . . .	50

---

4.5	Summary . . . . .	53
Chapter 5 Fiber Nonlinearity Mitigation/Compensation Based on Optical and Digital Approaches		54
5.1	Improving Nonlinear Degradation by Combining Optical and Digital Compensation Techniques . . . . .	54
5.1.1	Overview . . . . .	54
5.1.2	Simulation Setup . . . . .	55
5.1.3	Results and Discussion . . . . .	56
	5.1.3.1 Effects of XPM-Suppressor and DBP in DM system . . . . .	56
	5.1.3.2 Performance Comparison Between DM and NDM Systems . . . . .	57
5.2	Digital Compensation for XPM-Induced Polarization Crosstalk Using Overlapped Fast Independent Component Analysis . . . . .	59
5.2.1	Overview . . . . .	59
5.2.2	Proposed Algorithm: Overlapped-FastICA . . . . .	61
5.2.3	Simulation Setup . . . . .	62
5.2.4	Simulation Results . . . . .	63
	5.2.4.1 Overview of Algorithm Performance . . . . .	65
	5.2.4.2 Performance for Multi-Level Modulation Format Signals . . . . .	67
	5.2.4.3 Effect of Combining Overlapped-FastICA and Other Nonlinearity-Compensation Algorithms . . . . .	70
5.3	Summary . . . . .	71
Chapter 6 Multistage SIC for Spectrally-Efficient Super-Nyquist Transmission		72
6.1	Overview . . . . .	72
6.2	Multistage SIC for ICI mitigation . . . . .	73
6.3	Simulation Results . . . . .	74
6.4	Transmission Experiment Results . . . . .	75
	6.4.1 Superimposed Transmission with M-SIC Scheme . . . . .	75
	6.4.2 Coded Superimposed Transmission with M-SIC Scheme . . . . .	78
6.5	Summary . . . . .	83



Chapter 7	State-Of-The-Art Space Division Multiplexing Transmission Progress and Challenges	84
7.1	Overview . . . . .	84
7.2	Recent Progress on SDM Transmission Experiments . . . . .	85
7.2.1	MCF Transmission . . . . .	86
7.2.2	MMF/FMF Transmission . . . . .	87
7.2.3	CC-MCF Transmission . . . . .	88
7.2.4	MC-FMF Transmission . . . . .	89
7.3	Issues and Methodologies on MIMO-SDM Transmission . . . . .	89
7.3.1	Matrix Propagation Model . . . . .	90
7.3.2	Methodologies for Dealing with DMD . . . . .	92
7.3.3	Methodologies for Dealing with MDL . . . . .	95
7.4	MIMO-SDM Transmission Strategies with Signal Processing for DMD and MDL Problems . . . . .	98
7.4.1	System Model . . . . .	99
7.4.2	MIMO Detection Schemes . . . . .	100
7.4.2.1	Linear MIMO Detection . . . . .	100
7.4.2.2	Interference Canceling Detection . . . . .	102
7.4.2.3	Maximum Likelihood Detection . . . . .	105
7.4.3	Computational Complexity . . . . .	107
7.4.4	Detection Performance . . . . .	109
7.5	Frequency Selectivity and Its Impact on MIMO-SDM Signal Processing . .	112
7.6	Summary . . . . .	114
Chapter 8	Space Division Multiplexing Transmission using Multicore and/or Multimode Fiber	116
8.1	Dense SDM (12-core $\times$ 3-mode) Transmission over 527 km with 33.2-ns Mode-Dispersion Employing Low-Complexity Parallel MIMO Frequency-Domain Equalization . . . . .	116
8.1.1	Overview . . . . .	116

8.1.2	Parallel MIMO FDE for Long-Haul DSDM Transmission Without DMD Management . . . . .	118
8.1.3	Adaptive Algorithms for DMD Equalization . . . . .	119
8.1.3.1	Single-carrier TDE . . . . .	120
8.1.3.2	Parallel MIMO TDE . . . . .	121
8.1.3.3	Parallel MIMO FDE . . . . .	121
8.1.4	Experimental Setup . . . . .	124
8.1.5	Transmission Results . . . . .	128
8.1.6	Summary . . . . .	128
8.2	Space-Time Coding-Assisted Transmission for Mitigation of MDL Impact on Mode-Division Multiplexed Signals . . . . .	130
8.2.1	Overview . . . . .	130
8.2.2	Proposed STC Scheme: Space-Time Spreading Implemented with the Orthogonal Transform . . . . .	132
8.2.3	Numerical Performance Analysis of Mode Scrambling and Space-Time Spreading . . . . .	133
8.2.4	Experimental Setup and Results . . . . .	135
8.2.5	Summary . . . . .	139
8.3	LDPC-Coded FMF Transmission Employing Unreplicated SIC for MDL-Impact Mitigation . . . . .	140
8.3.1	Overview . . . . .	140
8.3.2	Proposed Detection Scheme: Unreplicated SIC . . . . .	141
8.3.2.1	U-SIC Detection at the First and Second Stage . . . . .	142
8.3.2.2	U-SIC Detection at the $k$ -th Stage . . . . .	145
8.3.3	Experimental Setup . . . . .	147
8.3.4	Experimental Results . . . . .	148
8.3.5	Summary . . . . .	151
Chapter 9	Conclusions	153
9.1	Spectrally-Efficient SMF-based Transmission Systems . . . . .	153
9.2	SDM Transmission Systems Scaling Beyond 100 Tb/s . . . . .	156

Bibliography

159

Author's Publication List

177

# List of Figures

1.1	Recent traffic growth and forecast in IP-based network [1]. . . . .	2
1.2	Recent traffic growth and forecast in data center network [2]. “Within DC”, “DC-DC”, “DC-user”, and “non-DC” respectively denote traffic that remains within the data center, traffic that flows from data center to data center, traffic that flows from data center to end-users, and traffic irrelevant to data center. A portion relative to total traffic for each category is also shown in percent. . . . .	2
1.3	The evolution of fiber-optic communication systems. . . . .	6
1.4	Schematic illustration of MCF-based (top) and MMF-based (bottom) transmission systems. . . . .	10
1.5	Chapter overview of this thesis. . . . .	11
2.1	Theoretical BERs for PDM-QPSK, 16QAM, or 64QAM signals driven at 30, 60, or 90 GBaud. The OSNR penalty switched from QPSK to 16QAM is $\sim 4$ dB, and one from QPSK to 64QAM is $\sim 8$ dB. . . . .	22
2.2	Schematic of Gaussian probability density of received samples. Shading region corresponds to the probability of erroneous ones. . . . .	24
2.3	Relation between BER and $Q$ -factor. . . . .	24
2.4	Theoretical $Q$ -factor for PDM-QPSK, 16QAM, or 64QAM signals driven at 30, 60, or 90 GBaud derived from eq. (2.21) through eq. (2.23). . . . .	25
3.1	Schematic illustration of 2-WI transmission system. The numbers in blocks indicate the channel number and shadings mean the degradation difference of optical signals between 2 channels. . . . .	33
3.2	Experimental setup. PPG: Pulse-pattern generator, Mod: IQ-modulator, VOA: Valuable optical attenuator. . . . .	34

3.3	(a) Temporal change in observed $Q$ -factor of ch1 and ch2. (b) Scatter plots of $Q$ -factors for the two channels. (c) Probability density of ch1, ch2, and interleaved channel as a function of $Q$ -factor. . . . .	34
3.4	Cumulative probabilities from experimental data (symbols) and fitted $C(x)$ obtained from eq. (3.2) with estimated parameters (solid curves) for ch <sub>1</sub> (a), ch <sub>2</sub> (b), and interleaved channel (c). . . . .	37
3.5	Estimated $Q$ -limit from eq. (3.3) as a function of outage probability for ch1, ch2 and interleaved channel. Note that error bars at outage probability of $10^{-2}$ , $10^{-4}$ , and $10^{-6}$ are estimated based on the 90 % confidence intervals of $\sigma$ and $\xi$ . . . . .	38
3.6	Simulated probability densities of $Q$ -factors for the channels without WI transmission, with 4-WI transmission, and with 8-WI transmission. . . . .	39
3.7	The $Q$ -penalty improvement in dB as a function of the number of interleaving wavelengths $n$ for a fixed outage probability of $10^{-6}$ . . . . .	39
4.1	A transmitter implementation of the WHT method for 2SC-DP-16QAM format. WHT: the Walsh-Hadamard transform, LD: laser diode, PBS: polarization beam splitter, PBC: polarization beam combiner, IQ-mod.: IQ-modulator.	44
4.2	$Q$ -factor as a function of the number of SCs. The “worst SC” corresponds to the one that is attenuated by a factor of 0.5. . . . .	46
4.3	$Q$ -factor as a function of $\rho$ . The “worst SC” corresponds to the attenuated one. . . . .	47
4.4	(a). Simulation setup. SC: subcarrier, WSS: wavelength selective switch, OBPF: optical bandpass filter, OFE: optical frontend., ADC: analog-to-digital converter, DSP: digital signal processing. (b). The implementation example of the butterfly-structured MMA. . . . .	49
4.5	$Q$ -factor penalty as a function of the number of cascaded WSSs for case-i. . . . .	51
4.6	Constellation diagrams after demodulation with and without the WHT-S method. The red (top) and blue (bottom) ones represent the best and worst performance SCs, respectively. . . . .	52

4.7	$Q$ -factor penalty as a function of center-frequency shift for both super-channel signal formats. . . . .	52
4.8	$Q$ -factor penalty as a function of the number of cascaded 3.75G-shifted WSSs for both super-channel signal formats. . . . .	53
5.1	Simulation setup. PDM: polarization division multiplexing, NRZ: non-return-to-zero, XPM: cross phase modulation, DM: dispersion-managed, NDM: non-dispersion-managed, DCF: dispersion-compensated fiber, VOA: valuable optical attenuator, NZDSF: non-zero dispersion-shifted fiber, OBPF: optical band pass filter. . . . .	56
5.2	$Q$ -factor improvement achieved with XPM-suppressor in DM system for various fiber launch power cases. . . . .	57
5.3	$Q$ -factor improvement by DBP for fiber launch power of 4 dBm as a function of inter-channel skew. Error bars indicate the standard deviation of the $Q$ -factor dataset. . . . .	58
5.4	Comparison of $Q$ -factor between XPM-suppressed-DM and NDM system before and after DBP. . . . .	58
5.5	PAPR in DM and NDM system as a function of number of spans. Note that PAPR is measured at NZDSF input in each span. . . . .	59
5.6	Schematic illustration of overlapped-FastICA. Area with diagonal hatching lines indicates overlapped symbols. The overlapping ratio is set to 50 % in the figure. . . . .	62
5.7	Simulation setup. SMF: single mode fiber, DCM: dispersion compensation module, OBPF: optical bandpass filter, LO: local oscillator, CD: chromatic dispersion. . . . .	62
5.8	The back-to-back performance for all modulation format signals as a function of OSNR. . . . .	64
5.9	Typical transitions of cost function as a function of iteration number. . . . .	64
5.10	The $Q$ -factor as a function of transmission distance for all format signals. The fiber input power was 3 dBm. . . . .	65

5.11	<i>Q</i> -factor improvement obtained with various compensation techniques for QPSK format signals as a function of transmission distance. . . . .	65
5.12	The <i>Q</i> -factor performance after 1000-km transmission for all modulation formats as a function of fiber launch power. . . . .	66
5.13	<i>Q</i> -factor improvement obtained with various compensation techniques as a function of fiber launch power for QPSK format signals. Bottom panels show the constellations (a) before compensation, (b) after NPCC, and (c) after overlapped-FastICA for each modulation format case. . . . .	66
5.14	<i>Q</i> -factor improvement with the same format in Fig. 5.13 for 8QAM format signals. . . . .	67
5.15	<i>Q</i> -factor improvement with the same format in Fig. 5.13 for 16QAM format signals. . . . .	67
5.16	The comparison of the <i>Q</i> -factor improvement performance of overlapped-FastICA that were applied after CD compensation and after CPR for the cases of (a) QPSK, (b) 8QAM, and (c) 16QAM signals. . . . .	68
5.17	DSP procedure cases. DBP: digital back-propagation. . . . .	68
5.18	<i>Q</i> -factor improvement achieved by DBP with/without applying overlapped-FastICA before it. . . . .	69
6.1	Processing flow of M-SIC. . . . .	74
6.2	<i>Q</i> -factor transitions as a function of SIC stages for (a) QPSK and (b) 16QAM signals. The constellations for both format signals before and after M-SIC are displayed at inset panels (bottom: before M-SIC, top: after M-SIC). . . . .	76
6.3	<i>Q</i> -factors before and after M-SIC as a function of OSNR. . . . .	76
6.4	Experimental setup. ECL: external-cavity laser, AWG: arbitrary waveform generator, SMF: single-mode fiber, EDFA: Erbium-doped fiber amplifier, DSO: digital storage oscilloscope, DSP: digital signal processing . . . . .	77
6.5	<i>Q</i> -factor after 195km-transmission as a function of carrier spacing factor $\alpha$ . . . . .	77
6.6	<i>Q</i> -factor for non-uniform power transmission as a function of power imbalance factor $\gamma$ . . . . .	78

6.7	Schematic of (1): imsuperimposed transmission (IST), and (2): coded superimposed transmission (CST) with spectral overlapping. . . . .	80
6.8	(a) $G_{SE}$ curves as a function of $\delta$ for $\eta_{CST} = 0.25$ (blue) and $\eta_{CST} = 0.125$ (red). (b) $G_{SE}$ contour plot for various $\delta$ and $\eta_{CST}$ . . . . .	80
6.9	The processing flow chart of CST with M-SIC scheme. . . . .	82
6.10	$Q$ -factor performance of CST and IST for various carrier space settings. $G_{SE}$ is displayed in percent. . . . .	82
7.1	Schematic illustration of DMD in 2-LP mode MMF. . . . .	94
7.2	Optical methodologies for DMD currently reported. . . . .	94
7.3	SDM transmission experiments over MCF, CC-MCF, FMF, and MC-FMF with the memory length used for each MIMO signal processing. . . . .	95
7.4	Schematic of an optical MIMO system. . . . .	95
7.5	Schematic illustration of MDL in 2-LP mode MMF. . . . .	98
7.6	Optical methodologies for MDL currently reported. . . . .	98
7.7	The detection process in a linear detector. . . . .	100
7.8	The detection in a SIC detector for the first two stages. . . . .	104
7.9	Complexity comparison between an MMSE, an SIC, and an ML detector to determine transmitted signals of QPSK or 16QAM. . . . .	109
7.10	Detection performance comparison among MMSE-based linear equalizer, SIC detector, and MLD for QPSK signals in the presence of MDL. . . . .	109
7.11	Experimental setup for estimation of transfer matrix of 12-core $\times$ 3-mode MC-FMF transmission line. LD: laser diode, IQM: IQ-modulator, PoL. MUX: polarization multiplexer, Mode MUX: mode multiplexer, FI: fan-in, FO: fan-out, MC-FMF: multicore-fewmode fiber, Mode DEMUX: mode demultiplexer, OTF: optical tunable filter, LO: local oscillator, PLC: planar lightwave circuit, DPOH: dual-polarization optical hybrid . . . . .	113
7.12	Estimated impulse response for (a) core#8 (small DMD), and (b) core#1 (large DMD). . . . .	113
7.13	Estimated MDL variation as a function of relative frequency. . . . .	115



7.14	Signal spectrums of LP <sub>01</sub> -X signals (a) in a back-to-back transmission and (b) after 5-span transmission of MC-FMF. . . . .	115
8.1	SDM WDM transmission distance vs. spatial multiplicity. . . . .	119
8.2	Required complexity for DMD compensation in recent FMF. . . . .	119
8.3	The schematic processing flow of the FDE scheme. . . . .	121
8.4	Comparison of the required complexity in each step for three equalization schemes. . . . .	122
8.5	Required complexity for DMD compensation. $M$ denotes the number of spatial channels. . . . .	124
8.6	(a) Experimental setup, (b) low symbol rate multi-carrier signal, and (c) cross section of 12-core $\times$ 3-mode low-DMD MC-FMF transmission fiber. .	124
8.7	Offline parallel MIMO processing flow. . . . .	127
8.8	$Q$ -factor transition as a function of transmission distance for core #6 (top panel) and #10 (bottom panel). . . . .	128
8.9	(a) $Q$ -factors after 527-km transmission. The number of SDM tributaries is defined as $(n - 1) \times 3 + m$ , where $n$ and $m$ is the core number and the mode number respectively ( $m = 1$ for LP <sub>01</sub> , $m = 2$ for LP <sub>11a</sub> , and $m = 3$ for LP <sub>11b</sub> ), (b) typical constellations for all spatial and polarization modes. . . .	129
8.10	(a): Schematic of the coding flow of the proposed method with $N = 3$ . (b), (c): constellation maps when applying eq. (8.15) to QPSK signals for (b) LP <sub>01</sub> and (c) LP <sub>11a</sub> /LP <sub>11b</sub> . . . . .	131
8.11	Schematic structures of the proposed STC system. . . . .	131
8.12	MDM system model with distributed noise loading. . . . .	135
8.13	Strongly-coupling effect brought by the introduction of MSs. (a) PDFs of overall MDL values with MSs (red) and without (MSs). (b) Mean MDL evolution as a function of number of spans for both cases. . . . .	135
8.14	Mean $Q$ -factors as a function of MDL per span. Error bars are represented as a standard deviation of 500 channel realizations.. . . .	136
8.15	Experimental setup of 12-core $\times$ 3-mode DSDM transmission. . . . .	136

---

8.16	Mean $Q$ -factor comparison as a function of transmission distance for both methods. (b) Received signals after 421-km transmission for each spatial mode (only signals of X-polarization are displayed). . . . .	137
8.17	$Q$ -factors as a function of transmission distance. . . . .	138
8.18	$Q$ -factor as a function of residual MDL for all spatial modes after 527-km transmission. . . . .	138
8.19	Schematic structures of SIC detectors comprising two stages. (a): conventional SIC, (b): unreplicated SIC. . . . .	142
8.20	Experimental setup. . . . .	148
8.21	Averaged BER obtained by linear MIMO equalizer/U-SIC before/after LDPC decoding as a function of OSNR. . . . .	149
8.22	MDL emulation by changing the input power into LP <sub>11</sub> ports. . . . .	150
8.23	Averaged BER obtained by linear MIMO equalizer/U-SIC before/after LDPC decoding as a function of MDL . . . . .	150
8.24	Required OSNR to achieve HD-FEC limit BER under FMF links with various DMD values. . . . .	151
8.25	Signal constellations detected using a linear MIMO equalization (top) or using the U-SIC scheme (bottom) after transmission over 15-km FMF at OSNR of 9 dB. . . . .	151

# List of Tables

3.1	ESTIMATED PARAMETERS FOR $ch_1$ , $ch_2$ , AND $ch_{int}$ . . . . .	36
4.1	SIGNAL FORMAT CANDIDATES ENABLING 400-Gb/s TRANSMISSION PER OPTICAL CARRIER. . . . .	42
7.1	CLASSIFICATION OF SDM FIBERS. . . . .	90
7.2	SUMMARY ON RECENT SDM TRANSMISSION EXPERIMENTS. . . . .	91
7.3	IMPACT OF FREQUENCY SELECTIVITY ON SIGNAL TRANSMISSION	112
8.1	CHARACTERISTICS OF THE MC-FMF. . . . .	126



# Abbreviations

ASE	Amplified spontaneous emission
AWG	Arbitrary waveform generator
AWGN	Additive Gaussian noise
BER	Bit-error rate
BIT	Bit-interleaving transmission
BSS	Blind source separation
CAGR	Compound annual growth rate
CC	Coupled-core
CD	Chromatic dispersion
CE	Channel estimation
CFS	Center-frequency shift
CPR	Carrier phase recovery
CSI	Channel stage information
C-SIC	Conventional successive interference cancellation
CST	Coded superimposed transmission
CW	Continuous wavelength
DA	Data-aided
DAC	Digital-to-analog converter
DBP	Digital back-propagation
DC	Data center
DCF	Dispersion compensation fiber
DCM	Dispersion compensation module
DD	Decision-directed
DEMUX	Demultiplexer
DFB	Distributed feedback
DFT	Discrete Fourier transform

---

DM	Dispersion managed
DMD	Differential mode delay
DMG	Differential modal gain
DQPSK	Differential quadrature phase shift keying
DS/CDMA	Direct spread code division multiple access
DSDM	Dense space division multiplexing
DSO	Digital storage oscilloscope
DSP	Digital signal processing
DVB-S2	Digital video broadcasting - satellite - second generation
ECL	External-cavity laser
EDFA	Erbium-doped fiber amplifier
FDE	Frequency domain equalization
ETDM	Electrical time domain multiplexing
EVS	Extreme value statistics
FDM	Frequency division multiplexing
FEC	Forward error correction
FFT	Fast Fourier transform
FI/FO	Fan-in fan-out
FIR	Finite impulse response
FMF	Fewmode fiber
FP	Fixed-point
GI	Graded-index
GV	Group velocity
GVD	Group velocity dispersion
HD	Hard decision
ICA	Independent component analysis
ICI	Inter-carrier interference
ICT	Information and communication technologies
IFFT	Inverse fast Fourier transform
IM-DD	Intensity-modulation with direct detection
IoT	Internet-of-things

---

IP	Internet protocol
IPNLMS	Improved proportionate normalized least mean square
IST	Imsuperimposed transmission
ITU-T	International telecommunication union telecommunication standardization sector
LASER	Light emitting by stimulated radiation
LDPC	Low density parity check
LMS	Least mean square
M2M	Machine-to-machine
MAP	Maximum-a-posteriori
MCF	Multicore fiber
MDL	Mode dependent loss
MDM	Mode division multiplexing
MIMO	Multiple-input multiple-output
MMA	Multi-modulus algorithm
MMF	Multimode fiber
MMSE	Minimum mean square error
MS	Mode scrambler
M-SIC	Multistage successive interference cancellation
MUX	Multiplexer
NDM	Non dispersion managed
NLSE	Nonlinear Schrödinger equation
NPC	Nonlinear polarization crosstalk
NPCC	Nonlinear polarization crosstalk canceler
NZDSF	Non-zero dispersion shifted fiber
OFDM	Orthogonal frequency domain multiplexing
OFC	Optical frontend
OPEX	Operational expenditure
OSIC	Ordered successive interference cancellation
OSNR	Optical signal-to-noise ratio
OTF	Optical tunable filter
PAPR	Peak-to-average power ratio

---

PBN	Passband narrowing
PRBS	Pseudo random binary sequence
PDM	Polarization division multiplexing
PDL	Polarization dependent loss
PIC	Parallel interference cancellation
PLC	Planar lightwave circuit
PMD	Polarization mode dispersion
POT	Peaks over threshold
QAM	Quadrature amplitude modulation
QRM-MLD	QR-decomposition and M-algorithm
RLS	Recursive least square
ROADM	Reconfigurable optical add/drop multiplexer
RZ	Return-to-zero
SC	Single carrier
SD	Soft decision
SE	Spectral efficiency
SDH	Synchronous digital hierarchy
SDM	Space division multiplexing
SI	Step-index
SIC	Successive interference cancellation
SINR	Signal-to-interference-plus-noise ratio
SONET	Synchronous optical networking
SOP	State-of-polarization
SMF	Single mode fiber
SNR	Signal-to-noise ratio
SSF	Split-step Fourier
STBC	Space-time block code
STC	Space-time code
SVD	Singular value decomposition
TDE	Time domain equalization
U-SIC	Unreplicated successive interference cancellation



---

VOA	Valuable optical attenuator
WDM	Wavelength division multiplexing
WHT	Walsh-Hadamard transform
WI	Wavelength-interleaving
WSS	Wavelength selective switch
XPM	Cross-phase modulation
ZB	Zettabyte



# Chapter 1

## Introduction

### 1.1 Growth of Today's Network Traffic

Information and communication technologies (ICT) is unquestionably at the crux of sustaining current social infrastructures such as water/electricity/transportation systems, logistics services and financial transaction. The evolution of the mobile communication technology including cellular networks, devices, and relevant services (e.g., a social networking service) emerged in the last decade has completely changed the whole situation with regard to interpersonal relationships and business on a grand scale. Fig. 1.1 shows global Internet protocol (IP) traffic growth and forecast from 2015 to 2020. The Cisco Visual Networking Index [1] forecasts that global IP traffic will exceed zettabyte (ZB) by the end of 2016, and keep increasing at a compound annual growth rate (CAGR) of 22 % over the next 5 years. A significant trend in global IP traffic growth is a larger CAGR of mobile traffic than that of fixed Internet. In that period, mobile traffic will be consistently dominated by smartphones and phablets, although total traffic share of machine-to-machine (M2M) category is going to grow from 2.7 % in 2015 to 6.7 % in 2020. Not only the emergence of new ICT services but also evolutions from lower-generation network connectivity (e.g., 2G) to higher-generation (e.g., 3G, 3.5G, and 4G or LTE) for mobile devices and connections will be a driver of more enormous global traffic flow. By the end of 2020, 5G deployments will come on the scene which offer significant advances including much higher system capacity and massive device connectivity.

Until around 2008, IP traffic was dominated by peer-to-peer traffic which is transmitted directly between communication devices. However, the current situation is no longer the case; data centers have a major role in delivering today's ICT services to end-users includ-

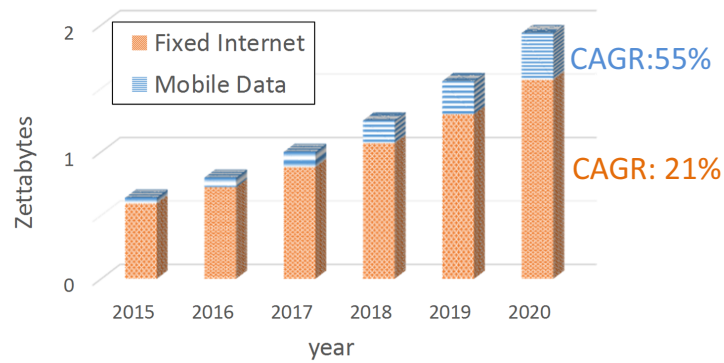


Fig. 1.1 Recent traffic growth and forecast in IP-based network [1].

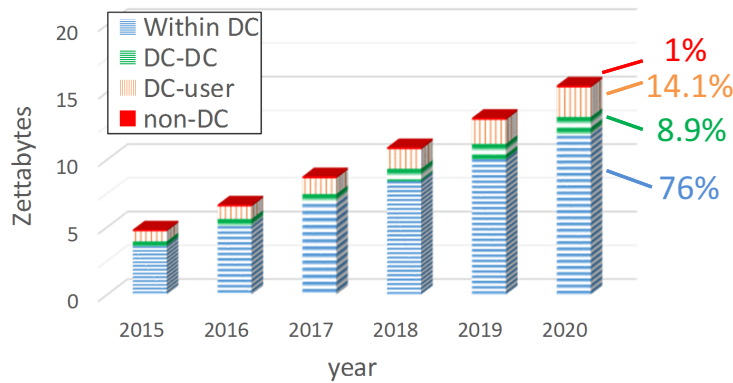


Fig. 1.2 Recent traffic growth and forecast in data center network [2]. “Within DC”, “DC-DC”, “DC-user”, and “non-DC” respectively denote traffic that remains within the data center, traffic that flows from data center to data center, traffic that flows from data center to end-users, and traffic irrelevant to data center. A portion relative to total traffic for each category is also shown in percent.

ing video streaming/broadcasting and cloud storage. Global data center traffic growth and forecast performed by the Cisco Global Cloud Index [2] is shown in Fig. 1.2. The figure indicates that global data center traffic and cloud-based IP traffic have already reached to several ZB in 2015, and will grow at a CAGR of around 30 % from 2015 to 2020. The traffic share irrelevant to data centers (“non-DC”) is also shown for a reference, which is, surprisingly, a much smaller portion even in 2015 when compared with that of DC-relevant traffic. On the other hand, a large portion of data center traffic is governed by “within data center” traffic. One of significant drivers for traffic increase within data center is big data, which is

expected to be enhanced from 10 % to 17 % of all traffic within the data center by 2020. Another remarkable feature of data center traffic is that traffic between data centers is growing faster than either traffic to end-users or traffic within the data center. This high growth is attributed to ongoing network architecture transition in content distribution networks and cloud services in pursuit of cost- and energy-efficiency that need to carry much larger traffic flow across data centers. Cutting-edge technologies such as data analytics based on big data, virtualization of data centers, and applications of M2M/ Internet-of-things (IoT) networks are promising which will bring a valuable development and growth to our society in the near future. Accordingly, intensive and rigorous research efforts including network architecture are continuously needed to build smarter communication systems which support a considerable amount of traffic transportation within/across data centers and all over IP-based network systems.

## 1.2 Evolutions of Optical Communication Systems from a Historical Perspective

### 1.2.1 The Beginning of Optical Communication Systems

One of the most dramatic revolutions in the network industry achieved in the 20th century was the commercialization of the optical communication systems. Optical communication systems that deploy optical fibers as a transmission medium have a capability to transport a huge amount of information data with high reliability and low latency over long distances. Silica-based single mode fibers (SMFs) particularly allow light waves having wavelength around  $1.3 \mu\text{m}$  and  $1.55 \mu\text{m}$  where  $\text{OH}^-$  absorption can be avoided to propagate, and hence the fiber loss becomes relatively low ( $\leq 0.35 \text{ dB/km}$ ). Corresponding frequency range is much higher than those of microwaves mainly used in wireless communications, which offers optical communication systems an extremely large capacity potential.

The intensive study on the optical communication technologies started by the invention of light emitting by stimulated radiation (LASER) in the early 1960s, and by the pioneering work of Charles Kao in 1966 [3] which provided a insight on the possibility of the glass fibers

as a transmission medium for communication purpose. In 1970, the operation of GaAlAs semiconductor lasers at room temperature in continuous wave (CW) regime and optical fiber loss reduction at less than 20 dB/km were respectively demonstrated by [4, 5] and [6]. Intrigued by these outstanding research results, the glass fibers that exhibited extremely low loss were achieved by improving manufacturing process based on  $\text{OH}^-$  removal in the 1970s, and the fiber loss was ultimately decreased down to 0.154 dB/km in 1986. Thus the research and development on the fundamental devices required for optical communication were intensively proceeded from the 1960s to the 1970s, and surprisingly, the first non-experimental optical fiber link installation started in UK in 1975, and soon after in the US and in Japan. The initial optical core networks in Japan had system capacity of 32 Mb/s and 100 Mb/s, and were succeedingly installed as submarine cable networks and access networks.

## 1.2.2 The Evolutions Towards Terabit-Capacity Systems

At an earlier era when transport networks began to deploy optical fibers for telecommunication use, the system capacity was increased mainly by developing electrical time domain multiplexing (ETDM) technologies. In ETDM transmission, multiple data streams are combined (multiplexed) into a single carrier, and eventually each has data-carrying interleaved pulses with short-term duration in a transmission medium. Multiplexing protocols are defined in synchronous optical networking (SONET) and synchronous digital hierarchy (SDH) standardized in the late 1980s to transport digital bit streams worldwide.

The next enabler for boosting the system capacity of fiber-optic transport networks was wavelength division multiplexing (WDM) technologies developed in the 1990s. Erbium-doped fiber amplifier (EDFA) plays a quite important role in WDM transmission. EDFA is used to simultaneously amplify a number of optical channels over a wide wavelength range (e.g., C-band (1530 nm – 1565 nm) or L-band (1565 nm – 1625 nm)). By introducing EDFAs into fiber-optic transmission links at a certain distance, the fiber loss effect is substantially diminished or canceled out, which contributes to cost-effective unrepeated long-haul transport systems. The commercial use of WDM-based transport networks with EDFA amplification began in 1996. As an alternative optical amplification scheme, Raman amplifiers based on stimulated emission were introduced in Japan's terrestrial commercial systems in

2003. Raman amplification is beneficial for mitigating signal-to-noise ratio (SNR) degradation due to its distributed amplification nature in regular optical silica fibers. However, intensity modulation with direct detection (IM-DD) was consistently employed as a means of modulation/detection scheme for optical signals from the ETDM system era, which was no longer ineffective to enhance signal data rate. This is because IM-DD signals above 10 Gb/s are susceptible to chromatic dispersion (CD) and polarization mode dispersion (PMD). The influence of those phenomena may be mitigated by exploring additional multiplexing degree while maintaining signal data rate, which is equivalently understood as the approach to enhance the spectral efficiency. This is because it contributes to bandwidth reduction occupied by an optical signal. Initial commercial attempts in Japan to utilize phase modulation as a new multiplexing degree started in 2007, which enhances signal data rate up to 40 Gb/s by using return-to-zero differential quadrature phase shift keying (RZ-DQPSK).

Digital coherent technologies which combine coherent detection with digital signal processing led optical communication systems to a new stage to achieve further capacity increase. Coherent detection technology was promising to enhance a receiver sensitivity, and hence had been intensively studied in the 1980s. The main technical challenge to commercialize optical coherent transmission at that period was to obtain the stability both of the frequency and phase in a receiver. Unfortunately, the great progress and success of WDM-based transmission systems in the mid-1990s relegated the coherent detection for at least two decades. The digital coherent transmission scheme proposed in 2005 was found to offer several outstanding advances, as well as a solution for the synchronization of the frequency and phase, for optical communication systems as follows:

1. Coherent detection drastically improves the receiver sensitivity with respect to conventional IM-DD schemes owing to the use of high-power local oscillator in a receiver.
2. Signal distortions of the received signals which arise from, say, CD, PMD, or fiber nonlinearity are principally removed or partially mitigated by applying digital signal processing.
3. Multilevel (high-order) modulation and polarization division multiplexing (PDM) techniques can be applied since the phase and polarization information is available due to both the linearity of coherent detection and receiver architecture with polarization

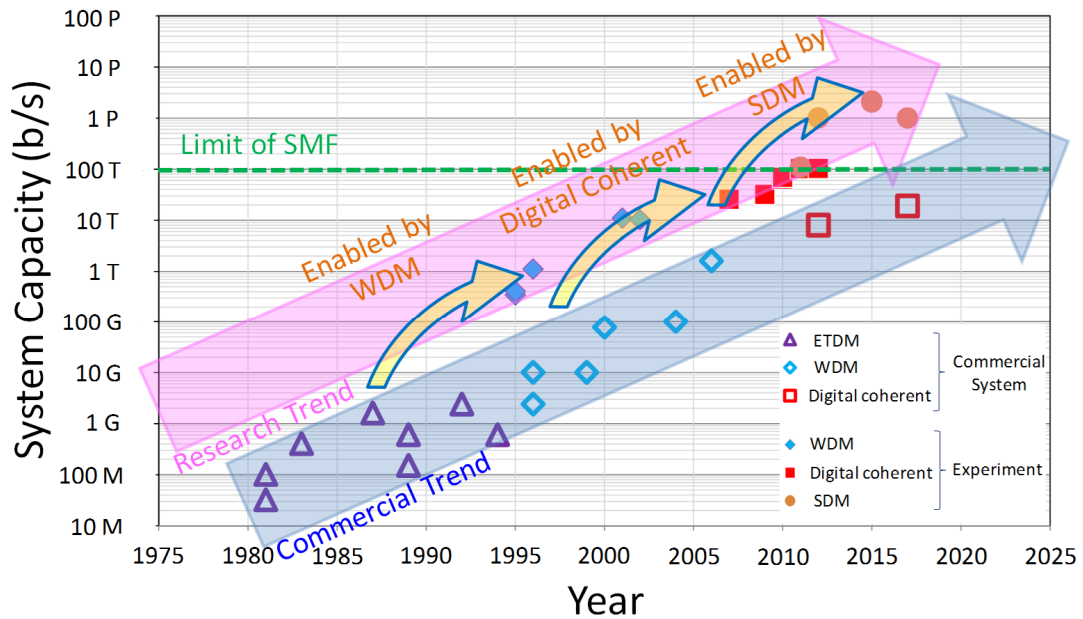


Fig. 1.3 The evolution of fiber-optic communication systems.

diversity, which directly doubles the spectral efficiency.

Digital coherent systems were installed in 2012 in Japan which support 100 Gb/s per channel. As of today, the data rate delivered by a single channel has been increased up to 400 Gb/s, which is particularly devoted networks for inter-data-center connection with the system capacity per optical fiber of 19 Tb/s. The fiber-optic communication systems's evolution is summarized in Fig. 1.3.

In the last three decades, these technological breakthroughs have met the growing demands of the higher-capacity communication systems. In fact, the system capacity has been increased by more than  $10^6$  times in that period. In addition to technologies described above, other advanced technologies including forward error correction (FEC) coding and high-speed electronics/optoelectronics applied to optical signal transmission also significantly contributed to the evolutions of optical communication systems. It is needless to say that the current Internet backbone networks would not emerge without these technologies.



### 1.3 The Capacity Limit in Optical Fibers

Information theory established by Claude Shannon [7] is the masterpiece which introduced the concept of *capacity* of a channel for the first time. The term of the “capacity” of a communication channel is used as the maximal information rate that can be achieved with arbitrarily low error rate over the channel of interest. For the additive white Gaussian noise channel with an input power constraint, the capacity in bits per second  $C$  is

$$C = B \log_2 \left( 1 + \frac{P}{N_0 B} \right), \quad (1.1)$$

where  $B$ ,  $P$ , and  $N_0$  respectively denote bandwidth occupied by a signal, signal power, noise power spectral density. The ratio  $\frac{P}{N_0 B}$  is referred to as signal-to-noise ratio (SNR). It is a quite interesting fact that the capacity is principally determined only by  $B$  and SNR for any communication channel including wired, wireless, and optical communication. Note that above capacity is achieved by employing signal transmission with “a continuous bidimensional Gaussian” constellation. The spectral efficiency SE in bits/s/Hz is readily obtained by dividing the capacity  $C$  in eq. (1.1) by signal bandwidth  $B$ , namely

$$\text{SE}[\text{bits/s/Hz}] = \log_2 (1 + \text{SNR}), \quad (1.2)$$

which can be used for the total capacity analysis of a communication channel.

Since it is obvious that the capacity (and also SE) increases logarithmically with SNR, an optical fiber channel would have no capacity limit if the communication system were to infinitely increase SNR. However, the capacity transition in optical glass fiber as a function of SNR behaves non-monotonically because of the *nonlinear* nature observed in optical fiber. The fiber nonlinearity, also called the optical Kerr effect, is known as phenomena in which a refractive index of a medium varies nonlinearly proportional to the amplitude of an electric field of optical signals. The nonlinear propagation effects induced by channels at different frequency (i.e., cross-phase modulation) appear as noise in the channel of the interest. It is intuitively understood that the theoretical capacity limit would be decreased in the higher input power regime since noise power arisen from the nonlinearity increases with the input power. In [8], by introducing the nonlinearity channel contribution into a linear channel

as multiplicative noise, analytical expression for the channel capacity was obtained which is now called the nonlinear Shannon limit. It should be noted that the capacity limit from this framework involves somewhat impractical assumption that, say, intra-channel nonlinearity (i.e., self-phase modulation) could be completely removed by using “nonlinear precompensation” [8]. In other words, the highest capacity we could practically achieve might be decreased, if the assumption were not satisfied.

While the nonlinear Shannon limit provides insightful implications regarding the achievable maximum information rate in a regular silica glass fiber on which we can make headway, it requires a variety of physical and system parameters to estimate the theoretical fiber capacity. Alternatively, a practical capacity limit can be roughly estimated by considering two facts described below.

1. For long-haul optical signal transmission which requires optical amplifications to compensate for fiber loss, the total amplification bandwidth presently available including C- and L-band is only around 10 THz.
2. The highest spectral efficiency ever reported over a 1000 km transmission is no more than 10 b/s/Hz [9].

The product of these parameters gives the rough estimation of the capacity limit for a long-haul transmission system to be around 100 Tb/s. Although exploring a new amplification bandwidth such as S-band (1460 nm – 1530 nm) could provide a further capacity increase by a factor of several times [10, 11], it never overcomes the catastrophic destruction of a silica glass fiber — called the “fiber fuse” effect [12]— which physically prohibits the fiber input power higher than 1.2–1.5 W per fiber [10].

## 1.4 Space Division Multiplexing as a New Transmission Technology

Space division multiplexing (SDM) transmission is a revolutionary approach that aims to expand aggregated transmission capacity per optical fiber by exploiting the *spatial* degree of freedom in a single cladding as independent waveguides for transmission of parallel data

streams. Considerable research efforts have been devoted to the development of SDM technologies in the last decade, since they are expected to offer a solution against capacity crunch of conventional single-mode optical fibers.

Medium that are currently investigated in SDM transmission as an extension of conventional SMF can be divided substantially into two categories. The first is a multicore fiber (MCF) that positions multiple independent cores into a single cladding. For an ideal “uncoupled” MCF, since signals transmitted over each core are supposed to propagate without power transition to other cores (i.e., without interfering between cores), the use of independent core waveguides provides capacity increase per optical fiber in accordance with core count. The second is a multimode fiber (MMF) that is designed to enlarge core diameter so that a propagation of multiple guided modes as spatial channels is allowed in the wavelength range employed. In the past, an MMF was commonly used in the early beginning of the fiber-optic communication systems, or short-reach interconnections over hundreds of meters, including local area networks (LAN) and data center networks as optical transmission media. This is because in MMF transmission a transmission reach is severely restricted mainly by modal dispersion (i.e., excursion time difference depending on modes) and intermodal coupling. Motivated by recent developments of signal processing techniques and devices in wireless communication, extensive attention has been focused on the capability of the employment of MMF for SDM transmission. Multi-input multi-output (MIMO) theory tells that impact of modal dispersion and inter-modal coupling on mode-multiplexed signals can be removed or mitigated by employing MIMO signal processing in principle, which implies the potential for the increase both of transmission reach and the available mode number as well. Schematic illustration of MCF-based and MMF-based transmission systems are displayed in Fig. 1.4. Since SDM transmission can be combined with existing multiplexing technologies such as TDM and WDM, it can be easily understood that an SDM transmission system is capable to scale the system capacity.

As of today, the highest core count and employed spatial mode number (without polarization) ever reported are respectively 37 [13] and 15 [14]. The combined approach of both, which is so-called MC-MMF, is also effective for the capacity expansion. Indeed, SDM fibers with spatial multiplicity over 100 have been reported in [15–17]. The challenges for the practical application of SDM transmission systems involve the research and development of not

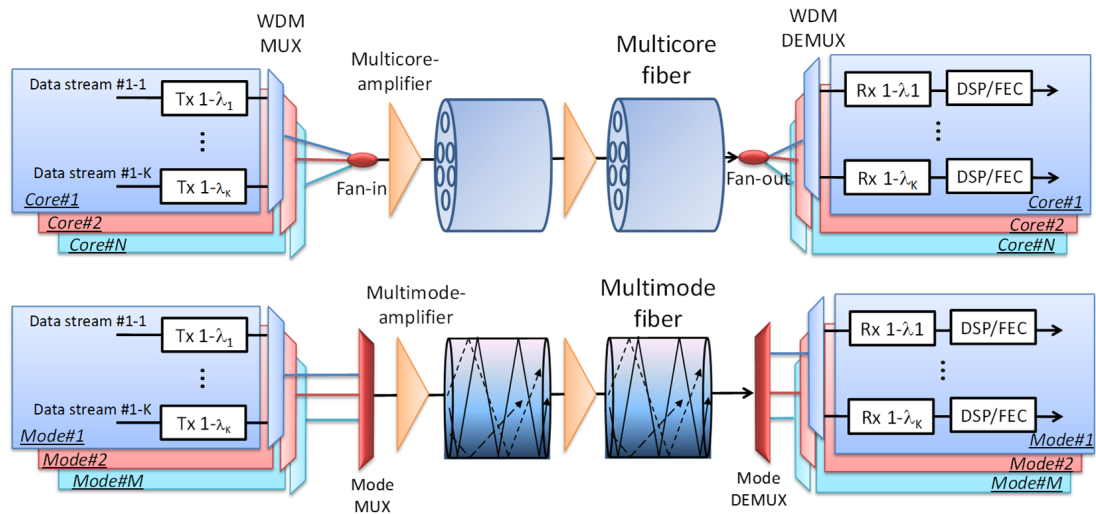


Fig. 1.4 Schematic illustration of MCF-based (top) and MMF-based (bottom) transmission systems.

only transmission medium itself, but also multiplexing/demultiplexing devices, connection devices, and optical SDM amplifiers. Nevertheless, a few SDM transmission experiments with Pb/s class capacity have been successfully demonstrated in recent years [18–21], which means that the SDM research field is now making a steady progress toward a realization of future’s optical SDM communication systems handling the extremely large capacity beyond 100 Tb/s. Detailed cutting-edge researches and other issues will be discussed in Chapter 7.

## 1.5 Contributions of This Thesis

The demand for higher transmission capacity in optical communication systems is expected to continuously grow over the next few decades. Although the present SMF-based optical communication systems allow little room for additional capacity per fiber, approaching the SMF capacity limit may be a cost-effective solution in terms of industrial market maturity. On the other hand, investigating and developing transmission techniques based on a novel waveguide medium is also essential to prepare for an era when a system handling the capacity exceeding 100 Tb/s is required. Therefore this thesis proposes some novel schemes based on statistical and signal processing approaches in consideration of both conventional SMF-based and MCF/MMF-based SDM transmission link systems. Overall relations of the contribution of each chapter is schematically summarized in Fig. 1.5.

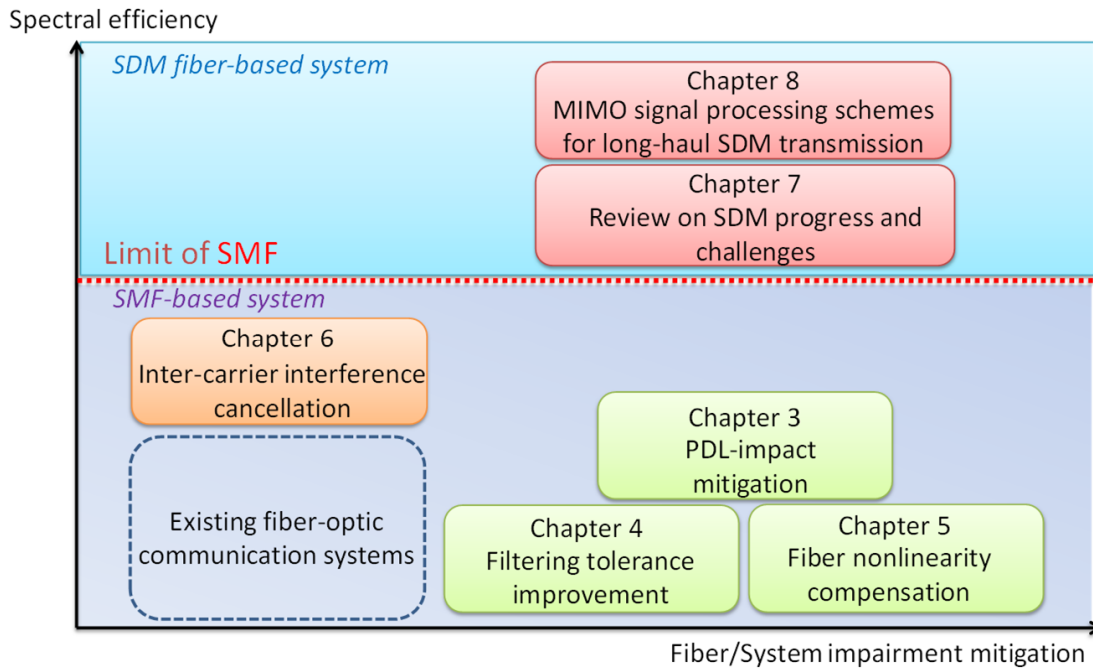


Fig. 1.5 Chapter overview of this thesis.

### 1.5.1 Fundamentals of Advanced Signal Processing

As described in Section 1.2, the developments and integration of various advanced technologies has contributed to supporting a transportation capability of a incredible large amount of data traffic in present optical communication systems. In particular, when discussing significant improvement both in system capacity and in transmission reach achieved after the 2000s, the knowledge on applications of signal processing techniques are inevitable. These are considered as key technologies to bring further system improvement. Chapter 2 provides some introductory reviews of the fundamentals used for optical signal transmission in present optical communication systems.

### 1.5.2 PDL Penalty Reduction by Wavelength-Interleaving Transmission

Multiplexing signals on the polarization domain provides a cost-effective way to double spectral efficiency in existing SMF-based transmission links. However, PDM signals often experience loss/gain difference in optical components depending on their polarization mode,

which is referred to as polarization dependent loss (PDL). This physical phenomena have impact on the theoretical system capacity, and even worse, time-varying frequency-dependent properties, which makes the system design more complicated. Chapter 3 proposes to apply the  $n$ -wavelength-interleaving technique for PDL-impaired transmission links. Utilizing the multiple optical channels located larger than *correlation wavelength* as a super carrier for single data stream is beneficial in averaging optical signal performances, which consequently provides the outage probability reduction. This effect is verified through both a transmission experiment and numerical simulation on the basis of extreme value statistics analysis.

### 1.5.3 Filtering-Tolerant Transmission for Super-Channel Beyond 100 Gb/s

Apart from point-to-point networks, reconfigurable optical add/drop multiplexer (ROADM) nodes are beneficial for reducing network operational expenditure (OPEX), because they are able to directly switch an optical signal at arbitrary frequency (i.e., colorless) into arbitrary ports (i.e., directionless) without optical-electrical conversion. In present metro/regional WDM systems, ROADM node are deployed to build software-provisionable networks. For an optical super-channel comprised of multiple optical subcarriers (SCs), substantial passband reduction due to multiple filtering and/or the center-frequency detuning are considered to be one of the dominant degradation factors in cascaded-ROADM networks. Chapter 4 proposes a novel solution which makes super-channel transmission robust against above optical filtering. Applying MIMO signal processing among SCs enables super-channel performance to be improved, and thus to pass through a larger number of cascaded ROADM nodes.

### 1.5.4 Fiber Nonlinearity Mitigation/Compensation Based on Optical and Digital Approaches

The great success of WDM-based transmission systems in conjunction with optical amplification by EDFAs in the mid-1990s that scaled the system capacity up to around Tb/s is mainly attributed to the increase of optical channel count employed in a single fiber. High

optical power density, however, causes fiber nonlinearities, which inherently decreases the theoretical capacity of a fiber. With an aim to overcome the nonlinear Shannon limit, signal distortions and noise due to fiber nonlinearities need to be removed or mitigated. Chapter 5 discusses and proposes the methodologies for combating with fiber nonlinearity effects by the interplay between optical and digital approaches. Conducted numerical simulation results indicate that the combined use of optical and digital compensation techniques in a dispersion-managed transmission link provides both the computation complexity reduction and the performance improvement as a consequence of mitigation of intra-channel nonlinear distortions. A novel signal processing technique with fast channel tracking property which modifies fast independent component analysis algorithm is also proposed to compensate for polarization crosstalk originated from inter-channel nonlinearity.

### 1.5.5 Multi-Stage SIC for Spectrally-Efficient Super-Nyquist Transmission

The upper bound of the theoretical information-carrying capability of a single fiber (i.e., the fiber capacity) is approximately evaluated on the basis of the nonlinear Shannon limit as described in Section 1.3. However, there still exists a gap between the capacity limit and the record capacities. One of the promising way to achieve the further spectral efficiency improvement is super-Nyquist signal transmission that packs subcarriers tightly with narrower than symbol-rate carrier spacing. A novel super-Nyquist scheme is proposed in Chapter 6 which deliberately superimposes a part of multiple subcarriers. The inter-carrier interferences are iteratively removed by reconstructing and subtracting *replica* signals in a multistage structure. The effects of the spectral efficiency increase are verified through numerical simulation and signal transmission experiments. In addition, the joint adaptation of the above interference mitigation scheme and an error-correcting coding scheme is proposed for further system improvement, which is also verified with the experimental demonstration.

### 1.5.6 State-Of-The-Art Space Division Multiplexing Transmission and Challenges

An astonishing breakthrough achieved in the last decade's optical communication research to overcome the capacity limit per optical fiber is SDM transmission that employs MCFs and/or MMFs as described in Section 1.4. A number of remarkable demonstrations of SDM transmission experiments including extremely-large capacity or long-haul SDM transmission have been reported in the last decade. Chapter 7 aims to provide a brief review of those SDM reports, and discuss remaining challenges to make a further progress toward SDM communication systems with ultimately-high capacity.

### 1.5.7 Space Division Multiplexing Transmission using Multicore and/or Multimode fiber

After reviewing recent progress and discussing challenges in SDM transmission in Chapter 7, three novel signal processing techniques are proposed to combat with them in Chapter 8. The first one is the parallel MIMO frequency-domain equalization to achieve low-complexity modal dispersion compensation. The second is a space-time coding method that spreads the spatial channels at the transmitter in the digital domain to bring the averaging effect for the performance of mode-multiplexed signals. The last is an interference cancellation technique that effectively removes intermodal crosstalk even for mode-multiplexed signals transmitted over channel with large memory. Experimental verifications of those proposed techniques are also provided by conducting a few SDM transmission experiments.



## Chapter 2

# Fundamentals of Advanced Signal Processing

### 2.1 Overview

The emergence of the joint use of coherent detection for optical modulated signals with digital signal processing opened new possibilities to handle phase and polarization as new multiplexing degree to enhance the signal bit rate. The evolution of a optical signal waveform during optical fiber propagation is governed by a nonlinear Schrödinger equation [22]. With the perfect knowledge of all physical parameters regarding with optical fibers and signals at different frequencies, the signal distortions induced by fiber impairments and/or by transmitter/receiver imperfections would be completely canceled, which is not satisfied in the practical optical signal transmission because of unknown parameters, noise accumulation, complicated system architecture. Nevertheless, digital signal processing on optical communication provides a powerful way to combat against these impairments to enable optical signals propagate over long distance with high reliability. Indeed, the DSP application is now essential key technologies for present commercial fiber-optic communication systems. This chapter briefly reviews typical DSP algorithms used in present optical signal transmissions with the aim to provide a deeper understanding for Chapter 3 through Chapter 8.

### 2.2 Waveform Evolution in Optical Fibers

Fiber-optic communication utilizes an electromagnetic wave propagating in an optical fiber to transport and exchange information between distant locations. However, dissipation and/or

dispersion of an optical pulse induces the erroneous communication. Thus, to establish the reliable and robust communication, the understanding on the waveform evolution in an optical fiber is a significantly important topic. The physical phenomena considered in this section includes the fiber loss, the chromatic dispersion, and the fiber nonlinearity, which account for how waveforms evolve during propagation in an optical fiber. The nonlinear Schrödinger equation (NLSE) offers comprehensive explanations of these effects, and has contributed not only to the modeling/analyzing the optical waveform evolutions in the nonlinear regime, but also to overcoming the fiber nonlinearity in conjunction with the digital processing techniques. In this section, the NLSE representation is briefly reviewed, followed by the description of the digital back-propagation algorithm.

### 2.2.1 Nonlinear Schrödinger Equation

The inherent power loss during propagation in an silica-based glass fiber is mainly induced from the  $\text{OH}^-$  absorption and Rayleigh scattering. The former has a few absorption peaks at around  $0.94 \mu\text{m}$ ,  $1.24 \mu\text{m}$ , and  $1.38 \mu\text{m}$ , which corresponds to the wavelength band of around  $0.85 \mu\text{m}$ ,  $1.3 \mu\text{m}$ , and  $1.55 \mu\text{m}$  used for optical communication purpose. Rayleigh scattering is a inevitable phenomena for a silica-based glass fiber which is arisen from the non-homogeneous density fluctuations occurred during manufacture. The intrinsic loss due to Rayleigh scattering has the wavelength-dependent variation proportional to  $\lambda^{-4}$ , where  $\lambda$  stands for the wavelength of interest. Therefore the Rayleigh scattering loss can be reduced by the wavelength range, say, from 1 dB/km at  $\lambda = 1 \mu\text{m}$  to 0.1 dB/km at  $\lambda = 1.6 \mu\text{m}$ .

Chromatic dispersion (CD) has a major impact on the waveform evolution in optical fiber propagation, which is arisen from the frequency dependency of the refractive index  $n(\omega)$ , where  $\omega$  is the angular frequency. Considering the fact that constituent of an optical pulse at each frequency travels at different speed of  $c/n(\omega)$ , where  $c$  is the speed of light in vacuum, CD phenomenon is intuitively understood as pulse broadening. The mode propagation constant  $\beta$  is expanded in a Taylor series about the center frequency  $\omega_0$  as [22]

$$\beta(\omega) = n(\omega) \frac{\omega}{c} = \beta_0 + \beta_1(\omega - \omega_0) + \frac{1}{2}\beta_2(\omega - \omega_0)^2 + \dots, \quad (2.1)$$

where

$$\beta_m = \left( \frac{d^m \beta}{d\omega^m} \right)_{\omega=\omega_0}. \quad (2.2)$$

The inverse of  $\beta_1$  is the group velocity (GV) defined as  $v_g \stackrel{\text{def}}{=} \frac{1}{\beta_1}$ , and  $\beta_2$  is responsible for the pulse broadening, which is referred to as group-velocity dispersion (GVD).

The evolution of the waveform envelop  $E(z, t)$  is governed by the NLSE expressed as

$$\frac{\partial E}{\partial z} + \beta_1 \frac{\partial E}{\partial t} + \frac{j}{2} \beta_2 \frac{\partial^2 E}{\partial t^2} + \frac{\alpha}{2} E = j\gamma |E|^2 E, \quad (2.3)$$

where  $\alpha$  and  $\gamma$  respectively denote the attenuation constant and the nonlinearity constant. While considering additional terms in eq. (2.3) including the effect of  $\beta_3$  will provide a more accurate insight on waveform evolution especially for ultrashort optical pulses with width  $\leq 100$  fs [22], it is the out of the scope of this thesis. Transforming eq. (2.3) into the so-called *retarded frame* is beneficial in the practical analysis on the waveform evolution, because the GV effect does not impose any distortion on the waveform. The retarded frame representation is obtained by using following transformation:

$$T = t - \frac{z}{v_g}. \quad (2.4)$$

Eq. (2.4) allows the NLSE to be rewritten in the retarded frame as

$$\frac{\partial E}{\partial z} + \frac{j}{2} \beta_2 \frac{\partial^2 E}{\partial t^2} + \frac{\alpha}{2} E = j\gamma |E|^2 E. \quad (2.5)$$

The second and third terms on the left-hand side in eq. (2.5) respectively account for the GVD and the fiber loss effects. The right-hand side term that represents the fiber nonlinearity effects explicitly involves the squared term of the waveform envelope, corresponding to the optical signal power.

## 2.2.2 Digital Back-Propagation

We have seen that the waveform evolution is governed by the NLSE in eq. (2.5). Although it may unveil complicated relationships among the fiber loss, the chromatic dispersion, and fiber nonlinearity with a knowledge of the fiber parameter, the analytic solution cannot be generally derived from eq. (2.5) because it is described in the form of the nonlinear partial

differential equation. The split-step Fourier (SSF) method is a well-known strategy to provide an numerical evaluation for eq. (2.5). The main idea behind the SSF method is that, during a small propagation step, the contribution on  $E$  from the linear term is assumed to be preserved while the evolution of  $E$  is exclusively from the nonlinear term, and vice versa. The SSF method starts from the definition of a linear operator  $\hat{D}$  and a nonlinear operator  $\hat{N}$  as

$$\hat{D} = -\frac{j}{2}\beta_2 \frac{\partial^2}{\partial t^2} - \frac{\alpha}{2}, \quad (2.6)$$

$$\hat{N} = j\gamma|E|^2. \quad (2.7)$$

Note that  $\hat{D}$  is performed in the Fourier domain. The waveform representation in the Fourier domain  $\tilde{E}(z, \omega)$  is obtained through the Fourier transform of  $E(z, t)$ , expressed as

$$\tilde{E}(z, \omega) = \mathcal{F}[E(z, t)], \quad (2.8)$$

where  $\mathcal{F}[\cdot]$  denotes the Fourier transform operation. Eq. (2.5) is now rewritten using eq. (2.7) as

$$\frac{\partial E}{\partial z} = (\hat{D} + \hat{N})E. \quad (2.9)$$

After excursion with a small propagation step  $h$  from  $z$ , eq. (2.9) to the first order becomes

$$E(z + h, t) = \exp(h\hat{D})\exp(h\hat{N})E(z, t), \quad (2.10)$$

where the noncommutating property between  $\hat{D}$  and  $\hat{N}$  is ignored [22]. The SSF scheme executes the nonlinear step and the linear step iteratively as follows [23]

- *Nonlinear step:* Perform the nonlinear operation in eq. (2.9) alone, which is equivalent to the phase rotation whose value is proportional to the instant signal power, namely,

$$E(z + h, t) = \exp(j\gamma h|E|^2)E(z, t). \quad (2.11)$$

- *Linear step:* Perform the linear operation in eq. (2.9) alone. By using eq. (2.8), the linear operation in eq. (2.9) acts as

$$\tilde{E}(z + h, \omega) = \exp\left[-\left(\frac{\alpha}{2} - j\frac{\beta_2}{2}\omega^2\right)h\right]\tilde{E}(z, \omega). \quad (2.12)$$

The combined expression of eq. (2.11) and eq. (2.12) yields

$$E(z + h, t) = \left[ \mathcal{F}^{-1} \exp \left[ - \left( \frac{\alpha}{2} - j \frac{\beta_2}{2} \omega^2 \right) h \right] \mathcal{F} \right] \exp(j\gamma|E|^2) E(z, t). \quad (2.13)$$

Applying fine step (i.e., small  $h$ ) and/or feeding the other signal waveform information at different frequency into the SSM method provides more accurate numerical prediction at the expense of high computational complexity.

As described in Chapter 1, the digital coherent transmission opens a new possibility into optical signal transmission technologies. Particularly, the linear coherent receiver allows to inform the received signal waveform in terms both of amplitude and phase. Digital back-propagation (DBP) in conjunction with coherent detection was proposed in [24] to perform joint fiber impairment compensation for linear and nonlinear effects simultaneously in the digital domain. The philosophy of DBP scheme is based on SSF method described above, and a straightforward approach in a sense that it solves the NLSE inversely started from a receiver end. The DBP representation with a small propagation step  $h$  is then readily obtained using eq. (2.13) as

$$E(z - h, t) = \exp(-j\gamma|E|^2) \left[ \mathcal{F}^{-1} \exp \left[ \left( \frac{\alpha}{2} - j \frac{\beta_2}{2} \omega^2 \right) h \right] \mathcal{F} \right] E(z, t). \quad (2.14)$$

In the DBP operation, adjusting the propagation step which brings reasonable performance improvement against the fiber nonlinearity often requires careful optimization. Fortunately, the step size equal to the length of a fiber span  $L$  may work with the reasonable performance and the computational complexity [23]. Assuming that signal input power is constant at the input of each fiber span by employing optical amplification, eq. (2.14) with the step size condition  $h = L$  can be simplified as

$$E(z - L, t) = \exp(-j\gamma|E|^2) \left[ \mathcal{F}^{-1} \exp \left[ - \left( j \frac{\beta_2}{2} \omega^2 \right) L \right] \mathcal{F} \right] E(z, t), \quad (2.15)$$

because the term of signal power variation during span propagation can be omitted. Alternatively, eq. (2.15) is understood that it performs the nonlinear rotation at the the fiber span input where signals exhibit the highest power in a fiber span, considering the fiber nonlinearity property which has the greater impact for higher signal power.

## 2.3 Performance Metric in Optical Signal Transmission

### 2.3.1 Optical Signal-to-Noise Ratio

As with an SNR or an SNR per bit (denoted as  $E_b/N_0$  where  $E_b$  is the average energy per bit per polarization) used in wireless communication, same metrics are also occasionally used for the performance evaluation of optical signal transmission of interest. The performance metric more commonly used, however, is the optical SNR (OSNR) which is defined as the power ratio of the optical signal power  $P$  to the noise power in a reference bandwidth  $B_{\text{ref}}$  normally set to be 0.1 nm corresponding to 12.5 GHz at the wavelength of 1550 nm. Since the OSNR is the metric in the optical domain, amplified spontaneous emission (ASE) noise produced by optical amplifiers including EDFAs and Raman amplifiers is considered to be a dominant noise source. Another important feature in evaluating OSNR is that the noise in both polarization states should be considered. The OSNR is hence written as [11]

$$\text{OSNR} = \frac{P}{2N_0 B_{\text{ref}}}, \quad (2.16)$$

where  $N_0$  is the noise spectral density per polarization. Note that, since only PDM signals are assumed in this thesis, the signal power  $P$  is calculated by summing up over both polarization states. The relations between SNR and OSNR is obtained from eq. (2.16) as

$$\text{OSNR} = \frac{B}{B_{\text{ref}}} \text{SNR}, \quad (2.17)$$

where  $B$  is the bandwidth occupied by the optical signal of interest. By assuming the signal waveform generated with the sinc function  $\text{sinc}(t)/t$  which assures a minimum bandwidth equal to signal symbol rate  $R_s$  based on the Nyquist criterion, an SNR per bit  $E_b/N_0$  is related with OSNR as

$$\frac{E_b}{N_0} = \frac{B_{\text{ref}}}{\log_2(M)B} \text{OSNR}, \quad (2.18)$$

where  $M$  is the modulation order (or, equivalently, the number of constellation points).

Theoretical BER equations for modulated signals under AWGN channel can be generally (or approximately) derived using some assumptions. For Gray-mapped rectangular QAM

signals, theoretical BER in the  $E_b/N_0$  form is approximately evaluated as [25]

$$BER \approx \frac{2(\sqrt{M} - 1)}{\sqrt{M} \log_2(M)} \operatorname{erfc} \left( \sqrt{\frac{3 \log_2(M) E_b}{2(M-1) N_0}} \right), \quad (2.19)$$

where  $\operatorname{erfc}(\cdot)$  stands for the complementary error function, defined as

$$\operatorname{erfc}(x) = \frac{2}{\sqrt{\pi}} \int_x^\infty \exp(-y^2) dy. \quad (2.20)$$

With eq. (2.18) and eq. (2.19), optical signal BER performance can be roughly analyzed under an optical signal transmission of interest (particularly for ideal coherent transmission). As simple examples, theoretical BERs of Gray-mapped optical PDM signals for QPSK, 16QAM, 64QAM formats are respectively obtained by substituting eq. (2.18) into eq. (2.19) as

$$BER_{\text{PDM-QPSK}} = \frac{1}{2} \operatorname{erfc} \left( \sqrt{\frac{E_b}{N_0}} \right) = \frac{1}{2} \operatorname{erfc} \left( \sqrt{\frac{B_{\text{ref}}}{2B} \text{OSNR}} \right) \quad (2.21)$$

for an optical PDM-QPSK signal, and

$$BER_{\text{PDM-16QAM}} = \frac{3}{8} \operatorname{erfc} \left( \sqrt{\frac{2E_b}{5N_0}} \right) = \frac{3}{8} \operatorname{erfc} \left( \sqrt{\frac{B_{\text{ref}}}{10B} \text{OSNR}} \right) \quad (2.22)$$

for an optical PDM-16QAM signal, and

$$BER_{\text{PDM-64QAM}} = \frac{7}{24} \operatorname{erfc} \left( \sqrt{\frac{E_b}{7N_0}} \right) = \frac{7}{24} \operatorname{erfc} \left( \sqrt{\frac{B_{\text{ref}}}{42B} \text{OSNR}} \right) \quad (2.23)$$

for an optical PDM-64QAM signal,

Fig. 2.1 shows theoretical BER curves of PDM-QPSK, 16QAM, or 64QAM signals driven at 30, 60, or 90 GBaud derived from eq. (2.21) through eq. (2.23). The important consequence implicated from Fig. 2.1 is that the required OSNR differs among different format signals with the same bit rate to achieve a particular BER. This difference is sometimes referred to as OSNR penalty. For example, the OSNR penalty between QPSK and 16QAM, and one between QPSK and 64QAM are respectively become  $\sim 4$  dB, and  $\sim 8$  dB. In an optical signal transmission in which multiple optical amplifications are performed, the OSNR penalty has a direct impact on the maximum transmission reach. Thus it can be understood that employing higher modulation format indeed enhances spectral efficiency at the expense of the achievable transmission reach.

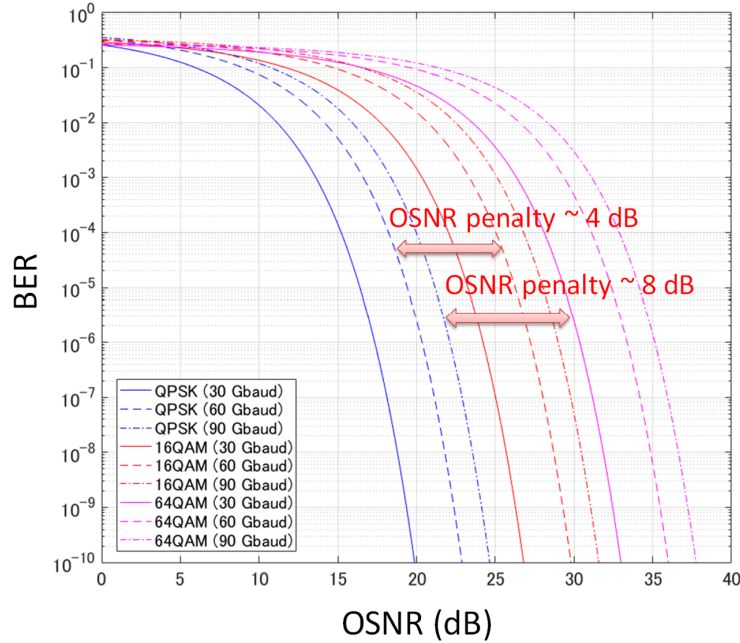


Fig. 2.1 Theoretical BERs for PDM-QPSK, 16QAM, or 64QAM signals driven at 30, 60, or 90 GBaud. The OSNR penalty switched from QPSK to 16QAM is  $\sim 4$  dB, and one from QPSK to 64QAM is  $\sim 8$  dB.

### 2.3.2 Bit Error Rate and Relations with $Q$ -factor

BER is considered as the fundamental performance metric to evaluate the statistical accuracy of digital bit-stream transmission. An alternative quantity is the  $Q$ -factor (also denoted as  $Q^2$ -factor in some literatures) that allows the system performance evaluation in the linear terms instead of the exponential terms for BER-based evaluation. Before deriving the relationships between BER and  $Q$ -factor, let us consider a decision circuit in a receiver for binary-data transmission. Fig. 2.2 schematically illustrates the probability density functions (PDFs) of received samples of binary data in a receiver-side decision circuit that was originally located either  $I_1$  corresponding to bit “1”, or  $I_0$  corresponding to bit “0” in a transmitter. If decision boundary is set to  $I_D$ , an error is observed if the sampled value  $I$  becomes  $I \leq I_D$  for bit 1 due to noise, or oppositely, if  $I \geq I_D$  for bit 0. Suppose that both bits are equally generated and transmitted, BER becomes

$$BER = p(1)p(0|1) + p(0)p(1|0) = \frac{1}{2} (p(0|1) + p(1|0)), \quad (2.24)$$



where  $P(i|j)$  is the probability of deciding  $i$  as the transmitted bit when  $j$  is transmitted. Assuming the case that a memory-less white additive Gaussian noise (AWGN) is imposed with variance of  $\sigma_i$  for bit  $i$  on received samples in which a noise source does not matter if it is either shot-noise, thermal-noise, or ASE noise,  $P(i|j)$  has the explicit form as

$$p(0|1) = \frac{1}{\sigma_1 \sqrt{2\pi}} \int_{-\infty}^{I_D} \exp\left(-\frac{(I - I_1)^2}{2\sigma_1^2}\right) dI = \frac{1}{2} \operatorname{erfc}\left(\frac{I_1 - I_D}{\sigma_1 \sqrt{2}}\right), \quad (2.25)$$

$$p(1|0) = \frac{1}{\sigma_0 \sqrt{2\pi}} \int_{I_D}^{\infty} \exp\left(-\frac{(I - I_0)^2}{2\sigma_0^2}\right) dI = \frac{1}{2} \operatorname{erfc}\left(\frac{I_D - I_0}{\sigma_0 \sqrt{2}}\right). \quad (2.26)$$

Replacing  $P(0|1)$  and  $P(1|0)$  in eq. (2.24) by eq. (2.25) and eq. (2.26) yields

$$BER = \frac{1}{4} \left[ \operatorname{erfc}\left(\frac{I_1 - I_D}{\sigma_1 \sqrt{2}}\right) + \operatorname{erfc}\left(\frac{I_D - I_0}{\sigma_0 \sqrt{2}}\right) \right]. \quad (2.27)$$

In the use of  $p$ - $i$ - $n$  photodiode, the same variance of noise and the decision boundary in the middle between  $I_1$  and  $I_0$  are commonly approximated as  $\sigma_1 = \sigma_0$  and  $I_D = (I_1 + I_0)/2$ . In that case, (2.27) is rewritten as

$$BER = \frac{1}{2} \operatorname{erfc}\left(\frac{Q}{\sqrt{2}}\right), \quad (2.28)$$

where  $Q$  is corresponding to  $Q$ -factor in the linear scale, which is defined as

$$Q \stackrel{\text{def}}{=} \frac{|I_D - I_i|}{\sigma_i}. \quad (2.29)$$

$Q$ -factor in the logarithmic domain is derived using (2.28) as

$$Q\text{-factor [dB]} = 20 \log_{10} \left[ \sqrt{2} \operatorname{erfcinv}(2 BER) \right], \quad (2.30)$$

where  $\operatorname{erfcinv}(\cdot)$  stands for the inverse complementary error function. Eq. (2.30) is practically used as a performance metric of optical signal transmission not only for BPSK but also for other multilevel format signals including QPSK, 8QAM, 16QAM, and higher, despite of the fact that their mappings are deviated from the strict definition of  $Q$ -factor described above. Nevertheless, the intuitive property of  $Q$ -factor to understand and compare the transmission performance is attractive in designing the fiber-optic systems as described in the ITU-T recommendation G.975.1. The  $Q$ -factor curve is shown in Fig. 2.3 as a function of BER derived from Eq. (2.30). Theoretical signal performance of PDM-QPSK, 16QAM, or 64QAM is again represented in Fig. 2.4 in the same format as Fig. 2.1 except that the vertical metric is changed from BER to  $Q$ -factor.

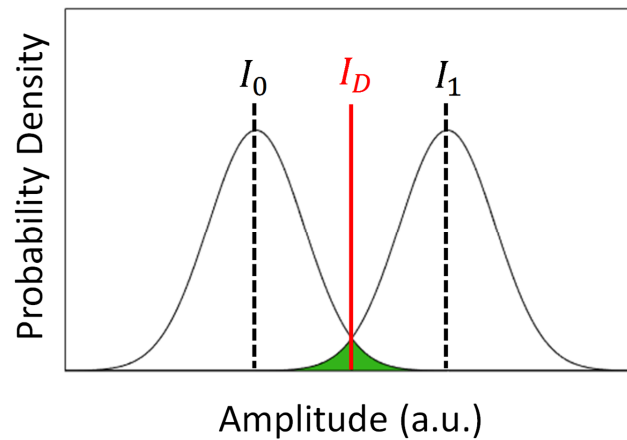


Fig. 2.2 Schematic of Gaussian probability density of received samples. Shading region corresponds to the probability of erroneous ones.

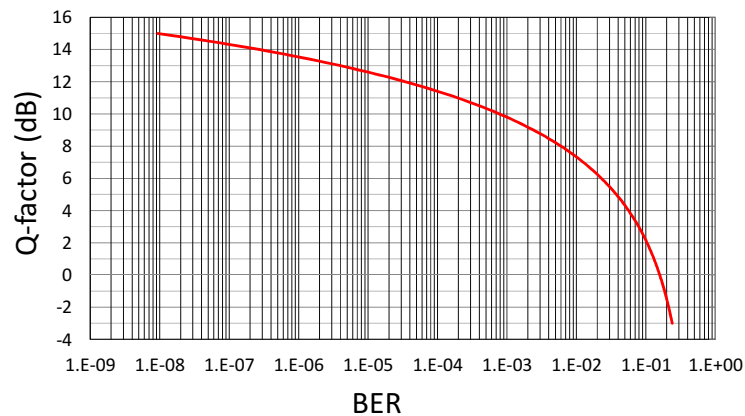


Fig. 2.3 Relation between BER and  $Q$ -factor.

## 2.4 Adaptive Filtering Techniques

As of today, a number of application of the adaptive filter theory can be found in such diverse fields as system identification, adaptive equalization for communications, digital representation of speech, echo and noise cancellation [26]. Due to its manageable simplicity, the adaptive filter has also succeeded in the fields of neural networks and machine learning. As with optical communications, the use of a linear receiver in digital coherent transmission allows us to deal with some fundamental physical phenomena in an SMF transmission including CD and PMD as linear distortions, although they were originally significant performance

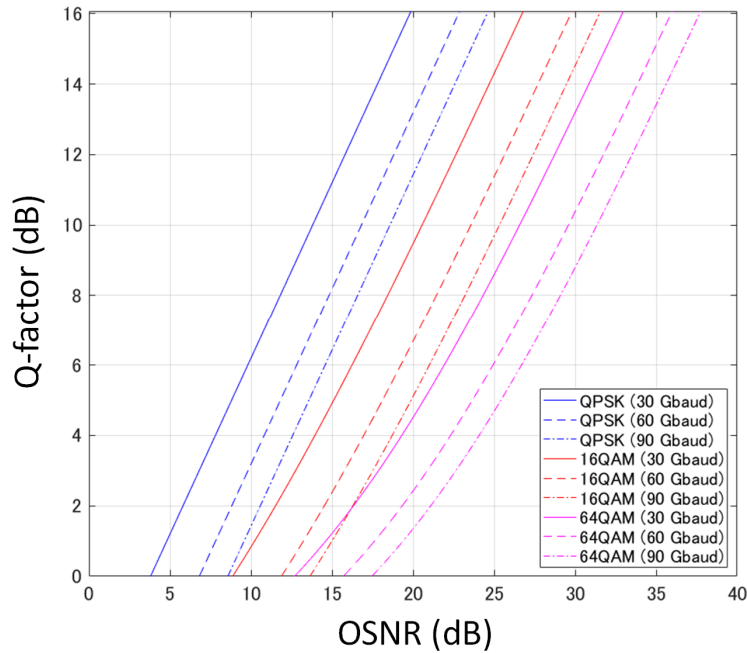


Fig. 2.4 Theoretical  $Q$ -factor for PDM-QPSK, 16QAM, or 64QAM signals driven at 30, 60, or 90 GBaud derived from eq. (2.21) through eq. (2.23).

limiting factors in high-speed IM-DD systems until the mid-2000s. For optical MIMO signal transmission which will be discussed in Chapter 7 and Chapter 8, modal crosstalk (i.e., mixing among spatial mode signals) is completely decoupled in the noise free regime by using an adaptive-filter-based MIMO equalizer, which has indeed contributed to recently-achieved transmission reach extension in optical MIMO signal transmission experiments. In this section, fundamentals of adaptive signal processing are briefly reviewed. A simple application example of the adaptive filter in optical signal transmission is also provided.

### 2.4.1 Classical Wiener Filter Theory

We first construct a transversal filter at time  $t$  which has a tap weight vector  $\mathbf{w}(t) = [w_0(t), w_1(t), \dots, w_{L-1}(t)]^T$ . Let us consider a problem in which  $\mathbf{w}(t)$  with memory length  $K$  is designed in a manner that an output signal from the transversal filter approaches the desired signal. The output, which is equivalent to the estimated transmitted signal  $\hat{x}(t)$ , is

obtained by

$$\hat{x}(t) = \sum_{k=0}^{K-1} w_l^*(t)y(t-k) = \mathbf{w}^H(t)\mathbf{y}(t), \quad (2.31)$$

where  $\mathbf{y}(t) = [y(t), y(t-1), \dots, y(t-K+1)]^T$  is the received signal vector. The estimation error  $e(t)$  is determined by the difference between the desired signal  $d(t)$  and the instant output  $\hat{x}(t)$  as

$$e(t) = d(t) - \hat{x}(t) = d(t) - \mathbf{w}(t)^H \mathbf{y}(t). \quad (2.32)$$

The mean squared error  $J(\mathbf{w})$  is defined as

$$J(\mathbf{w}) \stackrel{\text{def}}{=} \mathbb{E}[e(t)e^*(t)]. \quad (2.33)$$

The Wiener theory ensures that minimizing  $J(\mathbf{w})$  in eq. (2.33) provides the optimum linear filter in the minimum mean square sense [26]. Substituting eq. (2.32) into eq. (2.33) gives

$$\begin{aligned} J(\mathbf{w}) &= \mathbb{E}[d(t)d^*(t)] - \mathbf{w}^H(t)\mathbb{E}[\mathbf{y}(t)d^*(t)] - \mathbb{E}[d(t)\mathbf{y}^H(t)]\mathbf{w}(t) + \mathbf{w}^H(t)\mathbb{E}[\mathbf{y}(t)\mathbf{y}^H(t)]\mathbf{w}(t) \\ &= \sigma_d^2 - \mathbf{w}^H(t)\mathbf{p} - \mathbf{p}^H\mathbf{w}(t) + \mathbf{w}^H(t)\mathbf{R}\mathbf{w}(t), \end{aligned} \quad (2.34)$$

where each quantity is respectively defined as  $\sigma_d^2 \stackrel{\text{def}}{=} \mathbb{E}[d(t)d^*(t)]$ ,  $\mathbf{p} \stackrel{\text{def}}{=} \mathbb{E}[\mathbf{y}(t)d^*(t)]$  which is called a cross-correlation vector, and  $\mathbf{R} \stackrel{\text{def}}{=} \mathbb{E}[\mathbf{y}(t)\mathbf{y}^H(t)]$  which is called correlation matrix.

Our purpose in this subsection is to find the bottom or minimum point of the error-performance-surface of  $J(\mathbf{w})$ , which is equivalent to the differentiation operation of  $J(\mathbf{w})$  with respect to  $\mathbf{w}$ . The famous analytical solution of eq. (2.34) known as the Wiener-Hopf equation is obtained under the assumption of the stationarity of both  $\mathbf{y}(t)$  and  $d(t)$ . In that case, the differentiation becomes

$$\begin{aligned} \frac{\partial J(\mathbf{w})}{\partial \mathbf{w}} &= \frac{\partial \sigma_d^2}{\partial \mathbf{w}} - \frac{\partial (\mathbf{w}^H \mathbf{p})}{\partial \mathbf{w}} - \frac{\partial (\mathbf{p}^H \mathbf{w})}{\partial \mathbf{w}} + \frac{\partial (\mathbf{w}^H \mathbf{R} \mathbf{w})}{\partial \mathbf{w}} \\ &= \mathbf{0} - 2\mathbf{p} - \mathbf{0} + 2\mathbf{R}\mathbf{w}. \end{aligned} \quad (2.35)$$

In (2.35), the fact that  $\sigma_d^2$  is a constant value is used. Therefore, by recalling that  $J(\mathbf{w})$  becomes  $\mathbf{0}$  at the the bottom or minimum point of the error-performance-surface, an optimum tap weight vector  $\mathbf{w}_o$  is obtained as

$$\begin{aligned} \mathbf{R}\mathbf{w}_o &= \mathbf{p} \\ \Leftrightarrow \mathbf{w}_o &= \mathbf{R}^{-1}\mathbf{p}. \end{aligned} \quad (2.36)$$

$\mathbf{w}_o$  is called the Wiener filter. Obviously, deriving  $\mathbf{w}_o$  requires the knowledge of  $\mathbf{p}$  and  $\mathbf{R}$ . This feature is likely to be impractical in a high-speed data communication including optical communication in which channel state and information data to be transmitted varies in a short-term period.

### 2.4.2 Adaptive Filtering Based on the Stochastic Gradient: LMS Algorithm

Despite of the significant feature of ease in designing the Wiener filter, the fact that it requires knowledge on the transmitted and desired signal makes it more difficult to apply for high-speed data communication. This drives a motivation to modify the Wiener filter for more practical framework, which is the main topic of this subsection. One promising way to do it is to employ the method of steepest descent method, which gives a dynamical approach to the issue. The main idea is that updating  $\mathbf{w}$  slightly at a certain time interval should eventually let it approach to  $\mathbf{w}_o$ . The tap-updating direction is determined by the differentiation operation of  $J(\mathbf{w})$  respective to  $\mathbf{w}$ , namely, eq. (2.35). In the recursive form, it can be written as

$$\begin{aligned}\mathbf{w}(t+1) &= \mathbf{w}(t) - \frac{1}{2}\mu \frac{\partial J(\mathbf{w})}{\partial \mathbf{w}}, \\ &= \mathbf{w}(t) + \mu[\mathbf{p} - \mathbf{R}\mathbf{w}(t)],\end{aligned}\tag{2.37}$$

where  $\mu$  is the step-size parameter. Comparison of eq. (2.40) with eq. (2.36) implies that the computation in eq. (2.40) is relatively simple in a sense that it requires no matrix inversion to obtain  $\mathbf{w}_o$ . However, the knowledge of  $\mathbf{p}$  and  $\mathbf{R}$  is still assumed, which means that it requires further modification toward the practical form.

Going back to eq. (2.34), let us redefine of  $J(\mathbf{w})$  by removing the expectation operation  $E[\cdot]$ :

$$J_{\text{re}}(\mathbf{w}) \stackrel{\text{def}}{=} e(t)e^*(t).\tag{2.38}$$

Taking the differentiation of  $J_{\text{re}}(\mathbf{w})$  gives

$$\frac{\partial J_{\text{re}}(\mathbf{w})}{\partial \mathbf{w}} = -2e(t)\mathbf{y}^*(t).\tag{2.39}$$

Accordingly, eq. (2.40) is rewritten as

$$\mathbf{w}(t+1) = \mathbf{w}(t) + \mu e(t)\mathbf{y}^*(t).\tag{2.40}$$

This approach aims to determine the tap-updating direction by using the instantaneous estimates based on  $\mathbf{y}(t)$  and  $e(t)$  at each updating time, which is called the adaptive least mean square (LMS) algorithm, also known as the stochastic gradient algorithm.

LMS approach might be seemingly ineffective for optical communication application in the case that the time scale of channel-state variation is less than the symbol interval of optical signals. Their feasibilities are, however, well exploited in a number of transmission experiments over both SMFs and SDM fibers, because a channel typically varies much slower than symbol interval.

At the end of this subsection, the practical strategy for application of LMS algorithm should be provided, particular for the feeding method of “desired signals” in computing  $e(t)$  in eq. (2.40). In the LMS application in optical signal transmission, two main strategies are typically chosen:

- *The data-aided (DA) LMS* in which the desired signals are fed in every update as the prior-known symbol sequences, or as the periodic training symbol sequences inserted in particular part of a transmitted frame.
- *The decision-directed (DD) LMS* which intends to estimate the desired signal  $\hat{d}(t)$  by using the tap weight vector obtained in the previous tap updating as  $\hat{d}(t) = \mathbf{w}^H(t - 1)\mathbf{y}(t)$ .

Practically, these two strategies are jointly employed in such a manner that the initial convergence is performed by DA-LMS as training mode, then switched to DD-LMS as tracking mode.

### 2.4.3 Adaptive MIMO Equalization in PDM Systems

In an ideal SMF with perfect cylindrical geometry and isotopic material, two polarization degenerate modes are permitted for propagation [22]. A practical SMF, however, is manufactured with a slight deviation from the ideal condition, which breaks the mode degeneracy. In addition, the ideal degenerate condition may also be not satisfied by other perturbations including macrobending and external stress. PDM transmission utilizes the resultant slight mode-propagation constant difference which is called modal birefringence as an additional

multiplexing degree in fiber-optic communication systems. PDM transmission directly doubles the spectral efficiency in a standard SMF, and now becomes the fundamental technology to support present large-capacity commercial fiber-optic communication systems after the 2010s. It should be noted that much contribution has been done in the success of PDM transmission systems by the coherent receiver with polarization-diversity structure and by digital signal processing technology for polarization demultiplexing. This subsection focuses on the latter topic from a perspective of adaptive filtering technique.

If propagation distance of PDM signals exceeds the correlation length (or the beat length), the polarization state launched into an SMF changes into arbitrary polarization [22]. Unfortunately, the polarization state observed at a receiver may change temporally and have the statistical property due to external stress or thermal variation, which makes optical polarization demultiplexing impractical. The adaptive filtering technique offers a powerful tool against this issue, since a coherent PDM transmission system can be modeled by a  $2 \times 2$  MIMO system (as we will see in eq. (7.11)). Denoting the quantity relevant to two polarization tributaries with  $X$  and  $Y$ , the channel transfer matrix  $\mathbf{H}$  with a memory length of  $K$  has a form of

$$\begin{aligned} \mathbf{H} &= \begin{pmatrix} \mathbf{h}_{XX} & \mathbf{h}_{XY} \\ \mathbf{h}_{YX} & \mathbf{h}_{YY} \end{pmatrix} \\ &= \begin{pmatrix} h_{XX,0} & h_{XX,1} & \cdots & h_{XX,K-1} & h_{XY,0} & h_{XY,1} & \cdots & h_{XY,K-1} \\ h_{YX,0} & h_{YX,1} & \cdots & h_{YX,K-1} & h_{YY,0} & h_{YY,1} & \cdots & h_{YY,K-1} \end{pmatrix}, \end{aligned} \quad (2.41)$$

where  $\mathbf{h}_{ij} = [h_{ij,0} \ h_{ij,1} \ \cdots \ h_{ij,K-1}]$  ( $i, j \in \{X, Y\}$ ).

#### 2.4.3.1 LMS-based Adaptive MIMO Equalization

We construct a  $2 \times 2$  transversal filter to extract one polarization tributary by which the two output signals from the filter is obtained as

$$\hat{x}_X(t) = \mathbf{w}_{XX}^T(t) \mathbf{y}_X(t) + \mathbf{w}_{XY}^T(t) \mathbf{y}_Y(t), \quad (2.42)$$

$$\hat{x}_Y(t) = \mathbf{w}_{YX}^T(t) \mathbf{y}_X(t) + \mathbf{w}_{YY}^T(t) \mathbf{y}_Y(t), \quad (2.43)$$

where  $\mathbf{w}_{ij}$  is a tap weight vector to obtain  $i$ -tributary signal by using the  $j$ -tributary input. The mean squared error  $e_i$  for  $i$ -tributary and the estimation error  $J_i$  and are respectively defined

as

$$e_i(t) \stackrel{\text{def}}{=} d_i(t) - \hat{x}_i(t), \quad (2.44)$$

and

$$J_X(\mathbf{w}_{XX}, \mathbf{w}_{XY}) \stackrel{\text{def}}{=} e_X(t)e_X^*(t), \quad (2.45)$$

$$J_Y(\mathbf{w}_{YX}, \mathbf{w}_{YY}) \stackrel{\text{def}}{=} e_Y(t)e_Y^*(t). \quad (2.46)$$

Differentiating eq. (2.46) with respect to each tap weight vector gives LMS-based tap weight updating equations as

$$\begin{aligned} \mathbf{w}_{XX}(t+1) &= \mathbf{w}_{XX}(t) + \mu e_X(t) \mathbf{y}_X^*(t) \\ \mathbf{w}_{XY}(t+1) &= \mathbf{w}_{XY}(t) + \mu e_X(t) \mathbf{y}_Y^*(t) \\ \mathbf{w}_{YX}(t+1) &= \mathbf{w}_{YX}(t) + \mu e_Y(t) \mathbf{y}_X^*(t) \\ \mathbf{w}_{YY}(t+1) &= \mathbf{w}_{YY}(t) + \mu e_Y(t) \mathbf{y}_Y^*(t) \end{aligned} \quad (2.47)$$

Equation (2.47) is the natural expansion of eq. (2.40) for  $2 \times 2$  MIMO LMS algorithm, and equivalent to a digital polarization demultiplexer. The significant advantage of this polarization demultiplexer is that it provides the functions not only for the polarization demultiplexing, but also for equalization of PMD, (residual) CD, and optical/electrical bandwidth limitation. Furthermore, due to its FIR-based structure, the resampling is simultaneously performed during the weight vector updating. Those properties come from the simple design criterion in which the weight vectors are updated in a manner that output signals approach the desired signals. Consequently, it is also called a linear MIMO equalizer.

#### 2.4.3.2 CMA-based Adaptive MIMO Equalization

In addition to the polarization coupling, another significant issue to be considered in coherent optical signal transmission is the phase recovery for the phase noise which is originated both from the light source and the receiver-side LO. Although several phase noise algorithms have been proposed including the Viterbi-Viterbi algorithm [27], they require the output signals whose contaminations are already removed to some extent. The promising approach in designing an FIR MIMO adaptive filter without considering the phase noise is the constant



modulus algorithm (CMA) [28] which requires no desired signals to update the weight vectors. Instead, these vectors are updated only based on simple design criteria in which the signals after equalization shall exhibit the constant modulus. This kind of approach is called is the blind source separation (BSS), and contributes to the requirement relaxation in an DSP circuit implementation because it does not need any synchronization or desired signal feeding. Thus, in CMA technique, the mean squared error  $e_i^{CMA}$  for  $i$ -tributary and the estimation error  $J_i^{CMA}$  are respectively defined as

$$e_i(t)^{CMA} \stackrel{\text{def}}{=} (1 - |\hat{x}_i(t)|^2)^2, \quad (2.48)$$

and

$$J_X^{CMA}(\mathbf{w}_{XX}, \mathbf{w}_{XY}) \stackrel{\text{def}}{=} e_X^{CMA}(t)e_X^{CMA*}(t), \quad (2.49)$$

$$J_Y^{CMA}(\mathbf{w}_{YX}, \mathbf{w}_{YY}) \stackrel{\text{def}}{=} e_Y^{CMA}(t)e_Y^{CMA*}(t). \quad (2.50)$$

By differentiating eq. (2.50), weight vector updating equations based on CMA are then given as

$$\begin{aligned} \mathbf{w}_{XX}(t+1) &= \mathbf{w}_{XX}(t) + \mu e_X^{CMA}(t) \hat{x}_X(t) \mathbf{y}_X^*(t) \\ \mathbf{w}_{XY}(t+1) &= \mathbf{w}_{XY}(t) + \mu e_X^{CMA}(t) \hat{x}_X(t) \mathbf{y}_Y^*(t) \\ \mathbf{w}_{YX}(t+1) &= \mathbf{w}_{YX}(t) + \mu e_Y^{CMA}(t) \hat{x}_Y(t) \mathbf{y}_X^*(t) \\ \mathbf{w}_{YY}(t+1) &= \mathbf{w}_{YY}(t) + \mu e_Y^{CMA}(t) \hat{x}_Y(t) \mathbf{y}_Y^*(t). \end{aligned} \quad (2.51)$$

Despite of the its basic designing philosophy in which the output signals are supposed to have the constant modulus, CMA has been applied to signal equalization with various kinds of modulation formats. In optical signal transmission, CMA technique is usually used for initial convergence in MIMO equalization.

## Chapter 3

# PDL Penalty Reduction by Wavelength-Interleaving Transmission

### 3.1 Overview

The use of polarization-division-multiplexing (PDM) transmission technique in a single mode fiber doubles the spectral efficiency, and is commercially used in the today's optical communication systems having the data rate of 100 Gb/s. However, PDM optical signals are more susceptible than single-polarized signals to degradation due to polarization-related phenomena, i.e., polarization mode dispersion (PMD) and polarization dependent loss (PDL) [29]. Equalization in the digital domain after coherent detection can perfectly remove PMD-induced effects in the noise-free regime. On the other hand, the PDL-induced non-unitary transfer channel that imposes attenuation on particular polarization mode at a different level causes degradation of system performance even with digital equalization. Moreover, as a consequence of random polarization coupling in the links, temporal variation of overall PDL makes the optical system design more complicated.

The  $n$ -wavelength-interleaving ( $n$ -WI) technique was originally proposed in [30] as a way to reduce the net burst error length in optical links with PMD. Assuming the worst case of optical signals splitting into two principal states of polarization, they evaluated the effect of the WI technique theoretically. They found that WI can enhance forward error correction (FEC) performance by interspersing the bit errors in different wavelength channels. While their main conclusion is that this technique can on average improve the performance of a system with FEC, it should be noted that WI transmission technique is also valid to reduce the penalty or outage probability caused by PDL even under conditions without FEC. This

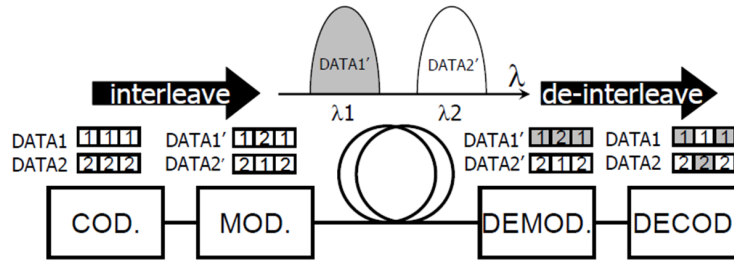


Fig. 3.1 Schematic illustration of 2-WI transmission system. The numbers in blocks indicate the channel number and shadings mean the degradation difference of optical signals between 2 channels.

chapter describes the experimental demonstration of using WI to improve the robustness to PDL-induced impairments via a statistical approach. In addition, through numerical simulation the mechanism is revealed by which WI reduces the PDL-induced penalty or the outage probability when the number of interleaving-channels  $n$  is increased.

### 3.2 $n$ -Wavelength-Interleaving Transmission

Fig. 3.1 illustrates an  $n$ -WI transmission system (for the case of  $n = 2$ ) to explain the principle of  $n$ -WI technique: in the transmitter, given blocks (e.g. bits, bytes, or frames) are interleaved between  $n$  channels. The subscript  $i$  and  $int$  respectively denote parameters related to the  $i$ -th original (non-coded) channels, and those related to interleaved channels. Note that in this context the original channels mean those to which WI has not yet been applied. In the presence of differential group delay (DGD), PDL at each  $n$  channels are statistically uncorrelated if they are allocated with sufficient carrier spacing larger than correlation wavelength [31]. Accordingly, PDL-induced degradations in the original channels are statistically independent. Since interleaved blocks are de-interleaved after demodulation at the receiver, the data of one channel is transmitted over  $n$  wavelength. Thus, the bit error rate (BER) of an interleaved channel is equivalently given by the averaging BERs over  $n$  channels:  $BER_{int} = BER_i/n$ . Such averaging is expected to reduce the variance of the probability density functions (PDFs) of the BERs (or  $Q$ -factors), which reduces outage probability. This *thinning effect* is experimentally confirmed later (Fig. 3.3 (c)).

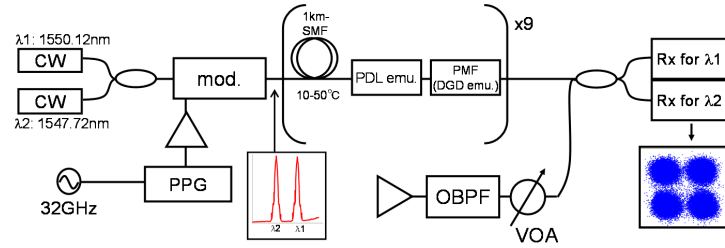


Fig. 3.2 Experimental setup. PPG: Pulse-pattern generator, Mod: IQ-modulator, VOA: Valuable optical attenuator.

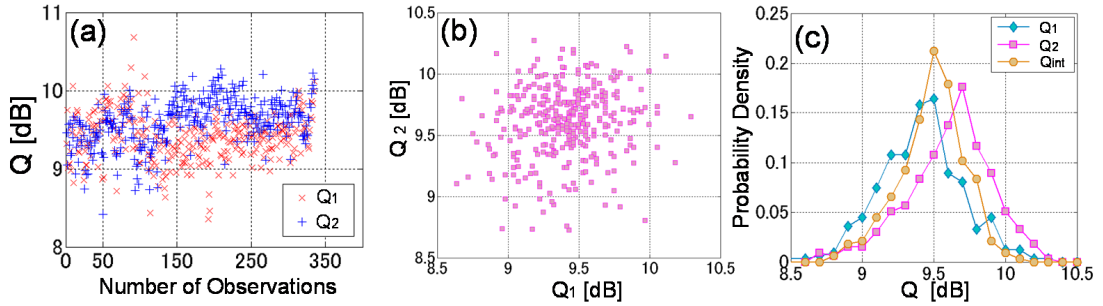


Fig. 3.3 (a) Temporal change in observed  $Q$ -factor of ch1 and ch2. (b) Scatter plots of  $Q$ -factors for the two channels. (c) Probability density of ch1, ch2, and interleaved channel as a function of  $Q$ -factor.

### 3.3 Experimental Setup and Results

To test the validity of WI transmission, an experiment was conducted using DGD- and PDL-emulators as shown in Fig. 3.2. Continuous-wave light of  $\lambda_1$  (1550.12 nm) and  $\lambda_2$  (1547.72 nm) was modulated by a  $2^{11} - 1$  PRBS pattern with a 32 GHz clock to create 128 Gb/s PDM-QPSK optical signals. Note that the two channels were separated by 300 GHz and modulated by the same optical modulator. Optical signals enter the DGD-PDL-emulated link nine sections, each of which has a 1-km single mode fiber (SMF), a PDL-emulator, and a polarization-maintaining fiber (which works as a DGD-emulator). Each DGD- and PDL-emulator had DGD of 10 ps and PDL of 1 dB, respectively. Under the assumption of the large number of emulators, the estimated link PMD was 27.6 ps and the link PDL was 2.8 dB.

To increase the exploration speed of DGD and PDL, 1-km SMFs were set in an isothermal chamber whose temperature randomly fluctuated between 10 and 50 C°. Before entering the optical frontend, amplified spontaneous emission (ASE) noise was added to optical signals to set the OSNR to 17 dB. Both optical signals were detected with synchronization, and stored in digital storage oscilloscope (DSO). After analog-to-digital conversion, the signals were demodulated by an offline processing to calculate the BER and  $Q$ -factor of channels 1 and 2. PMD-induced distortion was well removed by  $2 \times 2$  adaptive MIMO equalization. The  $Q$ -factor sequence of both channels was recorded every minute for 5.7 hours (accordingly, the total number of datasets was 340). Fig. 3.3 shows the statistical properties of the recorded  $Q$ -factors. As mentioned above, the  $Q_{int}$  ( $Q$ -factor of the interleaved channels) is equivalently obtained by averaging  $BER_1$  and  $BER_2$ . Fig. 3.3(a) shows the temporal change in  $Q$ -factor for channels 1 and 2. Fluctuations in the  $Q$ -factor can be caused by changes of the PDL itself and the relative angle between the polarization states of optical signals and PDL-axes. The scatter plots of  $Q_1$  and  $Q_2$  for the two channels were shown in Fig. 3.3(b). They indicate that  $Q_1$  and  $Q_2$  are statistically uncorrelated: the calculated correlated coefficient was 0.102. Fig. 3.3(b) represents the PDFs of  $Q_1$ ,  $Q_2$ , and  $Q_{int}$ . It is noteworthy that the calculated variance of  $Q_{int}$  (0.052) is significantly smaller than that of  $Q_1$  (0.092) and  $Q_2$  (0.090).

### 3.4 Analysis by Extreme Value Statistics

In this section extreme value statistics (EVS) is adopted to assess outage probability asymptotically, using the datasets obtained in the above experiment. EVS is usually used to model extremely rare events, such as cataclysmic earthquakes or torrential rain floods. It is demonstrated both experimentally and theoretically in [32] that the probability of the logarithm of BER in an optical link with PMD follows a Gumbel distribution based on EVS. Thus, in the analysis discussed here too, the application of EVS may reveal the validity of WI transmission more quantitatively. The peaks over threshold (POT) analysis is used here which can be found in EVS literature [33]. Note that POT analysis is designed for estimating maxima given a large number of data points; the analysis conducted here should deal with  $-Q$  values (i.e.,  $Q$ -factors multiplied by -1) as stochastic variables in order to estimate minimum  $Q$ -factors. Let the obtained  $Q$ -factor sequence be one of identically and independently random variables.

Table 3.1 ESTIMATED PARAMETERS FOR  $ch_1$ ,  $ch_2$ , AND  $ch_{int}$ .

	$ch_1$	$ch_2$	$ch_{int}$
$u$ (threshold)	-9.5	-9.5	-9.5
$\sigma$ (scale)	0.31	0.30	0.24
$\xi$ (shape)	-0.20	-0.19	-0.24

If  $X$  is defined as  $X = -Q - u$  for a given threshold  $u$ , EVS gives the conditional probability

$$C(x) = \Pr\{x > X|X > 0\}, \quad (3.1)$$

where  $C(x)$  is the probability that  $X$  does not exceed  $x$  under the condition of  $X > 0$ , i.e.  $-Q > u$ , which is referred to as the generalized Pareto distribution. Cumulative probability  $C(x)$  has the explicit form of

$$C(x) = 1 - \left(1 + \frac{\xi x}{\sigma}\right)^{-1/\xi}, \quad (3.2)$$

where  $\sigma$  and  $\xi$  are the scale parameter and the shape parameter, respectively.

Parameters  $\sigma$  and  $\xi$  are estimated on the basis of the maxima likelihood method. Since there may still be uncertainty in setting appropriate threshold level  $u$ , it is determined by using the mean excess function, which is a familiar EVS technique (see [33] for more information). Fitted  $C(x)$  and the cumulative probabilities calculated from the experiment data are plotted in Fig. 3.4; they show excellent agreement. The estimated parameters are summarized in Table 3.1.

Given the experimental system described above, now the minimum  $Q$ -factor within  $m$ -observations can be estimated, which is expressed as  $Q_m$  below. From eq. (3.2),  $Q_m$  is approximated with estimated parameters after simple algebraic transformation as

$$Q_m = -u - \frac{\sigma}{\xi} \left[ \left(m \frac{k}{N}\right)^\xi - 1 \right], \quad (3.3)$$

where  $N$  and  $k$  are respectively the total number of experimental data elements and the number of data elements exceeding threshold  $u$ . On the basis of eq. (3.3) and the estimated parameters ( $u$ ,  $\sigma$  and  $\xi$ ), we can ascertain the expected minimum  $Q$ -factor  $Q_m$  for a given  $m$ : for example, if we were to observe  $Q$ -factor  $m = 10^8$  times for  $ch_1$  in this system, it can be expected that you would, on average, witness the minimum  $Q$ -factor  $Q_m$  of 8.0 dB once. It

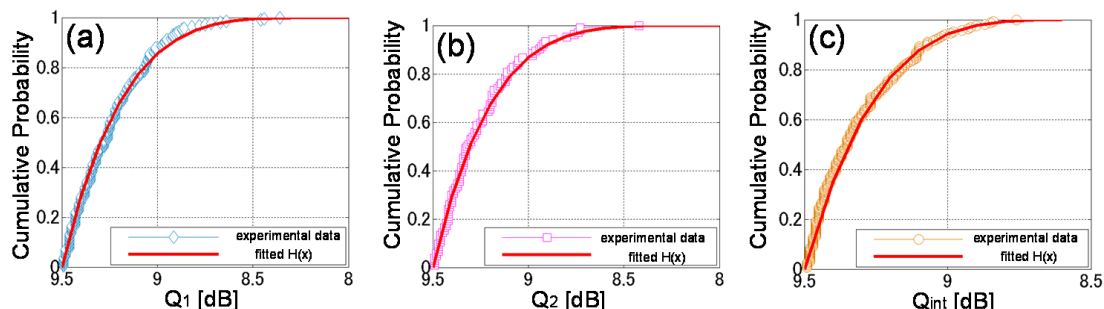


Fig. 3.4 Cumulative probabilities from experimental data (symbols) and fitted  $C(x)$  obtained from eq. (3.2) with estimated parameters (solid curves) for  $ch_1$  (a),  $ch_2$  (b), and interleaved channel (c).

can be also interpreted that this example corresponds to a link system in which the designed  $Q$ -limit is 8.0 dB and the outage probability is  $10^{-8}$ , because outage probability is given by  $1/m$ . From this viewpoint of system design, the  $Q$ -limit curve can be drawn as a function of outage probability (as in Fig. 3.5). This reveals the reduction effect of WI transmission for PDL-induced  $Q$ -penalty or outage probability, as in the following two scenarios:

1. For a fixed outage probability of  $10^{-6}$ , the  $Q$ -limit can be mitigated from 8.1 to 8.6 dB, which can also be explained as the  $Q$ -penalty being improved by 0.5 dB.
2. For a fixed  $Q$ -limit of 8.5 dB, outage probability can be decreased from  $10^{-3}$  to  $10^{-6}$ .

It should be noted that the  $Q$ -limit generally depends on which FEC code is applied and what corrected BER is required for the system, and that outage probability generally depends on the required system reliability. In principle, there may be also another WIT's effects: if  $Q$ -penalty and the outage probability are fixed, more total PDL in the optical link system can be tolerated. Even though the above analysis considers only the case of two interleaving channels, it is reasonable to expect that WI transmission across interleaving channels  $n$  ( $n > 2$ ) will decrease PDL-induced impairments more effectively. In the next section, a numerical simulation is performed in which  $n$  is increased to 3 or more for the purpose of revealing the mechanism by which WI mitigates the PDL-induced penalty or outage probability.

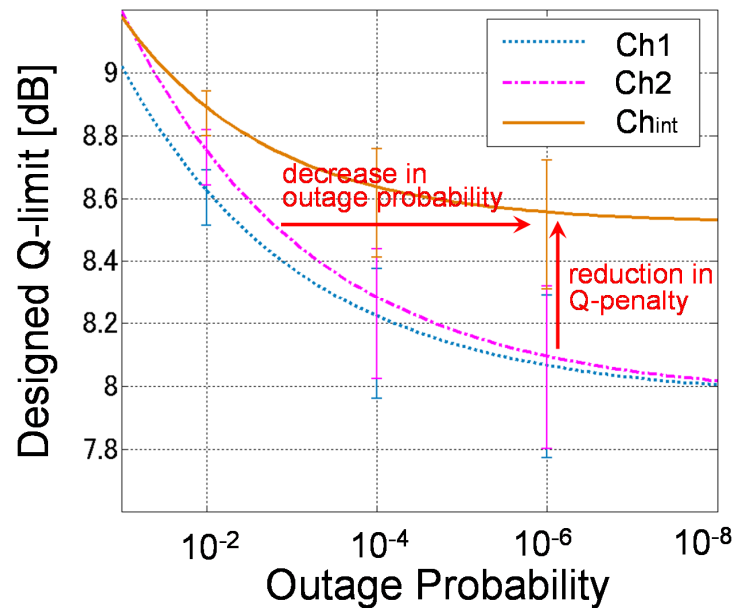


Fig. 3.5 Estimated  $Q$ -limit from eq. (3.3) as a function of outage probability for ch1, ch2 and interleaved channel. Note that error bars at outage probability of  $10^{-2}$ ,  $10^{-4}$ , and  $10^{-6}$  are estimated based on the 90 % confidence intervals of  $\sigma$  and  $\xi$ .

### 3.5 Numerical Simulation

In the following simulation, the number of interleaving channels  $n$  is increased from 2 to 8. In the simulation, the transmission line has nine sections, each of which has a 10-ps DGD and a 1-dB PDL emulator. However, instead of installing 1-km SMFs in an isothermal chamber, which changes the angles of the principal axes for both the DGD- and PDL-emulators between sections, DGD- and PDL-emulators are installed with random angles in each section. ASE noises are added to the optical signals so that the  $Q$ -factor of the transmitted optical signal becomes 10.8 dB when the total PDL of the optical link is 0 dB, which was the case in the experiment. Note that BERs (i.e.,  $Q$ -factors) of transmitted channels are statistically independent in the simulation, and that, as in the case of the experiment, the impact of PMD-induced penalty is assumed to be removed using adaptive FIR-structured equalizing filter. In each simulated case of different  $n$ , the number of datasets for  $Q$ -factor sequence is 500. Fig. 3.6 depicts the PDFs of  $Q$ -factors for a single channel, a 4-WI channel, and a 8-WI channel.



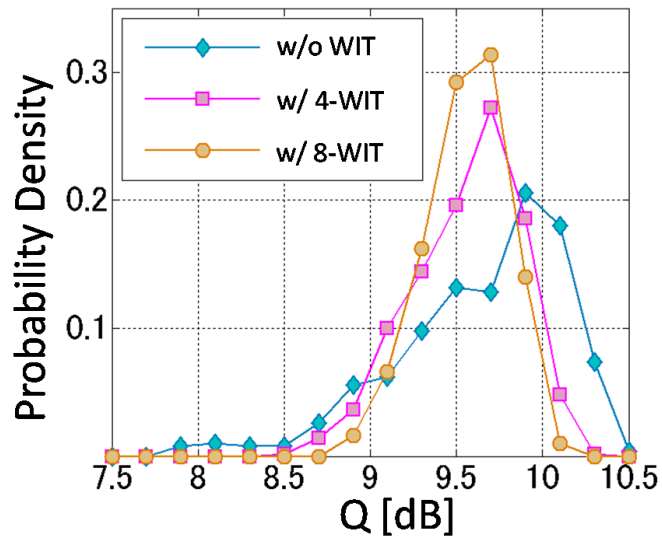


Fig. 3.6 Simulated probability densities of  $Q$ -factors for the channels without WI transmission, with 4-WI transmission, and with 8-WI transmission.

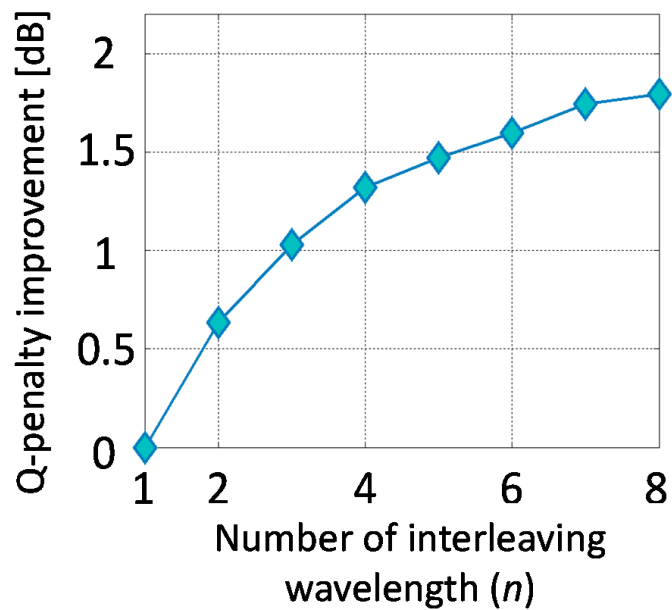


Fig. 3.7 The  $Q$ -penalty improvement in dB as a function of the number of interleaving wavelengths  $n$  for a fixed outage probability of  $10^{-6}$ .

Compared to Fig. 3.3(c), it is obvious that the variance of the PDF for an  $n$ -WI channel is likely to become smaller as the number of interleaved channels  $n$  increases. Therefore, it is

expected that the effect of WI transmission on reducing PDL-induced impairments may be enhanced when  $n$  becomes larger. As in Section 3.4, here too an EVS analysis is applied to the simulation results. The parameters for the generalized Pareto distribution are estimated in the same way as in Section 3.4. Fig. 3.7 summarizes the improvement achieved in  $Q$ -penalty reduction for a fixed outage probability of  $10^{-6}$  when  $n$  is increased from 2 to 8. It can be seen that the reduction effect enhances monotonically; in particular, the  $Q$ -penalty for the 8-WI channel improves by about 1.8 dB. Furthermore, it is noteworthy that the reduction effect has a tendency to saturate as  $n$  increases. This saturation phenomenon can be explained as follows: As  $n$  becomes closer to infinity, the PDF of the  $Q$ -factor for an  $n$ -WI channel approaches a delta-function-like shape, which has its mean around 9.5 dB in this case (one may be able to visualize this with an analogy of the central limit theorem). Accordingly, the upper bound of the PDF integrated area that gives the fixed outage probability of  $10^{-6}$  becomes larger monotonically towards the mean  $Q$ -factor of 9.5 dB, which establishes the fact that the reduction effect has an upper limit.

## 3.6 Summary

Subjecting experimental measured data to EVS analysis successfully demonstrated that WI transmission can decrease the  $Q$ -penalty or outage probability caused by PDL. Furthermore, numerical simulation revealed that this reduction effect tends to enhance as the number of interleaving channels  $n$  increases, and also that the amount of the reduction of PDL-induced impairments saturates towards an upper limit, which is explained by an analogy of the central limit theorem.

## Chapter 4

# Filtering-Tolerant Transmission for Super-Channel Beyond 100 Gb/s

### 4.1 Overview

With the growing demand for increased traffic levels, in the last few years commercial system installation supporting PDM-QPSK signals with 100 Gb/s has succeeded in expanding capacity seamlessly toward sub-10 Tb/s for long-haul terrestrial and submarine systems. Reconfigurable add-drop multiplexer (ROADM) nodes have also been widely used in ring- or mesh-topology networks to achieve the flexibility needed for wavelength routing and assignment, and eventually to meet the demand for cost-effective networks [34, 35]. In these nodes optical signals are flexibly switched to the desired destination without the need for optical-electrical conversion using wavelength-selective switches (WSSs).

In next-generation fiber optic communication systems, technical breakthroughs are required which expand the signal bit rate beyond 100 Gb/s and enhance higher spectral efficiency (SE). The demand for increased signal bit rate can be met by using optical carriers with higher-order modulation formats at the cost of the achievable transmission reach [36–39]. As another solution, recent studies have reported that super-channel transmission with Nyquist-WDM channel allocation is a promising way to increase the channel bit rate as well as SE. This method combines multiple optical subcarriers (SCs) into a single super-channel with payloads from 400 Gb/s to 1 Tb/s, and these SCs are allocated in the narrower spectral slot around the Nyquist bandwidth [40–44]. The single/super-channel format candidates for achieving the 400 Gb/s per channel are listed in Table 4.1 with their properties. In the table, polarization multiplexing and spectral grid with 12.5 GHz resolution defined in ITU-T

Table. 4.1 SIGNAL FORMAT CANDIDATES ENABLING 400-Gb/s TRANSMISSION PER OPTICAL CARRIER.

Signal format No.	(reference)	Single-Carrier Channel			Super Channel	
		(1)	(2)	(3)	(4)	(5)
Modulation format	QPSK	QPSK	16QAM	64QAM	QPSK	16QAM
Symbol rate w/ FEC (Gbaud)	32	128	64	43.7	32	32
Number of SCs	1	1	1	1	4	2
Channel occupancy (GHz)	37.5	137.5	75	50	150	75
Net bit rate (Gb/s)	100	400	400	400	400	400
SE (b/s/Hz)	2.67	2.91	5.33	8.00	2.67	5.33
Required OSNR at BER = $10^{-2}$ (dB)	11.4	17.4	21.0	24.8	11.4	18.0
OSNR penalty (dB)	0.0	6.0	9.6	13.4	0.0	6.6

Recommendation G.694.1 are assumed. While formats (1) through (3) can reach the 400-Gb/s signal bit rate only by the single carrier, formats (4) and (5) comprise of multiple SCs, corresponding to the super-channel format. The format (1) is promising at a first sight, however, the creation of extremely high symbol rate signals cannot be easily achieved using current matured inexpensive electronics or optoelectronics devices. Higher OSNR penalty will restrict the maximum transmission reach for the formats (2) and (3), which does not meet the cost-effectiveness. In addition, the employment of the higher symbol rate or higher modulation order will make DSP circuit more complicated, which may decrease the energy-efficiency. Super channel formats (4) and (5) does not impose stringent requirement on electronics/optoelectronics devices, and will provide the seamless upgrade towards the signal bit rate expansion of 400 Gb/s.

If one assumes the situation in which the super-channel propagates the transmission link with cascaded ROADMs nodes that contain WSSs as switching devices, it is not difficult to imagine that WSSs may be responsible for the optical filtering distortions of a super-channel in a narrow spectral slot, because the spectral margin between outermost SCs and filter edge is reduced due to Nyquist-WDM channel allocation. One specific physical phenomenon that causes such distortions in the aforementioned systems is passband narrowing (PBN). This is caused by a successive-WSS configuration that reduces the overall optical bandwidth [45,46]. Another problem that such systems encounter is random center-frequency shift (CFS) of a

WSS, which arises from component imperfections, optical device misalignment, or internal and external stress [45, 46]. Although super-channel transmission effectively increases the channel capacity and SE, super-channel performance severely degrades when distortions occur due to optical filtering of particular SCs.

Given this situation, this chapter proposes a novel and simple solution suitable for making super-channel transmission robust to the degradation of particular SCs. The proposed approach is the first that utilizes the frequency degree of freedom in optical signal transmission, which is equivalent to that of space in wireless communications from the viewpoint of MIMO systems. In developing this solution, this chapter focuses on reducing the filtering-induced penalty suffered by super-channels with multiple SCs allocated in a narrow spectral slot. It will be demonstrated that the method improves super-channel performance by dispersing the distortions of particular SCs over all SCs through a linear transformation. Through numerical simulation it is also showed that it enables the filtering-induced penalty to be effectively reduced, thus enabling optical super-channels to pass through a larger number of cascaded WSSs.

## 4.2 Proposed Method: WHT-Spreading

The concept of the proposed method is based on the wireless MIMO techniques that enhance transmission reliability by using spatial and temporal diversity. In wireless MIMO, one data stream is transmitted through several paths with different fading in free space. In fiber-optic communication systems, each of the channels (including polarization channels) that together form one super-channel degrades differently due to linear and nonlinear effects during its propagation. On the basis of an analogy to wireless MIMO transmission, it may be feasible to apply the MIMO concepts to SCs of a super-channel in a fiber-optic communication system. Several studies have been reported in which space-time block codes (STBCs), also referred to as *polarization-time codes*, were applied to polarization channels of a single polarization multiplexed channel [47–50]. They showed that STBCs are beneficial in mitigating the penalty induced by polarization dependent loss (PDL).

With the proposed approach, each symbol's power is interspersed equally over all data streams (i.e., SCs) by the Walsh-Hadamard transform (WHT). Mathematically, if one lets the

original and the transformed symbol of the  $n$ -th SC for a super-channel comprising  $N$  SCs be  $s_n(t)$  and  $x_n(t)$  respectively, the transformed signal vector  $\mathbf{x}(t) = [x_1(t), x_2(t), \dots, x_N(t)]^T \in \mathbb{C}^{N \times 1}$  is obtained through WHT using the input signal vector  $\mathbf{s}(t) = [s_1(t), s_2(t), \dots, s_N(t)]^T \in \mathbb{C}^{N \times 1}$  ( $(\cdot)^T$  denotes transpose operation):

$$\mathbf{x} = \frac{1}{\sqrt{N}} \mathbf{H}_N \mathbf{s}, \quad (4.1)$$

where  $\mathbf{H}_N \in \mathbb{R}^{N \times N}$  is the  $N$ -th order WHT matrix. For instance, a super-channel with two SCs in the proposed scheme transmits the signal vector  $\mathbf{x}$  that is obtained by

$$\begin{pmatrix} x_1 \\ x_2 \end{pmatrix} = \frac{1}{\sqrt{2}} \mathbf{H}_2 \begin{pmatrix} s_1 \\ s_2 \end{pmatrix} = \frac{1}{\sqrt{2}} \begin{pmatrix} 1 & 1 \\ 1 & -1 \end{pmatrix} \begin{pmatrix} s_1 \\ s_2 \end{pmatrix}. \quad (4.2)$$

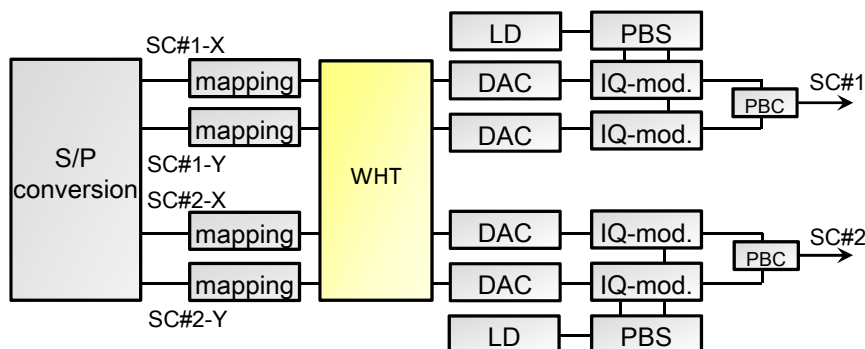


Fig. 4.1 A transmitter implementation of the WHT method for 2SC-DP-16QAM format. WHT: the Walsh-Hadamard transform, LD: laser diode, PBS: polarization beam splitter, PBC: polarization beam combiner, IQ-mod.: IQ-modulator.

$\mathbf{H}_{2N}$  is recursively obtained via the general relation between  $\mathbf{H}_N$  and  $\mathbf{H}_{2N}$ , expressed as

$$\mathbf{H}_{2N} = \frac{1}{\sqrt{2}} \begin{pmatrix} \mathbf{H}_N & \mathbf{H}_N \\ \mathbf{H}_N & -\mathbf{H}_N \end{pmatrix}. \quad (4.3)$$

Note that, taking polarization multiplexing into account, the WHT matrix has  $8 \times 8$  dimensions ( $\mathbf{H}_8$ ) for 4SC-DP-QPSK signals and  $4 \times 4$  dimensions ( $\mathbf{H}_4$ ) for 2SC-DP-16QAM signals. Hereafter, this technique is called the WHT-spreading (WHT-S).

Fig. 4.1 depicts an implementation example of a transmitter for 2SC-DP-16QAM. After serial-parallel conversion, each bit sequence is mapped to 16QAM format signals and then interspersed over all streams by the WHT-S method. The driving voltage with transformed signal is fed into an optical IQ-modulator to create the optical SCs. Because of the linear coupling process in the transmitter, the SC in the receiver is demodulated on the basis of conventional butterfly-structured adaptive FIR filters described in Chapter 2.

### 4.3 Analysis of the WHT Spreading

This section provides an overview of what WHT-S brings to all SCs by constructing a simple system model to show the performance difference between the conventional and the WHT-S method.

#### 4.3.1 System Model

Here a transmitter is assumed that creates a super-channel comprising  $N$  SCs after applying the WHT-S for  $N$  parallel input signals. In the transmission link, an optical device of some kind causes the signal power of one SC to decrease as the attenuation factor  $\rho$  ( $0 \leq \rho \leq 1$ ) decreases. The channel matrix representing this attenuation effect is expressed as  $\mathbf{T} = \text{diag}(1, 1, \dots, \sqrt{\rho}) \in \mathbb{R}^{N \times N}$ . After additive white Gaussian noise  $\mathbf{z} \in \mathbb{C}^{N \times 1}$  is loaded to the  $N$  SCs, they are converted to  $N$  parallel digital signals through independent coherent receivers. Thus the received signal vector  $\mathbf{y} \in \mathbb{C}^{N \times 1}$  is expressed as

$$\mathbf{y} = \mathbf{T} \mathbf{x} + \mathbf{z} = \frac{1}{\sqrt{N}} \mathbf{T} \mathbf{H}_N \mathbf{s} + \mathbf{z} = \mathbf{J} \mathbf{s} + \mathbf{z}, \quad (4.4)$$

where  $\frac{1}{\sqrt{N}} \mathbf{T} \mathbf{H}_N$  is replaced with  $\mathbf{J}$ . The equalizer weight matrix of the minimum mean square error (MMSE) equalizer  $\mathbf{W} \in \mathbb{C}^{N \times N}$  obtained by minimizing the mean square error defined as  $E[\|\mathbf{s} - \mathbf{W}^T \mathbf{y}\|^2]$ , where  $E(\cdot)$  denotes the expectation operation, becomes [51]

$$\mathbf{W} = \left( \mathbf{J}^\dagger \mathbf{J} + \frac{1}{\gamma_0} \mathbf{I}_N \right)^{-1} \mathbf{J}^\dagger, \quad (4.5)$$

where  $\gamma_0$  is the back-to-back SNR for a SC and  $\dagger$  is the complex conjugate operation. In this chapter the signal-to-interference-plus-noise ratio (SINR) is used instead of SNR to calculate BER. This evaluation method corresponds to treating interference noise due to imperfect

equalization by using  $\mathbf{W}$  as complex Gaussian random variable based on the Gaussian Approximation [52]. The SINR for the  $i$ -th SC after separation by eq. (4.5), written as  $\gamma_i$ , becomes

$$\gamma_i = \frac{1}{(\mathbf{I}_N + \gamma_0 \mathbf{J}^\dagger \mathbf{J})_i^{-1}} - 1, \quad (4.6)$$

where  $(\cdot)_i^{-1}$  denotes the  $i$ -th diagonal element of the matrix inverse. Recalling that a super-channel originally transmits a single bit sequence,  $Q$ -factors calculated from averaged BERs over all SCs are used as the system performance evaluation.

Taking a modulation format into account, the BERs for a SC and a super-channel are easily obtained by using eq. (4.6). Note that, in the analysis for a super-channel using a conventional scheme, one can readily compute BER by replacing  $\frac{1}{\sqrt{N}}\mathbf{H}_N$  with  $\mathbf{I}_N$  in eq. (4.4).

### 4.3.2 $Q$ -factor Characteristics

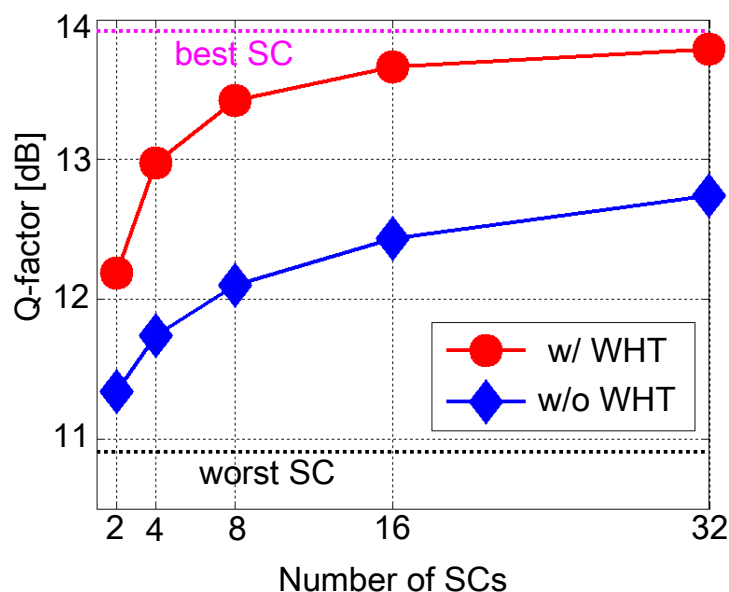


Fig. 4.2  $Q$ -factor as a function of the number of SCs. The “worst SC” corresponds to the one that is attenuated by a factor of 0.5.

Fig. 4.2 displays the calculated  $Q$ -factor of each SC and super-channel as a function of the number of SCs for  $\rho$  of 0.5 (i.e., 3-dB attenuation). In the figure, OSNR is set to 18 dB (in 0.1 nm resolution) and each SC is modulated with QPSK-format driven at 32 Gbaud. The



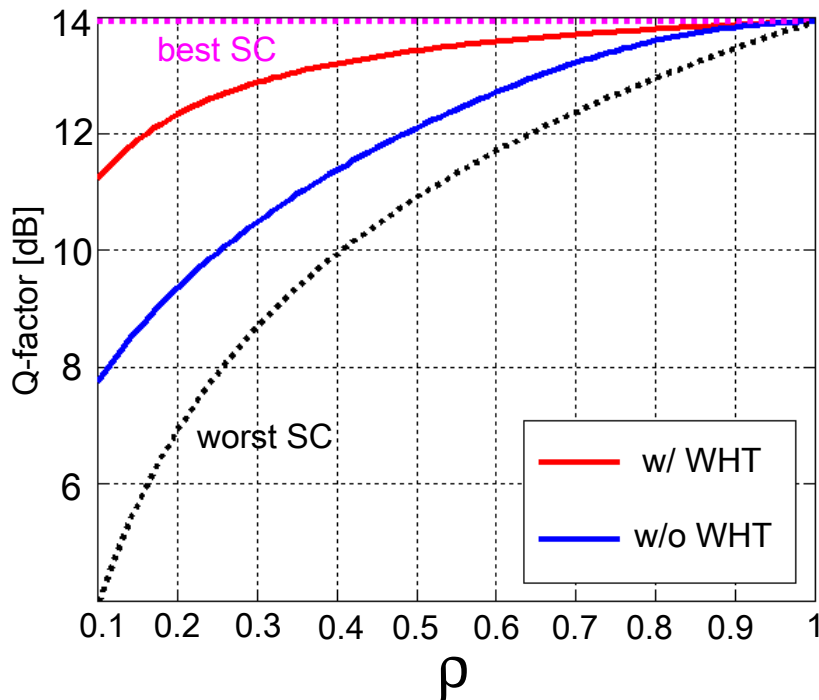


Fig. 4.3  $Q$ -factor as a function of  $\rho$ . The “worst SC” corresponds to the attenuated one.

$Q$ -factors for the SCs and the super-channel are plotted by dotted and solid lines, respectively. It is obvious that the WHT-S method outperforms the conventional method (denoted as “w/o WHT” in the figure), although the super-channel performance improves for both methods as the number of SCs increases. It should be noted that the operation of the WHT-S method with a large  $N$  (the number of SCs) is likely to increase a complexity of the receiver-side MIMO signal processing for demultiplexing. One of the approaches to avoid this is employing the processing in the frequency domain rather than in the time domain. In principle the complexity of the process is expected be reduced from  $O(N^2)$  to  $O(N \log N)$  by switching from the time-domain processing to the frequency-domain one [53], because the convolution calculation in the time domain is replaced by FFT-based scalar multiplications in the frequency domain.

Next,  $\rho$  was varied in the range from 0.1 to 1 and assumed the same conditions shown in Fig. 4.2 except that the number of SCs was fixed to eight. Fig. 4.3 shows the  $Q$ -factor as a function of  $\rho$  for each SC and super-channel. It is confirmed that compared with the conventional method, the WHT-S method enables the degradation due to the attenuated SC

to be effectively mitigated even for small  $\rho$  values.

On the basis of the results in Fig. 4.2 and Fig. 4.3, the difference between the conventional and the WHT-S methods can be intuitively explained as follows: averaging the BER for all SCs in the conventional method is approximately equivalent to evaluating symbol- or bit-interleaving transmission (BIT), which intersperses transmit data in a symbol-by-symbol or bit-by-bit manner over all SCs. BIT sometimes improves the system performance as a whole in a somewhat specified situation. In discussing BIT and its advantages in Chapter 3 and [54], assuming a condition such that frequency separation of SCs are sufficiently large ( $>100$  GHz), it was concluded that BIT reduces the PDL-induced outage probability in the statistical sense since it decreases the variance of each SC's frequency-dependent performance. On the other hand, the WHT-S method enhances the BER performance directly by interspersing signal distortions over all SCs and consequently changing net SINR.

## 4.4 Numerical Simulation

In this section numerical simulations were conducted to investigate the proposed WHT-S method's performance. For the simulations a more practical system model was assumed with optical nodes that include optical filters (WSSs) and optical amplifiers inside the transmission link. In the evaluation, PBN (i.e., overall optical bandwidth reduction due to cascaded WSS) and CFS (i.e., WSS's random frequency-shift due to optical imperfections) effects on the super-channel performance were mainly focused.

### 4.4.1 Simulation Setup

For purposes of evaluating the WHT-S method two super-channel formats were assumed: one has four 32 Gbaud SCs of DP-QPSK format in the 150 GHz spectrum slot (case-i) and the other has two 32 Gbaud SCs of DP-16QAM format in the 75 GHz spectrum slot (case-ii). Each SC was driven at 32 Gbaud and reshaped by a squared raised-cosine filter with 0.1 roll-off factor. The channel spacing between each SC was set to 37.5 GHz so that the degradation due to inter-carrier crosstalk would be negligible. Fig. 4.4(a) illustrates the channel allocation and the configuration of the optical devices used in the simulations. Two cascaded WSSs

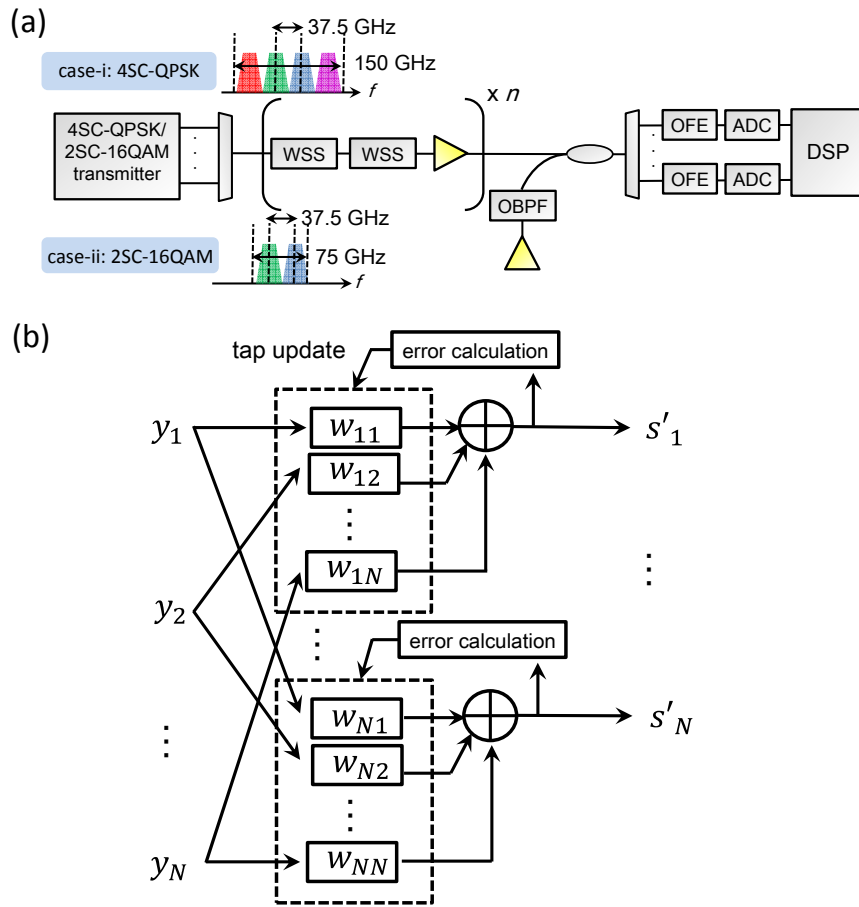


Fig. 4.4 (a). Simulation setup. SC: subcarrier, WSS: wavelength selective switch, OBPF: optical bandpass filter, OFE: optical frontend, ADC: analog-to-digital converter, DSP: digital signal processing. (b). The implementation example of the butterfly-structured MMA.

with sixth-order super-Gaussian functions were inserted in each span to emulate a ROADM node. Each WSS has 6-dB bandwidth of 150 GHz for case-i and 75 GHz for case-ii. By adding ASE noise to signals before they entered the coherent receivers, the received OSNR was set to be 15 dB in case-i and 22 dB in case-ii. After the conversion to digital signals, semi-inverse WHT including polarization demultiplexing was carried out through  $N \times N$  butterfly-structured adaptive FIR filters with 23  $T/2$ -spaced taps on the basis of a multi-modulus algorithm (MMA) [55]. The detailed implementation of this filter is illustrated in Fig. 4.4(b). In the figure and eq. (4.7) through eq. (4.9), an implementation example with single tap equalizer is discussed for simplicity. Letting  $w_{ij}$  be the  $(i, j)$  entry of  $\mathbf{W}^H$ , the

equalizer output  $\hat{s}_i$  is obtained as

$$\hat{s}_i = \sum_{j=1}^N w_{ij} y_j, \quad (4.7)$$

where  $y_i$  is the  $i$ -th received signal. The error in MMA is defined as

$$e_i = \Re(\hat{s}_i)(\Re(\hat{s}_i)^2 - a_{Re}^2) + j \cdot \Im(\hat{s}_i)(\Im(\hat{s}_i)^2 - a_{Im}^2), \quad (4.8)$$

where  $\Re(\cdot)$  and  $\Im(\cdot)$  denote respectively real and imaginary part of a complex number, and  $a_{Re}$  and  $a_{Im}$  are defined respectively as the dispersion constant for the real and imaginary parts of  $\hat{s}_i$ . The corresponding tap updating equation with the step-size parameter  $\mu$  becomes

$$w_{ij} \leftarrow w_{ij} + \mu e_i y_j^*. \quad (4.9)$$

After equalization, the Viterbi-Viterbi phase recovery algorithm [27] was applied to cancel carrier phase noise and differential decoding to count errors. In the back-to-back configuration,  $Q$ -factors for both cases became 9.8 dB.

#### 4.4.2 Simulation Results

The evaluation starts from the investigation on the PBN tolerance enhancement brought by the WHT-S method. Fig. 4.5 shows the  $Q$ -factor penalty as a function of the number of cascaded WSSs for case-i. The WHT-S method clearly decreased the PBN penalty, since the effect of the filtering-induced distortion due to the outermost two SCs was mitigated by the method. Although not shown in Fig. 4.5, there was no significant difference between the conventional and the WHT-S transmission in case-ii. This is because in both transmission types the SCs were degraded symmetrically due to the PBN effect.

To explore the effects produced solely by CFS, it is assumed that signals pass through a frequency-shifted WSS only once. In this case, the WSS filters the edge of only one SC. Fig. 4.6 compares the constellations after equalizing for SCs that passed through an 8-GHz-shifted WSS in case-i and case-ii with and without the WHT method. Whereas without the method each of the SCs degraded differently, with it all the SCs showed almost the same performance since SINR of each SC becomes almost the same with the method's averaging effect.

Fig. 4.7 represents the  $Q$ -factor penalty induced by CFS. The  $Q$ -factor penalty was successfully suppressed for both cases. The suppression effect for case-ii was slightly smaller

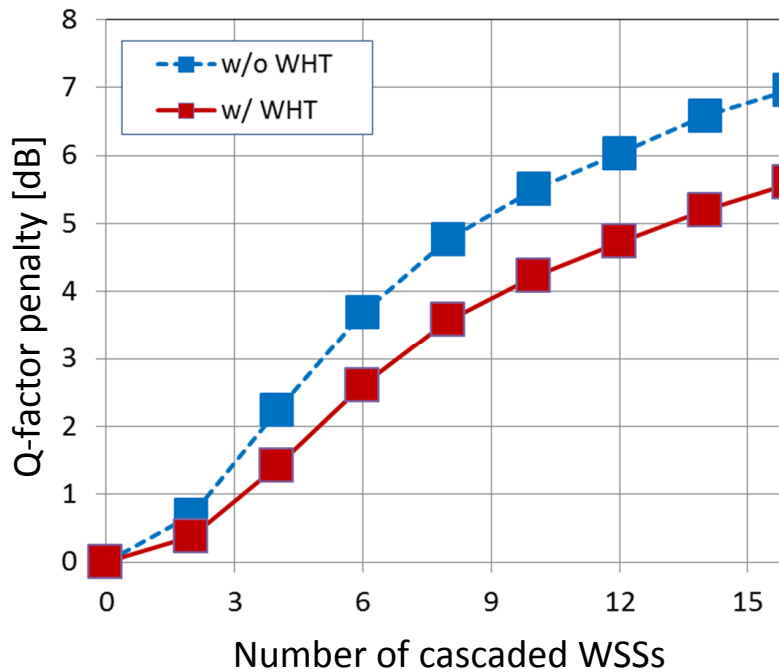


Fig. 4.5  $Q$ -factor penalty as a function of the number of cascaded WSSs for case-i.

than that for case-i. This may be explained by the number of non-degraded SCs (SCs that are not affected by CFS) for each case.

In the aforementioned simulations somewhat impractical situations were assumed, such as one in which the CFS was 10 GHz and occurred alone, without PBN. Therefore, it is required to assess the WHT-S transmission performance in more practical situations where CFS and PBN occur simultaneously. Assuming the net CFS range to be within 2.5 GHz for filter detuning and 1.25 GHz for laser detuning [46], the signals were transmitted with the worst-case scenario in which all WSSs were uniformly shifted at 3.75 GHz to the same direction in the frequency domain. Consequently, the overall bandwidth for a super-channel was severely reduced due to successive filtering uniformly-3.75-GHz-shifted. Fig. 4.8 depicts the  $Q$ -factor penalty as a function of the number of cascaded frequency-shifted WSSs. The penalty rose sharply as the number increased since the multiple filtering that the WSSs executed negatively affected the signals. The figure shows clearly that the WHT-S method improves the performance of a super-channel for both cases. Moreover, because of the WHT-S transmission, the number of cascaded WSSs for a fixed  $Q$ -factor penalty of 4 dB increased from 5 to 8 for case-i and from 4 to 5 for case-ii. Thus, a super-channel is transmitted over a larger

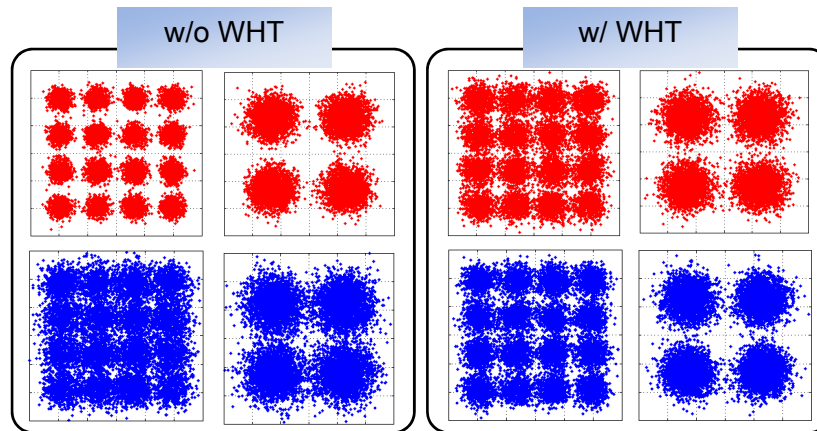


Fig. 4.6 Constellation diagrams after demodulation with and without the WHT-S method. The red (top) and blue (bottom) ones represent the best and worst performance SCs, respectively.

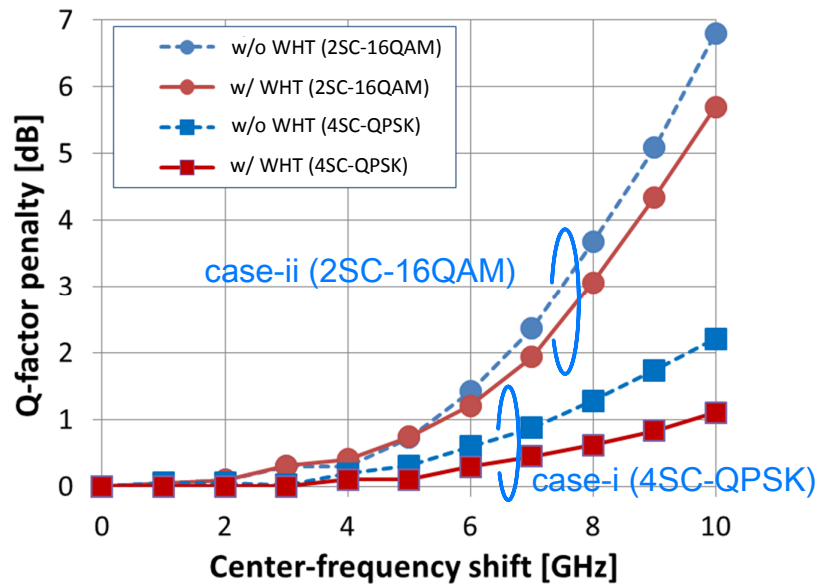


Fig. 4.7  $Q$ -factor penalty as a function of center-frequency shift for both super-channel signal formats.

number of WSSs by using the WHT-S method.

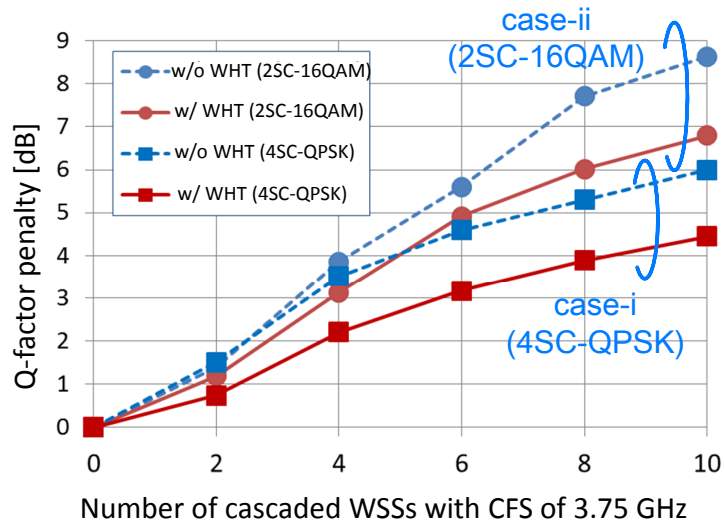


Fig. 4.8  $Q$ -factor penalty as a function of the number of cascaded 3.75G-shifted WSSs for both super-channel signal formats.

## 4.5 Summary

In this chapter, a novel filtering-tolerant technique is proposed that applies the WHT to SCs of a super-channel. In the scheme, each information symbol's power is equally distributed over all SCs in a transmitter, and gathered in a receiver. The proposed WHT-spreading method is suitable for application to super-channel transmission against multiple optical-filter (i.e., WSS) crossings since it improves super-channel performance by dispersing degradation occurring in particular SCs over all SCs. It was also numerically demonstrated that the method effectively mitigated the filtering penalty induced by WSSs, and that the number of cascaded WSSs was increased by the WHT-spread transmission for a fixed  $Q$ -factor penalty.

## Chapter 5

### Fiber Nonlinearity

### Mitigation/Compensation Based on Optical and Digital Approaches

#### 5.1 Improving Nonlinear Degradation by Combining Optical and Digital Compensation Techniques

##### 5.1.1 Overview

Nonlinear signal distortion remains a major obstacle for long-haul transmission in optical fiber link systems. Signal degradation due to fiber Kerr nonlinearity can be categorized into intra-channel and inter-channel nonlinearity. While the former contains self-phase modulation (SPM), intra-channel cross-phase modulation and intra-channel four-wave mixing, the latter contains cross-phase modulation (XPM) and four-wave mixing [56]. Digital signal processing (DSP) techniques can powerfully compensate for linear distortion due to, for instance, chromatic dispersion (CD) and polarization mode dispersion (PMD) [57]. Moreover, recent studies have demonstrated that intra-channel nonlinear distortion can be deterministically compensated for by inversely propagating the received signal waveforms referred to as the digital back-propagation (DBP) algorithm [24].

Inter-channel nonlinearity can be also compensated for or mitigated to some extent by means of digital [58] and optical approaches [59, 60]. One effective way to optically reduce XPM influence is span-by-span CD compensation, which introduces deliberate skews among



optical channels. In [59, 60], it was shown that an optical *XPM-suppressor* can successfully mitigate XPM-induced nonlinear degradation for PDM QPSK systems. Whereas these compensation/mitigation techniques are attractive as means to reduce the nonlinear degradation, much still remains unveiled when they are combined. Section 5.1 numerically investigates their combined effects by applying DBP and optical XPM-suppressing techniques to transmitted signals through a dispersion-managed (DM) system, and by comparing performance between DM and non-DM (NDM) systems.

### 5.1.2 Simulation Setup

Conducted simulation assumed three-channel PDM-NRZ-QPSK optical signals with 128 Gbps bit rate and 50 GHz channel spacing, which were transmitted over the DM or NDM link as schematically illustrated in Fig. 5.1. Each channel was modulated by independent PRBS data sequences with different length, and ASE noise was added span by span to set OSNR to 15 dB at the receiver. The transmission link consisted of 16 spans of 40-km non-zero dispersion shifted fibers (NZDSFs) with a CD coefficient of 6 ps/nm/km, a loss coefficient of 0.26 dB/km, and a nonlinear parameter of  $2.5 \text{ W}^{-1}\text{km}^{-1}$ . In the DM system, a dispersion compensation fiber (DCF) was installed after the NZDSF in each span; these DCFs fully compensate for CD. In the NDM system the DCFs were replaced by variable optical attenuators (VOAs) to keep the level diagram unchanged. Additionally, in the DM system, an XPM suppressor with a wavelength selective switch and variable optical delay lines was inserted before the NZDSF.

After transmission, the center channel at a wavelength of 1590 nm was demodulated through the DSP-based receiver. The demodulation process included polarization demultiplexing based on a constant modulus algorithm, frequency offset compensation, Viterbi-Viterbi phase recovery, and finally differential decoding. Note that when these procedures were used, CD compensation or DBP were carried out prior to executing them, and that the DBP applied here included the cross-polarization effect [61].

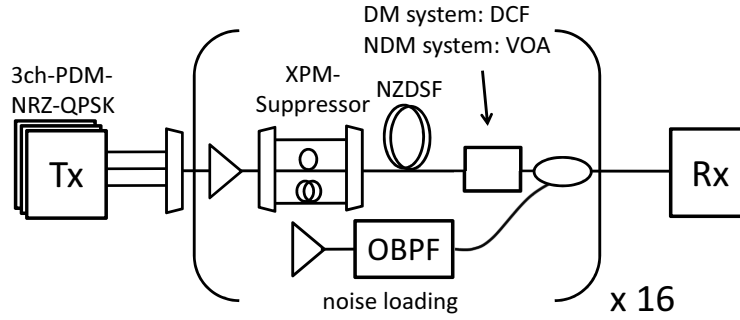


Fig. 5.1 Simulation setup. PDM: polarization division multiplexing, NRZ: non-return-to-zero, XPM: cross phase modulation, DM: dispersion-managed, NDM: non-dispersion-managed, DCF: dispersion-compensated fiber, VOA: valuable optical attenuator, NZDSF: non-zero dispersion-shifted fiber, OBPF: optical band pass filter.

### 5.1.3 Results and Discussion

#### 5.1.3.1 Effects of XPM-Suppressor and DBP in DM system

Fig. 5.2 shows how the  $Q$ -factors increased as a function of inter-channel skew with the XPM-suppressor in the DM system.  $Q$ -factor increase appeared to saturate by one symbol duration delay per span. This saturation is consistent with the results reported in [61]. Next, the DBP algorithm was applied to the XPM-suppressed signals. It is noteworthy that the number of DBP iteration stages is greatly reduced in the DM system due to the following reason. Assuming the condition in which the nonlinear calculation point is set at the connection point between a DCF and a NZDSF, a backward linear operator with step-size  $h$  can be expressed as  $-h\hat{D}$  for the NZDSF case and  $h\hat{D}$  for the DCF case. Denoting the backward nonlinear operator as  $h\hat{N}$ , the electrical field of the DBP output  $E_{\text{comp}}$  becomes

$$\begin{aligned} E_{\text{comp}} &= \exp(-h\hat{D}) \exp(h\hat{N}) \exp(-h\hat{D}) \dots \exp(h\hat{N}) \exp(h\hat{D}) E_{\text{rec}} \\ &= \exp(-h\hat{D}) \exp(hM\hat{N}) \exp(h\hat{D}) E_{\text{rec}}, \end{aligned} \quad (5.1)$$

where  $E_{\text{rec}}$  and  $M$  are respectively the received field and the total number of spans. Thus the number of iterations needed for span-by-span DBP can be reduced from  $M$  to the single stage. Fig. 5.3 summarizes  $Q$ -factor improvement by DBP for fiber launch power of 4 dBm as a function of inter-channel skew. Note that the  $Q$ -factor values shown represent average values

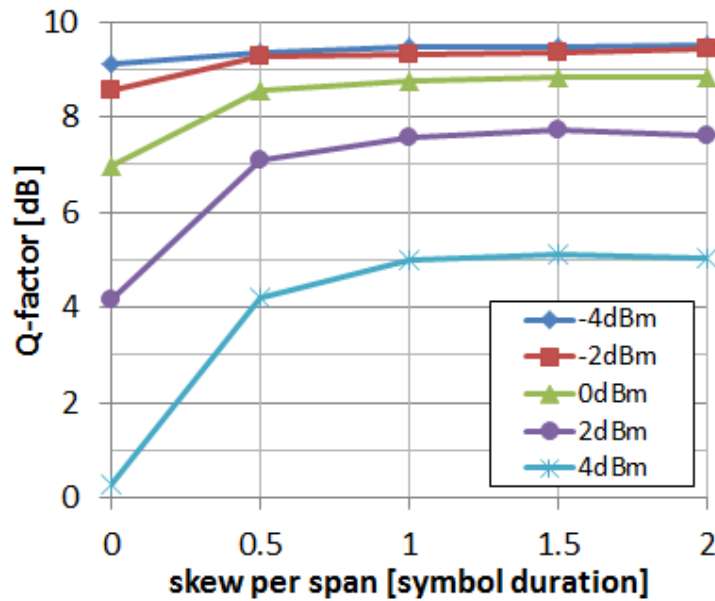


Fig. 5.2  $Q$ -factor improvement achieved with XPM-suppressor in DM system for various fiber launch power cases.

obtained for different ten runs. It is clear that  $Q$ -factor improvement tends to increase as inter-channel skew increases. This indicates that DBP, which cancels SPM-induced nonlinear distortion, works better when XPM is suppressed.

### 5.1.3.2 Performance Comparison Between DM and NDM Systems

Fig. 5.4 compares the  $Q$ -factors for the XPM-suppressed-DM and NDM systems with and without DBP. Even without DBP the  $Q$ -factors in the DM system exceeded those in the NDM system for all launch power cases. Fig. 5.5 shows peak-to-average power ratio (PAPR) at NZDSF input as a function of the number of spans. It was confirmed that the PAPR in the DM system was more moderate than that in the NDM system, since the waveform distortion due to CD was compensated for in every span by the DCFs in the DM system. This implies that the fiber nonlinearity in the DM system is suppressed compared to that in the NDM system. The  $Q$ -factor improvement brought about by DBP is not significantly different between the two systems. It should be noted that, however, even though for the NDM system DBP was repeated with sixteen steps (i.e., once for each span), comparable  $Q$ -factor improvement was achieved only by the single stage of DBP for the DM system.

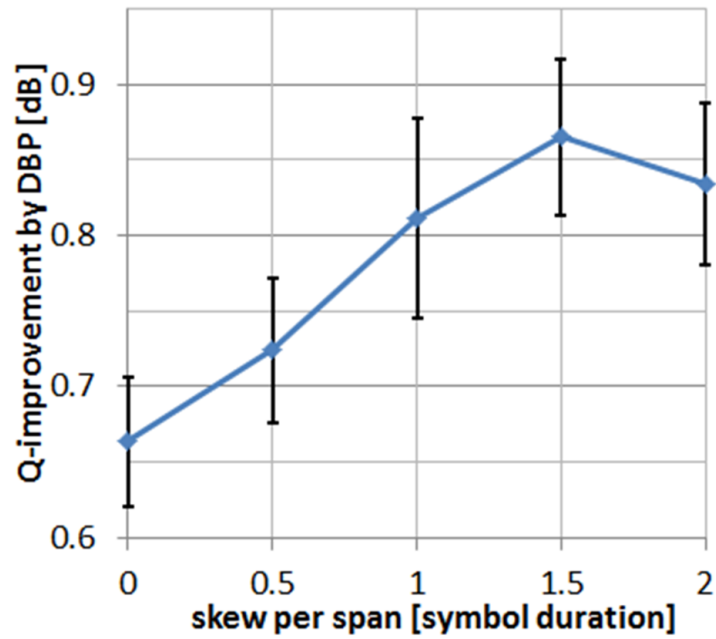


Fig. 5.3  $Q$ -factor improvement by DBP for fiber launch power of 4 dBm as a function of inter-channel skew. Error bars indicate the standard deviation of the  $Q$ -factor dataset.

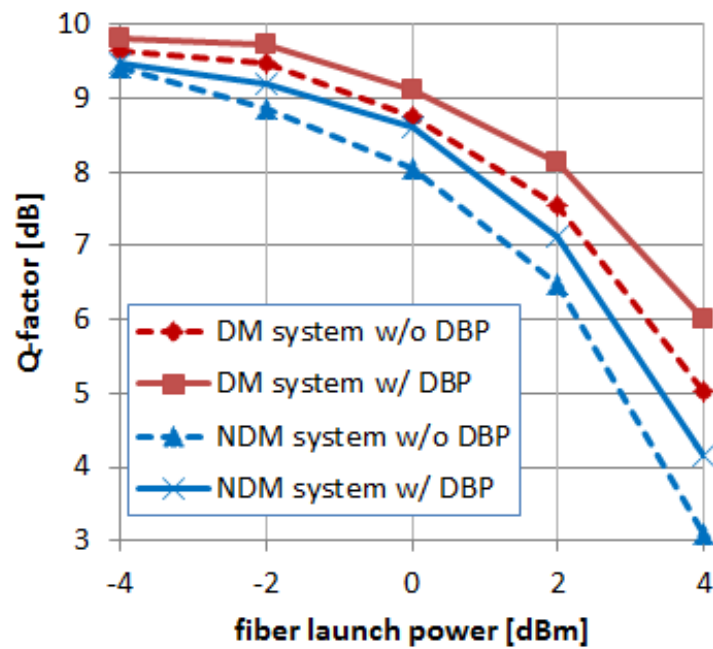


Fig. 5.4 Comparison of  $Q$ -factor between XPM-suppressed-DM and NDM system before and after DBP.

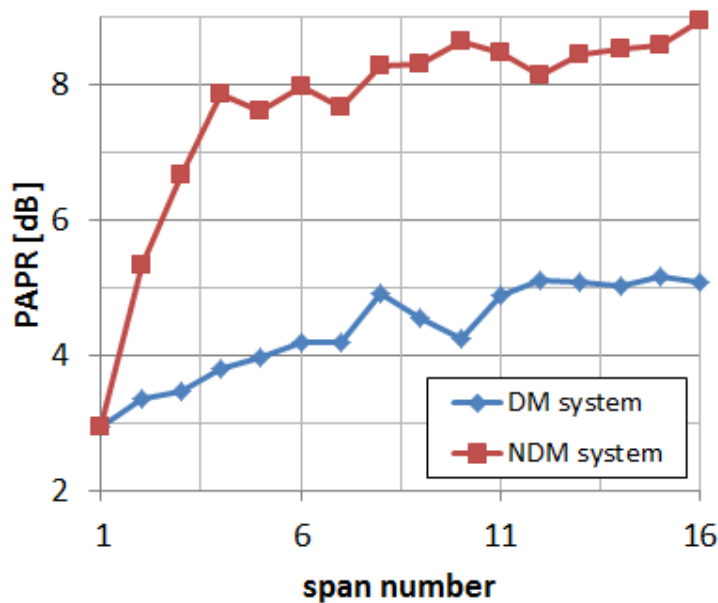


Fig. 5.5 PAPR in DM and NDM system as a function of number of spans. Note that PAPR is measured at NZDSF input in each span.

## 5.2 Digital Compensation for XPM-Induced Polarization Crosstalk Using Overlapped Fast Independent Component Analysis

### 5.2.1 Overview

In fiber-optic communication systems, the power density in optical fibers keeps enhancing annually in accordance with the development of large-capacity transmission techniques to meet the growing demand for the traffic increase. It is well known that optical signals suffer from severe degradation due to the Kerr effect in a high-power transmission system. In recent years, a number of compensation or mitigation techniques in the digital domain have been proposed and demonstrated to overcome the nonlinear distortions. Signal degradation caused by intra-channel nonlinearity is effectively reduced by the split-step-based algorithms, e.g., the digital back-propagation method [24]. However, inter-channel nonlinear distortions

still have a severe impact on the optical signals, since one can hardly know information about channels at different frequencies in general. PDM signal propagations in optical fibers are described by the Manakov equation [62], which includes the intensity-dependent terms and the state-of-polarization (SOP)-dependent term as cross phase modulation (XPM) effect from other channels. In PDM systems, the latter induces polarization scattering since the SOPs of PDM signals are switched symbol-by-symbol, which results in nonlinear polarization crosstalk (NPC) and consequent severe signal degradation in the receiver [63, 64].

An analytical model for NPC is described in [64]. With it, denoting the original signal vector as  $\mathbf{x} = [x_X \ x_Y]^T$ , and the scattered signal vector as  $\mathbf{y} = [y_X \ y_Y]^T$ , the XPM impact is modeled as mixing matrix  $\mathbf{M}$  by the Jones representation:

$$\begin{pmatrix} y_X \\ y_Y \end{pmatrix} = \mathbf{M} \begin{pmatrix} x_X \\ x_Y \end{pmatrix} = \begin{pmatrix} \sqrt{1 - |c_{XY}|^2} e^{j\Delta\theta} & c_{XY} \\ c_{YX} & \sqrt{1 - |c_{YX}|^2} e^{-j\Delta\theta} \end{pmatrix} \begin{pmatrix} x_X \\ x_Y \end{pmatrix}, \quad (5.2)$$

where  $e^{j\Delta\theta}$  is the XPM phase noise difference between the polarization and  $c_{XY/YX}$  is the NPC factor. Since  $\mathbf{M}$  changes at the speed of several tens of symbol intervals (i.e., at the order of GHz), it is hard to find a separation matrix  $\mathbf{W}$  using the conventional polarization-demultiplexing algorithm based on the steepest descent method due to its slow convergence. To date, a few NPC compensation techniques in the digital domain have been proposed [65, 66]. One of them, a simple decision-aided algorithm called NPC canceller (NPCC), was introduced in [65]; the authors used it to directly estimate  $\mathbf{M}$  from the received data on the assumption of  $|c_{XY/YX}|^2$ , and evaluated its performance.

This section proposes a novel blind equalization algorithm for NPC based on overlapping the fast independent component analysis (FastICA) technique. Conducted numerical simulation will reveal that the proposed algorithm outperforms the conventional method to equalize NPC for the transmission of QPSK modulation format. Next, the application of the proposed method is expanded to the signals with higher-order modulation order. The interaction of the joint application with other DSP algorithms is also surveyed when used with or in the step prior to them.

### 5.2.2 Proposed Algorithm: Overlapped-FastICA

Independent component analysis (ICA) provides a powerful solution for the blind source separation (BSS) problem without any knowledge of transmitted signals and the mixing process used during their propagation. The most important and interesting characteristics of ICA is that it solves BSS problems only by the statistical independence between received signals. In fiber-optic communication, ICA has been applied for polarization-demultiplexing [67–69]. In the ICA framework  $\mathbf{W}$  can be updated by not only the steepest descent scheme but the fixed-point (FP) scheme. The FastICA algorithm for complex-valued signals introduced in [70] finds  $\mathbf{W}$  in quite small iteration numbers, since it updates  $\mathbf{W}$  on the basis of the FP method. This advantage is likely to be useful for fast estimation of  $\mathbf{W}$  in the NPC estimation problem considered here. Based on the framework given in [70], FastICA updates  $\mathbf{W}$  to maximize non-Gaussianity of each signal. The negentropy-based cost function for complex-valued signals is defined as

$$J = \text{E} \left[ G(|\mathbf{w}^\dagger \mathbf{y}|^2) \right], \quad (5.3)$$

where  $\mathbf{w}$  is a column vector of  $\mathbf{W}$ ,  $G(x)$  is any non-quadratic smooth function,  $\text{E}[\cdot]$  is expectation operation, and the superscript  $\dagger$  is the Hermitian transpose.  $G(x)$  is here empirically assumed to have the form of

$$G(x) = \log(\cosh(x)). \quad (5.4)$$

The updating equation can be obtained by searching the extrema of  $J$  under the constraint condition of  $\text{E}[|\mathbf{w}^\dagger \mathbf{y}|^2] = 1$ . Thus, the updating equations for one unit become

$$\mathbf{w} \leftarrow \text{E} \left[ \mathbf{y}(\mathbf{w}^\dagger \mathbf{y})^* g(|\mathbf{w}^\dagger \mathbf{y}|^2) \right] - \text{E} \left[ g(|\mathbf{w}^\dagger \mathbf{y}|^2) + |\mathbf{w}^\dagger \mathbf{y}|^2 g'(|\mathbf{w}^\dagger \mathbf{y}|^2) \right] \mathbf{w}, \quad (5.5)$$

$$\mathbf{w} \leftarrow \frac{\mathbf{w}}{\|\mathbf{w}\|} \quad (5.6)$$

where  $g(x)$  and  $g'(x)$  are the first and second derivative function of  $G(x)$  respectively.

FastICA works on the block-wised batch processing, which means that it needs block sample input to estimate  $\mathbf{W}$ . The block-by-block estimation, however, may be not sufficient for fast tracking the change in  $\mathbf{W}$  since mixed signals are separated by the constant  $\mathbf{W}$  during one block period. Accordingly, a FastICA algorithm is modified to have fast tracking property,

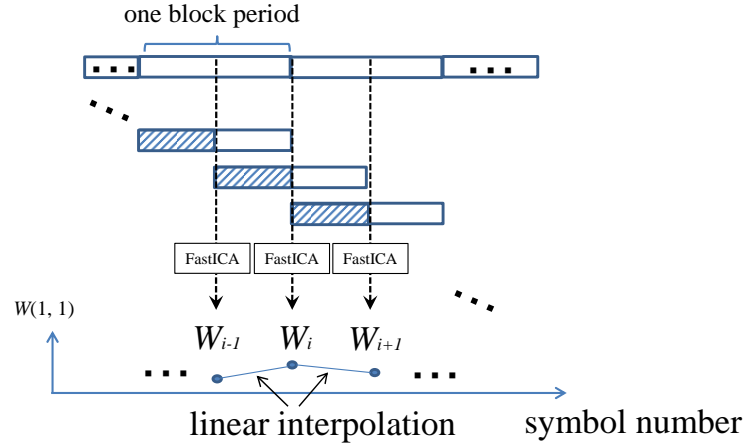


Fig. 5.6 Schematic illustration of overlapped-FastICA. Area with diagonal hatching lines indicates overlapped symbols. The overlapping ratio is set to 50 % in the figure.

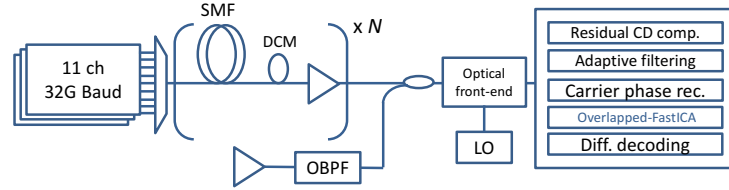


Fig. 5.7 Simulation setup. SMF: single mode fiber, DCM: dispersion compensation module, OBPF: optical bandpass filter, LO: local oscillator, CD: chromatic dispersion.

which is called *overlapped-FastICA* whose process is schematically drawn in Fig. 5.6. The estimated  $\mathbf{M}_i$  for the  $i$ -th block is applied for its center symbol separation. The next FastICA processing is done for the neighboring  $(i + 1)$ -th block with overlapping ratio of  $k$  % between the  $i$ -th block and the  $(i + 1)$ -th block. The separation matrix  $\mathbf{W}$  for the symbols between the center symbols of the  $i$ -th and the  $(i + 1)$ -th blocks can be simply estimated by linear interpolation of  $\mathbf{M}_i$  and  $\mathbf{M}_{i+1}$ . In this chapter, overlapping ratio  $k$  is set to 50 %. Note that initial  $\mathbf{W}$  is set to the  $2 \times 2$  identity matrix before the first update process of each block.

### 5.2.3 Simulation Setup

This subsection describes simulation setup to investigate the performance of the proposed algorithm. The configuration of the optical devices used in the simulations is drawn in



Fig. 5.7. Eleven Nyquist PDM optical signals driven at 32 Gbaud with 0.1 roll-off factor and 50-GHz channel spacing were transmitted through the dispersion-managed optical link. Here three kinds of modulation formats for the central measured channel are used: QPSK, 8QAM, and 16QAM. Ten optical signals with QPSK format were used as dummy channels to cause inter-channel nonlinearity. The transmission link consisted of 50-km single mode fibers (SMFs) with a polarization mode dispersion coefficient of  $0.05 \text{ ps}/\sqrt{\text{km}}$  and a nonlinear parameter of  $1.3 \text{ /W/km}$ . An in-line dispersion compensation module (DCM) was installed after each SMF, which compensated for dispersion at a 105 % rate. Before the signals entered the optical front end, ASE noise was added to set the received OSNR. In the receiver after analog-to-digital conversion, DSP procedures were applied for demodulation of signals as follows. First, in Subsections 5.2.4.1 and 5.2.4.2, overlapped- FastICA is applied after carrying out the standard DSP procedures, including residual CD compensation, adaptive MIMO equalization based on a multi-modulus algorithm, and Viterbi-Viterbi carrier phase recovery. Next, in Subsection 5.2.4.3, the application stage of overlapped-FastICA processing is changed to another in the receiver: DBP is added to the DSP procedures. In both implementation cases, errors were counted by differential decoding. The performance in each implementation case was evaluated by comparing the  $Q$ -factor calculated from BERs. Using the above demodulation process in the receiver, the back-to-back performance of each modulation format signals was obtained and displayed in Fig. 5.8 for a reference purpose.

#### 5.2.4 Simulation Results

Before showing the performance improvement obtained with the proposed algorithm, it is necessary to discuss a somewhat trivial but still important point: it is not clear how the optimum parameters can be determined, i.e., the block length, the iteration numbers for the proposed algorithm, and the averaging window size for NPCC. In this work, the optimum block length and window size were determined in such a manner that the largest  $Q$ -factor improvement was obtained. Fig. 5.9 depicts a typical transition of cost function as a function of iteration number. As the figure shows,  $\mathbf{W}$  is converged after eight iterations in most cases. It is confirmed, however, that there is no significant difference in the proposed algorithm's performance whether six or eight iterations are performed. Thus, in this work the update

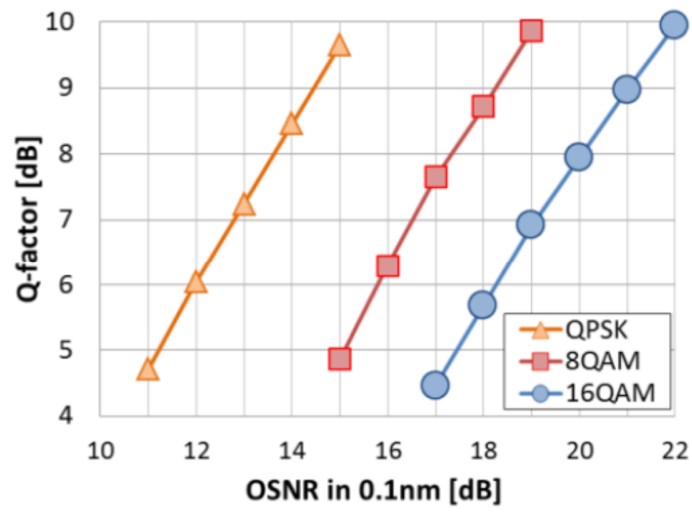


Fig. 5.8 The back-to-back performance for all modulation format signals as a function of OSNR.

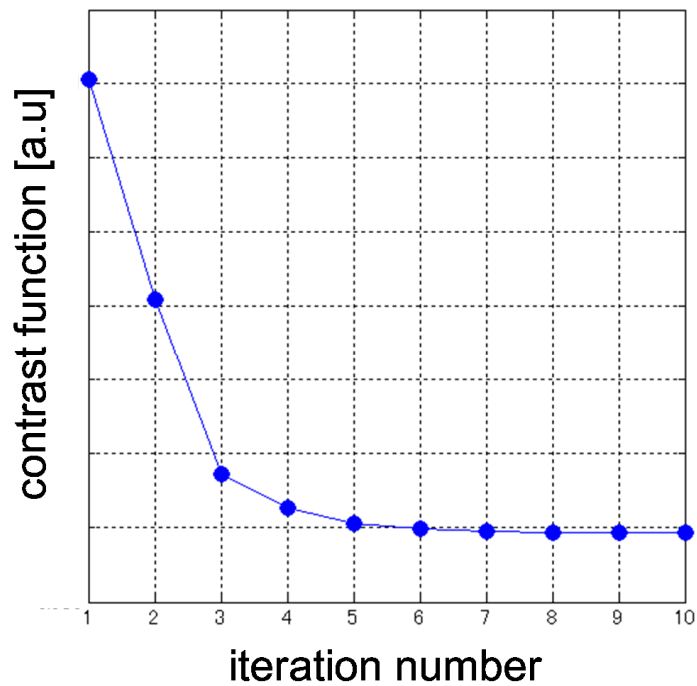


Fig. 5.9 Typical transitions of cost function as a function of iteration number.

process are repeated six times.

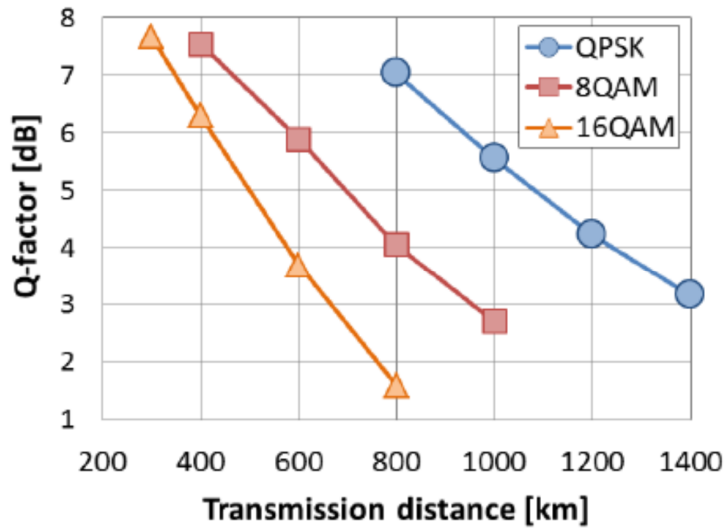


Fig. 5.10 The  $Q$ -factor as a function of transmission distance for all format signals. The fiber input power was 3 dBm.

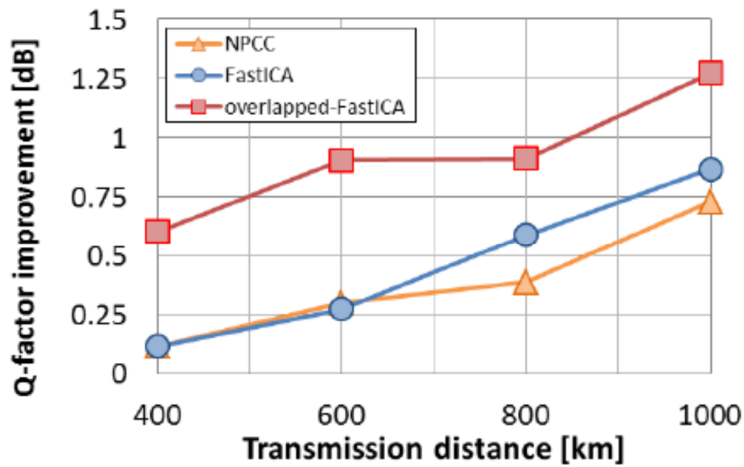


Fig. 5.11  $Q$ -factor improvement obtained with various compensation techniques for QPSK format signals as a function of transmission distance.

#### 5.2.4.1 Overview of Algorithm Performance

This subsection starts with an overview of the performance of overlapped-FastICA using the results obtained when it was applied to transmitted signals. Fig. 5.10 shows the  $Q$ -factor after transmission for all modulation format signals. For all transmission cases, the fiber launch power was set to 3 dBm. OSNR settings were changed depending on the modula-

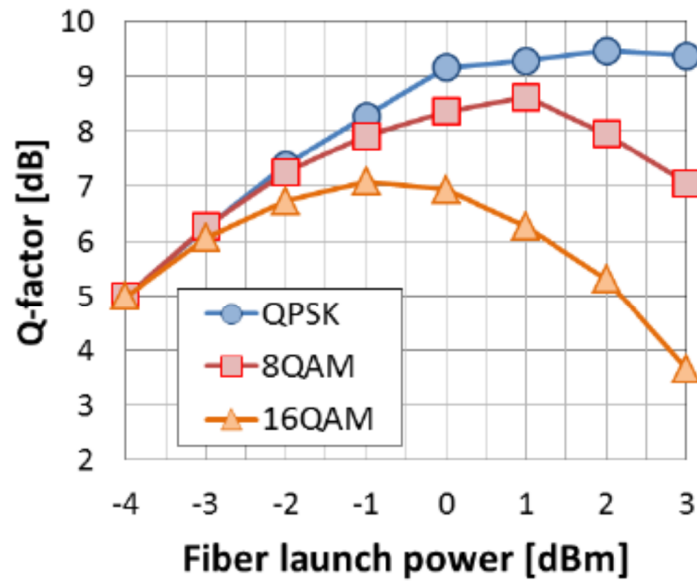


Fig. 5.12 The  $Q$ -factor performance after 1000-km transmission for all modulation formats as a function of fiber launch power.

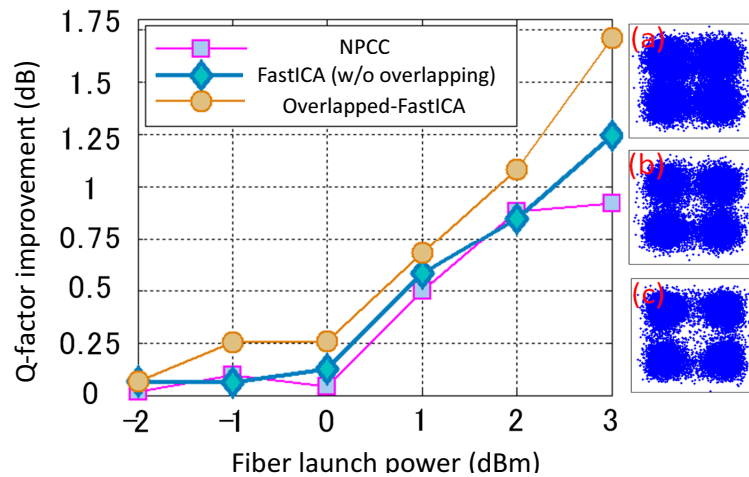


Fig. 5.13  $Q$ -factor improvement obtained with various compensation techniques as a function of fiber launch power for QPSK format signals. Bottom panels show the constellations (a) before compensation, (b) after NPCC, and (c) after overlapped-FastICA for each modulation format case.

tion format; 16 dB for QPSK, 20 dB for 8QAM, and 23 dB for 16QAM. Fig. 5.11 depicts the  $Q$ -factor improvement obtained by NPCC, FastICA, and overlapped-FastICA for QPSK-format signals. It shows FastICA improves the  $Q$ -factor as much as or slightly more than

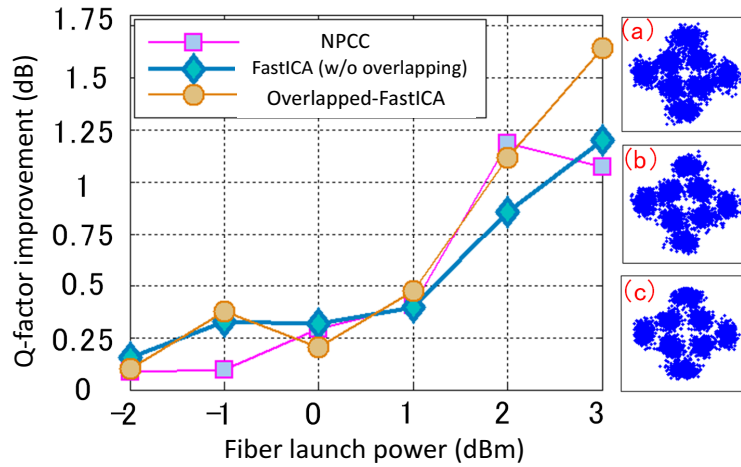


Fig. 5.14  $Q$ -factor improvement with the same format in Fig. 5.13 for 8QAM format signals.

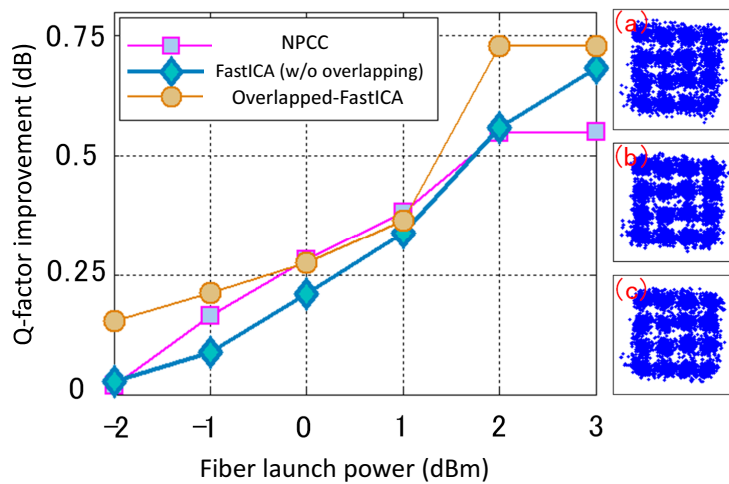


Fig. 5.15  $Q$ -factor improvement with the same format in Fig. 5.13 for 16QAM format signals.

NPCC, while overlapped-FastICA outperforms both by 0.2-0.5 dB, although it requires the largest computational load among the three. For all three techniques the improvement rises as transmission distance becomes larger; this is because the NPC factors in eq. (5.2) enhance as signals propagate over longer distances.

#### 5.2.4.2 Performance for Multi-Level Modulation Format Signals

Next, above compensation techniques are applied to 8QAM and 16QAM as well as QPSK format signals in order to verify the proposed algorithm's efficacy for higher order modulation format signals. The OSNR was set so that the  $Q$ -factor in each modulation format

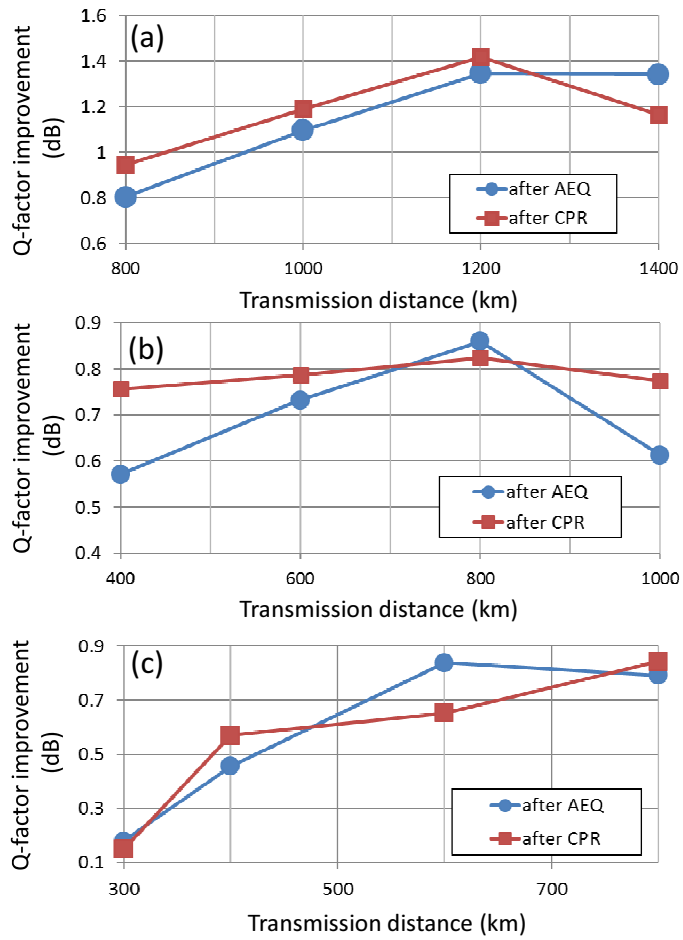


Fig. 5.16 The comparison of the  $Q$ -factor improvement performance of overlapped-FastICA that were applied after CD compensation and after CPR for the cases of (a) QPSK, (b) 8QAM, and (c) 16QAM signals.

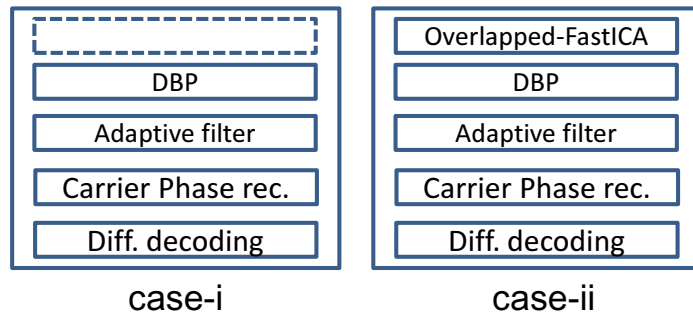


Fig. 5.17 DSP procedure cases. DBP: digital back-propagation.

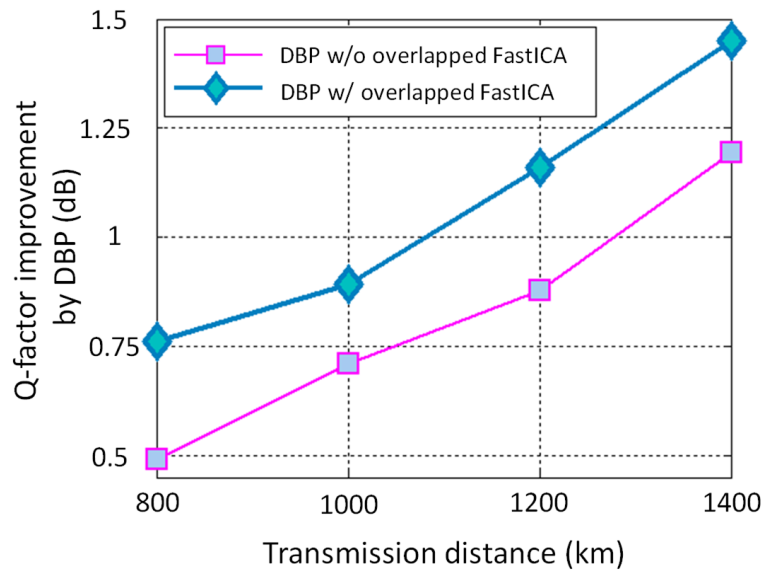


Fig. 5.18  $Q$ -factor improvement achieved by DBP with/without applying overlapped-FastICA before it.

signals became 5 dB at fiber launch power of -4 dBm in the linear transmission regime. Otherwise, the simulation conditions were the same as related in Subsection 5.2.4.1. The  $Q$ -factor performance of signals after 1000-km-transmission is displayed in Fig. 5.12. Fig. 5.13 through Fig. 5.15 show the  $Q$ -factor improvement achieved by NPCC, FastICA, and overlapped-FastICA when they were applied to the signals of QPSK (Fig. 5.13), 8QAM (Fig. 5.14), and 16QAM (Fig. 5.15) after transmission for various fiber launch power cases. The error bars were calculated from the standard deviation of ten transmission data with different input SOP for the transmission link. It should be noteworthy here that the updating equations and the cost function of FastICA and overlapped-FastICA were unchanged for all modulation format cases. It is clear from these figures that overlapped-FastICA compensates NPC effectively for all modulation formats. This feasibility may bring an advantage to the DSP circuit, since the proposed algorithm does not require any change of processing depending on the modulation format of input signals. Constellations before equalization and after NPCC or after overlapped-FastICA are also plotted at the bottom panels in the figure, which indicates these compensation techniques removed NPC. While overlapped-FastICA mostly outperforms NPCC and FastICA for the QPSK and 16QAM signals, it yields marginal improvements for 8QAM signals if compared to the performance of NPCC. Moreover, it im-

proves the  $Q$ -factor less for the 16QAM format signals than for the QPSK and 8QAM signals. It may be able to obtain larger  $Q$ -factor improvement if the non-quadratic smooth function  $G(x)$  is chosen carefully, although it is out of the scope of this study.

#### 5.2.4.3 Effect of Combining Overlapped-FastICA and Other Nonlinearity-Compensation Algorithms

There is one significant difference between NPCC and the proposed algorithm: while NPCC uses temporarily determined symbol information, overlapped-FastICA can be applied not only after CPR but also after other DSP procedures. This is because FastICA estimates  $W$  only by using the statistical independence of mixed signals. To demonstrate this, overlapped-FastICA is applied in the different stages of DSP procedures. Fig. 5.16 compares the  $Q$ -factor improvement by applying overlapped-FastICA after CD compensation and after CPR to the transmitted signals. The  $Q$ -factor performance before applying overlapped-FastICA is given in Fig. 5.10. As expected, the figure indicates that overlapped-FastICA also works even just after CD compensation.

Then, for the purpose of examining the effect of combining overlapped-FastICA and other DSP algorithms, the demodulation of received signals is performed by adding DBP processing to the DSP procedures that was different from those given in the previous subsections above. Two DSP procedure cases are assumed: in the first (case-i), the demodulation process included DBP, adaptive filtering combined with polarization-demultiplexing, and CPR. In the second (case-ii), overlapped-FastICA processing was added before DBP (Fig. 5.17). The expectation was the combination effect could be obtained by comparing the performance between the two (note that residual CD was compensated in the DBP processing). Fig. 5.18 shows the  $Q$ -factor improvement achieved solely by applying DBP to received signals for both cases. The DBP processing was executed once per span. The figure shows the  $Q$ -factor improvement in case-ii was clearly larger than that in case-i for all transmission distances. This fact implies the combination effect of overlapped-FastICA and DBP; that is, since overlapped-FastICA compensates for inter-channel nonlinearity in the step prior to DBP, improved performance is obtained for the DBP, which uses signal intensity information to equalize intra-channel nonlinearity.

Thus, as demonstrated above, it is reasonable to expect that the performance of other



DSP algorithms will be improved by combining overlapped-FastICA with them or applying overlapped-FastICA before them. For example, FastICA-based adaptive filtering may help to decrease convergence time or avoid the singularity problem [67]. Another example is that applying CPR after overlapped-FastICA may improve precision in phase estimation or decrease the occurrence rate of cycle slips.

### 5.3 Summary

Section 5.1 has successfully demonstrated the combined effects of optical and digital compensation techniques in a dispersion-managed (DM) system. The performance of digital back-propagation (DBP), which is devoted to the compensation for intra-channel nonlinear distortion in the digital domain, improves when inter-channel nonlinearity is optically suppressed. In addition, the periodic CD profile in the DM system contributes to a sharp reduction in the number of DBP iteration stages compared to the non-DM (NDM) system.

In Section 5.2, a novel algorithm is proposed that overlaps the fast independent component analysis (FastICA) algorithm to equalize nonlinear polarization crosstalk (NPC). The overlapped-FastICA algorithm shows better performance than the conventional algorithms due to its fast and direct estimation of the separation matrix only by statistical independence of received signals. It was also verified that overlapped-FastICA has the significant feature of modulation format-free efficacy and the combination effect with other DSP algorithms; the numerical simulation demonstrated that overlapped-FastICA successfully removed NPC independent of modulation formats, and that the performance of DBP was improved by applying overlapped-FastICA in the step prior to it since it effectively compensates for inter-channel nonlinear distortions.

## Chapter 6

# Multistage SIC for Spectrally-Efficient Super-Nyquist Transmission

### 6.1 Overview

The spectral shaping techniques with digital preprocessing in a transmitter has contributed to the substantial spectral efficiency (SE) increase for the Nyquist wavelength division multiplexing (WDM) transmission in which optical carriers are allocated with almost symbol-rate carrier spacing [39]. The super-Nyquist signal transmission that confines carriers tightly within symbol-rate carrier spacing is promising to achieve the further SE improvement. Two main strategies have been investigated to exploit a super-Nyquist transmission, including sole detection of a carrier managing the inter-symbol interference (ISI) [71, 72], and joint detection of carriers controlling the inter-carrier interference (ICI) [73, 74].

As the ISI-managing approach, the duobinary shaping is used for the frequency occupancy reduction of a signal, and most probable signal sequences are determined for the received signals contaminated with ISI by a maximum likelihood sequence estimator (MLSE) [71]. Time frequency-packing transmission proposed in [72] achieved the super-dense carrier spacing by removing ISI-induced bit errors using the turbo decoder. As alternative ICI-controlling approach, the ICI arisen from the SCs' overlap can be partially removed by using the adjacent SCs' information. The joint signal processing among adjacent SCs was demonstrated for ICI cancellation in which the received signal waveforms from independent neighboring receivers were jointly input to single adaptive LMS-based MIMO equalizer [73, 74].

The schemes for undesired signal nulling have been intensively exploited in wireless communication fields, including co-channel interference cancellation in satellite communication

systems [75], and successive interference cancellation (SIC) in wireless DS/CDMA or MIMO communication systems [76]. These schemes both utilize replica construction of undesired signals for interference cancellation.

This chapter first proposes to apply multistage successive interference cancellation (M-SIC) to remove ICI by reconstructing interference signals. Its feasibility as an ICI cancellation method was verified through numerical simulation and in 195-km transmission experiments. It was also demonstrated that combining M-SIC with non-uniform power transmission enabled system performance improvement. Furthermore, the joint adaptation of the M-SIC scheme and FEC coding for ICI mitigation is also proposed, which is here referred to as a coded superimposed transmission (CST). The conducted transmission experiments demonstrated that the CST performance outperformed the conventional transmission with no ICI management in terms both of SE and  $Q$ -factor.

## 6.2 Multistage SIC for ICI mitigation

The fundamentals of SIC has been already described in Chapter 2. The key feature of the SIC scheme is to detect data stream individually rather than simultaneously by removing interference streams detected in the preceding stages. For the M-SIC application, dual PDM SCs are assumed that are located with frequency spacing of  $\Delta f$  and driven at a symbol rate of  $B$ . Two parameters are defined to investigate ICI effects: the SC spacing factor,  $\alpha = \Delta f/B$ , and the power imbalance factor,  $\gamma = 10 \log_{10}(P_2/P_1)$ , where  $P_i$  is the  $i$ -th SC's power. Fig. 6.1 depicts the processing flow of the proposed M-SIC for dual SCs in the receiver. At the 0th M-SIC stage, the received signals of SC- $i$  ( $i = 1, 2$ ) are equalized and polarization-demultiplexed by a  $2 \times 2$  equalizer without cancelling ICI. Then the equalizer output X/Y signals are input to slicers that make symbol decisions, following by the replica reconstruction through a pulse-shaping filter with a prior-known roll-off factor. The replicas are shifted by the prior-known spacing of  $\pm\Delta f$ , and fed into the inputs to a  $4 \times 2$  equalizer as interference signals. The received signals of SC- $i$  ( $i = 1, 2$ ) are fed into the other two inputs of the equalizer as the desired signals. Consequently, ICI for SC- $i$  is cancelled by the equalizer in the 1st SIC stage. Cancellation for SC- $i$  is successively done in the 2nd stage using the replicas for SC- $i$  reconstructed on the basis of the output from the 1st stage. In this way, the

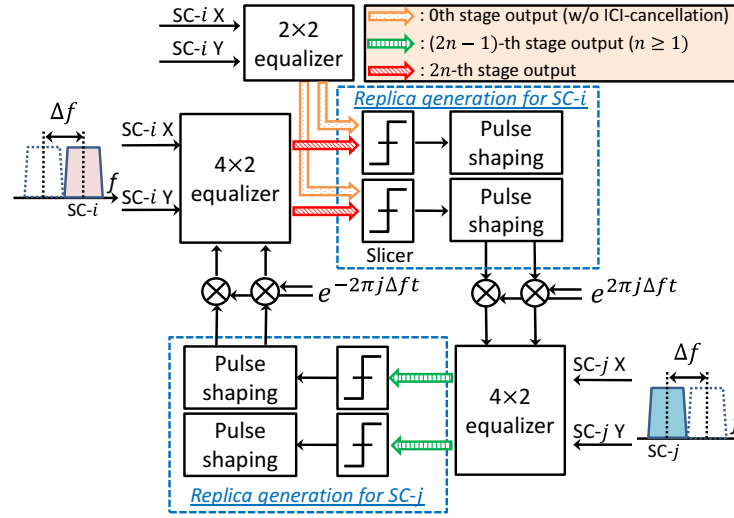


Fig. 6.1 Processing flow of M-SIC.

process can be expanded to a multistage ICI equalizer process by using replicas reconstructed in the preceding stage.

### 6.3 Simulation Results

This section provides an overview of the performance of M-SIC for ICI cancellation through numerical simulations. Dual SCs with PDM-QPSK or -16QAM signal formats were created, each of which was reshaped by a root-raised-cosine filter with a roll-off factor of 0.01. Setting  $B$  and  $\gamma$  to 16 Gbaud and 0 dB respectively,  $\Delta f$ , and accordingly  $\alpha$ , are changed for the purpose of investigating the ICI effect. Generated signals were transmitted in a back-to-back configuration and ASE noise was added to them to set OSNR at 19 dB with a 0.1-nm resolution bandwidth for QPSK and 26 dB for 16QAM signals before they entered the receiver. The ICI-removing process was first performed for SC-1 by using the replicas for SC-2 (1st stage), then for SC-2 by using the replica for SC-1 (2nd stage) and continued in the same way as described in the previous section. An LMS-based adaptive filter was used as an MIMO equalizer with 33  $T/2$ -spaced taps and recovered phase noise simultaneously. 32000 symbols were used for initial convergence of taps in the data-aided mode. The adaptation algorithm was then switched to the decision-directed mode. Bit errors

were counted by means of differential decoding and finally calculated  $Q$ -factors by using the measured BERs.

Fig. 6.2 shows  $Q$ -factors as a function of the number of stages for (a) QPSK and (b) 16-QAM signals. Note that  $Q$ -factors after the odd (even)-number stages correspond to those for SC-1(2). It is clear from the figures that  $Q$ -factors were enhanced as the number of stages increased for both format signals, indicating that the replicas were more precisely generated in the latter stages. It was also found that the performance improvement saturated after the 4th or 5th stages. This is because M-SIC corrected the symbol errors induced not by noise but by ICI only. The method is expected to reduce carrier spacing by up to 20 % for QPSK signals with 1.1-dB  $Q$ -penalty, and up to 5 % for 16QAM signals with 0.8-dB  $Q$ -penalty. Next the received OSNR was varied in the 16-19 dB range for QPSK signals with  $\alpha$  of 0.8. Fig. 6.3 shows  $Q$ -factors obtained before and after M-SIC as a function of OSNR. In the low OSNR regime, the ICI cancelling effect is likely to degrade since slicers are prone to make incorrect decisions due to relatively large noise. However, it was confirmed that ICI was still mitigated at OSNR of 16 dB. The  $Q$ -factor improvement achieved after the 4th SIC stage for OSNR of 16 and 19 dB were respectively 2.6 and 4.0 dB.

## 6.4 Transmission Experiment Results

Next, transmission experiments were conducted to show the performance of M-SIC. The proposed M-SIC scheme is firstly adopted to dual-carrier transmission in which they have spectral overlapping over standard SMFs in Subsection 6.4.1. An enhanced performance of higher spectral efficiency is demonstrated by M-SIC jointly used with a coding scheme in Subsection 6.4.2.

### 6.4.1 Superimposed Transmission with M-SIC Scheme

In the first transmission experiment, 195-km SMFs comprising four spools were employed. The experimental setup is illustrated in Fig. 6.4. At the transmitter, an external cavity laser (ECL) was used as a 1568-nm CW light source. The signal format was identical to that in the simulation except that only QPSK signals were employed. The voltage that drives

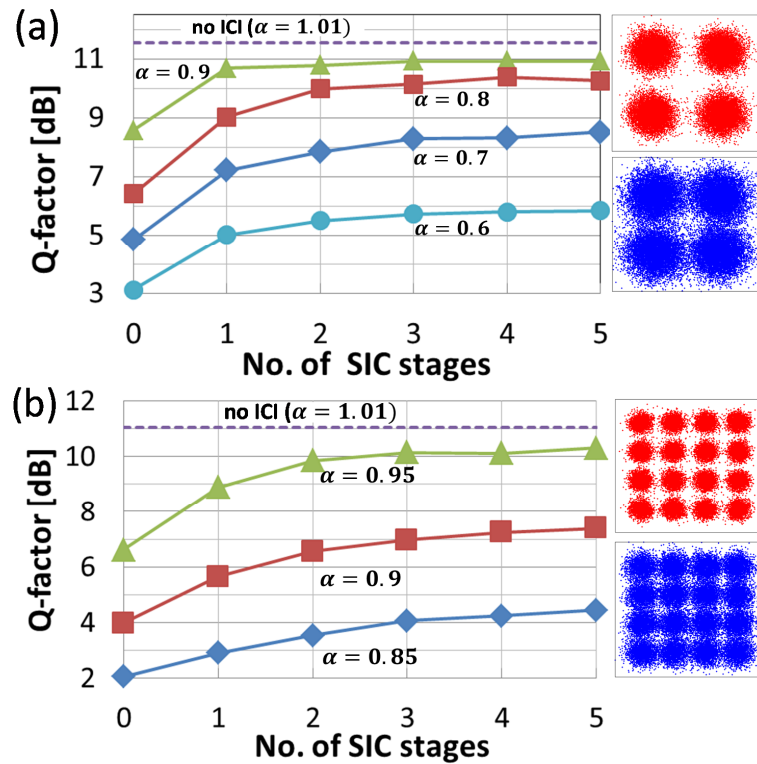


Fig. 6.2  $Q$ -factor transitions as a function of SIC stages for (a) QPSK and (b) 16QAM signals. The constellations for both format signals before and after M-SIC are displayed at inset panels (bottom: before M-SIC, top: after M-SIC).

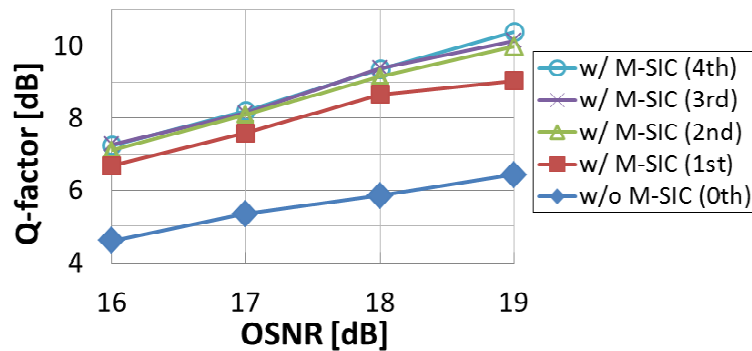


Fig. 6.3  $Q$ -factors before and after M-SIC as a function of OSNR.

the dual SCs was produced by an arbitrary waveform generator (AWG) and fed into optical IQ-modulators. The transmission line consisted of four spans, each of which included 50-km SMF (except for the fourth span with 45-km SMF) with chromatic dispersion of 17.8

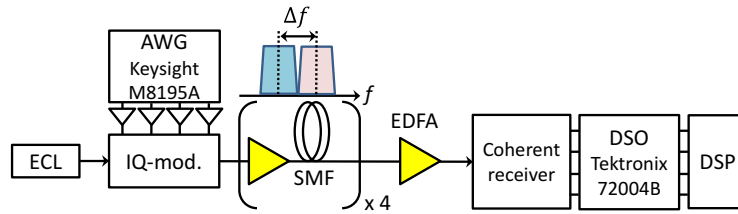


Fig. 6.4 Experimental setup. ECL: external-cavity laser, AWG: arbitrary waveform generator, SMF: single-mode fiber, EDFA: Erbium-doped fiber amplifier, DSO: digital storage oscilloscope, DSP: digital signal processing

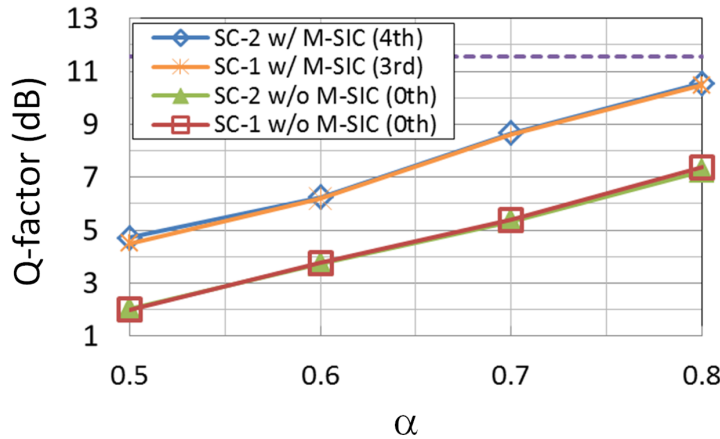


Fig. 6.5  $Q$ -factor after 195km-transmission as a function of carrier spacing factor  $\alpha$ .

ps/nm/km and EDFA. The fiber launch power in each span was set at -5 dBm per SC so that nonlinear distortions could be neglected. After transmission over 195 km, the measured OSNR was 24 dB. After coherent detection, analog signals were digitized at 50 GS/s and stored by using a digital storage oscilloscope (DSO). Then the signals were demodulated, followed by ICI removal through offline processing in the same way as done in the simulation.

Fig. 6.5 depicts measured  $Q$ -factors before and after M-SIC was applied as a function of  $\alpha$ . The results confirmed that the method suppresses carrier spacing by 20 % within 1-dB  $Q$ -penalty. In the SIC operation scheme, one of the most commonly used cancellation methods is ordered SIC, which ranks signals in order of their signal-to-interference-plus-noise ratio (SINR) and then successively decoded them in the order of their SINR values. Accordingly,  $\gamma$  was deliberately changed to make the SINR different for the dual SCs and transmitted them with non-uniform power profile [77], while maintaining the total power of both SCs as -2

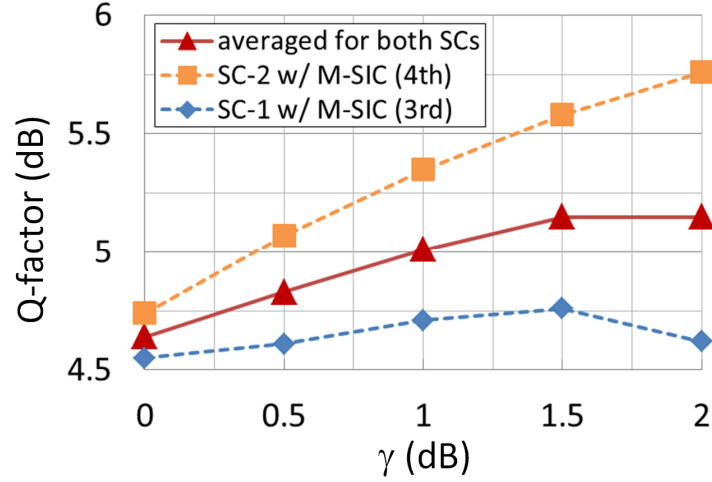


Fig. 6.6  $Q$ -factor for non-uniform power transmission as a function of power imbalance factor  $\gamma$ .

dBm. In the evaluation,  $\alpha$  was fixed at 0.5 and  $\gamma$  was varied in the range from 0 dB to 2 dB. Fig. 6.6 shows the  $Q$ -factors of SC-1 and -2 respectively obtained after the 3rd and 4th SIC stages as a function of  $\gamma$ . It is noteworthy to point out that  $Q$ -factors not only for SC-2 but also for SC-1 increased in the  $0 \text{ dB} \leq \gamma \leq 1.5 \text{ dB}$  range. This  $Q$ -factor's behaviour is explained as follows: as  $\gamma$  became larger, the replicas for SC-2 were reconstructed more precisely in the 0th SIC stage with SINR improvement. Thus the non-uniform power transmission improved the ICI cancellation performance. When  $\gamma$  exceeded 2 dB, the  $Q$ -factors for SC-1 decreased since SC-1 was transmitted with low OSNR (the low-OSNR-induced M-SIC performance degradation has already been shown in Fig. 6.3). Nevertheless, Fig. 6.6 indicates that the averaged signal performance calculated from averaged BERs for both SCs was improved by 0.5 dB at  $\gamma$  of 1.5 dB. This improvement would bring narrower carrier spacing to super-Nyquist transmission.

#### 6.4.2 Coded Superimposed Transmission with M-SIC Scheme

The previous subsection focused on the sole adaptation of the M-SIC scheme for superimposed transmission, and has proved that the M-SIC scheme allows SCs to be allocated with channel spacing smaller than symbol rate with certain  $Q$ -penalty. ICI induced the SC superimposition is likely to be mitigated not only by the M-SIC scheme but also by means of FEC coding scheme. Thus, this subsection further proposes to superimpose coded dual-SC trans-



mission with carrier spacing below symbol rate. Specifically, the coding for ICI mitigation is supposed to be performed for one of dual SCs. The expectation is that the ICI-free replica construction can be achieved by the use of FEC coding, which is used for the M-SIC scheme. Fig. 6.7 illustrates both the conventional insuperimposed transmission (IST) and the proposed coded superimposed transmission (CST). Note that in both transmission regimes FEC coding is assumed for fiber impairment mitigation with FEC overhead of  $\eta_0$  ( $\eta_0 \geq 0$ ). In CST, SC#2 is coded with FEC overhead of  $\eta_{\text{CST}}$  ( $\eta_{\text{CST}} \geq 0$ ) for ICI mitigation, and superimposed with SC#1. Dual SCs are decoded jointly in the receiver with ICI mitigation by the combined use of the M-SIC scheme and FEC decoding. Assuming signal modulation order of  $M$ , SE in IST,  $S_{\text{IST}}$ , within the bandwidth of  $2B$  becomes

$$\begin{aligned} S_{\text{IST}} &= \frac{2^{\frac{\log_2(M)B}{1+\eta_0}}}{2B} \\ &= \frac{\log_2(M)}{1+\eta_0}. \end{aligned} \quad (6.1)$$

In CST, since the total FEC overhead differs between two SCs, SE in CST,  $S_{\text{CST}}$ , is calculated as

$$\begin{aligned} S_{\text{CST}} &= \frac{\frac{\log_2(M)B}{1+\eta_0} + \frac{\log_2(M)B}{(1+\eta_0)(1+\eta_{\text{CST}})}}{2B\delta} \\ &= \frac{\log_2(M)}{2\delta(1+\eta_0)} \left( 1 + \frac{1}{1+\eta_{\text{CST}}} \right), \end{aligned} \quad (6.2)$$

where  $\delta$  denotes the carrier spacing compression factor which is defined as

$$\delta = \frac{B + \Delta f}{2B}. \quad (6.3)$$

The SE-related parameter called SE gain  $G_{\text{SE}}$  is also defined in this chapter by the ratio of those SE parameters, which is explicitly expressed as

$$\begin{aligned} G_{\text{SE}} &= \frac{S_{\text{CST}}}{S_{\text{IST}}} \\ &= \frac{1}{2\delta} \left( 1 + \frac{1}{1+\eta_{\text{CST}}} \right). \end{aligned} \quad (6.4)$$

Obviously from the definition in eq. (6.4), the regime in which  $G_{\text{SE}}$  exceeds unity corresponds to CST having higher SE than IST brought by the carrier spacing suppression, even under the consideration of the FEC-induced SE decrease. The higher-SE region of CST differs

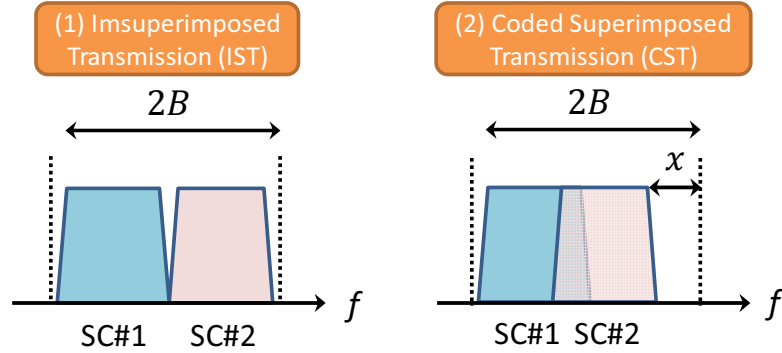


Fig. 6.7 Schematic of (1): imsuperimposed transmission (IST), and (2): coded superimposed transmission (CST) with spectral overlapping.

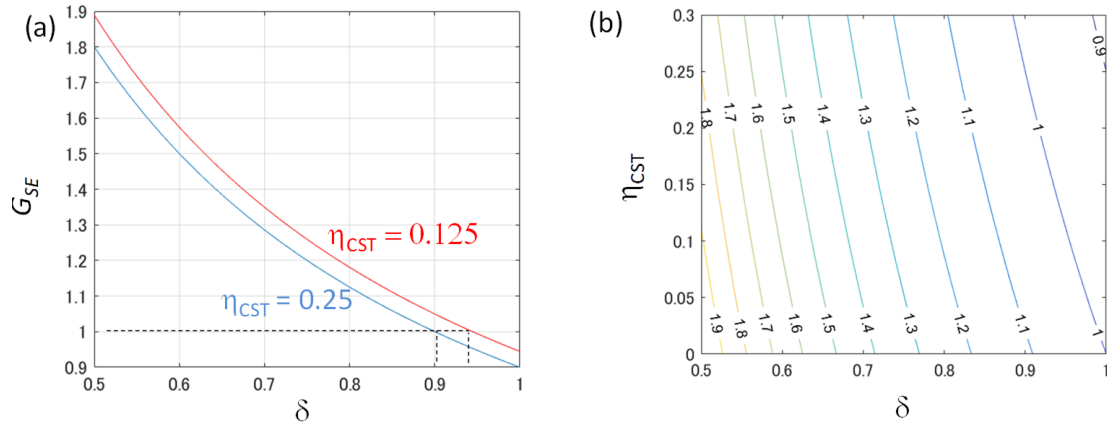


Fig. 6.8 (a)  $G_{SE}$  curves as a function of  $\delta$  for  $\eta_{CST} = 0.25$  (blue) and  $\eta_{CST} = 0.125$  (red). (b)  $G_{SE}$  contour plot for various  $\delta$  and  $\eta_{CST}$ .

depending on  $\eta_{CST}$ . For example,  $G_{SE}$  becomes larger than unity at  $\delta = 0.9$  with  $\eta_{CST} = 0.25$ , and at  $\delta = 0.94$  with  $\eta_{CST} = 0.25$  (Fig. 6.8(a)). The more comprehensive analysis is performed in Fig. 6.8(b) for various  $\delta$  and  $\eta_{CST}$ . The numbers in the figure corresponds to  $G_{SE}$  obtained by the pair of certain  $(\delta, \eta_{CST})$ . For a fixed  $G_{SE}$ , higher  $\eta_{CST}$  may bring lower erroneous transmission because of its higher correction capability. On the contrary, lower  $\eta_{CST}$  is preferable in terms of the decoding complexity.

The transmission experiments were conducted to exploit the CST performance with M-SIC scheme. The transmission setup was basically identical to the one used in the previous subsection except for the employment of dual PDM-QPSK signals each driven at 6 Gbaud. The optical signals were transmitted in the back-to-back configuration with various received

ONSR. The signal processing flow is summarized in Fig. 6.9 which contains M-SIC processing. For initial setting, an integer variable counting the number of “outer iteration”  $l$  is set to 1. The iteration number of M-SIC  $N_{\text{M-SIC}}$  and one of outer iteration,  $L$ , are respectively set to 2 and 3. The processing of CST started with M-SIC for ICI cancellation, followed by the FEC decoding for SC#2 to remove bit errors induced by ICI. In this subsection, LDPC code was implemented on SC#2 with code rate of  $4/5$  (which is corresponding to  $\eta_{\text{CST}} = 0.25$ ) defined in DVB-S2 [78]. In the decoding process, errors are supposed to be removed by the soft-decision sum-product algorithm in the logarithm domain with 10 iterations. Next step diverges depending either on syndrome of LDPC code or on  $l$  value. If the syndrome calculation for the decoded bit with the parity check matrix becomes 0 (which is corresponding to the error-free condition), or  $l$  reaches  $L$ , ICI cancelling is performed for SC#1 by using replicas of SC#2 constructed in the previous step. Otherwise,  $l$  is incremented by one, then the above processing containing M-SIC and the FEC decoding for SC#2 is repeated, which is here referred as *outer iteration*. The last step again checks the syndrome and the value of  $l$  and with the aim to confirm that all errors on SC#2 are completely removed or not. If the error-free condition is not satisfied, the ICI cancelling on SC#2 is eventually carried out.

Fig. 6.10 depicts the transmission result of  $Q$ -factor averaged over both SCs with OSNR ranging from 5 dB to 11 dB with  $\Delta f$  of 4.2 GHz, 3.5 GHz, and 3.1 GHz, each corresponding to  $G_{\text{SE}}$  of 5.9 %, 13.7 %, and 18.7 %. The  $Q$ -factor performances of IST with  $\Delta f = 6$  GHz and of the ICI-free transmission with  $\Delta f = 6.5$  GHz are also presented in Fig. 6.10 for a reference purpose, which indicates that the ICI-penalty in IST becomes  $\sim 0.2$  dB due to a slight frequency overlap of dual SCs. It can be seen in Fig. 6.10 that CST outperforms IST in terms both of SE and  $Q$ -factor in a certain OSNR range, say, in the OSNR range  $\geq \sim 9.6$  dB for  $G_{\text{SE}} = 18.7$  %. This range corresponds to the region in which the decoded bits of SC#2 exhibited almost no error, hence the quasi ICI-free replica construction was successfully achieved in the M-SIC scheme as expected. The obtained  $Q$ -factor increase for CST with  $G_{\text{SE}} = 18.7$  % yielded  $\sim 0.7$  dB. In the OSNR range  $\leq \sim 9.6$  dB, however, the  $Q$ -factor curve of CST with  $G_{\text{SE}} = 18.7$  % dropped steeply, which corresponds to the cliff region of LDPC code. The  $Q$ -factor curves with  $G_{\text{SE}} = 5.9$  % and 13.7 % represented almost the same properties, except that the cliff regions respectively became lower to  $\sim 7.7$  dB and to  $\sim 6.2$  dB, indicating that they achieved higher noise tolerance at the expense of lower  $G_{\text{SE}}$ .

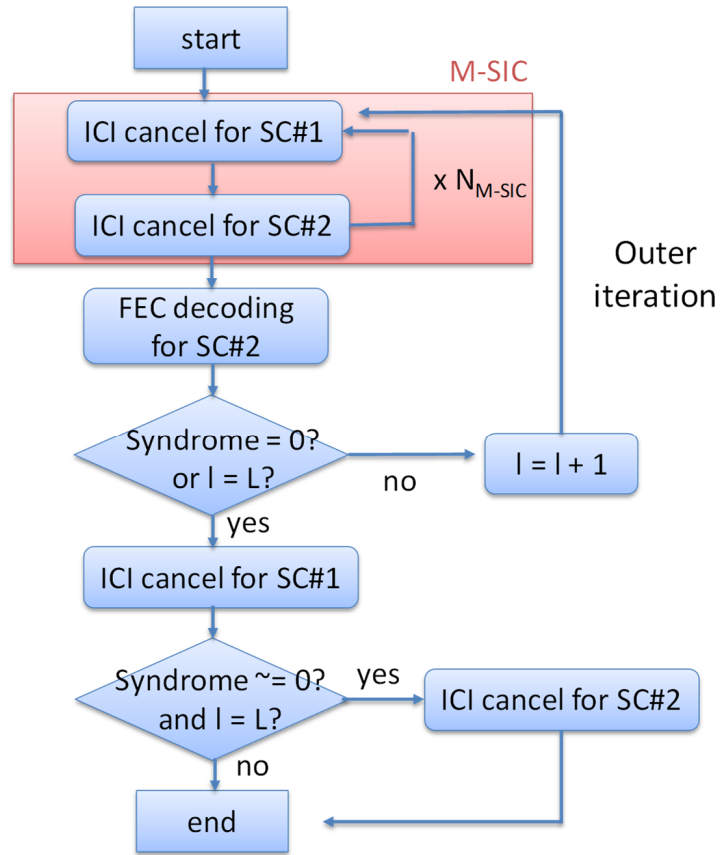


Fig. 6.9 The processing flow chart of CST with M-SIC scheme.

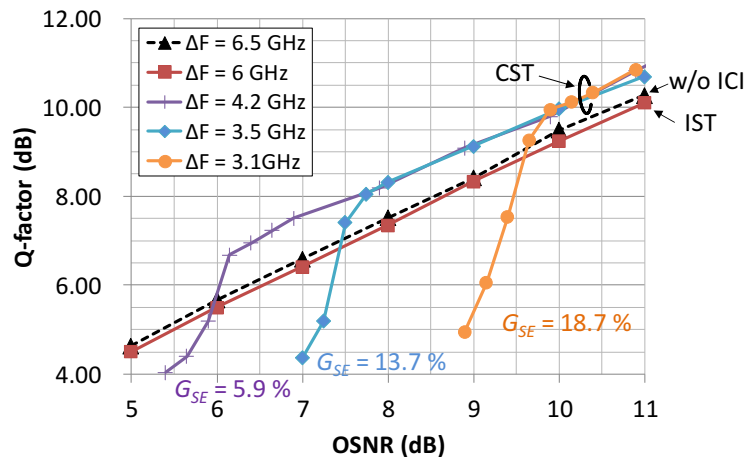


Fig. 6.10  $Q$ -factor performance of CST and IST for various carrier space settings.  $G_{SE}$  is displayed in percent.

## 6.5 Summary

In this chapter, the scheme of the M-SIC method incorporated with the prior knowledge of adjacent carriers is proposed as a means to achieve super-Nyquist transmission. It was demonstrated numerically and experimentally that M-SIC effectively canceled ICI and enabled 20 % carrier spacing suppression for QPSK signals. Conducted experiments showed that the signal performance was improved by combining M-SIC with non-uniform power transmission. Also proposed was the CST with M-SIC scheme for further system performance improvement. By adapting error-correction coding scheme to the transmission comprised of dual superimposed SCs, the system performance improvement was achieved in both of SE and  $Q$ -factor.

## Chapter 7

# State-Of-The-Art Space Division

# Multiplexing Transmission Progress and Challenges

### 7.1 Overview

The fiber nonlinearity declines the achievable information rate inferred from the classical Shannon's theory as discussed in Section 1.3. Assuming a standard SMF as a transmission medium and physical and system parameters relevant to it, the capacity limit of an SMF-based transmission link system is roughly estimated to be around 100 Tb/s [10]. Indeed, the highest capacity over an SMF without SDM technology ever reported was around 100 Tb/s [79, 80].

To accommodate the demand for future energy-efficient fiber-optic communication systems with extremely large capacity, space division multiplexing (SDM) transmission technologies employing multicore (MC) and/or multimode fibers (MMFs) have been intensively developed in recent years. Specifically, a few SDM transmission demonstrations handling Pb/s-class capacity have been performed employing MCFs [18, 19, 21], and MC-MMFs [20]. While this fact may convince us that SDM transmission technology will offer a solution against the capacity crunch, much still remains to be unclarified issues.

An SDM transmission can be categorized into two regimes, including *uncoupled* and *coupled* transmission. Transmission over an MCF is an uncoupled transmission regime in which interference leaked from other cores is well suppressed by means of fiber and/or system design. In this regime, little signal processing modification would be required with respect to transmission over a conventional SMF. On the other hand, in the coupled transmission

regime, the use of multi-input multi-output (MIMO) signal processing is vitally required to undo couplings between spatial channels, especially for long-haul transmission longer than correlation length [81]. Throughout this work an SDM transmission which employs MIMO signal processing is referred to as an MIMO-SDM transmission.

An MIMO-SDM transmission characteristics is modeled by an MIMO channel [82], which is considered to be the general expansion of  $2 \times 2$  Jones matrix representation used for polarization effect description in an SMF. This feature implies that MIMO signal processing techniques offer powerful tools in detecting MIMO-SDM signals, which are widely used in present wireless communication systems. With it, an employment of multiple transmitters and receivers enables larger system throughput and/or higher transmission reliability than that of single-input single-output (SISO) communication system. However, the transmission performance of MIMO-SDM signals that utilizes spatial mode as independent waveguides for parallel data streams are significantly affected by differential mode delay (DMD) and mode dependent loss (MDL). They yet remain dominant performance restriction factors in MIMO-SDM transmission [83]. Most MIMO-SDM transmission experiments employed linear MIMO equalization techniques with adaptive weight updating algorithms as a means of demultiplexing spatial channels. Nonlinear MIMO detection schemes which generally provide higher transmission performance are also applicable to optical MIMO-SDM transmission, although their performance have been investigated in a few SDM transmission experiments/simulations in the context of optical MIMO transmission having spatial channels larger than two (i.e., polarization channels in an SMF) [82, 84].

One of the main challenges for future's practical application of long-haul dense SDM transport systems is to overcome underlying phenomena of DMD and MDL. The aim of Chapter 7 is to review the current progress of SDM transmission experiments and fundamental techniques for mitigating DMD and MDL. Also discussed is applications of advanced MIMO signal processing to deal with these issues.

## 7.2 Recent Progress on SDM Transmission Experiments

SDM fibers have been used to enjoy the spatial degrees of freedom in a optical fiber which accommodates independent data streams into multiple cores and/or guided modes as spatial

channels. A parameter characterizing an SDM fiber is the spatial multiplicity  $\Gamma$ , defined as the product of the core count with the spatial mode number (excluding polarizations). Spatial efficiency  $\eta_{\text{spatial}}$  is also used to quantitatively discuss how densely independent spatial paths are confined in a single SDM fiber, defined as the spatial multiplicity in a unit cross-sectional area [85]. Equivalently,  $\eta_{\text{spatial}}$  is obtained with

$$\eta_{\text{spatial}} = \frac{\Gamma}{\pi D^2}. \quad (7.1)$$

where  $D$  is a cladding diameter. Table 7.2 summarizes the recently-achieved progress on SDM transmissions. Mainstream fibers commonly used in SDM transmission include an MCF, an MMF, an CC-MCF, an MC-FMF, each of which represents distinct SDM-transmission features as shown in Table 7.2. In this section, a brief review on SDM-transmission characteristics is independently provided over each SDM fiber.

### 7.2.1 MCF Transmission

An MCF possesses multiple cores in a single cladding, each of which is designed to transmit parallel data streams in distinct cores. As of today,  $\Gamma$  ranges from 7 [71, 86] to 37 [13]. Power leakage arisen from optical signals propagating in other cores is referred to as inter-core crosstalk, and considered to be a fundamental parameter to be considered in designing an MCF transmission system. While the introduction of higher-order modulation signals into an MCF transmission obviously has an advantage in increasing the spectral efficiency, they are more susceptible to the inter-core crosstalk [87]. Since the regime of lower inter-core crosstalk is preferable for reliable long-haul and spectrally-efficient MCF transmission, a major challenge from the standpoint of transmission over an MCF is the inter-core crosstalk management. The designs of the core arrangement in a cladding have been studied to reduce the inter-core crosstalk, including structures of one-ring [86], dual-ring [87, 88], hexagonal [71], and square lattice [21, 89]. The employment of the heterogeneous structure [89] which introduces a slight difference of the propagation constants between the adjacent cores, or of the trench-assisted structure [90] which has *trench* with lower refractive index profile around the core of interest. As an approach based on a system design, the bidirectional MCF transmission scheme called propagation-direction interleaving (PDI) transmission in which



signal propagation directions are assigned to be opposite between adjacent cores in order to avoid inter-core coupling was found to be also beneficial in mitigating inter-core crosstalk with respect to the unidirectional MCF transmission [87, 88]. While enlarging the cladding diameter may be seemingly a promising solution for the issue of the inter-core crosstalk suppression, it was pointed out in [17] that the allowable maximum cladding diameter is limited to 250  $\mu\text{m}$  in terms of the long-term mechanical reliability.

Since each core in an MCF is capable to accommodate independent data stream with negligible crosstalk, a lot of well-established transmission techniques and devices developed in SMF transmission are applicable to MCF transmission. Accordingly MCF transmission significantly contributes to the development of SDM transmission in terms both of fiber capacity and transmission distance. The first Pb/s-class transmission over 12-core MCF was reported in [18], followed by 22-core MCF transmission with 2.15-Pb/s capacity [19], and 32-core heterogeneous MCF transmission with 1.001-Pb/s capacity [21]. A few studies have already succeeded in thousands-of-km MCF transmission experiments in the past few years, including 12-core MCF transmission over 14,350 km [91] with capacity-distance product of 1.51 Eb/s-km and low-crosstalk 32-core MCF over 1,644.8 km [89].

## 7.2.2 MMF/FMF Transmission

Despite of the fact that the use of an MMF led the early stage of fiber-optic communication systems in the 1970s, it did not fully exploit the high information-carrying potential, namely, the spatial degree of freedom in an MMF. Indeed, since in an MMF system transmission reach is severely restricted by modal dispersion and inter-modal crosstalk, the use of MMF has been mainly devoted to the short-reach interconnection until recently. FMF is a transmission medium that is designed to manage the allowable number of the guided modes by designing the normalized frequency  $V$  with the fiber parameters of a wavelength  $\lambda$ , a core radius  $a$ , a core index  $n_1$ , and a cladding index  $n_2$  [92]:

$$\begin{aligned} V &= \frac{2\pi a}{\lambda} \sqrt{n_1^2 - n_2^2} \\ &\approx \frac{2\pi a n_1}{\lambda} \sqrt{2\Delta}, \end{aligned} \quad (7.2)$$

where  $\Delta \stackrel{\text{def}}{=} \frac{n_1 - n_2}{n_1}$  is the refractive index difference. Since in a typical fiber used for fiber-optic communication  $\Delta$  is far small than unity, weakly-guiding approximation is valid to simply describe the guided mode with linearly polarized (LP) mode [92]. For the region of  $V < \sim 2.405$ , a fiber can support only the fundamental  $LP_{01}$  mode which is used as single mode fiber. When  $V$  is exceeding 2.405, the light of the higher order mode is permitted to propagate. Generally, the total number of allowable number of the guided modes  $N_{\text{total}}$  in the step-index MMF is evaluated as

$$N_{\text{total}} \approx \frac{V^2}{2}. \quad (7.3)$$

MIMO-SDM transmission can scale the system capacity in accordance with the spatial mode number employed by decoupling the inter-modal crosstalk. MIMO-SDM transmission techniques using an MMF or an FMF have been investigated as SDM fibers in which mutually-coupled spatial signals are supposed to be decomposed by MIMO signal processing techniques. To date, MIMO-SDM signal transmission experiments have been reported which have the spatial mode number ranging from 3 [93–96] to 15 [14]. The highest capacity ever reported on FMF transmission was 115.2 Tb/s employing 10 spatial modes over 87 km [97]. The achieved FMF transmission reach is still limited to around 1,000 km [94–96].

### 7.2.3 CC-MCF Transmission

An CC-MCF is alternative SDM fiber enabling MIMO-SDM transmission, which has closely-spaced multiple cores so that optical lights propagating in different cores couple each other. In contrast to an uncoupled MCF that positions cores with relatively larger spacing to have sufficiently smaller inter-core crosstalk, cores within a cladding of an CC-MCF are arranged to have smaller core pitch, typically  $20 \mu\text{m}$  [98] to  $30 \mu\text{m}$  [99]. The coupled-mode analysis performed in [100, 101] indicates an CC-MCF offers the *supermode* propagation with linear combination of independent core modes. The strong coupling between nondegenerate modes is beneficial in mitigating the accumulation both of DMD and MDL in a statistical sense [102]. Therefore, CC-MCF transmission has been mainly devoted to the transmission reach expansion of MIMO-SDM signals in the past few years [98, 99, 103]. The record transmission reach of 5,500 km over CC-MCF supporting 4 spatial modes was reported in [98] in which the equalizer memory length was well suppressed less than 20 ns even after 5,500 km

transmission. Another advantage of CC-MCF is that the standard cladding diameter of 125  $\mu\text{m}$  is maintained in the design of an CC-MCF, which may contribute to the spatial density increase and to the adaptation of existing manufacturing, splicing, connecting process used for a standard 125- $\mu\text{m}$  SMF. By managing fiber-twisting rate, an CC-MCF having the highest core count with 125- $\mu\text{m}$  cladding diameter of 12 was fabricated in [104].

### 7.2.4 MC-FMF Transmission




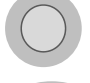
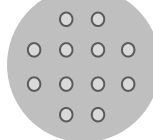
An MC-FMF offers spatial multiplicity  $\Gamma$  larger than 100 by fully utilizing the spatial degree of freedom with a combined structure both of an MCF and an FMF, which means that individual core of an MC-FMF supports a propagation of a few spatial modes. The first dense SDM transmission over 12-core  $\times$  3-mode MC-FMF with  $\Gamma$  of 36 was reported in [105]. The largest  $\Gamma$  of 114 was achieved in the past few years by employing 19-core  $\times$  6-mode MC-FMF [16, 17]. With the advantage of high  $\Gamma$ , the highest aggregate spectral efficiency of 947 b/s/Hz was reported in [106]. The extremely-large capacity transmission with 2.05-Pb/s was demonstrated in [20] over a 19-core  $\times$  6-mode MC-FMF. Long-haul dense SDM transmission experiments over 527 km using 12-core  $\times$  3-mode MC-FMF was successfully demonstrated in [107] which will be described in Chapter 8.1.

The main difficulty to handle an MC-FMF is involved with severe tolerance of core displacement/rotation at connections between fiber sections and under-developing SDM devices used for multiplexing/demultiplexing and amplification. The MC-FMF design with small  $D$  is preferable in terms both of mechanical reliability [17] and of fiber impairment reduction including fiber loss and MDL. Among MC-FMFs fabricated with  $\Gamma$  exceeding 100, 19-core  $\times$  6-mode MC-FMF fabricated in [17] is the only one which has small  $D$  below 250  $\mu\text{m}$ , consequently achieving  $\eta_{\text{spatial}} = 2398.6 / \text{mm}^2$ .

## 7.3 Issues and Methodologies on MIMO-SDM Transmission

Section 7.3 is devoted to providing the review of optical methodologies for DMD and MDL issues. Prior to the topic, a brief description with regard to DMD and MDL with the matrix propagation model is provided which is useful to get the deeper understanding of their

Table. 7.1 CLASSIFICATION OF SDM FIBERS.

Fiber Type	Cross Section View	$D$ ( $\mu\text{m}$ )	$\Gamma$	MIMO DSP for spatial channel	Ref.
SMF		125	-	unnecessary	-
Uncoupled MCF		195 to 260	7 to 37	unnecessary	[13, 18, 19, 21, 71, 86, 88, 89, 91]
Core-coupled MCF		125	3 to 12	necessary	[98, 99, 103, 104]
FMF		125	3 to 15	if coupled, necessary	[14, 93–97, 108, 109]
MC-FMF		229 to 318	36 to 114	if coupled, necessary	[16, 17, 105–107]

properties.

### 7.3.1 Matrix Propagation Model

Matrix propagation model was originally proposed for the analysis of polarized signals in a single mode fibers. In the model, a fiber is divided into multiple sections, each of which is represented with a matrix having an uncoupled DMD and MDL effects. The overall channel transfer matrix  $\mathbf{H}$  is obtained with the concatenation of these matrices. For a sufficiently narrow frequency slot, the channel transfer matrix of the  $k$ -th span at angular frequency  $\omega$  is given for expressing DMD effects to the first order as [102]

$$\mathbf{H}_{\text{DMD}}^{(k)}(\omega) = \mathbf{V}^{(k)} \mathbf{\Lambda}^{(k)}(\omega) \mathbf{U}^{(k)\dagger}, \quad (7.4)$$

where  $\mathbf{U}^{(k)}$  and  $\mathbf{V}^{(k)}$  are unitary matrices which account for the relationships between input and output at the connection of the  $k$ -th section. The matrix  $\mathbf{\Lambda}^{(k)}$  is the diagonal matrix expressed as

$$\mathbf{\Lambda}^{(k)} = \begin{pmatrix} \exp(-j\omega\tau_1^{(k)}) & & 0 \\ & \ddots & \\ 0 & & \exp(-j\omega\tau_N^{(k)}) \end{pmatrix}, \quad (7.5)$$

Table 7.2 SUMMARY ON RECENT SDM TRANSMISSION EXPERIMENTS.

Fiber Type	Ref.	Fiber Parameter			Transmission Parameter					
		Spatial Multiplicity	Cladding Diameter ( $\mu\text{m}$ )	$\eta_{\text{spatial}}$ ( $1/\text{mm}^2$ )	Capacity (Tb/s)	Distance (km)	Aggregate SE (b/s/Hz)	Memory Length (ns)	Amplification Scheme	Wavelength Band
Uncoupled MCF	[71]	7	196	232.0	140.7	7326	28	1.3	MC-EDFA	C
	[86]	7	195	234.4	120.7	204	53.6	-	RO MC-EDFA + DRA	C
	[18]	12	227	296.5	1010	52	91.4	-	-	C+L
	[88]	12	225	301.8	$2 \times 344$	1500	3.56	1.4	EDFA + DRA	C+L
	[91]	12	-	-	105.1	14350	38.4	-	SM-EDFA	C
	[110]	12	-	-	519.6	8830	58.3	-	SM-EDFA	C+L
	[19]	22	260	414.4	2150	31	215.6	0.35	-	C+L
	[89]	32	243	690.0	1.58	1644.8	201.5	2.7	MC-EDFA	C
[21]	32	243	690.0	1001	205.6	217.6	0.53	SM-EDFA	C	
Coupled-core MCF	[99]	3	125	244.5	1.2	4200	4.03	20	SM-EDFA	C
	[98]	4	125	326.0	34.6	5500	11.5	20	SM-EDFA	C
	[103]	6	125	488.9	18	1705	18	20	SM-EDFA	C
FMF	[93]	3	125	244.5	57.6	119	12	6.3	FM-EDFA	C
	[94]	3	125	244.5	27.7	500	7.6	-	FM-EDFA	C
					3	1000	-	21.1	-	-
	[95]	3	125	244.5	11.52	900	9	30	SM-EDFA	C
	[96]	3	125	244.5	18	1050	9	33.3	DRA	C
	[108]	6	125	488.9	6.1	708	16	20	SM-EDFA	C
	[97]	10	125	814.9	23.2	125	29	33.3	-	C
					115.2	87	-	-	-	-
[109]	10	125	814.9	67.5	87	58	33.3	-	C	
[14]	15	125	1222.3	17.2	22.8	43.6	30	-	C	
MC-FMF	[105]	36	229	874.1	61.97	40	247.9	58.1	-	C
		(12-core $\times$ 3-mode)								
	[107]	36	230	866.5	23.6	527	94.3	64	FM-EDFA	C
		(12-core $\times$ 3-mode)								
	[15]	108	306	1468.6	-	5.5	-	8.0	-	C
		(36-core $\times$ 3-mode)								
[16]	114	318	1435.4	2050	9.8	456	33.3	-	C	
	(19-core $\times$ 6-mode)									
[106]	114	318	1435.4	-	9.8	947	50	-	C	
	(19-core $\times$ 6-mode)					665				

where  $\tau_i^{(k)}$  denotes the uncoupled group delay of the  $i$ -th mode at the  $k$ -th section. Similarly, MDL of the  $k$ -th span at angular frequency  $\omega$  is contributes as

$$\mathbf{H}_{\text{MDL}}^{(k)}(\omega) = \mathbf{V}^{(k)} \mathbf{G}^{(k)}(\omega) \mathbf{U}^{(k)\dagger}, \quad (7.6)$$

where  $\mathbf{G}^{(k)}$  is the uncoupled modal gain expressed as

$$\mathbf{G}^{(k)} = \begin{pmatrix} \exp\left(\frac{1}{2}g_1^{(k)}\right) & & 0 \\ & \ddots & \\ 0 & & \exp\left(\frac{1}{2}g_N^{(k)}\right) \end{pmatrix}, \quad (7.7)$$

where  $g_i^{(k)}$  denotes the uncoupled MDL of the  $i$ -th mode at the  $k$ -th section.

The overall channel transfer matrix  $\mathbf{H}$  is obtained by concatenating of matrices at each

section represented as eq. (7.5) and eq. (7.7). More specifically, overall DMD is calculated from the eigenvalue difference of the group delay operator  $\Omega$ , defined as

$$\Omega \stackrel{\text{def}}{=} j \frac{\partial \mathbf{H}^\dagger}{\partial \omega} \mathbf{H}, \quad (7.8)$$

and overall MDL is calculated from the eigenvalue ratio of the MDL operator  $\Xi$ , defined as

$$\Xi \stackrel{\text{def}}{=} \mathbf{H}^\dagger \mathbf{H}. \quad (7.9)$$

MDL is also evaluated based on the singular value decomposition of  $\mathbf{H}$ .

### 7.3.2 Methodologies for Dealing with DMD

Let us use an example of a mode-multiplexing system supporting 2 LP modes to consider DMD problems as illustrated in Fig. 7.1. In an MIMO-SDM transmission, each excited mode signal experiences slight group delay which induces propagation time difference between propagated modes, and referred to as DMD. In a regime of weak coupling, since spatial modes having different propagation constants (i.e., nondegenerate modes) rarely couple each other, DMD effects may appear as temporal pulse isolation, which accumulates linearly with a fiber length. On the contrary, in a strongly-coupled regime, DMD scales with the square root of the fiber length, and eventually combined effects of DMD and multiple power transitions between spatial modes broadens signal pulse. In both regimes, however, pulse spreading occurs more quickly along a fiber with respect to polarization mode dispersion (PMD) in an SMF. As will be discussed, DMD-induced pulse spreading enhances a complexity of MIMO signal processing due to the memory length increase.

Methodologies to combat DMD currently reported include employing graded-index (GI) MMF [94, 95, 107] CC-MCF [98, 99, 103, 104], optical DMD compensation [95], and digital DMD compensation approaches [105, 107] (Fig. 7.2). GI-MMF approach successfully suppresses DMD due to its characteristic (e.g., parabolic) index profile,  $n(r)$ , which decreases as the distance from the center of the core increases.

$$n(r) = \begin{cases} n_1 \sqrt{1 - 2\Delta(r/a)^2} & (r \leq a) \\ n_2 & (r \geq a) \end{cases} \quad (7.10)$$

for GI-MMF with the parabolic index profile. CC-MCF is another promising fiber-based approach (as already discussed in Section 7.2) which is designed to utilize strong inter-core crosstalk by reducing core pitch so that signals propagating in CC-MCF behave as supermodes [98, 99, 103]. The significant advantage of it is that accumulated DMD scales with the square-root of transmission distance in CC-MCF. As for optical DMD compensation, it is a straightforward approach that employs concatenated multiple opposite-sign-DMD fiber segments to cancel accumulated DMD [95]. Recently, it was reported that DMD-managed MMF transmission was achieved since DMD in each MMF can be flexibly tuned by designing a multi-step index profile [111]. Although these techniques are promising ways to decrease or compensate for DMD, it does not mean that they fully compensate for total DMD and mode coupling effects. Consequently, it is preferable to apply receiver-side digital DMD compensation in conjunction with the above-cited optical approaches to cancel DMD effects, especially for long-haul MMF transmission. Most widely-used signal processing technique is an adaptive linear MIMO equalization. However, as transmission distance increases, a larger number of equalizer taps is required to compensate for wide range of pulse spreading resulted from DMD and modal coupling, which increases MIMO equalizer complexity. Another strategy using MIMO-SDM is MIMO-less transmission which is especially suitable for short-reach SDM communication systems. In [112], real-time FMF transmission over 0.5 km was demonstrated with quasi parallel SMF transmission by using an elliptical-core FMF which avoided coupling between non-degenerate modes.

Once a symbol rate of transmitted signals  $B$  and the MIMO equalizer tap length  $L$  are given, the equalizer memory length  $T$  is readily estimated as  $T = \frac{L}{Bp}$ , where  $p$  is the oversampling rate. Fig. 7.3 summarizes recent SDM transmission experiments over MCF, CC-MCF, FMF, and MC-FMF listed in Table 7.2 with the calculated memory length used for linear MIMO equalization as a function of transmission distance. Dotted lines in the figure show the equalizer memory length per unit length  $\tau$  of 1, 10, 100, and 1000 ps/km. For MCF transmission,  $\tau$  is quite low because chromatic dispersion, which is the dominant dispersion phenomenon in an MCF transmission link, has been typically compensated by using the fixed equalizer prior to the linear MIMO equalizers. As explained above, DMD accumulation in CC-MCF is suppressed so that  $\tau$  presents around 10 ps/km even after a few thousands-of-km transmission. By employing optical approaches of GI-FMFs and/or optical DMD compensation, long-haul

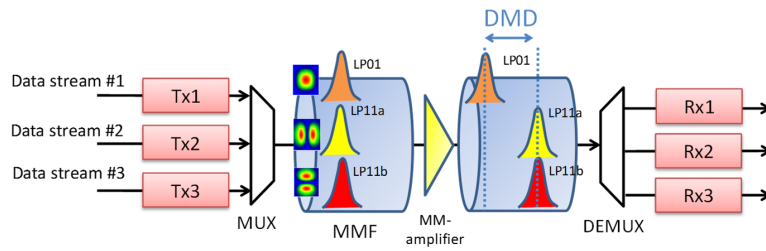


Fig. 7.1 Schematic illustration of DMD in 2-LP mode MMF.

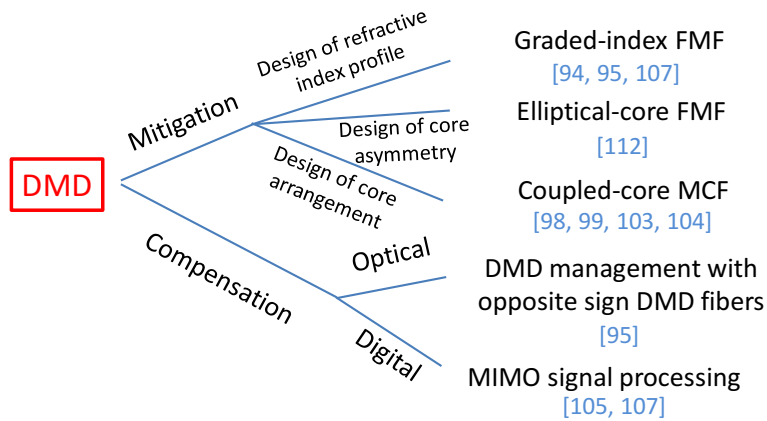


Fig. 7.2 Optical methodologies for DMD currently reported.

FMF transmission experiments have succeeded in managing  $\tau$  below 100 ps/km, except for FMF transmissions employing more than 10 spatial modes [14, 97, 109]. As for MC-FMF transmission, it is likely to be technically hard to manage by means of the optical DMD compensation approach, because DMD factor typically differs depending on propagating core. Consequently,  $\tau$  exceeds 1000 ps/km except for 527-km GI MC-FMF transmission in [107].

To mitigate the complexity of a linear MIMO equalization, the employment of parallel MIMO frequency-domain equalization (FDE) instead of conventional single-carrier time-domain equalization (TDE) was proposed in [105, 107]. In the proposed parallel MIMO FDE, two distinguishing schemes are employed. The first is low-symbol-rate multicarrier transmission. A single carrier is divided into individual subcarriers to reduce the required number of equalizer tap length [105]. The second is employing an FDE algorithm. The use of FDE helps to significantly reduce the number of multiplications in convolution steps for output/update calculations. The complexity of parallel MIMO FDE is only about 1.5 %



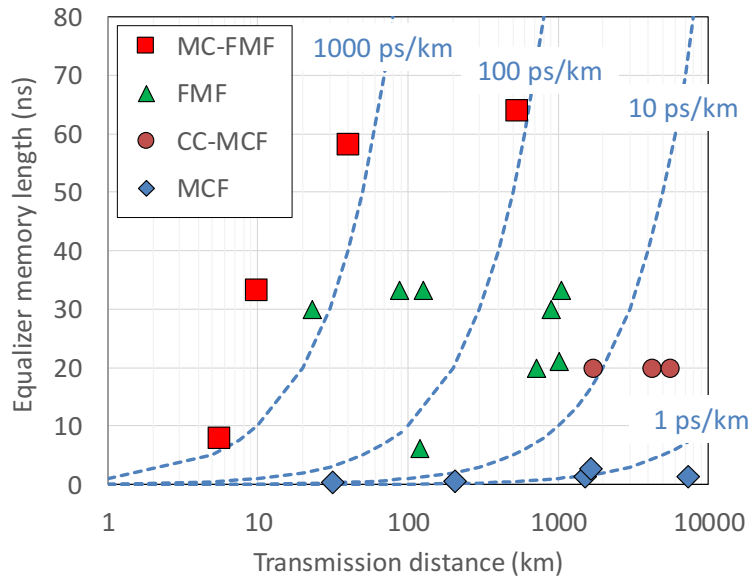


Fig. 7.3 SDM transmission experiments over MCF, CC-MCF, FMF, and MC-FMF with the memory length used for each MIMO signal processing.

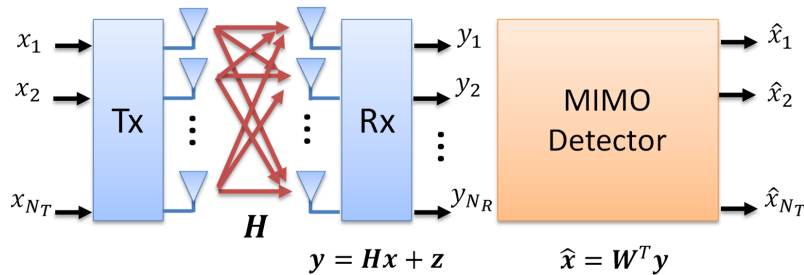


Fig. 7.4 Schematic of an optical MIMO system.

relative to that of an equivalent single-carrier TDE for a total DMD of 30 ns [107]. The detailed description of the parallel MIMO FDE scheme will be provided in Section 8.1 with the DSDM transmission experiment results.

### 7.3.3 Methodologies for Dealing with MDL

MIMO-SDM signals are also exposed to different gain or loss depending on their excited modes, and these can be collectively treated as an MDL phenomenon. MDL is considered to be mainly arisen from imperfect connection between fiber sections, SDM amplifiers, and optical inline components including multiplexing/demultiplexing devices, couplers.

The impact of MDL on system capacity can be intuitively understood by considering the following extreme case. If extremely large MDL were to be imposed on a particular spatial channel, it would substantially prohibit propagation on that channel, and equivalently reduce the number of spatial channels. According to MIMO theory, MDL has an impact on the system capacity of MIMO-SDM signals. Let us consider the static optical MIMO system with  $N_T$  transmitters and  $N_R$  receivers shown in Fig. 7.4 which is modeled as

$$\mathbf{y} = \mathbf{H}\mathbf{x} + \mathbf{z}, \quad (7.11)$$

where  $\mathbf{x}, \mathbf{y}, \mathbf{z}, \mathbf{H}$  respectively denote the  $N_T \times 1$  transmitted symbol vector, the  $N_R \times 1$  received symbol vector, the  $N_R \times 1$  zero-mean circularly symmetrical complex noise vector, and the  $N_R \times N_T$  overall channel transfer matrix. If the transmitter has no information of the MIMO channel, the transmission strategy in which independent signals are assigned to each transmitter with equal transmitted power is considered to be optimum [113]. The system capacity of a MIMO system  $C$  in such a case is given by [114]

$$C = \log_2 \det \left[ \mathbf{I}_{N_R} + \frac{P}{N_T N_0} \mathbf{H}\mathbf{H}^\dagger \right], \quad (7.12)$$

where  $\dagger$  denotes the complex conjugate transpose operation,  $P$  is the total transmitted signal power,  $N_0$  is the noise power received by each receiver, and  $\mathbf{I}_k$  is the  $k \times k$  identity matrix. The fact that  $\mathbf{H}\mathbf{H}^\dagger$  is an  $N_R \times N_R$  positive semidefinite Hermitian matrix allows us to decompose it by eigenvalue decomposition with eigenvalues  $\lambda_i$  that satisfy  $\lambda_i \geq 0$  ( $i \in \{1, 2, \dots, N_R\}$ ). The decomposed form of  $\mathbf{H}\mathbf{H}^\dagger$  is then given by

$$\mathbf{H}\mathbf{H}^\dagger = \mathbf{U}\mathbf{\Lambda}\mathbf{U}^\dagger, \quad (7.13)$$

where  $\mathbf{U}$  is the  $N_R \times N_R$  unitary matrix, and  $\mathbf{\Lambda} \stackrel{\text{def}}{=} \text{diag}[\lambda_1 \lambda_2 \cdots \lambda_{N_R}]$ . By using eq. (7.13), eq. (7.12) simplifies to

$$\begin{aligned} C &= \log_2 \det \left[ \mathbf{I}_{N_R} + \frac{P}{N_T N_0} \mathbf{U}\mathbf{\Lambda}\mathbf{U}^\dagger \right] \\ &= \log_2 \det \left[ \mathbf{I}_{N_R} + \frac{P}{N_T N_0} \mathbf{\Lambda} \right] \\ &= \sum_{i=1}^{N_R} \log_2 \left[ \mathbf{I}_{N_R} + \frac{P}{N_T N_0} \lambda_i \right], \end{aligned} \quad (7.14)$$

in which the determinant conversion of  $\det[\mathbf{I}_m + \mathbf{A}\mathbf{B}] = \det[\mathbf{I}_n + \mathbf{B}\mathbf{A}]$  is used for  $m \times n$  matrix  $\mathbf{A}$  and  $n \times m$  matrix  $\mathbf{B}$ . Equation (7.14) indicates that the achievable MIMO system capacity (without knowledge of the channel at the transmitter) becomes the sum of the capacity of parallel  $N_R$  SISO channels, each of which has a power gain of  $\lambda_i$  [114]. Recalling that (linear) MDL is defined by the ratio between the maximum eigenvalue ( $\max(\lambda_i)$ ) and the minimum eigenvalue ( $\min(\lambda_i)$ ) of  $\mathbf{H}\mathbf{H}^\dagger$ , it is understood from eq. (7.14) that the MIMO system capacity is reduced in the presence of MDL. Note that, while MDL characterizes one of the system capacity aspects, exact evaluation of overall capacity requires the knowledge of all eigenvalues.

Unlike DMD, MDL has a severe impact on MIMO-SDM signal detection performance due to a MDL-induced non-unitary channel if the use of a linear MIMO equalization technique is assumed as a spatial demultiplexing detector. A much efforts have been devoted to reducing MDL itself or impairment relevant to MDL. By employing ring-core (RC)-EDF, differential modal gain (DMG) observed in a FM amplifier was suppressed less than 1.8 dB between 2 LP modes [115]. Free-space optics MDL equalizer directly compensated for MDL by 3 dB used in [83] by utilizing a spatial filter that imposes larger attenuation to the fundamental mode (i.e., LP<sub>01</sub>) relative to the higher order mode (i.e., LP<sub>11</sub>) light. Introducing mode scramblers (MSs) is another optical approach for MDL mitigation [116, 117]. By employing inline MSs, forced modal coupling occurs at each MS, hence signals propagate over an MMF link in quasi strongly coupled regime. MDL impact can be also partially mitigated by advanced signal processing techniques. In [116], the authors showed receiver-side maximum-likelihood (ML) detection scheme to MDL-impaired signals. A few studies can be found that applied space-time coding (STC) to MIMO-SDM transmission, which utilizes diversity of both space and time [84, 118, 119]. In [118], the space-time spreading method was proposed that distributed the information symbol's power of each spatial channel at the transmitter side in the digital domain by using orthogonal transformation. It was found found that it brought performance averaging for MDL-impaired signals because it interspersed distortions of particular spatial channels through MIMO equalization stage at the receiver end. Above methodologies against MDL is summarized in Fig. 7.6. The detail description and performance evaluation will be also provided in Section 8.2.

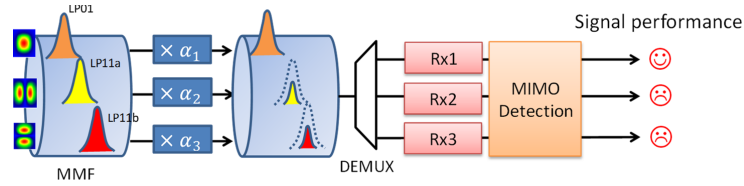


Fig. 7.5 Schematic illustration of MDL in 2-LP mode MMF.

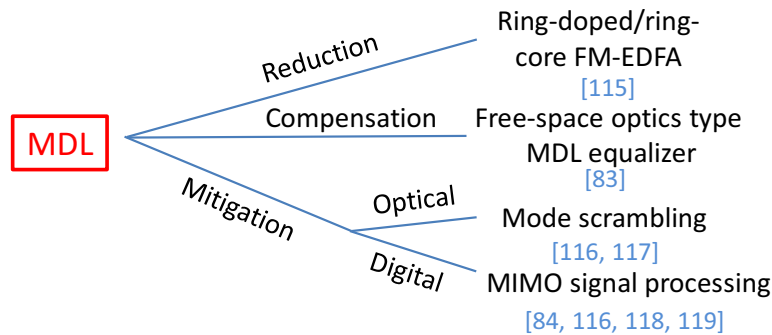


Fig. 7.6 Optical methodologies for MDL currently reported.

## 7.4 MIMO-SDM Transmission Strategies with Signal

### Processing for DMD and MDL Problems

If we look around, many sophisticated signal processing techniques developed in wireless communication systems could be found that may provide a stronger decomposing function for mutually-coupled spatial channels in the presence of DMD and MDL.

If channel state information (CSI) is known at the transmitter, precoding a signal vector by using singular value decomposition (SVD) of a channel before launching them, known as beamforming, may be beneficial to enhance the signal transmission performance. Adaptive bit loading assigns the proper modulation order to each subcarrier at each frequency in multicarrier transmission on the basis of CSI and SNR information. However, these approaches may be ineffective in optical MMF/FMF transmission because of fast channel variation, when the round trip time between the transmitter and the receiver is considered.

The next choice to be considered is whether CSI can be used at the receiver or not. Linear and nonlinear MIMO equalizers work as spatial demultiplexing filters. A successive interfer-

ence canceller (SIC) detects signal streams one by one by sequentially performing ordering, nulling, slicing, and canceling. An ML detector finds the most probable transmitted signal vector from a large number of transmitted symbol vector candidates. These three MIMO detectors are well investigated in wireless MIMO systems. The schemes including repetition, maximum ratio combining (MRC), space-time block code (STTC), and space-time trellis code (STTC) are usually used to obtain the diversity gain and/or the coding gain rather than the multiplexing gain at the expense of system throughput. As an approach that requires no CSI in the transmitter and receiver but uses pre-processing in the transmitter, the transmission with spatial and temporal spreading in the digital domain enables spatial signal performance to be averaged over all mode signals [118], which has been already introduced in Section 7.3. Most of recent MMF/FMF transmission experiments employ a receive-side linear MIMO equalizer with least mean squares (LMS) or recursive least squares (RLS) updates. As a technique relevant to an adaptive linear MIMO equalization, an improved proportionate normalized LMS (IPNLMS) update technique was proposed in [120].

The following discussion in Section 7.4 will concentrate on three spatial detectors which principally contribute system throughput improvement through spatial multiplexing only by using the knowledge of CSI in a receiver, i.e., a linear MIMO equalizer, an SIC detector, and an ML detector. Note that a nonlinear MIMO equalizer (i.e., a decision-feedback equalizer (DFE)) is not discussed in this work, since it is fundamentally equivalent to an SIC detector [121]. Their fundamentals are described with the discussion of their properties in terms of required computational complexity, detection performance, and application in optical MIMO transmission over MMFs/FMFs.

### 7.4.1 System Model

A MIMO system model described in eq. (7.11) is used here again. To discuss this more simply, an independent and identically distributed (i.i.d.) Rayleigh flat fading channel is assumed in this work [82], although the discussion will be expanded to include a frequency-selective channel in Section 7.5. Equation (7.11) indicates that each component of  $\mathbf{y}$  comprises a linear combination of the transmitted signals excluding noise effects. Note that the fiber nonlinearity effect is ignored in eq. (7.11). The goal of each detection scheme is to

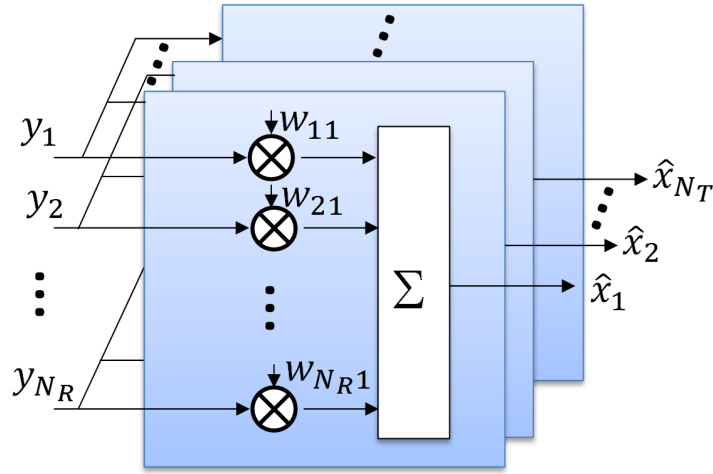


Fig. 7.7 The detection process in a linear detector.

determine the transmitted symbol vector  $\hat{\mathbf{x}}$ .

## 7.4.2 MIMO Detection Schemes

### 7.4.2.1 Linear MIMO Detection

The strategy of the linear detection, which is also referred to as an MIMO equalization, is a straightforward approach that extracts the  $i$ -th data stream by multiplying an  $N_R \times 1$  MIMO equalizer weight vector  $\mathbf{w}_i$  with  $\mathbf{y}$  as

$$\hat{x}_i = \mathbf{w}_i^T \mathbf{y}, \quad (7.15)$$

or equivalently, by constructing an  $N_R \times N_T$  MIMO equalizer matrix as  $\mathbf{W} = [\mathbf{w}_1, \mathbf{w}_2, \dots, \mathbf{w}_{N_T}]$ , eq. (7.15) is expressed in more collective matrix form:

$$\hat{\mathbf{x}} = \mathbf{W}^T \mathbf{y}, \quad (7.16)$$

which is schematically illustrated in Fig. 7.7.

In linear detection scheme, two design criterion of  $\mathbf{W}$  can be chosen: zero-forcing (ZF) or minimum mean square error (MMSE) criterion. ZF-based MIMO equalizer matrix  $\mathbf{W}_{\text{ZF}}$  is obtained through the pseudo-inverse of  $\mathbf{H}$  as

$$\mathbf{W}_{\text{ZF}}^T = (\mathbf{H}^\dagger \mathbf{H})^{-1} \mathbf{H}^\dagger, \quad (7.17)$$

where  $\dagger$  denotes the complex conjugate transpose operation. Suppose the perfect knowledge of  $\mathbf{W}_{ZF}$ , inter-modal interferences can be completely removed from  $\hat{x}_i$ . The main drawback of the employment of  $\mathbf{W}_{ZF}$  is that it may induce a noise enhancement under low signal-to-noise ratio (SNR) regime.

Unlike ZF-based equalizer, an MIMO equalizer based on MMSE criterion avoids a noise enhancement by taking all the received signal information into account in the design of  $\mathbf{W}$ . Consequently an MMSE-MIMO equalizer matrix  $\mathbf{W}_{MMSE}$  is designed to minimize the mean square error as

$$\mathbf{W}_{MMSE} = \arg \min_{\mathbf{W} \in \mathbb{C}^{N_R \times N_T}} \mathbb{E} \left[ \|\mathbf{W}^T \mathbf{y} - \mathbf{x}\|^2 \right], \quad (7.18)$$

where  $\mathbb{E}[\cdot]$  and  $\|\cdot\|$  denotes the expectation operation and the  $L_2$  norm of the vector, respectively. By defining the cost function as  $J = \mathbb{E} \left[ \|\mathbf{W}^T \mathbf{y} - \mathbf{x}\|^2 \right]$ , eq. (7.18) can be transformed as

$$\begin{aligned} J &= \mathbb{E} \left[ \|\mathbf{W}^T \mathbf{y} - \hat{\mathbf{x}}\|^2 \right] \\ &= \mathbb{E} \left[ (\mathbf{W}^T \mathbf{y} - \mathbf{x})^\dagger (\mathbf{W}^T \mathbf{y} - \mathbf{x}) \right] \\ &= \mathbb{E} \left[ \text{tr} \left( (\mathbf{W}^T \mathbf{y} - \mathbf{x}) (\mathbf{W}^T \mathbf{y} - \mathbf{x})^\dagger \right) \right] \\ &= \mathbb{E} \left[ \text{tr} (\mathbf{W}^T \mathbf{y} \mathbf{y}^\dagger \mathbf{W}^*) \right] - \mathbb{E} \left[ \text{tr} (\mathbf{x} \mathbf{y}^\dagger \mathbf{W}^*) \right] - \mathbb{E} \left[ \text{tr} (\mathbf{W}^T \mathbf{y} \mathbf{x}^\dagger) \right] + \mathbb{E} \left[ \text{tr} (\mathbf{x} \mathbf{x}^\dagger) \right] \\ &= \text{tr} (\mathbf{W}^T \mathbb{E} [\mathbf{y} \mathbf{y}^\dagger] \mathbf{W}^*) - \text{tr} (\mathbb{E} [\mathbf{x} \mathbf{y}^\dagger] \mathbf{W}^*) - \text{tr} (\mathbf{W}^T \mathbb{E} [\mathbf{y} \mathbf{x}^\dagger]) + \text{tr} (\mathbb{E} [\mathbf{x} \mathbf{x}^\dagger]) \end{aligned} \quad (7.19)$$

Differentiating eq. (7.19) with respect to  $\mathbf{W}$  gives

$$\begin{aligned} \frac{\partial J}{\partial \mathbf{W}} &= \mathbb{E} [\mathbf{y} \mathbf{y}^\dagger] \mathbf{W}^* - [\mathbf{y} \mathbf{x}^\dagger] \\ &= \mathbf{0}. \end{aligned} \quad (7.20)$$

Therefore,  $\mathbf{W}_{MMSE}$  is obtained as

$$\mathbf{W}_{MMSE} = \mathbb{E} [\mathbf{y}^\dagger \mathbf{y}^T]^{-1} \mathbb{E} [\mathbf{y}^\dagger \mathbf{x}^T], \quad (7.21)$$

which is equivalent to the Wiener filter we have seen in eq. (2.36).

By evaluating the expectation parts as

$$\begin{aligned} \mathbb{E} [\mathbf{y}^\dagger \mathbf{y}^T] &= \mathbf{H}^* \mathbb{E} [\mathbf{x}^* \mathbf{x}^T] \mathbf{H}^T + \mathbb{E} [\mathbf{z}^* \mathbf{z}^T] \\ &= P_X \mathbf{H}^* \mathbf{H}^T + P_z \mathbf{I}_{N_R}, \end{aligned} \quad (7.22)$$

and

$$\begin{aligned} \mathbb{E} \left[ \mathbf{y}^\dagger \mathbf{x}^T \right] &= \mathbf{H}^* \mathbb{E} \left[ \mathbf{x}^* \mathbf{x}^T \right] \\ &= P_x \mathbf{H}^*, \end{aligned} \quad (7.23)$$

where  $\mathbf{I}_k$  and  $P_x$  are respectively the  $k \times k$  identity matrix and a total input signal power, eq. (7.21) becomes

$$\mathbf{W}_{\text{MMSE}} = \left( \mathbf{H}^* \mathbf{H}^T + \frac{1}{\gamma} \mathbf{I}_{N_R} \right)^{-1} \mathbf{H}^* \quad (7.24)$$

$$= \mathbf{H}^* \left( \mathbf{H}^T \mathbf{H}^* + \frac{1}{\gamma} \mathbf{I}_{N_T} \right)^{-1}, \quad (7.25)$$

where  $\gamma = \frac{P_x}{P_z}$  corresponds to the mode-averaged SNR. To express in more practical form, taking the transpose of eq. (7.25) gives

$$\mathbf{W}_{\text{MMSE}}^T = \left( \mathbf{H}^\dagger \mathbf{H} + \frac{1}{\gamma} \mathbf{I}_{N_T} \right)^{-1} \mathbf{H}^\dagger. \quad (7.26)$$

$\mathbf{W}_{\text{MMSE}}$  in eq. (7.26) has a generalized form of  $\mathbf{W}_{\text{ZF}}$ , which means that eq. (7.26) becomes equivalent to eq. (7.17) in the high SNR regime. In the low to moderate SNR regime, the term of  $\frac{1}{\gamma} \mathbf{I}_{N_T}$  regulates the signal-to-interference-plus-noise ratio (SINR) between the noise enhancement and the residual inter-modal crosstalk.

Equations (7.17) and (7.26) indicate that  $\mathbf{W}$  requires CSI ( $\mathbf{H}$ ) and/or SNR. In addition, the matrix inverse computation may enhance the complexity, as will be discussed later. On the practical use of an MIMO equalizer, however, an allowable performance may be achieved based on the stochastic gradient method, or LMS algorithm that approaches to  $\mathbf{W}_{\text{MMSE}}$  in an iterative manner after sufficient convergence time without the knowledge of  $\mathbf{H}$  and SNR. This low-complexity and easy-to-use property of an MMSE-MIMO equalizer is attractive in fiber-optic communication systems in which, like mobile wireless systems, CSI varies in time and frequency.

#### 7.4.2.2 Interference Canceling Detection

Interference cancellation techniques have been developed in direct spread code division multiple access (DS/CDMA) systems for multi-user detection, and two main schemes are well known, namely parallel interference cancellation (PIC) and SIC. An SIC detector can achieve



the detection performance improvement with the complexity comparable to the linear detection, while a few iterations in detection and decoding are required in an PIC detector, which makes the system complicated [122]. Hence this section concentrates on the SIC scheme. An SIC detector consists of multiple stages, each of which aims to individually extract one data stream from  $\mathbf{y}$  by sequential processing of interference signal removal (*canceling*) and signal detection (*nulling*). The interference signals are reconstructed by using signal patterns based on CSI that are already detected in the preceding stages, and called *replica*. Here a linear MIMO equalization scheme is employed in a nulling step.

Obviously an inaccurate replica construction generally has negative impact on a detection performance in an SIC scheme, known as error propagation. One efficient way to avoid propagating errors is to employ the ordered SIC (OSIC) scheme, which starts from data stream detection with highest post-processing SNR. Alternatively, the use of soft replica instead of hard replica for interference cancellation may improve the SIC detection performance at the expense of the computational complexity.

The SIC detection starts from calculating an MIMO equalizer matrix used in the initial stage  $\mathbf{W}^{(1)}$  based on eq. (7.17) (ZF criterion) or eq. (7.26) (MMSE criterion). Note that superscript number in parenthesis of each quantity represents the SIC stage number. In the initial stage, data stream index to be detected  $k_1$  is determined through on the post-processing SNR basis. This *ordering* is simply done by finding a column of  $\mathbf{W}^{(1)}$  which gives the minimum  $L_2$  norm as [76]

$$k_1 = \arg \min_{j \in \{1, 2, \dots, N_T\}} \|(\mathbf{W}^{(1)})_j\|^2 \quad (7.27)$$

where  $(\cdot)_j$  denotes the  $j$ -th column of a matrix. Then first data stream is demultiplexed from  $\mathbf{y}$  through linear detection process eq. (7.15) without any interference cancellation, corresponding to *nulling* step, represented as

$$\hat{x}^{(1)} = (\mathbf{W}^{(1)})_{k_1}^T \mathbf{y}^{(1)}, \quad (7.28)$$

where  $\mathbf{y}^{(1)} = \mathbf{y}$  in the initial stage. Following steps are devoted to the preparation of the second data stream detection. *Slicing* is carried out in which each transmitted symbol of the first data stream  $\tilde{x}^{(1)}$  is determined through

$$\tilde{x}^{(1)} = \mathbf{Q}(\hat{x}^{(1)}), \quad (7.29)$$

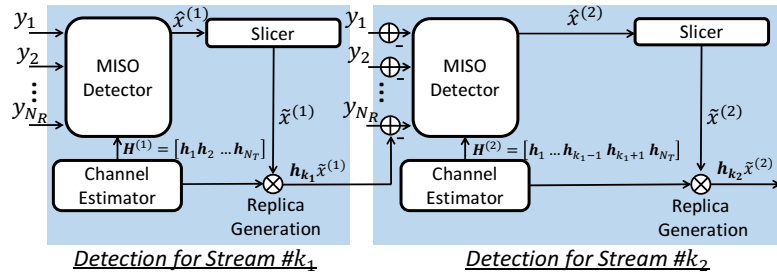


Fig. 7.8 The detection in a SIC detector for the first two stages.

where  $Q(\cdot)$  is the quantization operation. The *canceled* of interference originated from the first data stream, which is generated by multiplying  $\mathbf{h}_{k_1} \stackrel{\text{def}}{=} (\mathbf{H})_{k_1}$  with  $\tilde{x}^{(1)}$  based on the knowledge of  $\mathbf{H}$ , is performed by

$$\mathbf{y}^{(2)} = \mathbf{y}^{(1)} - \mathbf{h}_{k_1} \tilde{x}^{(1)}. \quad (7.30)$$

Compared to the original received signal vector  $\mathbf{y}$  whose  $N_R$  entries consisted with the linear combination of  $N_T$  signals (excluding noise contribution), the constituent parts of  $\mathbf{y}^{(2)}$  are reduced to  $N_T - 1$ , which provides diversity gain to an SIC detector in the second detection stage. At this moment, the impact from the detected data stream of  $x^{(1)}$  is supposed to be completely removed, which allows us to omit the  $k_1$ -th column of  $\mathbf{H}$  as

$$\mathbf{H}^{(2)} = [\mathbf{h}_1 \cdots \mathbf{h}_{k_1-1} \mathbf{h}_{k_1+1} \cdots \mathbf{h}_{N_T}] \quad (7.31)$$

Above detection flows are illustrated in Fig. 7.8.

The processing is handled over the succeeding stages with the similar steps, and data stream detection is continued in a recursive manner until the  $N_T$ -th stream is detected. In the  $i$ -th

stage, the detection flow of  $x^{(i)}$  is summarized in eq. (7.32).

$$\begin{aligned}
\text{Ordering} : k_i &= \arg \min_{j \notin \{k_1, k_2, \dots, k_{i-1}\}} \|(\mathbf{W}^{(i)})_j\|^2, \\
\text{Nulling} : \hat{x}^{(i)} &= (\mathbf{W}^{(i)})_{k_i}^T \mathbf{y}^{(i)}, \\
\text{Slicing} : \tilde{x}^{(i)} &= \mathbf{Q}(\hat{x}^{(i)}), \\
\text{Canceling} : \mathbf{y}^{(i+1)} &= \mathbf{y}^{(i)} - \mathbf{h}_{k_i} \tilde{x}^{(i)}, \\
\mathbf{H}^{(i+1)} &= [\mathbf{h}_1 \cdots \mathbf{h}_{k_{i-1}} \mathbf{h}_{k_{i+1}} \cdots \mathbf{h}_{N_T}], \\
\mathbf{W}^{(i+1)T} &= \begin{cases} (\mathbf{H}^{(i+1)\dagger} \mathbf{H}^{(i+1)})^{-1} \mathbf{H}^{(i+1)\dagger} & \text{(ZF)} \\ \left( \mathbf{H}^{(i+1)\dagger} \mathbf{H}^{(i+1)} + \frac{1}{\gamma} \mathbf{I}_{N_T-i+1} \right)^{-1} \mathbf{H}^{(i+1)\dagger} & \text{(MMSE)} \end{cases}, \\
i &= i + 1.
\end{aligned} \tag{7.32}$$

#### 7.4.2.3 Maximum Likelihood Detection

Recalling a relationship between a transmitter and receiver in eq. (7.11), it is intuitively understood that joint detection may outperform the independent or successive detection. Maximum likelihood (ML) detection is a straightforward approach to detect all mutually-coupled data streams simultaneously, and known as an optimum detection scheme. Despite of its simplicity of the basic idea, ML detector indeed outperforms the linear detector and the SIC detector. ML scheme searches the most probable transmitted symbol vector  $\hat{\mathbf{x}}_{ML}$  from the set of all possible vector candidates.

Let us start to consider the maximum-a-posteriori (MAP) detector which finds the transmitted symbol vector candidate  $\check{\mathbf{x}}_s$  to maximize the a posteriori probability  $P(\check{\mathbf{x}}_s|\mathbf{y})$  given that  $\mathbf{y}$  is received. Suppose an  $M$ -QAM information symbol in each spatial channel having a known finite alphabet  $\mathcal{X}$  of size  $M$ ,  $\check{\mathbf{x}}_s$  is chosen from a set of  $\mathcal{X}^{N_T}$ . Based on the Bayes' theorem,  $P(\check{\mathbf{x}}_s|\mathbf{y})$  is expressed as

$$P(\check{\mathbf{x}}_s|\mathbf{y}) = \frac{p(\mathbf{y}|\check{\mathbf{x}}_s)P(\check{\mathbf{x}}_s)}{p(\mathbf{y})}. \tag{7.33}$$

In communication systems, all transmitted symbol vectors are generally of equal probability, and  $p(\mathbf{y})$  serves as a normalization term. Therefore the MAP detector becomes equivalent to

the ML detector. Our task is now to find  $\check{\mathbf{x}}_s$  which maximizes  $p(\mathbf{y}|\check{\mathbf{x}}_s)$ :

$$\hat{\mathbf{x}}_{\text{ML}} = \arg \max_{\check{\mathbf{x}}_s \in \mathcal{X}^{N_T}} p(\mathbf{y}|\check{\mathbf{x}}_s). \quad (7.34)$$

Multiplying the transmitted symbol vector candidate  $\check{\mathbf{x}}_s$  with  $\mathbf{H}$  gives the received symbol vector candidate  $\check{\mathbf{y}}_s$  as

$$\check{\mathbf{y}}_s = \mathbf{H}\check{\mathbf{x}}_s. \quad (7.35)$$

By defining the difference between  $\mathbf{y}$  and  $\check{\mathbf{y}}_s$  as  $\check{\mathbf{z}}_s \stackrel{\text{def}}{=} \mathbf{y} - \check{\mathbf{y}}_s$ , the conditional probability  $p(\mathbf{y}|\check{\mathbf{x}}_s)$  in eq. (7.34) can be obtained from the multivariate Gaussian distribution as

$$p(\mathbf{y}|\check{\mathbf{x}}_s) = \frac{1}{\det(\pi\mathbf{R}_z)} \exp\left(-\check{\mathbf{z}}_s^\dagger \mathbf{R}_z^{-1} \check{\mathbf{z}}_s\right), \quad (7.36)$$

where  $\mathbf{R}_z$  is the noise covariance matrix of  $\check{\mathbf{z}}_s$ , which is rewritten as

$$\begin{aligned} \mathbf{R}_z &= E\left[\check{\mathbf{z}}_s \check{\mathbf{z}}_s^\dagger\right] \\ &= E\left[\mathbf{z} \mathbf{z}^\dagger\right] \\ &= P_z \mathbf{I}_{N_R}. \end{aligned} \quad (7.37)$$

By using eq. (7.37),  $\mathbf{R}_z$  in eq. (7.36) is substituted as

$$\begin{aligned} p(\mathbf{y}|\check{\mathbf{x}}_s) &= \frac{1}{(\pi P_z)^{N_R}} \exp\left(\frac{-\check{\mathbf{z}}_s^\dagger \check{\mathbf{z}}_s}{P_z}\right) \\ &= \frac{1}{(\pi P_z)^{N_R}} \exp\left(\frac{-\|\mathbf{y} - \check{\mathbf{y}}_s\|^2}{P_z}\right). \end{aligned} \quad (7.38)$$

Taking logarithms in eq. (7.38) yields

$$\log(p(\mathbf{y}|\check{\mathbf{x}}_s)) = -N_R \log(\pi P_z) - \frac{\|\mathbf{y} - \check{\mathbf{y}}_s\|^2}{P_z}. \quad (7.39)$$

Thus searching  $\hat{\mathbf{x}}_{\text{ML}}$  in eq. (7.34) is equivalent to

$$\begin{aligned} \hat{\mathbf{x}}_{\text{ML}} &= \arg \min_{\check{\mathbf{y}}_s} \|\mathbf{y} - \check{\mathbf{y}}_s\|^2 \\ &= \arg \min_{\check{\mathbf{x}}_s \in \mathcal{X}^{N_T}} \|\mathbf{y} - \mathbf{H}\check{\mathbf{x}}_s\|^2 \end{aligned} \quad (7.40)$$

Consequently, ML detector needs to calculate the Euclidean distance between  $\mathbf{y}$  and  $\mathbf{H}\check{\mathbf{x}}_s$  for all symbol vector candidates, which may consume significant computation resources.

### 7.4.3 Computational Complexity

Next a computational complexity comparison that is required in each detection schemes is performed. Computational complexity is here defined as complex multiplication or division required to detect all  $N_T$  spatial channels. This section assumes a processing to estimate a channel to be commonly used for three schemes, therefore the complexity in channel estimation is neglected in this work for the complexity comparison purpose. Moreover, in the complexity estimation the MMSE criteria is only considered for a linear MIMO detection and an SIC detection.

The processing of a linear MMSE detection contains  $2N_T^2N_R$  complex multiplication in matrix multiplication involved with  $\mathbf{W}_{\text{MMSE}}^T$  eq. (7.26),  $N_TN_R$  complex multiplication in nulling eq. (7.16). The inverse computation requires  $\frac{N_T^3}{2} + \frac{N_T^2}{2}$  complex multiplication or division based on Gauss-Jordan elimination algorithm. Hence, the total complexity of MMSE detection  $C_{\text{MMSE}}$  becomes

$$C_{\text{MMSE}} = \frac{N_T^3}{2} + 2N_T^2N_R + \frac{N_T^2}{2} + N_TN_R + N_T. \quad (7.41)$$

To calculate the complexity for an SIC detector with  $N_T$  detection stages, it is convenient to consider the detection at the  $i$ -th stage. Prior to ordering and nulling, the MMSE MIMO weight matrix  $\mathbf{W}_{\text{MMSE}}$  needs to be calculated, which contains  $(N_T - i + 1)^3/2 + (N_T - i + 1)^2/2$  complex multiplication or division for the matrix inverse computation and  $2N_R(N_T - i + 1)^2 + (N_T - i + 1)$  complex multiplication for the matrix multiplication computation. In addition to above,  $N_R(N_T - i + 1)$  complex multiplications are required in the ordering step, and  $N_R$  are required in the nulling step. Slicing is performed in a way that a most probable transmitted symbol is determined via Euclidean distance calculations between a detected symbol and an original symbol candidate, which accordingly needs  $M$  complex multiplication. In a canceling step, a replica symbol vector is constructed by  $N_R$  complex multiplications. These calculations are iterated in each stage, consequently the overall SIC

complexity  $C_{\text{SIC}}$  is obtained by summing above complexities up as

$$\begin{aligned}
C_{\text{SIC}} &= \sum_{i=1}^{N_T} \left[ \frac{(N_T - i + 1)^3}{2} + \frac{(N_T - i + 1)^2}{2} \right. \\
&\quad + 2N_R(N_T - i + 1)^2 + (N_T - i + 1) \\
&\quad \left. + N_R(N_T - i + 1) + 2N_R + M \right] \\
&= \frac{1}{8}N_T^2(N_T + 1)^2 + \frac{1}{12}N_T(N_T + 1)(2N_T + 1)(4N_R + 1) \\
&\quad + \frac{1}{2}N_T(N_T + 1)(N_R + 1) + N_T(2N_R + M).
\end{aligned} \tag{7.42}$$

For each symbol vector candidate, ML detector requires  $N_T N_R$  complex multiplications to generate a received symbol vector candidate  $\check{\mathbf{y}}_s$ , and  $N_R$  complex multiplications to calculate an Euclidean distance between  $\mathbf{y}$  and  $\mathbf{H}\check{\mathbf{x}}_s$ . The total complexity for ML detection  $C_{\text{ML}}$  is then estimated by considering all sets of symbol vector candidates as

$$C_{\text{ML}} = M^{N_T} (N_T N_R + N_R). \tag{7.43}$$

Suppose a spatial degree of freedom is fully exploited in which all spatial channels are assigned as independent information-carrying optical paths, it is reasonable to set  $N_R = N_T$ . This situation allows us to perform complexity comparison more intuitively. From eq. (7.41) and eq. (7.42), the complexity for an MMSE and an SIC detector respectively have orders of  $O(N_T^3)$  and  $O(N_T^4)$ . Obviously the most of the computational efforts are involved with the matrix inverse and multiplication computation in the MMSE MIMO weight matrix calculation, which is supposed to be performed in  $N_T$  detection stages. So-called square-root algorithm was proposed in [123] which effectively suppresses SIC complexity to  $O(N_T^3)$ . In contrast to an MMSE and an SIC detector, a modulation order of signals employed has a significant impact on the complexity of MLD in eq. (7.43). Specifically, it grows up exponentially due to the domination from  $M^{N_T}$  in eq. (7.43). A few algorithms have been proposed for an ML detection which aims the complexity suppression, including sphere decoding algorithm [124], and the combined use of QR-decomposition and M-algorithm (QRM-MLD) [125], both of which aim to reduce the number of transmitted symbol vector candidates.

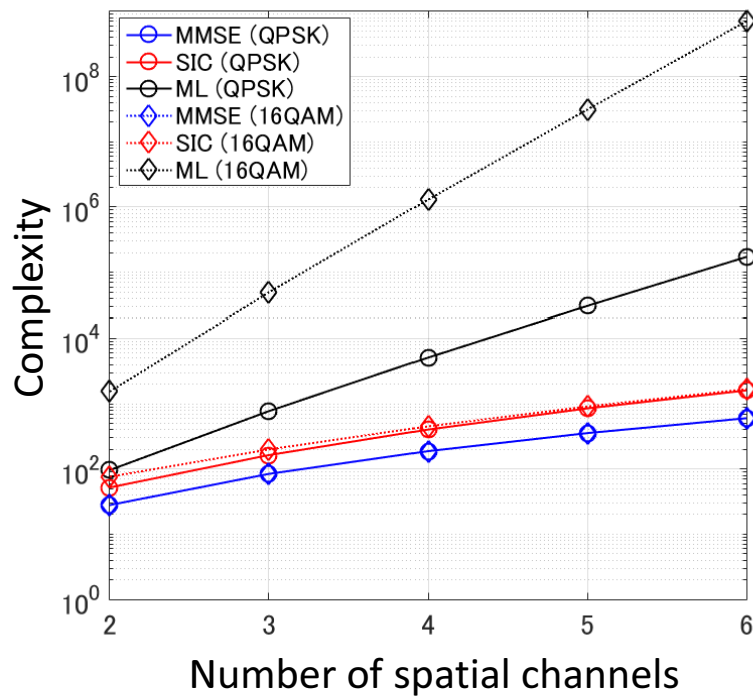


Fig. 7.9 Complexity comparison between an MMSE, an SIC, and an ML detector to determine transmitted signals of QPSK or 16QAM.

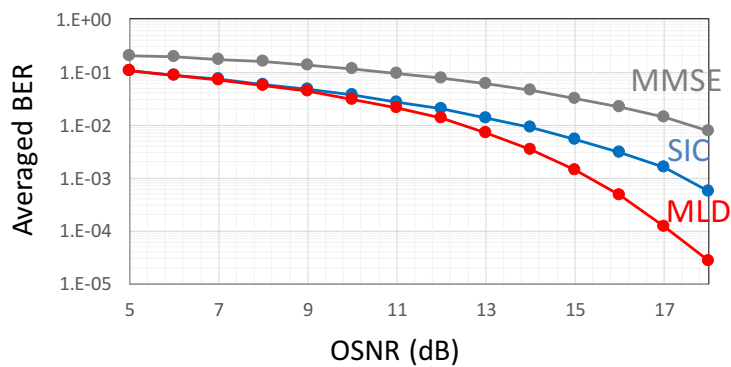


Fig. 7.10 Detection performance comparison among MMSE-based linear equalizer, SIC detector, and MLD for QPSK signals in the presence of MDL.

#### 7.4.4 Detection Performance

Comparing detection performance between distinct MIMO detectors generally requires some assumptions. As did in previous sections, a fully-loaded optical MIMO system and an i.i.d. Rayleigh flat channel are also assumed. An asymptotic analysis of detection perfor-

mance comparison is provided in wireless literatures, which is referred to as the diversity order  $d$ , represented as the negative BER slope as a function of SNR in log-log scale [126, 127]. The diversity order is intuitively understood as the metric showing how fast BER decays as SNR improves. Mathematically,  $d$  is defined as

$$\lim_{\text{SNR} \rightarrow \infty} \frac{\log p_{\text{out}}(\text{SNR})}{\log(\text{SNR})} = -d, \quad (7.44)$$

where  $p_{\text{out}}$  denotes output BER of an MIMO detector. While an ML detector achieves  $d_{\text{ML}} = N_R$  independent of the number of transmitters, the diversity order of an MMSE linear detector is reduced to  $d_{\text{MMSE}} = N_R - N_T + 1$  [126], since, in each data stream detection of an MMSE linear detector, other  $N_T - 1$  interfering signals consume the degree of freedom. This diversity order analysis obviously indicates that the ML detection outperforms the MMSE linear detection for a fixed (high) SNR condition. Considering a sequential interference canceling operation employed in an SIC scheme, one can deduce a more reliable detection performance of an SIC detector in latter detection stages. Indeed, the diversity order at  $i$ -th stage of an SIC detector is improved to have  $d_{\text{SIC}, i} = N_R - N_T + i$  [127, 128]. However, since its overall performance is dominated at the initial detection stage, hence the diversity order of an overall SIC detector becomes  $d_{\text{SIC}} = N_R - N_T + 1$ , even if the optimal ordering is employed [127]. In the analysis performed here, the common assumption in a fully-loaded optical MIMO transmission (i.e.,  $N_R = N_T$ ) leads the results of  $d_{\text{MMSE}} = d_{\text{SIC}} = 1$ . It should be noted that, since the diversity-order-based analysis might be valid especially in high SNR regime, more comprehensive detection performance comparison will be required, taking an additional case into consideration in which other signal processing schemes are jointly adopted including coding and time/frequency diversity techniques.

Fig. 7.10 compares the signal detection performance among the MMSE-based linear MIMO equalizer, SIC, and ML detection schemes. The figure shows the numerical results of averaged BERs as a function of SNR. In the simulation, 12.5-Gbaud two-mode QPSK signals were transmitted over the MDL-impaired MIMO channel having  $\mathbf{H}$  of

$$\mathbf{H} = \begin{bmatrix} 0.7004 & -0.4208 \\ -0.4208 & 0.3941 \end{bmatrix}, \quad (7.45)$$

corresponding to MDL value of 20 dB. It clearly shows that SIC and MLD outperform MMSE detection, which means they provide MDL-impact mitigation. However, it should be noted



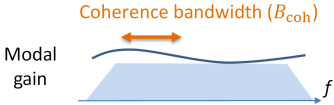
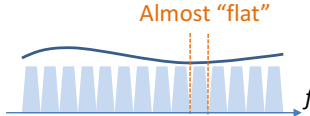
that a perfect knowledge of the transfer channel matrix is assumed in this simulation, otherwise the performance of these detectors will be degraded.

As Fig. 7.10 has shown, the detections based on SIC or ML approaches would provide superior performance than conventional linear MIMO equalizer. However, we need to overcome at least following issues for their practical applications in optical MIMO-SDM transmission.

1. *CSI*: The higher detection performance of SIC and ML detector would be enjoyed as long as a receiver knows a correct CSI. Acquiring CSI in optical MIMO transmission at the receiver end may be possible, say, by inserting and analyzing pilot symbol sequences, although they would substantially reduce the transmission efficiency (i.e., the net signal bit rate) and require additional signal processing efforts.
2. *Synchronization*: The issues of timing, phase, and frequency synchronization especially in coherent MIMO transmission should be addressed because they have a severe impact on the accuracy of replicas or symbol vector candidates used in these detection schemes.
3. *Complexity*: SIC or ML-based detectors require higher computationally complexity than a linear MIMO equalizer as is implicated in Fig. 7.9.

The slow-fading regime in an optical MIMO channel in which temporal channel variations are much slower than the signal symbol rate driven at several tens of Gbaud [129] enables us to apply the adaptive filtering techniques with LMS or RLS algorithms in the weight vector update of a linear MIMO equalizer, which may not require any channel estimation to demultiplex data streams. Indeed, the recent progress achieved in long-haul MIMO-SDM transmission experiments including those listed in Table 7.2 indicates that the allowable transmission performance with manageable complexity may be obtained by the use of a linear MIMO equalization. However, further research on more sophisticated optical MIMO detection schemes including SIC and ML detection schemes in terms of practical application and complexity mitigation will be needed.

Table. 7.3 IMPACT OF FREQUENCY SELECTIVITY ON SIGNAL TRANSMISSION

Wideband Signal ( $B \gg B_{\text{coh}}$ )	Narrowband Signal ( $B \ll B_{\text{coh}}$ )
	
<ul style="list-style-type: none"> <li>•Frequency selectivity causes inter-symbol interference.</li> <li>•Memory length is increased.</li> </ul>	<ul style="list-style-type: none"> <li>•Channel is treated as flat in narrowband signal bandwidth.</li> <li>•Single-tap processing may work well.</li> </ul>

## 7.5 Frequency Selectivity and Its Impact on MIMO-SDM

### Signal Processing

Section 7.5 discusses the impact of frequency selectivity on signal processing in MIMO-SDM transmission. DMD spread causes the memory length expansion required in the MIMO detectors. In [102], it was pointed out that the MDL profile represents frequency selectivity in the presence of DMD. From an analogy of the coherence bandwidth used in wireless communication systems, MDL coherence bandwidth can be defined to be approximately the inverse of DMD spread [102].

With fixed coherence bandwidth, the impact of frequency selectivity differs depending on the signal's symbol rate. For a wideband signal occupying bandwidth far larger than the coherence bandwidth, frequency selectivity causes inter-symbol interference, resulting in enhanced equalizer tap length to deal with it. In contrast, for a narrowband signal occupying bandwidth far smaller than the coherence bandwidth, the channel is treated as flat, and single-tap signal processing may work well. Multicarrier (e.g., OFDM) signal transmission is well known as a strategy that converts a frequency-selective channel into a flat fading channel in each subcarrier bandwidth. As already discussed in Section 7.3, a parallel MIMO transmission techniques have been developed in recent years in which the strategy with low-symbol-rate multicarrier transmission contributed to the complexity reduction for DMD compensation. In a multicarrier transmission scenario, the use of advanced signal processing techniques including SIC and ML detection schemes described in Section 7.4 are straightforwardly ap-

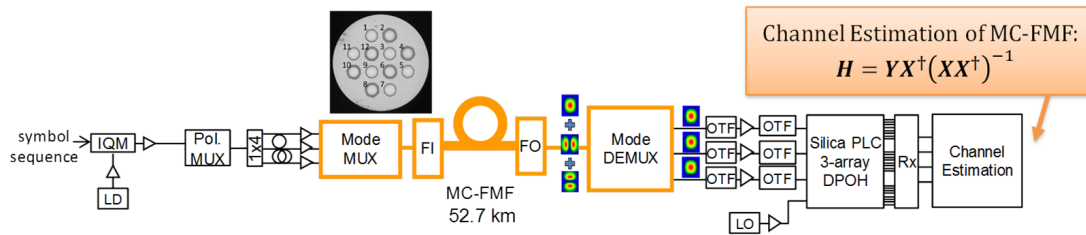


Fig. 7.11 Experimental setup for estimation of transfer matrix of 12-core  $\times$  3-mode MC-FMF transmission line. LD: laser diode, IQM: IQ-modulator, PoL. MUX: polarization multiplexer, Mode MUX: mode multiplexer, FI: fan-in, FO: fan-out, MC-FMF: multicore-fewmode fiber, Mode DEMUX: mode demultiplexer, OTF: optical tunable filter, LO: local oscillator, PLC: planar lightwave circuit, DPOH: dual-polarization optical hybrid

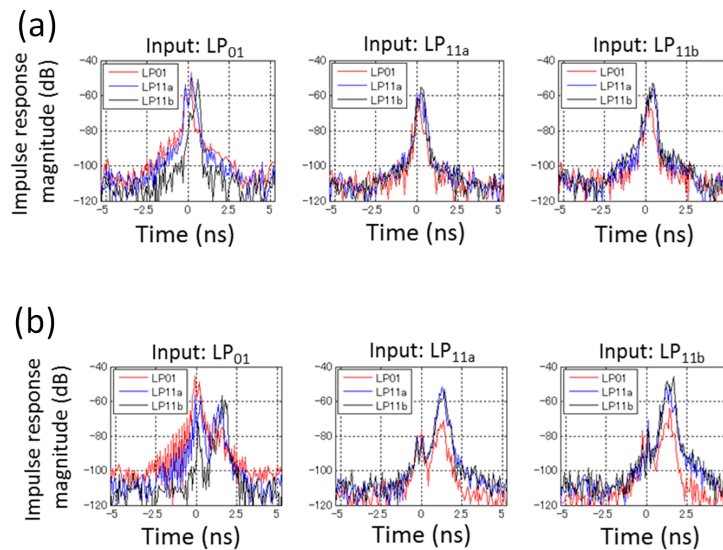


Fig. 7.12 Estimated impulse response for (a) core#8 (small DMD), and (b) core#1 (large DMD).

plicable to an optical MIMO-SDM transmission, which may bring improvement in robustness and reliability against noisy environment and SDM fiber impairments.

To examine a frequency selective channel of an MIMO-SDM transmission, channel characteristics over 12-core  $\times$  3-mode MC-FMF was experimentally evaluated. The transmission comprised of GI MC-FMF fiber having 12-core, each of which supports propagation of 2 LP modes. The detailed parameter description of the fiber are given in Section 8.1 and [107]. Note that the total number of the spatial channels are 6 including 2 LP modes and polarizations. Here, a least squares channel estimator was used to estimate the 6  $\times$  6 channel transfer

matrix at each frequency. If  $\mathbf{X}, \mathbf{Y}$ , and  $\mathbf{H}$  are respectively denoted as a transmitted symbol matrix, a received symbol matrix, and a transfer matrix,  $\mathbf{H}$  is simply estimated by

$$\hat{\mathbf{H}} = \mathbf{Y}\mathbf{X}^\dagger(\mathbf{X}\mathbf{X}^\dagger)^{-1}. \quad (7.46)$$

With the estimated  $\hat{\mathbf{H}}$ , substantial relative leakage power from a  $i$ -th mode input to  $j$ -th mode output  $P_{ij}$  is estimated as

$$P_{ij} = |\hat{h}_{ij}|^2, \quad (7.47)$$

where  $h$  denotes  $(i, j)$ -th entry of  $\mathbf{H}$ . Fig. 7.12 compares obtained  $|\hat{h}_{ij}|^2$  of small-DMD core #8 and large-DMD core #1 after single span propagation. Note that in the evaluation, the averaging over polarization was performed. Pulse spreading induced by DMD appears as, say, temporal separation of two distinct peaks as shown Fig. 7.12(b).

Then the estimation of MDL was performed based on eigenvalue analysis of channel transfer matrix. Fig. 7.13 shows estimated MDL variation as a function of frequency in the signal bandwidth. In contrast to the back-to-back result in which MDL profile behaves almost *flat* over the entire bandwidth, it is noteworthy that clear frequency-dependent MDL properties appear even after single span propagation. Frequency spacing at which MDL profiles become statistically uncorrelated with each other corresponds to MDL coherence bandwidth. The coherence bandwidth for the larger-DMD core appears narrower with respect to the smaller-DMD core, which agrees with the mode coupling model [102]. Spectrums of LP<sub>01</sub>-X signals in a back-to-back transmission and after 5-span propagation are also displayed in Fig. 7.14, which verified that optical MIMO-SDM signals were received with a severe frequency dependent gain. Such a frequency-dependent feature in an optical MIMO link should be taken into account in design of a robust and reliable MIMO-SDM transmission.

## 7.6 Summary

Chapter 7 has reviewed methodologies of optical and digital approaches to deal with DMD and MDL. Also discussed was a frequency selective channel observed in a SDM fiber and its impact on signal performance depending on the relationship between a signal's symbol rate and the coherence bandwidth. On the basis of channel estimation results obtained for multicore few-mode fiber, various DMD types and frequency selectivity was experimentally

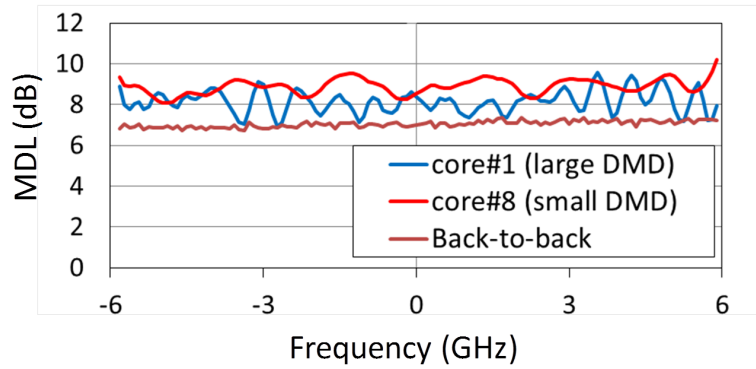


Fig. 7.13 Estimated MDL variation as a function of relative frequency.

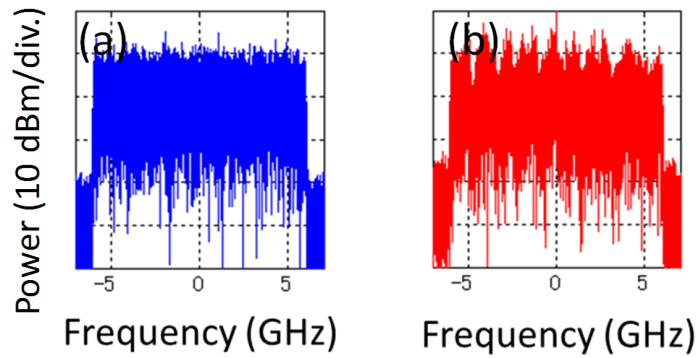


Fig. 7.14 Signal spectrums of  $LP_{01}$ -X signals (a) in a back-to-back transmission and (b) after 5-span transmission of MC-FMF.

observed even after single span transmission. For future thousands-of-km long-haul dense space division multiplexing transmission, further research including sophisticated digital signal processing scheme development is needed to overcome these inherent features.

## Chapter 8

# Space Division Multiplexing Transmission using Multicore and/or Multimode Fiber

### 8.1 Dense SDM (12-core $\times$ 3-mode) Transmission over 527 km with 33.2-ns Mode-Dispersion Employing Low-Complexity Parallel MIMO Frequency-Domain Equalization

#### 8.1.1 Overview

SDM techniques have contributed to the substantial enhancement of transmission capacity per optical fiber by utilizing MCF and/or FMF [10,14–16,71,93–95,97,105,130,131]. Spatial multiplicity has risen to  $M_{\text{MCF}} = 37$  using MCF [13] and  $M_{\text{FMF}} = 15$  using FMF [14], where  $M_{\text{MCF}}$  and  $M_{\text{FMF}}$  are respectively the number of cores and spatial modes. It was previously demonstrated unrepeated 40.4 km dense SDM (DSDM) transmission with spatial multiplicity of 36 (12-core  $\times$  3-mode) by computationally-efficient parallel MIMO equalization using low baud rate multi-carriers [105].

Increasing the transmission reach for DSDM signals is essential for the practical application of DSDM systems. The most important issues for realizing such long-haul DSDM MC-FMF transmission include how to accommodate the accumulation of inter-core crosstalk for MCF transmission, and that of differential mode delay (DMD) for FMF transmission. As already demonstrated in [87,88], the inter-core crosstalk is effectively suppressed by employ-

ing propagation-direction interleaved transmission that alternates propagation direction between adjacent cores. To combat the DMD accumulation, most previous studies on long-haul FMF transmission have taken a DMD management approach. In [95], 900-km FMF transmission was achieved by canceling DMD with concatenated multiple opposite-signs-DMD fiber segments. In [94], it was reported that 1000-km transmission with low-DMD FMF had been achieved without optical DMD compensation. These required high-complexity digital DMD time-domain equalization (TDE), because optical approaches perform non-perfect DMD compensation/reduction. In a weakly-coupled regime, it was demonstrated in [16] that dividing a single MIMO equalizer into “partial MIMO” equalizers in which TDE processing was carried out for lower- and higher-order mode signals independently enabled to reduce the equalizer complexity. As another approach, the use of frequency-domain equalization (FDE) techniques is promising to mitigate the equalizer complexity [132–134].

Section 8.1 proposes to apply a novel low-complexity DMD compensation technique using low baud rate multicarrier signal with parallel MIMO equalization. Digital compensation for DMD of over 30 ns was achieved by employing the low-complexity parallel MIMO and FDE, in combination with the newly-developed graded-index (GI) MC-FMF with low DMD, and a low mode-dependent gain FM erbium-doped fiber amplifier (EDFA). Using these technologies, this thesis demonstrate 527-km MC-FMF DSDM inline-repeated transmission without DMD management with spatial multiplicity of 36 (12-core  $\times$  3-mode), resulting in an achieved spectral efficiency of 2.62 b/s/Hz/core/mode. The rest of the section is organized as follows: Subsection 8.1.2 discusses the significance of equalization for DMD in long-haul DSDM transmission, and its complexity reduction by parallel MIMO TDE and FDE. Subsection 8.1.3 provides a description of equalization algorithms for DMD and their required complexity. Subsection 8.1.4 describes the experimental setup that used in the experiment, including the optical devices and signal processing technique used. The experiment results are shown in Subsection 8.1.5, and Subsection 8.1.6 concludes this chapter with a summary.

### 8.1.2 Parallel MIMO FDE for Long-Haul DSDM Transmission Without DMD Management

This subsection first discusses how an equalization algorithm to achieve long-haul DSDM transmission has been developed and clarify its significance in DSDM transmission. Fig. 8.1 shows the results achieved in recent SDM WDM transmission experiment. In this experiment, DSDM signals were successfully transmitted with the spatial multiplicity of 36 over 500 km, which was more than ten times the distance relative to the previous work reported in [105]. This thesis addressed the increase of DMD by implementing parallel MIMO FDE. As transmission reach increases or signal baud rate becomes higher, the required computational complexity for digital DMD compensation increases. One of the promising solutions to this is employing low symbol rate multi-carrier signals with receiver-side parallel MIMO TDE [105]. However, as will be seen in Section 8.1.3, the complexity scales linearly with increased DMD when a TDE technique is used. Adaptive FDE algorithms for fiber-optic communication systems were proposed in [133, 134]. They used the well-known feature of FDE; it effectively reduces the computational complexity since computation of a convolution in the time domain is replaced by FFT-based scalar multiplication [135].

In this section, FDE scheme in conjunction with low symbol rate multi-carrier signals was implemented, which is called here *parallel MIMO FDE*, to further decrease the complexity of DMD compensation. Fig. 8.1.2 depicts the required computational complexity per carrier per mode which was defined by complex multiplications for calculating output/equalizer-updating and FFT/IFFT as a function of total DMD (or equivalent equalizer memory length). The area in the Fig. 8.1.2 is divided into three regions for digital DMD compensation: single-carrier (SC) TDE region, parallel MIMO TDE region [105], and parallel MIMO FDE region. The borders were set under the assumption that 10-Gbaud-SC or 10-FDM 1-Gbaud multi-carrier signals are transmitted through FMF with DMD. Fig. 8.1.2 is helpful to approximately estimate the required complexity of each equalization scheme for signals with arbitrary symbol rate. Whereas the total DMD of 33.2 ns in the experiments was the largest among recent SDM experiments, the use of parallel MIMO FDE significantly suppressed the complexity and enabled successful transmission with considerably lower-complexity than was achieved



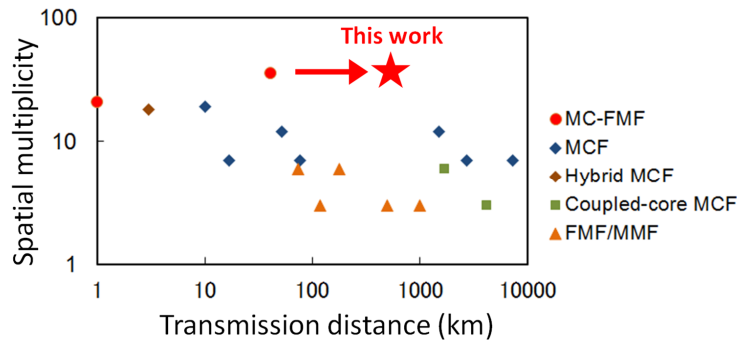


Fig. 8.1 SDM WDM transmission distance vs. spatial multiplicity.

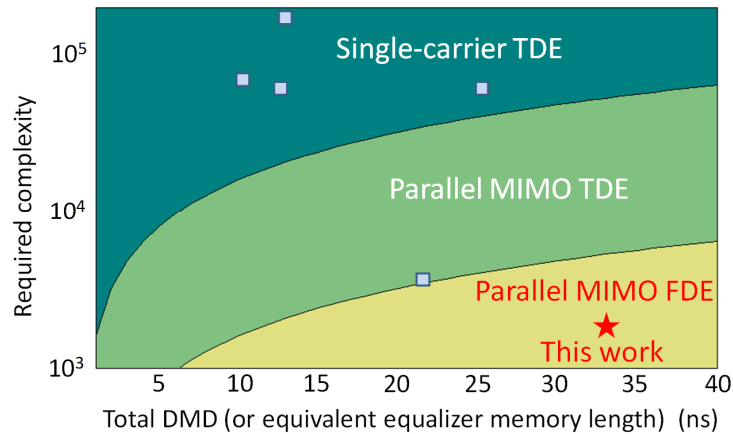


Fig. 8.2 Required complexity for DMD compensation in recent FMF.

with other methods. Switching SC-TDE to parallel MIMO FDE is expected to reduce the complexity by a factor of around 33.

### 8.1.3 Adaptive Algorithms for DMD Equalization

This subsection briefly describes three adaptive equalization algorithms: SC-TDE, parallel MIMO TDE [105], and parallel MIMO FDE. Also derived and compared are the required computational complexity for three schemes. The complexity is defined as the number of complex multiplications per symbol per mode in each scheme in this section.

### 8.1.3.1 Single-carrier TDE

Starting with the definition of  $\Delta\tau$ ,  $N_t$ ,  $N_m$ ,  $R_o$ , and  $R_s$  which respectively denote total DMD, the number of equalizer taps for SC-TDE, the number of spatial and polarization modes, the oversampling rate, and the symbol rate. Note that only integer value for  $R_o$  is considered in this thesis. If positive and negative DMD effects are taken into account,  $N_t$  is equal to  $2\Delta\tau R_o R_s$ . If the  $k$ -th received signal for  $i$ -th mode is denoted as  $y_{i,k}$ , the  $k$ -th received signal vector for the  $i$ -th mode is expressed as  $\mathbf{y}_{i,k} = [y_{i,k-\lfloor N_t/2 \rfloor} \ y_{i,k-\lfloor N_t/2 \rfloor+1} \ \cdots \ y_{i,k+\lceil N_t/2 \rceil-1}]^T$ , where superscript  $T$ ,  $\lfloor \cdot \rfloor$ , and  $\lceil \cdot \rceil$  respectively denote the transpose operation, the floor function, and the ceiling function. The complex-valued  $N_t N_m \times N_m$  equalizer matrix  $W$  is defined as

$$W = [\mathbf{w}_{ij}], \quad (8.1)$$

where  $\mathbf{w}_{ij}$  denotes the  $(i, j)$ -th column vector of  $W$ . The  $k$ -th symbol of the equalizer output for the  $i$ -th mode  $x_{i,k}$  is obtained as

$$x_{i,k} = \sum_{j=1}^{N_m} \mathbf{w}_{ij}^T \mathbf{y}_{j,k}. \quad (8.2)$$

Note that  $\mathbf{y}_{i,k}$  and  $\mathbf{w}_{ij}$  are vectors of length  $N_t$ . This section employs a data-aided or decision-directed LMS method for equalizer update. Thus, using the  $k$ -th desired output symbol for  $i$ -th mode  $d_{i,k}$ , the error signal  $e_{i,k}$  becomes

$$e_{i,k} = d_{i,k} - x_{i,k}. \quad (8.3)$$

The corresponding equalizer updating equation with the step-size parameter  $\mu$  is derived as

$$\mathbf{w}_{ij} \leftarrow \mathbf{w}_{ij} + \mu e_{i,k} \mathbf{y}_{j,k}^*. \quad (8.4)$$

Equations (8.1) through (8.4) implies that  $N_t N_m$  multiplications are needed for one symbol output per mode and  $(N_t N_m + 1)$  multiplications are needed for equalizer updating. Thus the complexity for SC-TDE is calculated as

$$\begin{aligned} C_{\text{SC-TDE}} &= 2N_t N_m + 1 \\ &= 4\Delta\tau R_o R_s N_m + 1. \end{aligned} \quad (8.5)$$

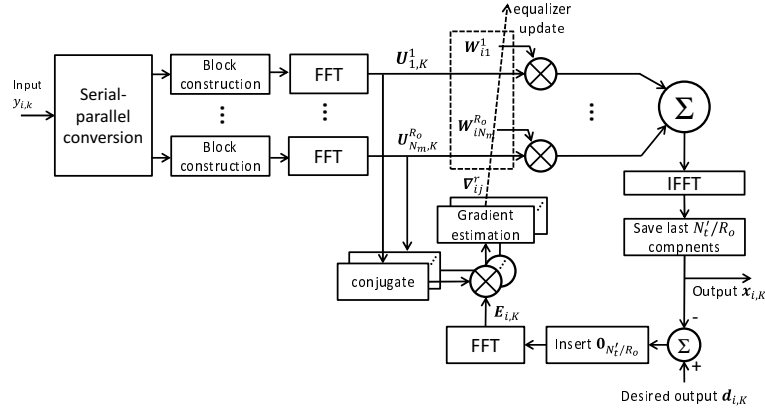


Fig. 8.3 The schematic processing flow of the FDE scheme.

### 8.1.3.2 Parallel MIMO TDE

If an optical carrier is divided into  $P$  subcarriers, each subcarrier has to be driven at a symbol rate of  $R_s/P$  to keep the data rate unchanged. Thus the equalizer length for multicarrier equalization algorithm  $N'_t$  becomes

$$N'_t = \frac{N_t}{P} = \frac{2\Delta\tau R_o R_s}{P}. \quad (8.6)$$

The adaptation algorithm for the parallel MIMO TDE is basically identical to that for SC-TDE.

While the number of symbols contained in a unit time for one subcarrier is decreased by a factor of  $P$  due to the lower symbol rate, the number of subcarriers increases by a factor of  $P$ . Consequently, the complexity for parallel MIMO TDE is calculated as

$$\begin{aligned} C_{P-TDE} &= \left(2N'_t N_m + 1\right) \left(\frac{1}{P}\right) P \\ &= \frac{4\Delta\tau R_o R_s N_m}{P} + 1. \end{aligned} \quad (8.7)$$

### 8.1.3.3 Parallel MIMO FDE

Here assumes parallel MIMO FDE that applies the overlap-and-save method with a 50% overlap ratio for simplicity [136]. The schematic processing flow of the FDE scheme is illustrated in Fig. 8.3. Note that an equalizer is split into  $R_o$  sub-equalizers  $w_{ij}^r$  with equalizer length of  $N'_t/R_o$  where superscript  $r$  represents an oversampling index ( $1 \leq r \leq R_o$ ), and that

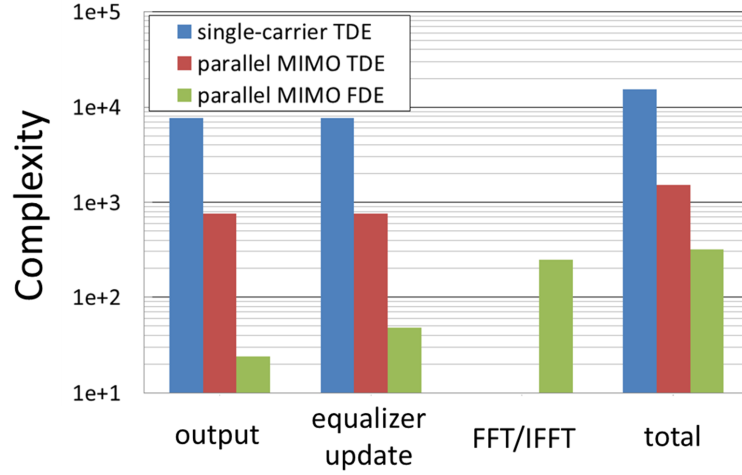


Fig. 8.4 Comparison of the required complexity in each step for three equalization schemes.

the block processing with the block size of  $2N'_t/R_o$  outputs the  $N'_t/R_o$  symbols. The first step is the converting the received serial sequence for each mode into  $R_o$  parallel sequences. Then the  $K$ -th block input  $\mathbf{U}_{i,K}^r$  is constructed by using  $N'_t/R_o$  samples from the current block and  $N'_t/R_o$  samples from the previous block:

$$\mathbf{U}_{i,K}^r = \text{diag}[\mathcal{F}(y_{i,KN'_t-N'_t}^r \ y_{i,KN'_t-N'_t+1}^r \ \cdots \ y_{i,KN'_t+N'_t-1}^r)], \quad (8.8)$$

where  $\text{diag}(\cdot)$  makes a diagonal matrix with a vector input and  $\mathcal{F}(\cdot)$  denotes FFT operation. A sub-equalizer in the frequency domain  $\mathbf{W}_{ij}^r$  is derived from the corresponding time-domain quantities as

$$\mathbf{W}_{ij}^r = \mathcal{F}[\mathbf{w}_{ij}^r \ \mathbf{0}_{N'_t/R_o}], \quad (8.9)$$

where  $\mathbf{0}_{N'_t/R_o}$  is a column vector with  $N'_t/R_o$ -length zeros. The  $K$ -th block equalizer output for the  $i$ -th mode  $\mathbf{x}_{i,K}$  is obtained as

$$\mathbf{x}_{i,K} = \text{last } N'_t/R_o \text{ components of } \mathcal{F}^{-1} \left[ \sum_{r=1}^{R_o} \sum_{j=1}^{N_m} \mathbf{U}_{j,K}^r \mathbf{W}_{ij}^r \right], \quad (8.10)$$

where  $\mathcal{F}^{-1}(\cdot)$  denotes IFFT operation. Note that  $\mathbf{U}_{j,K}^r$  and  $\mathbf{W}_{ij}^r$  have respectively size of  $2N'_t/R_o \times 2N'_t/R_o$  and  $2N'_t/R_o \times 1$ . By expanding eq. (8.3) to the vector form, the error signal vector for the  $K$ -th block  $\mathbf{E}_{i,K}$  is calculated in the frequency domain as

$$\mathbf{E}_{i,K} = \mathcal{F}[\mathbf{0}_{N'_t/R_o} (\mathbf{d}_{i,K} - \mathbf{x}_{i,K})], \quad (8.11)$$

where  $\mathbf{d}_{i,K}$  and  $\mathbf{x}_{i,K}$  are respectively the  $K$ -th desired output vector and the  $K$ -th output vector for  $i$ -th mode. The block gradient estimate  $\nabla_{ij}^r$  becomes

$$\nabla_{ij}^r = \text{first } N'_t/R_o \text{ components of } \mathcal{F}^{-1}[\mathbf{U}_{j,K}^{rH} \mathbf{E}_{i,K}], \quad (8.12)$$

where  $H$  denotes the complex conjugate transpose operation. Thus the equalizer updating equation is finally obtained as

$$\mathbf{W}_{ij}^r \leftarrow \mathbf{W}_{ij}^r + \mu \mathcal{F}[\nabla_{ij}^r \mathbf{0}_{N'_t/R_o}]. \quad (8.13)$$

Equations (8.8) through (8.13) indicate that  $2N'_t N_m$  multiplications are needed for output calculation and  $4N'_t N_m$  for equalizer updating. The total number of FFT/IFFT operations becomes  $(2 + R_o + 2R_o N_m)$  including  $R_o$  FFT in the input sequence transform, 2 FFT/IFFT in the processing to derive  $\mathbf{E}_{i,K}$ , and  $2R_o N_m$  FFT/IFFT in the gradient estimation and the equalizer updating. Assuming the implementation of FFT/IFFT with FFT-size of  $L$  by the radix-2 algorithm that needs  $(L/2) \log_2 L$  complex multiplications, and recalling that FFT-size is equal to  $2N'_t/R_o$ , the complexity for parallel MIMO FDE can be calculated as

$$\begin{aligned} C_{\text{P-FDE}} &= (2 + R_o + 2R_o N_m) \log_2 \left( \frac{2N'_t}{R_o} \right) + 6N_m R_o \\ &= (2 + R_o + 2R_o N_m) \log_2 \left( \frac{4\Delta\tau R_s}{P} \right) + 6N_m R_o. \end{aligned} \quad (8.14)$$

Fig. 8.4 compares the required complexity in each step for adaptive equalization schemes. In the figure, parameters  $N_t, N_m, R_o$  and  $P$  are respectively set to 1280, 6, 2, and 10. The figure shows that the complexity in the parallel MIMO FDE scheme is reduced mainly due to simplification of the output and equalizer-updating calculations. It can be also found that a computationally-effective FFT/IFFT algorithm would contribute to further reduction of the complexity [137], although it is not discussed here since it is out of the scope of this thesis.

Fig. 8.5 compares the complexity for various total DMD values in spatial mode number cases of 1, 3, 6, and 10. It turns out that the complexity for single-carrier TDE scales linearly with the total DMD. However, using parallel MIMO FDE offers significant complexity reduction. The complexity of parallel MIMO FDE is only about 1.5 % relative to that of an equivalent single-carrier TDE for a total DMD of 30 ns.

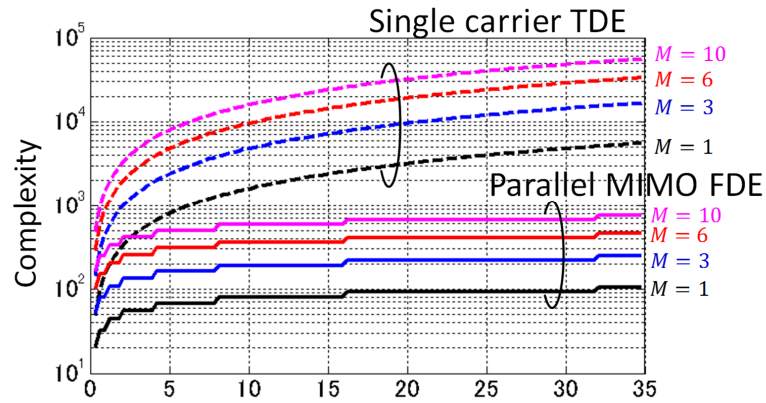


Fig. 8.5 Required complexity for DMD compensation.  $M$  denotes the number of spatial channels.

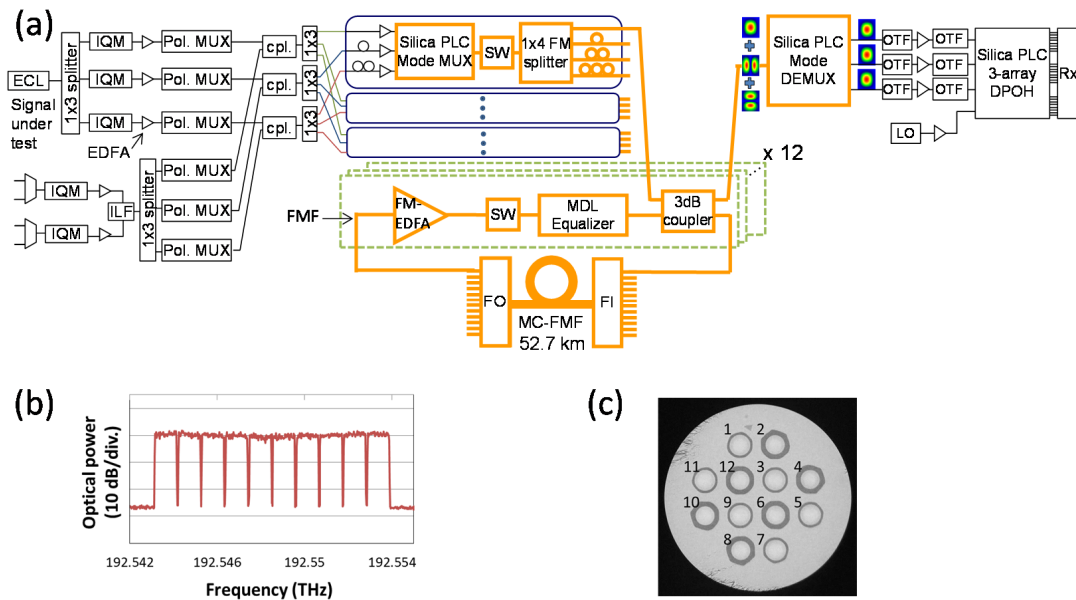


Fig. 8.6 (a) Experimental setup, (b) low symbol rate multi-carrier signal, and (c) cross section of 12-core  $\times$  3-mode low-DMD MC-FMF transmission fiber.

### 8.1.4 Experimental Setup

Next, a DSDM transmission experiment was conducted. The experimental setup is depicted in Fig. 8.6(a). At the transmitter, a test and 19 dummy channels were respectively generated by a tunable external-cavity laser (ECL) with a 25-kHz linewidth and by DFB

lasers with a 2-MHz linewidth. The 12.5-GHz-spaced CW carriers (1556.0-1557.9 nm) were separately multiplexed into even/odd channels. The 1.04-GHz-spaced 10-FDM multi-carrier QPSK signals were digitally generated, each of them was driven at 1-Gbaud and reshaped by a root-raised-cosine filter with a roll-off factor of 0.01. Each mode signal was modulated independently by different binary patterns using pieces of the PRBS of length  $2^{23} - 1$ . The frame of 31250 symbol-length comprised 1.63% overhead for the training sequence, 20% overhead for forward error correction (FEC), and a payload. The transmitter frequency response was pre-equalized in a zero-forcing manner. The even/odd channels were combined by 12.5/25 GHz interleave filters and then fed into a PDM-emulator with 275 ns delay to create the PDM channels. This yielded 20-ch 12.5-GHz-spaced 40 Gb/s PDM-QPSK signals, resulting in a net data rate of 32.79 Gb/s and SE of 2.62 b/s/Hz/core/mode. An optical spectrum with 20 MHz resolution is shown in Fig. 8.6(b). The independently-modulated PDM signals were each split into three ports, delayed, preamplified, and input to  $LP_{01}$ ,  $LP_{11a}$ , and  $LP_{11b}$  input ports of three silica planar lightwave circuit (PLC) mode multiplexers (MUXs). The mode-multiplexed signals were each split by a  $1 \times 4$  FM splitter, delayed, and input to 12 recirculating loops operated synchronously. All 36 DSDM tributaries at the fan-in (FI) input of the MC-FMF had their power set at -9 dBm/wavelength/core/mode.

The transmission line consisted of a newly developed GI low-DMD MC-FMF with 52.7-km length. The DMD was varied core-to-core in the range from -41 ps/km to 63 ps/km for the C-band where positive (negative) DMD corresponds to the case in which  $LP_{01}$  ( $LP_{11}$ ) mode signals propagate earlier. The physical parameters of the fiber are summarized in Table 8.1. The FM cores were designed with two types of trench-assisted GI profiles having different propagation constants placed next to each other in a square lattice arrangement with a view to minimizing core-to-core crosstalk (see Fig. 8.6(c)). The core pitch, the cladding diameter, and the worst core-to-core crosstalk after 500-km transmission were 43  $\mu\text{m}$ , 230  $\mu\text{m}$ , and -48.4 dB between  $LP_{11}$  modes, respectively, and the dispersion of the  $LP_{01}$  mode was 19.8 ps/nm/km at 1550 nm. The attenuation loss at 1550 nm was 0.218 and 0.228 dB/km for the  $LP_{01}$  and  $LP_{11}$  modes, respectively, and the effective area at 1550 nm was 110  $\mu\text{m}^2$  for the  $LP_{01}$  mode. The total span loss at 1550 nm of the transmission fiber with physical contact type fan-in/fan-out (FI/FO) devices was 12.0-13.4 dB for the  $LP_{01}$  mode and 11.9-14.9 dB for the  $LP_{11}$  mode. Each loop included a ring-core FM erbium-doped fiber amplifier (FM-EDFA)

Table. 8.1 CHARACTERISTICS OF THE MC-FMF.

Parameters	Spatial mode	Value
Attenuation	LP <sub>01</sub>	0.218 dB/km
	LP <sub>11</sub>	0.228 dB/km
Effective area	LP <sub>01</sub>	110 $\mu\text{m}^2$
Inter-core crosstalk with FI/FO devices	LP <sub>11</sub>	< -48.4 dB <sup>a</sup>
DMD in the C-band	Max.	63 ps/km
	Min.	-41 ps/km
	Average	29 ps/km
Length	-	52.7 km
Cladding diameter	-	230 $\mu\text{m}$
Core pitch	-	43 $\mu\text{m}$

<sup>a</sup> after 500-km transmission.

and a free-space optics type mode dependent loss (MDL) equalizer. A FM-EDFA has a gain of > 18 dB, a typical differential modal gain of < 1.4 dB, and the noise figure of < 5.2 dB for LP<sub>01</sub> mode and of < 5.8 dB for LP<sub>11</sub> mode [115]. The total input and output power of a FM-EDFA were -4.4 dBm/core and 16.7 dBm/core on average, respectively. A MDL equalizer that compensates for the loss difference of 3 dB between LP<sub>01</sub> and LP<sub>11</sub> modes within a loop consists of a collimator pair and a small dot shaped neutral density (ND) filter. The LP<sub>01</sub> mode signals are attenuated heavily, because its modal intensity profile is strongly overlapped with the ND filter. On the other hand, the LP<sub>11</sub> mode signal's loss becomes small due to its small overlap-integral. Note that twelve parallel FM-EDFAs were fabricated and employed in the transmission experiment. These optical devices allowed the transmission to suppress MDL to as low as 0.2 dB per loop on average.

At the receiver, the core under test was selected for each measurement through spatial demultiplexing by the FO device and then mode-demultiplexed by the PLC mode DEMUX. The signals were injected to the optical tunable filters (OTFs) one by one for wavelength demultiplexing and input together to a PLC 3-array integrated dual polarization optical hybrid (DPOH) module designed for 6 × 6 MIMO signal processing. The received signals were dig-



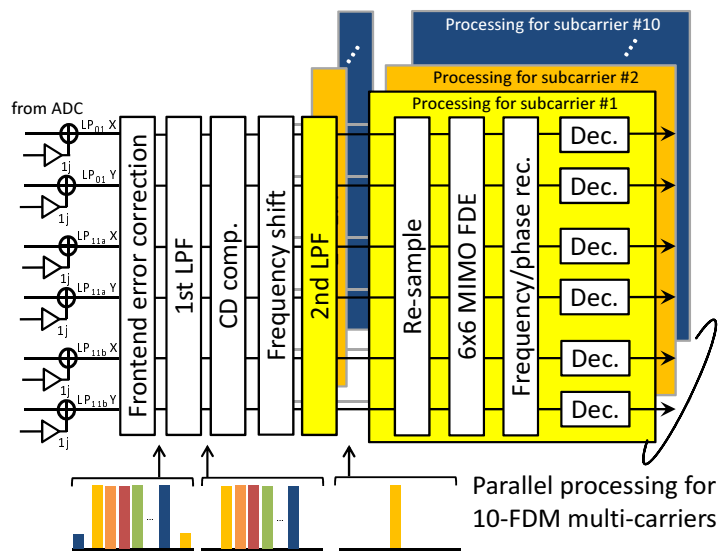


Fig. 8.7 Offline parallel MIMO processing flow.

itized at 40 GS/s using a 12-ch digital storage oscilloscope, and stored in sets of 8 M samples. Fig. 8.7 explains the offline parallel MIMO processing flow that was employed in the experiment. After frontend error correction and chromatic dispersion compensation, out-of-band noise was removed by the first low-pass digital filter. The combined processing of frequency shift and second low-pass filtering worked as a band-pass filter to extract the target subcarrier. Then equalization and DMD compensation were carried out in a parallel processing for 10-FDM multi-carriers by using adaptive  $6 \times 6$ -MIMO FDE with half-symbol-spaced taps and frequency/phase recovery. In the  $6 \times 6$ -MIMO FDE process, fast convergence was achieved by using a data-aided normalized-LMS-based equalizer update. The adaptation algorithm was then switched to decision-directed mode. Note that no cyclic prefix was added in the FDE scheme since the overlap-and-save method was used [137], and that the equalizer tap length for FDE was varied depending on the transmission distance to appropriately compensate DMD (e.g., 128 taps were used in 527 km transmission for the total DMD of 33.2 ns). 2.5 M bits to count bit-error ratio (BER) per carrier per mode were used for evaluation by means of differential decoding. Finally, the  $Q$ -factor was calculated from the measured BER.

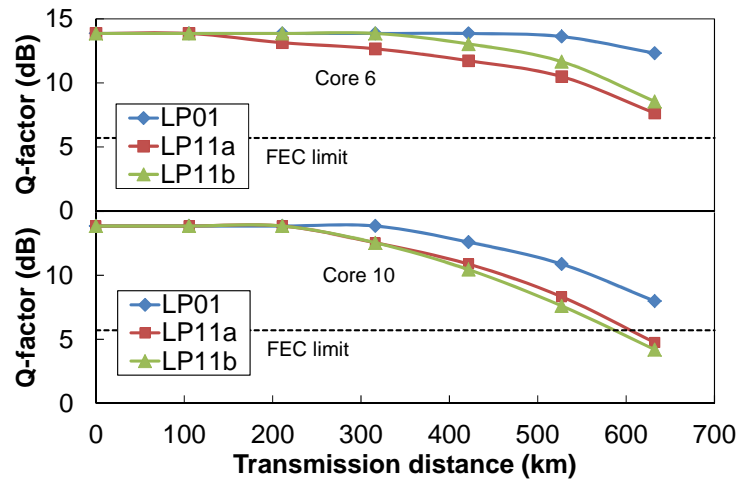


Fig. 8.8  $Q$ -factor transition as a function of transmission distance for core #6 (top panel) and #10 (bottom panel).

### 8.1.5 Transmission Results

The transmission characteristics of core #6 and #10 was examined, which respectively have the largest and average DMD among all cores. Fig. 8.8 shows the  $Q$ -factors as a function of transmission distance for core #6 and #10 of  $\lambda_{11}$  of the WDM channels. The achievable transmission distance of core #10 was shorter than that of core #6 which, as mentioned above, has the largest DMD. The residual MDL of the core #10 recirculating loop was 0.35 dB/loop, whereas the average for all the cores was 0.2 dB/loop. This larger MDL could be the main factor that limited the transmission distance of core #10. Fig. 8.9(a) shows the measured  $Q$ -factor performance for all channels after 527-km transmission. It was confirmed that the measured  $Q$ -factors for all 36 SDM tributaries for the 20 wavelengths exceeded the  $Q$ -limit of 5.7 dB of LDPC convolutional codes using a layered decoding algorithm with 20% FEC overhead [138]. Fig. 8.8(b) shows the constellations of core #11,  $\lambda_{10}$ , and subcarrier #4.

### 8.1.6 Summary

The conducted experiment has successfully achieved the 12-core  $\times$  3-mode dense space-division-multiplexing (DSDM) 527-km transmission with 33.2-ns differential mode delay

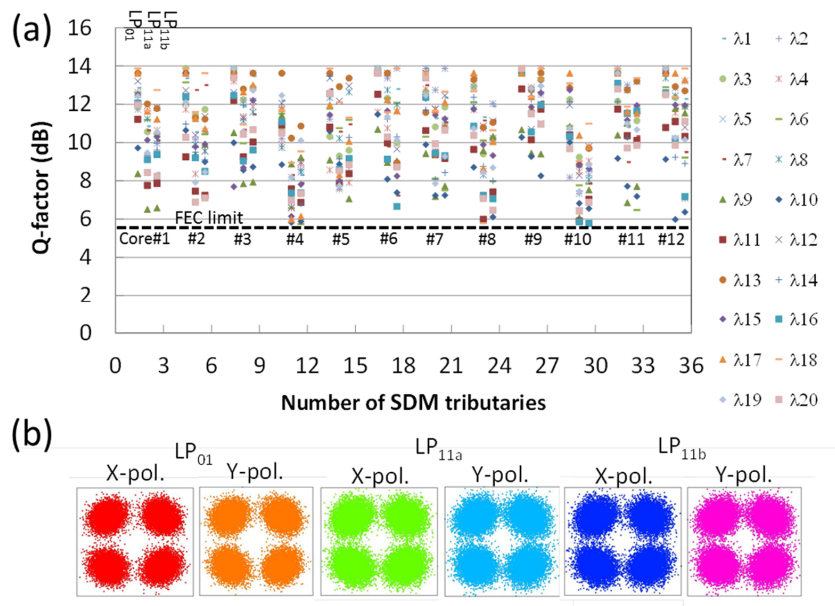


Fig. 8.9 (a)  $Q$ -factors after 527-km transmission. The number of SDM tributaries is defined as  $(n-1) \times 3 + m$ , where  $n$  and  $m$  is the core number and the mode number respectively ( $m = 1$  for LP<sub>01</sub>,  $m = 2$  for LP<sub>11a</sub>, and  $m = 3$  for LP<sub>11b</sub>), (b) typical constellations for all spatial and polarization modes.

(DMD). In order to compensate for the large DMD without optical DMD management, low complexity parallel multiple-input multiple-output (MIMO) frequency-domain equalization (FDE) was implemented into the low baud rate multi-carrier transmission. The newly-developed graded-index (GI) multi-core few-mode fiber (MC-FMF) with DMD of 63 ps/km was also employed. It was found that the use of an FM erbium-doped fiber amplifier with improved differential modal gain and a mode dependent loss equalizer reduced mode-dependent gain/loss to as low as 0.2 dB on average. Experiment results showed that the combination of parallel MIMO FDE and GI MC-FMF is a promising solution for achieving long-distance DSDM transmissions.

## 8.2 Space-Time Coding-Assisted Transmission for Mitigation of MDL Impact on Mode-Division Multiplexed Signals

### 8.2.1 Overview

In an SDM transmission system that employs multi-mode or few-mode (FM) fibers, mode dependent loss (MDL) has been one of the most serious problems to be addressed for the practical application of SDM systems [83]. MDL arises in FM amplifiers or optical components. In [139], MDL-induced penalty was found to be reduced by advanced MIMO signal processing techniques such as receiver-side maximum-likelihood (ML) detection, although they required high computational complexity. On the other hand, gathering channel state information (CSI) at a transmitter would be useful for an MDL-impaired transmission link, it is likely to be unsuitable since overall MDL varies statistically according to the random matrix model analysis in [102].

When no knowledge of CSI at a transmitter is available, MDL impact can be mitigated by scrambling mode-multiplexed signals. As an optical mode-mixing approach, mode scramblers were introduced after the mode multiplexing and after each FM amplifier in [116]. Digital-domain mode-mixing is also a powerful tool for mitigation of MDL. One of the promising schemes for it is employing space-time coding (STC) that utilizes diversity of both space and time. As of today, a few studies have applied STC to SDM transmission in fiber-optic communication systems [84, 119]. In [84], they numerically demonstrated that STC techniques based on linear threaded algebraic STC in conjunction with receiver-side ML detection mitigates MDL-induced penalty in a 6-mode SDM system. In [119], a round-robin coding scheme was employed in both a transmitter and a receiver to equalize spatial inter-channel performance by interleaving symbols over all modes and polarizations. It is desirable that an MDL-tolerant STC scheme is established which does not lose system performance (e.g., throughput) as well as being easy to implement.

The STC scheme for SDM transmission described in this section is the first one that is

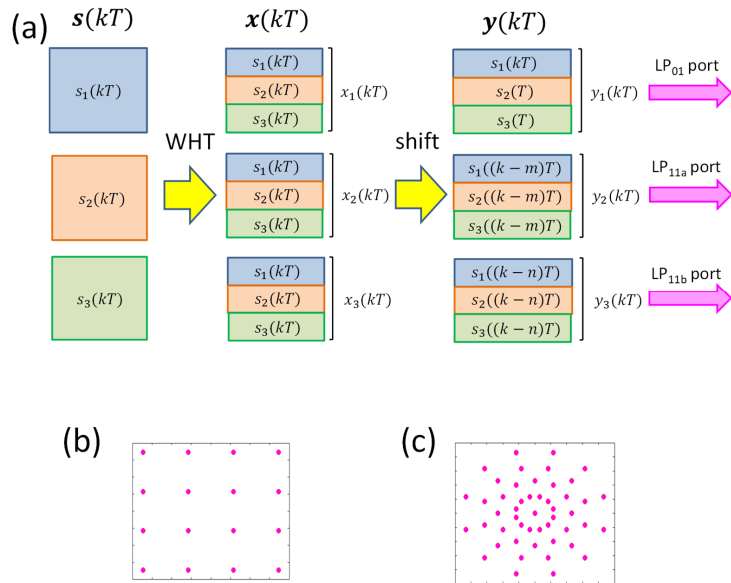


Fig. 8.10 (a): Schematic of the coding flow of the proposed method with  $N = 3$ . (b), (c): constellation maps when applying eq. (8.15) to QPSK signals for (b)  $LP_{01}$  and (c)  $LP_{11a}/LP_{11b}$ .

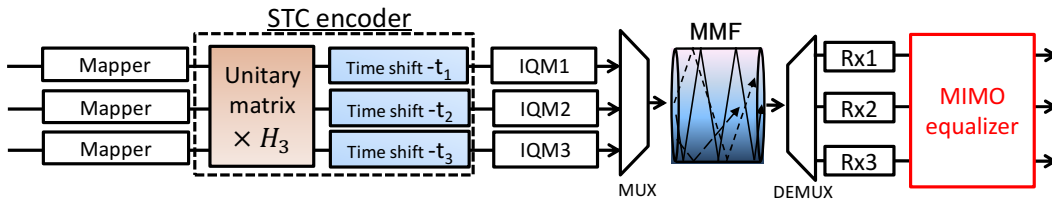


Fig. 8.11 Schematic structures of the proposed STC system.

implemented only through simple transmitter-side processing. The method requires no additional optical devices or receiver-side demodulation processes. also experimentally verified its feasibility with respect to the MDL problem, and demonstrated that it enhanced transmission reach by 20% in dense SDM (DSDM) systems using multi-core FM fibers.

## 8.2.2 Proposed STC Scheme: Space-Time Spreading Implemented with the Orthogonal Transform

The STC is widely used to enhance transmission reliability in today's wireless MIMO systems. Similarly, the basic concept of the proposed method is based on STC in a MIMO system: it equally spreads each symbol's power over all modes. Here the discrete Fourier transform (DFT) matrix is employed as a spatial spreading matrix. A similar method have been previously proposed and applied it to a superchannel transmission in [140] and Chapter 4. The method was revealed to directly improve signal-to-interference-plus-noise ratio (SINR), especially for the worst subcarriers. The schematic processing flow of the method is depicted in Fig. 8.10. If one constructs the original and transformed symbol sequence vectors respectively as  $\mathbf{s}(t) = [s_1(t) \ s_2(t) \ \cdots \ s_{N_T}(t)]^T$  and  $\mathbf{s}'(t) = [s'_1(t) \ s'_2(t) \ \cdots \ s'_{N_T}(t)]^T$ , where the subscripts appearing in each quantity,  $T$ , and  $N_T$  respectively denote the index numbers of modes, the total number of spatial modes and/or polarizations, and transpose operation,  $\mathbf{s}'(t)$  is obtained through DFT:

$$\mathbf{s}'(t) = \frac{1}{\sqrt{N_T}} D \mathbf{s}(t), \quad (8.15)$$

where  $D$  denotes a DFT matrix. A transmitted symbol sequence vector  $\mathbf{x}(t)$  is obtained through decorrelation of  $s'_1(t), \dots, s'_N(t)$ , namely through shift  $s'_i(t)$  by  $t_i$ . Thus  $\mathbf{x}(t)$  can be expressed as

$$\mathbf{x}(t) = \begin{pmatrix} s'_1(t) \\ s'_2(t - t_2) \\ \vdots \\ s'_N(t - t_N) \end{pmatrix}. \quad (8.16)$$

Since few-mode fiber transmission is explored in the current work, the number of modes  $N_T$  was set to 3, even though it can be easily expanded to the scheme for larger dimensions including spatial modes as well as polarization. In this section  $D$  is given as

$$D = \begin{pmatrix} 1 & 1 & 1 \\ 1 & \omega & \omega^2 \\ 1 & \omega^2 & \omega \end{pmatrix}, \quad (8.17)$$

where  $\omega = \exp(\frac{2\pi j}{3})$ . These symbol sequences are fed into transmitter-side signal preprocessing stages including pulse shaping, followed by optical IQ modulator to convert them to optical SDM signals. Accordingly, every symbol is substantially transmitted over the optical paths of all modes. At the receiver, received signals are transformed to the original symbol sequences by employing conventional FIR-structured adaptive MIMIO equalizers, which means that the decoding is carried out in a conventional DSP architecture and requires no complex signal processing for demodulation.

### 8.2.3 Numerical Performance Analysis of Mode Scrambling and Space-Time Spreading

This subsection provides numerically analysis of the proposed ST spreading and MS schemes based on the matrix channel propagation model with distributed noise loading (Fig. 8.12). The considered transmission system supports three spatial modes comprising  $K$  spans, with every span containing an MMF and an MM amplifier (MMA). An MS and an ST encoder are also introduced if they are to be used. The parameters  $D$ ,  $M_k$ ,  $T_k$ ,  $G_k$ , and  $z_k$  denote an DFT matrix, a random unitary matrix of an MS, an MMF transfer function matrix, a diagonal gain matrix of MMA with DMG (i.e., MDL), and a noise vector, respectively. Note that subscript  $k$  denotes the physical quantity of the  $k$ -th span, and that  $M_k$  is replaced by the  $3 \times 3$  identity matrix when the use of MSs is not employed. A unitary matrix  $U_k$  is placed at the end of each span to regulate the degree of mode coupling between adjacent spans, which is constructed as

$$U_k = R_z(\alpha_k)R_y(\beta_k)R_x(\gamma_k), \quad (8.18)$$

with Euler angles  $\alpha_k$ ,  $\beta_k$ , and  $\gamma_k$ , where  $R_i$  denotes a rotation matrix about the  $i$ -axis in three dimensions ( $i \in \{x, y, z\}$ ). Euler angle parameters  $\alpha_k$ ,  $\beta_k$ , and  $\gamma_k$  respectively obey von Mises distribution  $f(\kappa, \mu)$  with shape parameter  $\kappa$  and location parameter  $\mu$ . In this work these parameters are set as  $(\kappa, \mu) = (100, 0)$ , which corresponds to a weakly coupling regime. The received signal vector  $\mathbf{y}$  is described as

$$\mathbf{y} = H\mathbf{x} + \mathbf{z}, \quad (8.19)$$

where  $H$ ,  $\mathbf{x}$ , and  $\mathbf{z}$  are an entire channel matrix, the original signal vector, and a received noise vector, respectively. Based on the matrix channel propagation model described above,  $H$  and  $\mathbf{z}$  are analytically described as

$$H = \prod_{k=1}^K (U_k G_k T_k M_k) D, \quad (8.20)$$

and

$$\mathbf{z} = \sum_{l=1}^{K-1} \prod_{k=l+1}^{K-1} (U_k G_k T_k M_k) U_l \mathbf{z}_l + U_K \mathbf{z}_K. \quad (8.21)$$

Overall MDL is determined by the singular value analysis of  $H$  in eq. (8.20). Fig. 8.13(a) shows the probability densities of overall MDL in both cases with and without MSs. In a weakly-coupled regime, the buildup of MDL is observed because the inter-modal transition rarely occurs. On the contrary, inserting MSs obviously suppresses the overall MDL accumulation. The mean MDL evolutions for both cases are displayed in Fig. 8.13(b). The mean MDL increase becomes almost linearly proportional to the number of spans when no MSs are used. If MSs were introduced, however, the mean MDL scales with square root of the number of spans. This is what the strongly-coupled regime brings to an link with MDM signals, and indeed has been investigated using CC-MCF transmission lines [98, 99, 103, 104].

Signal performance evaluation after transmission over arbitrary number of spans can be carried out based on eq. (8.20) and eq. (8.21). Assuming MDM 10-Gbaud 16QAM signals, BERs are calculated using the MMSE-based MIMO equalizer. The MDL arising from MMA was varied in the range from 0.1-0.7 dB/span, and 500 channel realizations were created for each MDL value. Received OSNR was set to 23 dB in the MDL-free case. Fig. 8.14 depicts the results of mean  $Q$ -factors after 15-span propagation that are calculated from averaged BERs over all spatial modes. When no MSs were used, the ST spreading methods obviously improved  $Q$ -factor performance. When MSs were inserted in each span, a further  $Q$ -factor increase was obtained even without the ST spreading. This is because the strong coupling effect induced by MSs makes the overall MDL decrease. The combined use of MSs and the ST spreading slightly outperformed the use of MSs alone. At the MDL value of 0.7 dB/span, the ST spreading, MS, and MS-STC methods respectively provided  $Q$ -factor increases of 1.1 dB, 1.9 dB and 2.2 dB. These results demonstrate that the ST spreading method brings MDL tolerance improvement, especially in weakly coupled regimes. However, it should



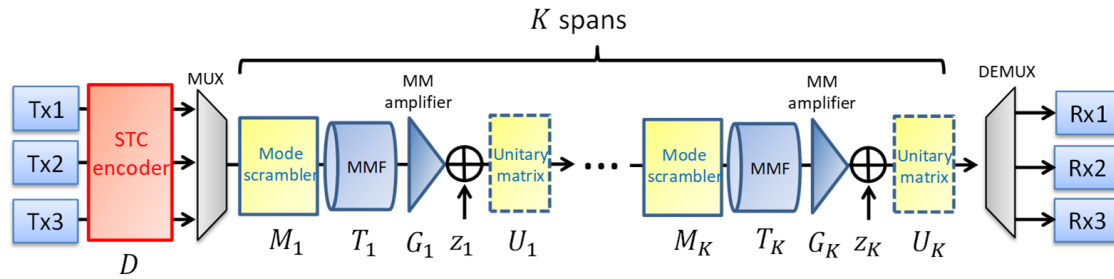


Fig. 8.12 MDM system model with distributed noise loading.

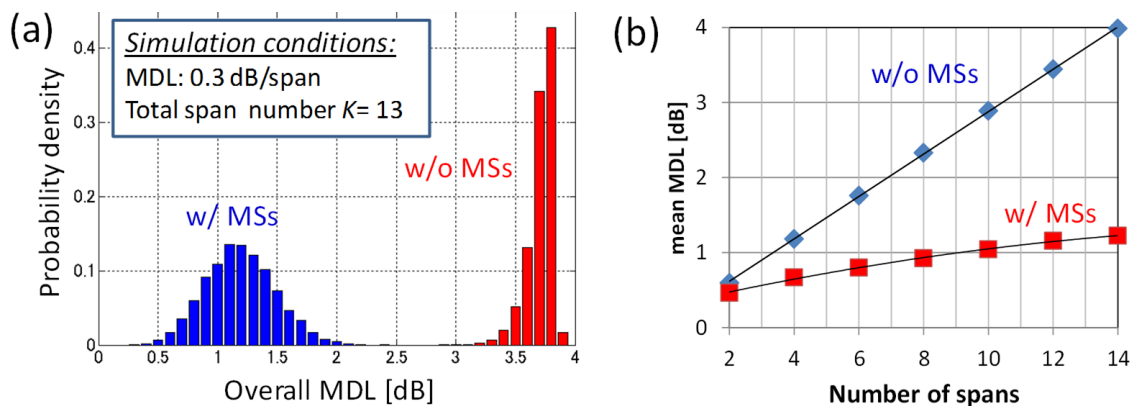


Fig. 8.13 Strongly-coupling effect brought by the introduction of MSs. (a) PDFs of overall MDL values with MSs (red) and without (MSs). (b) Mean MDL evolution as a function of number of spans for both cases.

be also noted that the ST spreading method works as ideal mode coupling at a transmitter without introducing additional insertion loss or MDL since it can be implemented in the digital domain.

## 8.2.4 Experimental Setup and Results

The performance of the proposed ST spreading method is evaluated through a DSDM transmission experiment. The setup is illustrated in Fig. 8.15, which is basically identical to the one used in Section 8.1. At the transmitter, a test channel and 9 dummy channels were respectively generated by a tunable external-cavity laser (ECL) with a 25-kHz linewidth and by DFB lasers with a 2-MHz linewidth. The 12.5-GHz-spaced CW carriers (1557.0–1557.9 nm) were separately multiplexed into even/odd channels. The 1-Gbaud QPSK signals

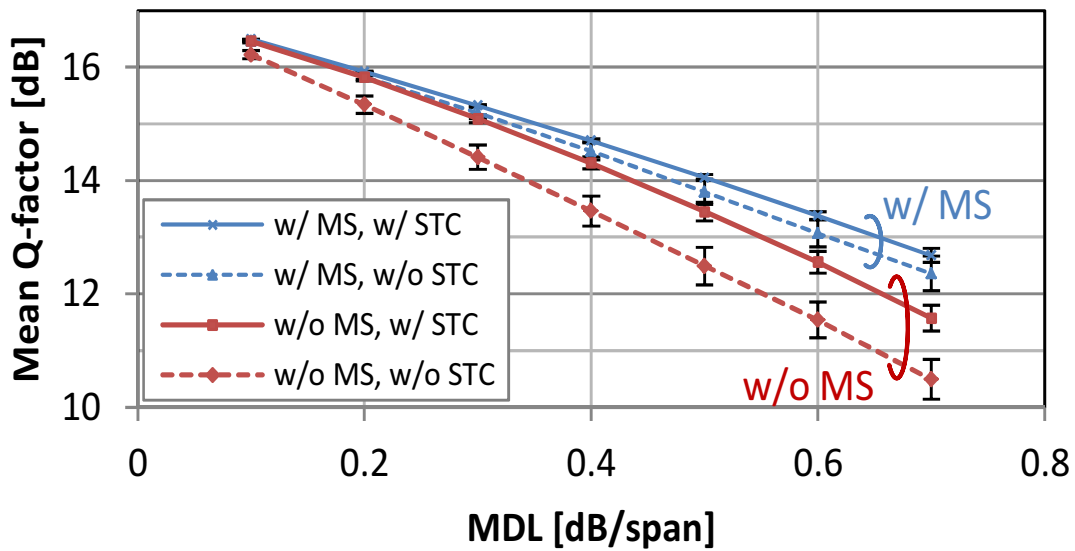


Fig. 8.14 Mean  $Q$ -factors as a function of MDL per span. Error bars are represented as a standard deviation of 500 channel realizations..

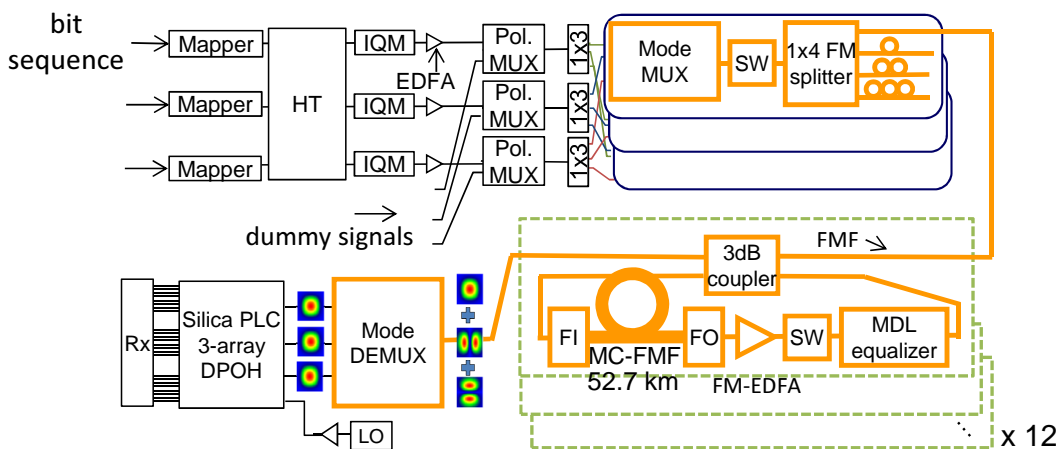


Fig. 8.15 Experimental setup of 12-core  $\times$  3-mode DSDM transmission.

were digitally generated and combined as 1.04-GHz-spaced 10-FDM multi-carrier signals. Three sets of transmitters were employed, each of which consisted of an arbitrary waveform generator (AWG), driver amplifiers, and an IQ modulator to create three independent signals. The even/odd channels were combined by 12.5/25 GHz interleave filters and then fed into PDM emulators with 275 ns delays to create the PDM channels. A recirculating loop was

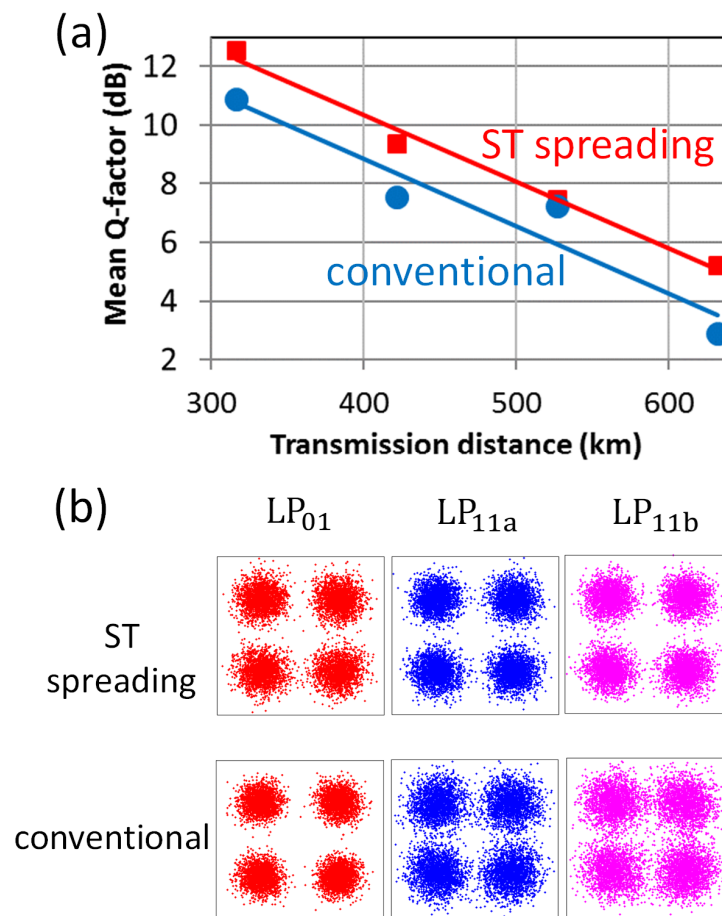
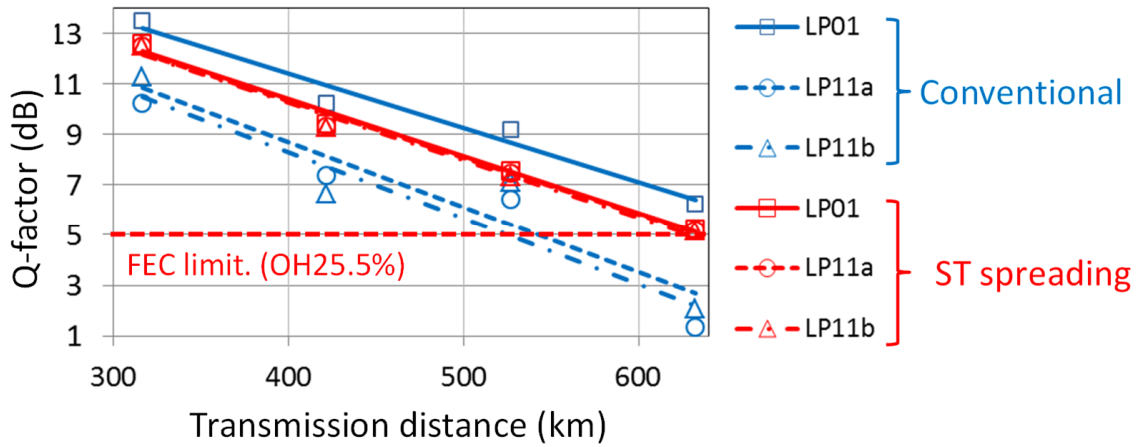
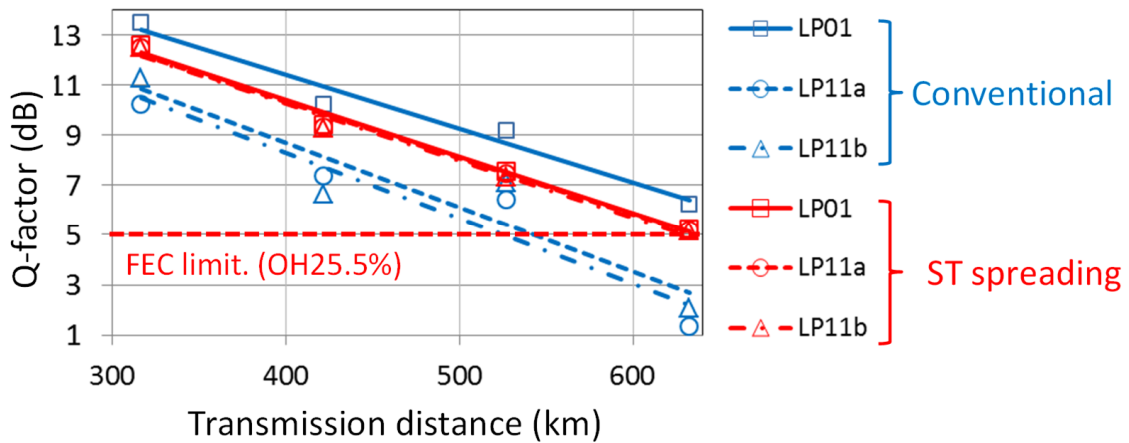


Fig. 8.16 Mean  $Q$ -factor comparison as a function of transmission distance for both methods. (b) Received signals after 421-km transmission for each spatial mode (only signals of X-polarization are displayed).

constructed as a transmission line that consisted of a 3-dB FM coupler, a fan-in device, 52.7-km MC-FMF, a fan-out device, a ring-core FM-EDFA, an FM switch, and a free-space optics type MDL equalizer [83]. The received sets of signals were mode demuxed and received by the coherent Rx module. The data stored in a 12 channel digital storage oscilloscope were offline processed by a parallel MIMO FDE technique which is the same as the one used in Section 8.1. First the “equalizing effect” is overviewed that the method brings to SDM transmission. Fig. 8.16(a) depicts the mean  $Q$ -factors for wavelength channel #11 and core #3 as a function of transmission distance, for both the proposed proposed method with DFT and a conventional method without it. The mean  $Q$ -factors were calculated from averaged BERs over all spatial modes and polarizations. The residual MDL was set to 0.55 dB per

Fig. 8.17  $Q$ -factors as a function of transmission distance.Fig. 8.18  $Q$ -factor as a function of residual MDL for all spatial modes after 527-km transmission.

loop by changing the attenuation for  $LP_{01}$  mode imposed by the spatial filters [83]. The result showed the proposed method clearly outperformed the conventional one. The  $Q$ -factor increased by as much as 2.3 dB after 632-km transmission. The constellations plotted in Fig. 8.16(b) indicate that while the signal performance differed from mode to mode in the conventional method, it was almost identical in the ST spreading method. This is because the ST spreading method intersperses distortions of particular mode signals over all mode signals in the receiver-side equalizer stage and consequently improves SINR directly. Thus the proposed method brings an “equalizing” effect over all modes to SDM transmission. Next the detailed  $Q$ -factor performance for each mode was investigated. Fig. 8.17 shows the  $Q$ -

factors obtained with both methods for all modes in the same way as in Fig. 8.16(a). In the conventional method, as transmission distance increased, the  $Q$ -factors of LP<sub>11a</sub> and LP<sub>11b</sub> modes degraded more severely than those of LP<sub>01</sub> mode due to the MDL accumulation. On the other hand, with the ST spreading method the  $Q$ -factor decrease was relatively mitigated. It was confirmed that the measured  $Q$ -factors for the ST spreading method after 632-km transmission exceeded the  $Q$ -limit of 5.0 dB of a spatially-coupled type irregular LDPC code with 25.5 % FEC overhead [141]. It turns out the transmission reach enhancement brought by the ST spreading method became 105.4 km, i.e., a 20 % increase. Then the residual MDL was varied in the range from 0.2 dB to 1.15 dB, and evaluated signal performance after 527-km transmission for both methods. Fig. 8.18 shows the obtained  $Q$ -factors as a function of residual MDL per loop. The figure shows that with the conventional method the  $Q$ -factors obviously decreased for links with larger residual MDL, especially for higher mode signals. The DFT-based spreading method, however, mitigated  $Q$ -factor degradation and consequently enabled all mode signals to be transmitted above the  $Q$ -limit even for residual MDL of 1.15 dB/loop.

### 8.2.5 Summary

In this section, a simple ST spreading scheme is proposed in which coding at the transmitter is implemented by using DFT for application to SDM transmission. The method intersperses each MDM symbol's power over all modes, thus enabling signal performance to be equalized. A DSDM transmission experiment conducted over 632 km successfully demonstrated that the method substantially improves MDL tolerance, thus enabling transmission reach to be increased by 20 %.

## 8.3 LDPC-Coded FMF Transmission Employing Unreplicated SIC for MDL-Impact Mitigation

### 8.3.1 Overview

MIMO signal processing is vital to detect data streams from mutually-coupled received signals, especially for MMF/FMF transmission with fiber length far larger than the correlation length [81]. One of the most widely-used signal processing schemes is an adaptive linear MIMO equalization scheme with LMS updating due to its manageable properties of low complexity and good channel tracking. Indeed, it contributes to recently-achieved transmission reach extension of MIMO signals [96, 107, 108].

MDL which mainly arises from optical inline components including MM amplifiers and MUX/DEMUX devices, is known to lead a non-unitary channel in a MMF transmission link and system capacity reduction [81]. Although MDL is considered to be a dominant factor for MIMO-SDM transmission reach restriction [83], sophisticated signal processing schemes instead of a linear MIMO equalization may offer solutions to overcome MDL problems. Using a ML detector was found to enhance MDL tolerance through numerical simulation at the expense of high complexity [116]. Detection performance improvement was experimentally demonstrated by employing MIMO-OFDM transmission with an SIC scheme [142]. From a perspective of a practical use, one of the technical difficulties in these approaches is that they principally require highly accurate channel estimation (CE) at each frequency within signal bandwidth. Therefore, it is necessary to carefully design systems with respect to the overhead portion associated with CE, symbol rate (i.e., single-carrier or multicarrier transmission) and modulation order. Otherwise a memory effect of a channel due to, say, electrical/optical bandwidth limitation and time-varying modal dispersion enhances hardware complexity and/or degrades detection performance.

In this section, a novel modified SIC scheme is proposed that bypasses replica signal generation, which is called *unreplicated SIC* (U-SIC). Its detection performance was experimentally evaluated under MDL-impaired channels with and without memory, and it was proved

that the proposed U-SIC provides MDL-tolerance improvement of 3.3 dB, and OSNR gain of  $> 4.5$  dB even under an FMF link with 39-ns DMD.

### 8.3.2 Proposed Detection Scheme: Unreplicated SIC

This subsection starts from a brief review of a conventional SIC (C-SIC) scheme, then followed by a description of proposed U-SIC. The detailed description of the C-SIC can be found in Chapter 7. An optical MIMO system with  $N_T$  transmitters and  $N_R$  receivers is considered here, and respectively define  $x_i$ ,  $y_i$ ,  $z_i$ , and  $h_i$  as the  $i$ -th transmitted signal, the  $i$ -th received signal, the  $i$ -th detected signal, and the  $i$ -th column vector of channel transfer matrix  $\mathbf{H}$ . For purposes of simplicity, a non-dispersive (memoryless) channel model is used, although it can be easily expanded to the more general case of a dispersive channel. Note that, although SIC can be implemented based on either ZF or MMSE criterion, this section focuses on the MMSE-SIC scheme. Hereafter the simple conditions are assumed in which a receiver knows CSI and the received data streams have been properly permuted in order of post-processing SINR such that the first data stream ( $x_1$ ) has the highest SINR and the  $N_T$ -th signal stream ( $x_{N_T}$ ) has the lowest, equivalently understood as OSIC scheme. This scenario allows the  $k$ -th stage to simply extract of  $k$ -th data stream.

An SIC detector consists of multiple stages (Fig. 8.19(a)), each of which is responsible for extracting single data stream from received signals by using a multi-input single-output (MISO) detector. In the initial stage, the first data stream  $x_1$  is detected by the MISO detector without interference cancellation as  $\hat{x}_1 = \mathbf{w}_1^T \mathbf{y}$ , where  $\mathbf{y} = [y_1 \ y_2 \ \cdots \ y_{N_R}]^T$  and  $\mathbf{w}_i$  is an equalizer coefficient vector used for the  $i$ -th data stream detection in the MISO detector. The detected signal is fed into a slicer that makes symbol decisions or an FEC decoder, and then multiplied by  $\mathbf{h}_1$  to generate a replica signal vector ( $\tilde{\mathbf{y}}_1$ ). Note that although updating  $\mathbf{w}_i$  by using an adaptive filter technique may allow the MISO detector to work even without CE, CE is still required for replica signal generation. The second stage first removes the  $\mathbf{y}_1$  component from each of the received signals by using  $\tilde{\mathbf{y}}_1$  before MISO detection. At this moment, the constituent parts of received signals are reduced to  $N_T - 1$ . The processing is handled over succeeding stages with similar procedures, and consequently  $(k - 1)$  replica information is known at the  $k$ -th stage. As argued above, the C-SIC detector requires CE with high accuracy,

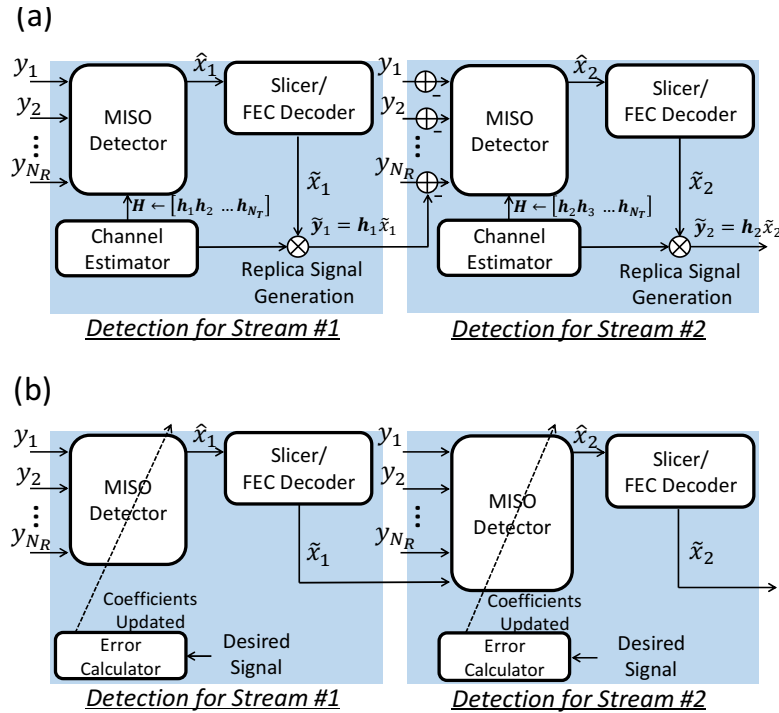


Fig. 8.19 Schematic structures of SIC detectors comprising two stages. (a): conventional SIC, (b): unreplicated SIC.

and thus it becomes more complicated to apply to time-varying dispersive channels.

### 8.3.2.1 U-SIC Detection at the First and Second Stage

Next, the proposed U-SIC detection scheme (Fig. 8.19(b)) will be described. The advantages it provides are that, first, it does not need CE, and second, it can be easily applied to channels with memory. The description of the U-SIC scheme starts with the detection flow at the first and second stage, followed by one at the  $k$ -th stage.

In the initial stage,  $\hat{x}_1$  is detected through the MISO detector. Note that in the U-SIC scheme described in this chapter it is assumed that all MISO detectors are controlled by an adaptive linear filtering algorithm. Then  $\hat{x}_1$  is injected into a slicer in which symbol decisions or decoding are performed, and output as  $\tilde{x}_1$ . So far, above processing is exactly identical to the one used in the C-SIC scheme. Next, the replica signal generation stage is skipped in a manner such that the output signal from the slicer at the first stage is directly input to the second MISO detector as the  $(N_R + 1)$ -th input signal, which is substantially interpreted that the  $(N_R + 1)$ -th received signal is transmitted over an transmission line without any inter-modal



coupling and noise. Thus, the MIMO system model described in eq. (7.11) is augmented to

$$\begin{pmatrix} \mathbf{y} \\ \tilde{x}_1 \end{pmatrix} = \underbrace{\begin{pmatrix} \mathbf{H} \\ 1 & 0 & \cdots & 0 & 0 \end{pmatrix}}_{N_T} \mathbf{x} + \begin{pmatrix} \mathbf{z} \\ 0 \end{pmatrix}, \quad (8.22)$$

or equivalently, eq. (8.22) is expressed in more collective matrix form as

$$\mathbf{y}^{(2)} = \mathbf{H}^{(2)} \mathbf{x} + \mathbf{z}^{(2)}, \quad (8.23)$$

where the superscript number in parenthesis denotes the U-SIC stage number, and each quantity is respectively defined as  $\mathbf{y}^{(2)} \stackrel{\text{def}}{=} [\mathbf{y}^T \tilde{x}_1]^T$ ,  $\mathbf{z}^{(2)} \stackrel{\text{def}}{=} [\mathbf{z}^T 0]^T$ , and

$$\mathbf{H}^{(2)} \stackrel{\text{def}}{=} \underbrace{\begin{pmatrix} \mathbf{H} \\ 1 & 0 & \cdots & 0 & 0 \end{pmatrix}}_{N_T}. \quad (8.24)$$

Recalling eq. (7.21), MMSE-MIMO weight matrix  $\mathbf{W}_{\text{MMSE}}^{(2)}$  is obtained by the product of  $\tilde{E} [\mathbf{y}^{(2)\dagger} \mathbf{y}^{(2)T}]^{-1}$  and  $\tilde{E} [\mathbf{y}^{(2)\dagger} \mathbf{x}^T]$ . Based on the MIMO model described in eq. (8.23), these statistical quantities are evaluated as

$$\begin{aligned} \tilde{E} [\mathbf{y}^{(2)\dagger} \mathbf{y}^{(2)T}] &= P_x \mathbf{H}^{(2)*} \mathbf{H}^{(2)T} + P_z \begin{pmatrix} 1 & & & & \\ & 1 & & & \\ & & \ddots & & \\ & & & \ddots & \\ & & & & 1 \end{pmatrix} \begin{matrix} \\ \\ \\ \\ \end{matrix} \left. \vphantom{\begin{pmatrix} 1 \\ \\ \\ \\ 1 \end{pmatrix}} \right\} N_R \\ &\quad \left( \underbrace{\hspace{10em}}_{N_R} \quad \quad \quad 0 \right) \\ &= P_x \mathbf{H}^{(2)*} \mathbf{H}^{(2)T} + P_z \begin{pmatrix} \mathbf{I}_{N_R} \\ 0 \end{pmatrix}, \end{aligned} \quad (8.25)$$

and

$$\tilde{E} [\mathbf{y}^{(2)\dagger} \mathbf{x}^T] = P_x \mathbf{H}^{(2)*}. \quad (8.26)$$

Therefore, combining the results in eq. (8.25) and eq. (8.26) provides

$$\begin{aligned} \mathbf{W}_{\text{MMSE}}^{(2)} &= \left[ P_x \mathbf{H}^{(2)*} \mathbf{H}^{(2)T} + P_z \begin{pmatrix} \mathbf{I}_{N_R} \\ 0 \end{pmatrix} \right]^{-1} P_x \mathbf{H}^{(2)*} \\ &= \left[ \mathbf{H}^{(2)*} \mathbf{H}^{(2)T} + \frac{1}{\gamma_0} \begin{pmatrix} \mathbf{I}_{N_R} \\ 0 \end{pmatrix} \right]^{-1} \mathbf{H}^{(2)*}. \end{aligned} \quad (8.27)$$

Taking the transpose of eq. (8.27) yields

$$\mathbf{W}_{\text{MMSE}}^{(2)T} = \mathbf{H}^{(2)\dagger} \left[ \mathbf{H}^{(2)} \mathbf{H}^{(2)\dagger} + \frac{1}{\gamma_0} \begin{pmatrix} \mathbf{I}_{N_R} & \\ & 0 \end{pmatrix} \right]^{-1}. \quad (8.28)$$

Particularly, the transpose of the second column of  $\mathbf{W}_{\text{MMSE}}^{(2)}$  is used for the extraction of  $\hat{x}_2$ . Let us perform the detail analysis of eq. (8.28). The inverse part in eq. (8.28) can be decomposed as

$$\begin{aligned} \left[ \mathbf{H}^{(2)} \mathbf{H}^{(2)\dagger} + \frac{1}{\gamma_0} \begin{pmatrix} \mathbf{I}_{N_R} & \\ & 0 \end{pmatrix} \right]^{-1} &= \left[ \begin{pmatrix} \mathbf{H}\mathbf{H}^\dagger & \mathbf{h}_1 \\ \mathbf{h}_1^\dagger & 1 \end{pmatrix} + \frac{1}{\gamma_0} \begin{pmatrix} \mathbf{I}_{N_R} & \\ & 0 \end{pmatrix} \right]^{-1} \\ &= \left( \begin{array}{c|c} \mathbf{H}\mathbf{H}^\dagger + \frac{1}{\gamma_0} \mathbf{I}_{N_R} & \mathbf{h}_1 \\ \hline \mathbf{h}_1^\dagger & 1 \end{array} \right)^{-1}. \end{aligned} \quad (8.29)$$

Equation (8.29) can be analyzed by the matrix inversion lemma in block form as

$$\left( \begin{array}{c|c} \mathbf{H}\mathbf{H}^\dagger + \frac{1}{\gamma_0} \mathbf{I}_{N_R} & \mathbf{h}_1 \\ \hline \mathbf{h}_1^\dagger & 1 \end{array} \right)^{-1} = \left[ \begin{array}{c|c} (\mathbf{H}_{\setminus 1} \mathbf{H}_{\setminus 1}^\dagger + \frac{1}{\gamma_0} \mathbf{I}_{N_R})^{-1} & -(\mathbf{H}_{\setminus 1} \mathbf{H}_{\setminus 1}^\dagger + \frac{1}{\gamma_0} \mathbf{I}_{N_R})^{-1} \mathbf{h}_1 \\ \hline -\mathbf{h}_1^\dagger (\mathbf{H}_{\setminus 1} \mathbf{H}_{\setminus 1}^\dagger + \frac{1}{\gamma_0} \mathbf{I}_{N_R})^{-1} & 1 + \mathbf{h}_1^\dagger (\mathbf{H}_{\setminus 1} \mathbf{H}_{\setminus 1}^\dagger + \frac{1}{\gamma_0} \mathbf{I}_{N_R})^{-1} \mathbf{h}_1 \end{array} \right], \quad (8.30)$$

where  $\mathbf{H}_{\setminus 1}$  is constructed by combining  $\mathbf{h}_i$  excluding  $\mathbf{h}_1$  defined as  $\mathbf{H}_{\setminus 1} = [\mathbf{h}_2 \ \mathbf{h}_3 \ \cdots \ \mathbf{h}_{N_T}]$ . Substituting eq. (8.30) into eq. (8.28) provides  $(\mathbf{W}_{\text{MMSE}}^{(2)})_k^T$  (i.e.,  $k$ -th column vector of  $\mathbf{W}_{\text{MMSE}}^{(2)}$ ) as follows:

$$\left( \mathbf{W}_{\text{MMSE}}^{(2)} \right)_k^T = \begin{cases} [\mathbf{0}_{N_R} \ 1] & (k = 1) \\ \left[ \mathbf{h}_k^\dagger (\mathbf{H}_{\setminus 1} \mathbf{H}_{\setminus 1}^\dagger + \frac{1}{\gamma_0} \mathbf{I}_{N_R})^{-1}, \ -\mathbf{h}_k^\dagger (\mathbf{H}_{\setminus 1} \mathbf{H}_{\setminus 1}^\dagger + \frac{1}{\gamma_0} \mathbf{I}_{N_R})^{-1} \mathbf{h}_1 \right] & (k \geq 2) \end{cases} \quad (8.31)$$

Recall that the aim of the second stage of the U-SIC scheme is to detect  $\hat{x}_2$ , which is obtained by the use of the result in eq. (8.31).

$$\begin{aligned} \hat{x}_2 &= (\mathbf{W}_{\text{MMSE}}^{(2)})_2^T \begin{pmatrix} \mathbf{y} \\ \tilde{x}_1 \end{pmatrix} \\ &= \left[ \mathbf{h}_2^\dagger (\mathbf{H}_{\setminus 1} \mathbf{H}_{\setminus 1}^\dagger + \frac{1}{\gamma_0} \mathbf{I}_{N_R})^{-1}, \ -\mathbf{h}_2^\dagger (\mathbf{H}_{\setminus 1} \mathbf{H}_{\setminus 1}^\dagger + \frac{1}{\gamma_0} \mathbf{I}_{N_R})^{-1} \mathbf{h}_1 \right] \begin{pmatrix} \mathbf{y} \\ \tilde{x}_1 \end{pmatrix}. \end{aligned} \quad (8.32)$$

The analytical performance is inferred from  $(\mathbf{W}_{\text{MMSE}}^{(2)})_2^T$  in eq. (8.32). The first  $1 \times N_R$  vector (i.e.,  $\mathbf{h}_2^\dagger (\mathbf{H}_{\setminus 1} \mathbf{H}_{\setminus 1}^\dagger + \frac{1}{\gamma_0} \mathbf{I}_{N_R})^{-1}$ ) is identical to the MMSE-MIMO weight vector used in

the second stage of the C-SIC scheme. However, interference is not removed at all by the multiplication of the vector, since  $y_i$  ( $i \in \{1, 2, \dots, N_R\}$ ) still contains interference from  $x_1$ . The rest entry (i.e.,  $-\mathbf{h}_2^\dagger (\mathbf{H}_{\setminus 1} \mathbf{H}_{\setminus 1}^\dagger + \frac{1}{\gamma_0} \mathbf{I}_{N_R})^{-1} \mathbf{h}_1$ ) is responsible for the interference cancellation. Equation (8.32) indicates that the detection performance for  $x_2$  by U-SIC is principally identical to that by C-SIC, if both approach the MMSE solution.

### 8.3.2.2 U-SIC Detection at the $k$ -th Stage

The similar analysis based on the augmentation of the MIMO system model described in eq. (7.11) is valid to investigate the detection in the  $k$ -th stage. At the  $k$ -th stage,  $(k-1)$  detected signal streams can be used for the interference removal. Again, the MIMO system in eq. (7.11) is augmented as

$$\begin{pmatrix} \mathbf{y} \\ \tilde{x}_1 \\ \tilde{x}_2 \\ \vdots \\ \tilde{x}_{k-1} \end{pmatrix} = \begin{pmatrix} & & & \mathbf{H} & & & \\ 1 & 0 & \cdots & 0 & 0 & \cdots & 0 \\ 0 & 1 & \cdots & 0 & 0 & \cdots & 0 \\ & & \ddots & & & \ddots & \\ 0 & 0 & \cdots & 1 & 0 & \cdots & 0 \end{pmatrix} \mathbf{x} + \begin{pmatrix} \mathbf{z} \\ 0 \\ 0 \\ \vdots \\ 0 \end{pmatrix}. \quad (8.33)$$

$\underbrace{\hspace{10em}}_{k-1} \qquad \underbrace{\hspace{10em}}_{N_T - k + 1}$

The more collective matrix form of eq. (8.33) becomes

$$\mathbf{y}^{(k)} = \mathbf{H}^{(k)} \mathbf{x} + \mathbf{z}^{(k)}, \quad (8.34)$$

where each quantity is respectively defined as  $\mathbf{y}^{(k)} \stackrel{\text{def}}{=} [\mathbf{y}^T \ \tilde{x}_1 \ \tilde{x}_2 \ \cdots \ \tilde{x}_{k-1}]^T$ ,  $\mathbf{z}^{(k)} \stackrel{\text{def}}{=} [\mathbf{z}^T \ \mathbf{0}_{N_R+k-1}]^T$ , and

$$\mathbf{H}^{(k)} \stackrel{\text{def}}{=} \begin{pmatrix} & & & \mathbf{H} & & & \\ 1 & 0 & \cdots & 0 & 0 & \cdots & 0 \\ 0 & 1 & \cdots & 0 & 0 & \cdots & 0 \\ & & \ddots & & & \ddots & \\ 0 & 0 & \cdots & 1 & 0 & \cdots & 0 \end{pmatrix}. \quad (8.35)$$

$\underbrace{\hspace{10em}}_{k-1} \qquad \underbrace{\hspace{10em}}_{N_T - k + 1}$

The augmented MIMO model in eq. (8.34) provides the MMSE MIMO weight matrix at the

$k$ -th stage as

$$\mathbf{W}_{\text{MMSE}}^{(k)T} = \mathbf{H}^{(k)\dagger} \left[ \mathbf{H}^{(k)} \mathbf{H}^{(k)\dagger} + \frac{1}{\gamma_0} \underbrace{\begin{pmatrix} \mathbf{I}_{N_R} & & & \\ & 0 & & \\ & & \ddots & \\ & & & 0 \end{pmatrix}}_{k-1} \right]^{-1}. \quad (8.36)$$

By constructing the sub channel matrix  $\mathbf{H}_{k-1} \stackrel{\text{def}}{=} [\mathbf{h}_1 \ \mathbf{h}_2 \ \cdots \ \mathbf{h}_{k-1}]$  and the deflated channel matrix  $\mathbf{H}_{\setminus\{1:k-1\}} \stackrel{\text{def}}{=} [\mathbf{h}_k \ \mathbf{h}_{k+1} \ \cdots \ \mathbf{h}_{N_T}]$ , the blockwise inversion allows to decompose the matrix inversion part in eq. (8.36) as

$$\begin{aligned} \left[ \mathbf{H}^{(k)} \mathbf{H}^{(k)\dagger} + \frac{1}{\gamma_0} \underbrace{\begin{pmatrix} \mathbf{I}_{N_R} & & & \\ & 0 & & \\ & & \ddots & \\ & & & 0 \end{pmatrix}}_{k-1} \right]^{-1} &= \left( \begin{array}{c|c} \mathbf{H}\mathbf{H}^\dagger + \frac{1}{\gamma_0}\mathbf{I}_{N_R} & \mathbf{H}_{k-1} \\ \hline \mathbf{H}_{k-1}^\dagger & \mathbf{I}_{k-1} \end{array} \right)^{-1} \\ &= \left( \begin{array}{c|c} \mathbf{V}_k^{-1} & \mathbf{V}_k^{-1}\mathbf{H}_{k-1} \\ \hline -\mathbf{H}_{k-1}^\dagger\mathbf{V}_k^{-1} & \mathbf{1} + \mathbf{H}_{k-1}^\dagger\mathbf{V}_k^{-1}\mathbf{H}_{k-1} \end{array} \right), \end{aligned} \quad (8.37)$$

where  $\mathbf{V}_k$  is defined as  $\mathbf{V}_k \stackrel{\text{def}}{=} (\mathbf{H}_{\setminus\{1:k-1\}} \mathbf{H}_{\setminus\{1:k-1\}}^\dagger + \frac{1}{\gamma_0} \mathbf{I}_{N_R})$ . Then  $(\mathbf{W}_{\text{MMSE}}^{(k)})_k^T$  (i.e., the  $k$ -th column of  $\mathbf{W}_{\text{MMSE}}^{(k)}$  ( $k \geq 2$ )) is obtained by substituting eq. (8.37) into eq. (8.36) as

$$\begin{aligned} (\mathbf{W}_{\text{MMSE}}^{(k)})_k^T &= (\mathbf{h}_k^\dagger \mathbf{V}_k^{-1}, -\mathbf{h}_k^\dagger \mathbf{V}_k^{-1} \mathbf{H}_{k-1}) \\ &= (\mathbf{h}_k^\dagger \mathbf{V}_k^{-1}, -\mathbf{h}_k^\dagger \mathbf{V}_k^{-1} \mathbf{h}_1, -\mathbf{h}_k^\dagger \mathbf{V}_k^{-1} \mathbf{h}_2, \dots, -\mathbf{h}_k^\dagger \mathbf{V}_k^{-1} \mathbf{h}_{k-1}). \end{aligned} \quad (8.38)$$

The detection of the  $k$ -th stream with interference cancellation is explicitly written as

$$\hat{x}_k = (\mathbf{W}_{\text{MMSE}}^{(k)})_k^T \mathbf{y}^{(k)} = (\mathbf{h}_k^\dagger \mathbf{V}_k^{-1}, -\mathbf{h}_k^\dagger \mathbf{V}_k^{-1} \mathbf{h}_1, -\mathbf{h}_k^\dagger \mathbf{V}_k^{-1} \mathbf{h}_2, \dots, -\mathbf{h}_k^\dagger \mathbf{V}_k^{-1} \mathbf{h}_{k-1}) \begin{pmatrix} \mathbf{y} \\ \tilde{x}_1 \\ \tilde{x}_2 \\ \vdots \\ \tilde{x}_{k-1} \end{pmatrix} \quad (8.39)$$

The weight vector of  $-\mathbf{h}_k^\dagger \mathbf{V}_k^{-1} \mathbf{h}_p$  ( $p \in \{1, 2, \dots, k-1\}$ ) in eq. (8.39) is responsible for interference cancellation of the  $p$ -th signal stream.

At the last part of this subsection, the description of how to obtain the weight vector  $\left(\mathbf{W}_{\text{MMSE}}^{(k)}\right)_l^T$  should be provided. As we have seen above, the MIMO weight matrix is supposed to be designed based on MMSE criterion, which means that the stochastic gradient approach including LMS algorithm can be applied to obtain those vectors, which is critically different from C-SIC operation. In its approach, after defining the estimation error  $e_k(t)$  at time  $t$  for the  $k$ -th signal stream with the desired signal  $d_k(t)$  as

$$\begin{aligned} e_k(t) &= d_k(t) - \hat{x}_k(t) \\ &= d_k(t) - \left(\mathbf{W}_{\text{MMSE}}^{(k)}\right)_l^T \mathbf{y}^{(k)}(t), \end{aligned} \quad (8.40)$$

the LMS updating equation for  $\left(\mathbf{W}_{\text{MMSE}}^{(k)}\right)_l$  becomes

$$\begin{aligned} \left(\mathbf{W}_{\text{MMSE}}^{(k)}\right)_l^T(t+1) &= \left(\mathbf{W}_{\text{MMSE}}^{(k)}\right)_l^T(t) + \mu e_k(t) \mathbf{y}^{(k)*}(t) \\ &= \left(\mathbf{W}_{\text{MMSE}}^{(k)}\right)_l^T(t) + \mu e_k(t) \begin{pmatrix} \mathbf{y}(t) \\ \tilde{x}_1(t) \\ \tilde{x}_2(t) \\ \vdots \\ \tilde{x}_{k-1}(t) \end{pmatrix}^*. \end{aligned} \quad (8.41)$$

This property also provides the advantages that the channel estimation and the computation of the matrix inverse are avoided, which contributes to the complexity reduction. Another advantage that U-SIC provides is that typical phase synchronization algorithms can be easily implemented because of the adaptive filtering structure of U-SIC.

### 8.3.3 Experimental Setup

The proposed U-SIC method's performance was evaluated through 2-LP-mode FMF transmission experiments whose setup is illustrated in Fig. 8.20. A test channel at 1556.353 nm and 24 dummy channels located from 1551.520 to 1551.216 nm were respectively generated by a tunable external-cavity laser (ECL) with a 25-kHz linewidth and by DFB lasers with a 2-MHz linewidth. As FEC codes, LDPC code was applied with code rate of 4/5 as an inner code defined in DVB-S2 [78], and 7 %-OH hard-decision FEC code comprised of RS(1023, 1007) and BCH(2047, 1952) as an outer code defined in G.975.111 to the partial PRBS

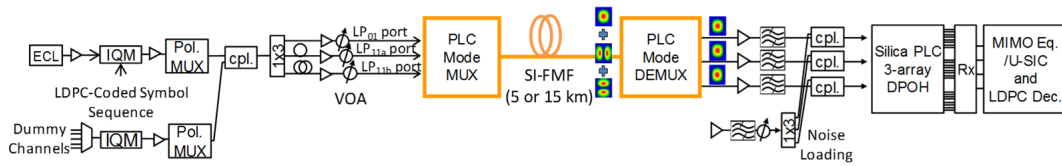


Fig. 8.20 Experimental setup.

patterns of length  $2^{23}-1$ , which was used for QPSK signal generation driven at 12 Gbaud. The modulated signals were fed into PDM emulators and then divided by a  $1 \times 3$  splitter to generate mode multiplexed signals. The transmission line consisted of a PLC-based mode MUX/DEMUX and a step-index (SI) FMF. The transmitted signals were mode demultiplexed and received by a coherent Rx module. The data stored in a digital storage oscilloscope were offline processed through a  $6 \times 6$  LMS-based adaptive linear MIMO equalizer, or through the proposed U-SIC detector in conjunction with frequency/phase recovery. The soft-decision error correction for LDPC code was performed to signals output from the above detectors by using the sum-product algorithm in the logarithm domain with 10 iterations. An MDL estimation in each configuration was also performed by using the least squares method described in Chapter 7.

### 8.3.4 Experimental Results

The experimental verification will start with OSNR performance evaluation in a back-to-back transmission where the estimated MDL (arisen from MUX/DEMUX) was 6.7 dB. Fig. 8.21 shows the obtained averaged BER over all six tributaries including polarization as a function of OSNR. Dotted and solid curves respectively correspond to BERs before and after LDPC decoding. Note that the BER curves before decoding are shown for reference purposes, although LDPC decoding was performed at each stage in the U-SIC scheme. The BER curve for linear MIMO equalizer begins to drop at OSNR of around 12 dB, while error-free results are obtained for U-SIC at the same OSNR. The resultant OSNR gain obtained with U-SIC was 4.5 dB at HD-FEC BER limit of  $2.26 \times 10^{-3}$ .

Then MDL was varied by changing the input power of the  $LP_{11a}$  and  $LP_{11b}$  ports before MUX to emulate various MDL values (Fig. 8.22). For every attenuation setting, the received

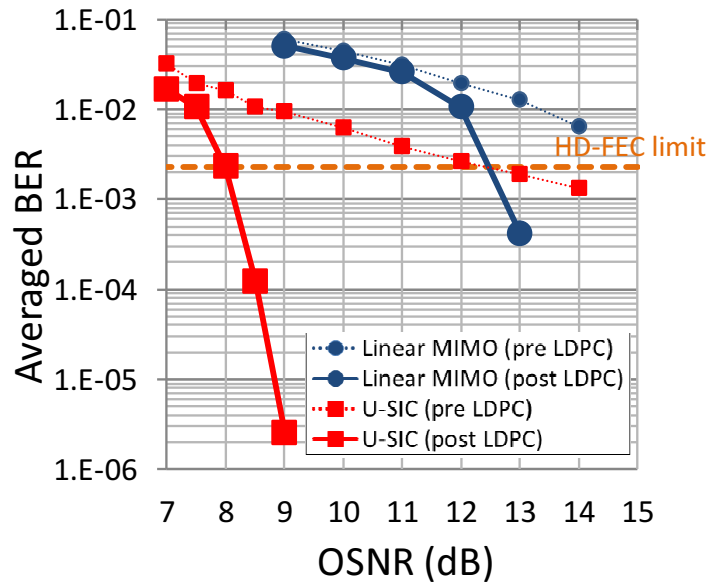


Fig. 8.21 Averaged BER obtained by linear MIMO equalizer/U-SIC before/after LDPC decoding as a function of OSNR.

OSNR of signals from  $LP_{11a}$  and  $LP_{11b}$  output ports was kept constant at 13 dB. BER dependence on MDL is shown in Fig. 8.23. U-SIC clearly outperforms the linear MIMO equalizer, and consequently improves MDL tolerance by 3.3 dB at the HD-FEC limit. The BER curve of U-SIC represents the steeper waterfall property when compared with that of the linear MIMO equalizer, because the former approaches the FEC limit of LDPC code in a larger MDL region.

Next the mode-multiplexed signals was transmitted over SI-FMF supporting 2-LP modes to investigate U-SIC performance under a channel with memory. One of two SI-FMF spools with 5 or 15 km length and with a 2.6-ns/km DMD parameter was used for evaluation. It was found that the MDL increase incurred by inserting the SI-FMF was negligible. Signal constellations are compared in Fig. 8.25 that were detected using a linear MIMO equalization (top) or using the U-SIC scheme (bottom) after 15-km FMF transmission at OSNR of 9 dB. The figure shows that the inter-modal crosstalk for the higher-order mode signals (especially for  $LP_{11a}$ ) was significantly removed by the use of the U-SIC detection. Fig. 8.24 displays required OSNR for achieving the HD-FEC limit under several DMD values. The figure indicates that OSNR gain around 4.5 to 4.9 dB was consistently obtained by employing U-

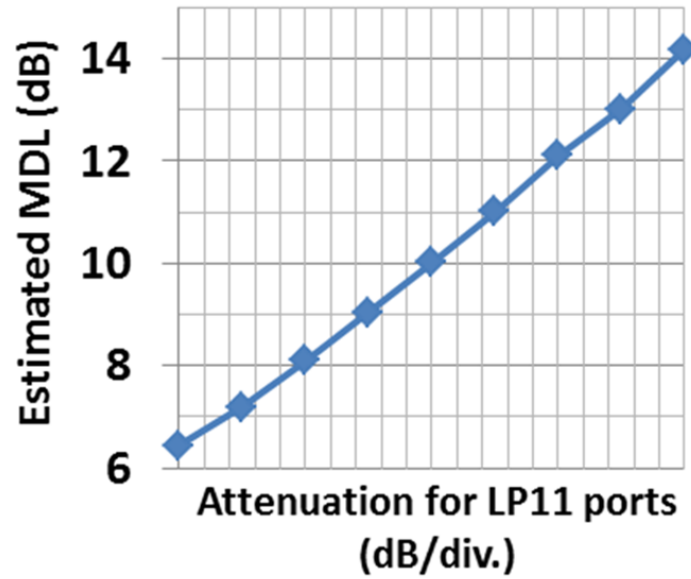


Fig. 8.22 MDL emulation by changing the input power into LP<sub>11</sub> ports.

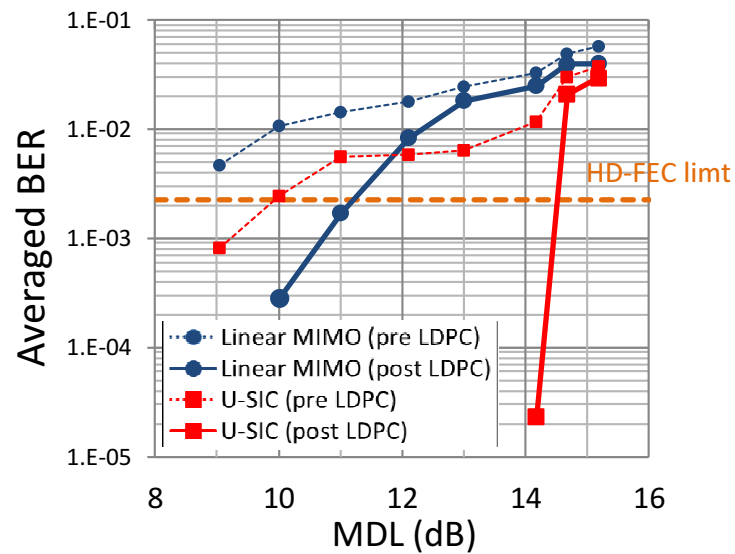


Fig. 8.23 Averaged BER obtained by linear MIMO equalizer/U-SIC before/after LDPC decoding as a function of MDL

SIC even under large DMD of 39 ns, with which the feasibility of U-SIC under a channel with memory is confirmed.



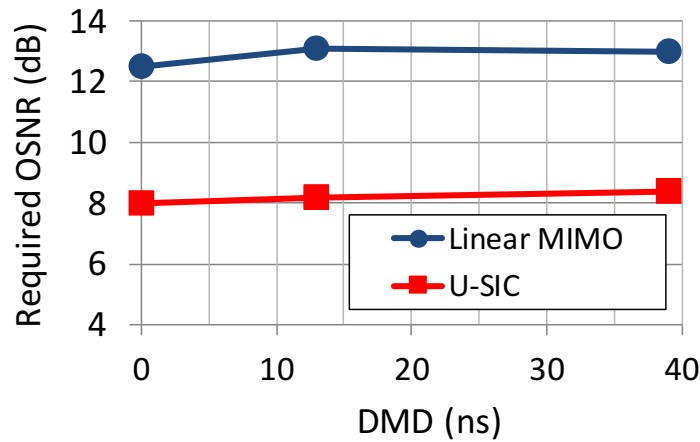


Fig. 8.24 Required OSNR to achieve HD-FEC limit BER under FMF links with various DMD values.

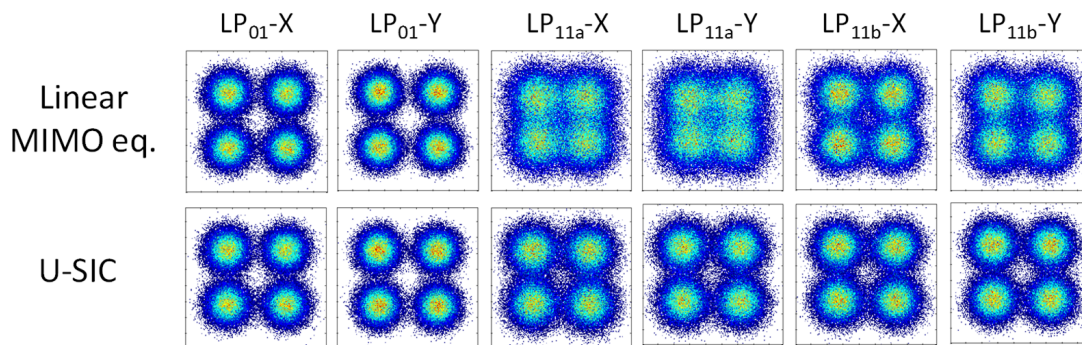


Fig. 8.25 Signal constellations detected using a linear MIMO equalization (top) or using the U-SIC scheme (bottom) after transmission over 15-km FMF at OSNR of 9 dB.

### 8.3.5 Summary

A novel scheme that effectively removes MDL-induced intermodal interferences is proposed. Compared with the conventional SIC approach, the proposed U-SIC can be applied to signals transmitted over a dispersive channel without channel estimation by skipping replica signal generation steps. Conducted experiment results showed that the proposed U-SIC scheme outperforms the widely-used linear MIMO equalizer scheme and provides MDL tolerance improvement of 3.3 dB and OSNR gain of > 4.5 dB even under large DMD as large

as 39 ns.

## Chapter 9

# Conclusions

It is indisputable that fiber-optic communication networks are crucially required to sustain and develop the today's information society. Meanwhile, we might eventually reach a capacity limit of SMF-based optical networks, if some effective breakthrough strategies were not taken as a means of replacing existing SMF-based optical networks. This thesis has discussed remaining challenges towards optical communication systems handling Pbit/s capacity, and also proposed some novel schemes based on statistical and signal processing approaches. As concluding remarks of the entire thesis, Chapter 9 briefly summarizes some key points obtained in each chapter, and also provides future perspectives.

### 9.1 Spectrally-Efficient SMF-based Transmission Systems

Information theory indicates that the maximal information rate over arbitrary information-carrying channel at each frequency increases logarithmically with SNR. Owing to the great progress and success of WDM transmission technologies in the mid-1990s that exploits the frequency-domain multiplexing, the system capacity of fiber-optic networks had been increased up to a few Tb/s in 2007. At the same time the optical power density in fiber had been enhanced in accordance with the increase optical channel count, which induces fiber nonlinearities (also called the optical Kerr effect). In the nonlinear transmission regime, the theoretical capacity limit of a fiber behaves non-monotonically with SNR increase, known as the nonlinear Shannon limit.

Suppose the practical physical parameters of a regular SMF (e.g., available wavelength range for EDFA), dispersion and nonlinear coefficients, achievable capacity might be around 100 Tb/s at most. In the 2010s, digital coherent systems have contributed to approaching

the above limit by employing advanced signal processing techniques that removes signal distortions arisen from linear (e.g., CD and PMD) and nonlinear (e.g., SPM) impairments. Indeed, current system capacity has increased up to 19 Tb/s per optical fiber by employing optical signals with the line rate of 400 Gb/s. From a standpoint of market maturity, it is desirable to exploit the rest of SMF “capacity resource”. There exists at least two approaches for it, namely, the developments of signal processing robust against fiber/system impairments (Chapter 3 through Chapter 5), and enhancing the spectral efficiency (Chapter 6).

Chapter 3 has proposed to apply  $n$ -WI transmission for PDL-impaired transmission links. When it comes to system design of optical link, PDL should be carefully taken into account because it has statistical property of time-varying frequency selectivity.  $n$ -WI transmission is beneficial in mitigating PDL-induced outage probability by utilizing the multiple optical channels located larger than correlation wavelength of PDL. Performance averaging effects brought by  $n$ -WI transmission was verified both through transmission experiments and numerical simulations. Moreover, subjecting experimental data to EVS analysis revealed that  $n$ -WI transmission enabled the outage probability to be decreased from  $10^{-3}$  to  $10^{-6}$ , or the  $Q$ -limit to be mitigated by 0.5 dB even in  $n = 2$  case. On the basis of the central limit theorem, further increased channel number of  $n$ -WI transmission is expected to bring better benefit to PDL-impaired link systems.

Chapter 4 has proposed a novel technique which improves the robustness against multiple filtering in a cascaded ROADMs networks. This technique can be understood as an MIMO signal processing among super-channel’s SCs. A single data stream is uniformly distributed over all SCs in the transmitter by an orthogonal transformation, and recovered in the receiver by an linear MIMO equalization. This enables a transmission performance of a super-channel to be improved, since signal degradation occurring in particular SCs due to, say, multiple filtering in cascaded WSSs, is interspersed over all SCs. As another advantage of the scheme, it was demonstrated that the number of cascaded WSSs was increased by 5 to 8 in a super-channel transmission comprising four QPSK-SCs, or 4 to 5 in that comprising two 16QAM-SCs.

Chapter 5 combats with the fiber nonlinearity on the basis of digital and optical methods. The evolution of the optical signal envelope is described by the nonlinear Schrödinger equation. Intrigued by this fact, DBP algorithm has been developed to compensate for intra-

channel nonlinear distortions by propagating signal inversely over a virtual transmission link in the digital domain at the receiver. As a means of optical mitigation of inter-channel non-linearity, XPM-suppressor has been used in DM systems which introduces deliberate skews among optical channels. To clarify the combined effects of these digital and optical for fiber nonlinearities, a numerical simulation was conducted in which optical signals were transmitted over DM and NDM systems, which led two results described below.

- Introducing XPM-suppressor in DM link systems improves the DBP performance, because signal waveform of the channel of interest with higher accuracy is obtained due to suppression of inter-channel nonlinearity in an optical link.
- The number of DBP iteration stages in DM systems can be reduced due to the periodic CD profile.

Furthermore, a novel algorithm is proposed to remove XPM-induced polarization crosstalk based on ICA approach, called overlapped-FastICA. The proposed overlapped-FastICA is beneficial to track the fast temporal variation of the polarization-mixing matrix induced by XPM. It was demonstrated numerically that the performance of the method outperformed conventional NPCC method. Due to the significant feature of ICA that solves BSS problems only by the statistical independence of the sources, it was shown that overlapped-FastICA works for NPC removal for any signals with different modulation formats, and that the DBP performance was improved by applying overlapped-FastICA in the step prior to DBP.

As alternative approach against fiber/system impairments mitigation, Chapter 6 aims to increase spectral efficiency by a super-Nyquist transmission based on the M-SIC scheme with and without the FEC coding technique. Multi-carrier transmission with multiple SCs allocated with almost symbol-rate spacing, also called Nyquist WDM, is promising to support signal bit rate beyond 100 Gb/s. Super-Nyquist transmission which packs SCs tightly with narrower than symbol-rate spacing has potential to bring further spectral efficiency improvement. M-SIC scheme removes inter-carrier interferences in an iterative manner by reconstructing adjacent SCs' waveform and subtracting them with the prior knowledge about parameters of adjacent SCs. The M-SIC performance was investigated numerically and experimentally, and revealed that it enabled 20 % carrier spacing suppression for QPSK signals. The dual-SC transmission with the combined use of the M-SIC and FEC coding for ICI mit-

igation was also proposed for further system performance improvement, called CST. The error-correction ability of FEC scheme was devoted to the ICI-free replica construction in the M-SIC scheme, hence the performance of CST outperformed the conventional dual-SC transmission with no signal overlap in terms of both SE and  $Q$ -factor.

Future work on SMF-based transmission systems investigated in Chapter 3 through Chapter 6 is expected as follows. Chapter 3 and Chapter 4 both have considered a frequency diversity approach for optical signal transmissions under optical frequency-dependent channels. In these chapters, a transmitter employed the frequency-diversity approach which distributed bit information (Chapter 3) or symbol's power (Chapter 4) equally over carriers located at different frequency. Obviously, outermost carriers located at the edge of a super-channel are more severely exposed to optical filtering, especially in a cascaded ROADMs described in Chapter 4. Taking such prior-knowledge into consideration, more sophisticated transmission strategy with *inequality* regarding assignment of modulation order, power loading based on the water filling theorem, and symbol rate optimization for each carrier should be explored. The SE-enhancing M-SIC schemes investigated proposed in Chapter 6 is applicable independent on signal modulation order. Therefore, M-SIC performance for signals with higher-order modulation order needs to be further clarified.

## 9.2 SDM Transmission Systems Scaling Beyond 100 Tb/s

As stated in Chapter 1 and above, the SMF-based system capacity beyond a few hundreds of Tb/s is not permitted physically and theoretically. Nevertheless, the demand to transport more enormous amount of traffic has been increasing exponentially. Therefore innovative and pioneering research on transmission technologies over a novel waveguide medium is required to overcome upcoming capacity crunch. SDM transmission technologies that exploits spatial degrees of freedom in an optical fiber is the prime candidate to achieve greater capacity in fiber-optic systems. Indeed, several transmission demonstrations of Pb/s-class capacity have been performed in the past few years [18–21]. Currently, however, there still exists some remaining challenges both in SDM signal transmission and in development/standardization of SDM devices to make further steps towards future practical application of SDM systems.

Chapter 7 has reviewed recent progress in SDM transmission and also discussed remain-

ing issues to be addressed from signal processing perspective. Aside from increasing system capacity, extending transmission reach is another important challenge in SDM transmission systems. Uncoupled MCF transmission in which signals propagate in independent core with negligible interference is relatively manageable, and a lot of well-established devices and technologies developed in SMF transmission are applicable. On the contrary, extending MIMO-SDM transmission reach in which intermodal coupling occur is severely restricted by inherent physical phenomena observed especially in MMF/FMF, including DMD and MDL. MIMO signal processing may reduce or mitigate the impact of DMD and MDL. Unlike PMD in SMF transmission typically ranging sub-ps per  $\sqrt{\text{km}}$ , DMD order ranges from several tens to hundreds ps/km. Hence it requires larger number of DMD equalizer taps to compensate for, which increases the computational complexity in MIMO signal processing. MDL exhibits non-unitary channel property and directly impacts on achievable MMF system capacity. Advanced MIMO signal processing instead of conventional widely-used linear MIMO equalization may offer solutions against MDL, though some inherent technical difficulties involved in applying them need to be addressed.

Chapter 8 has proposed three novel MIMO signal processing schemes that address issues discussed in Chapter 7. The first one is parallel MIMO transmission with FDE to reduce computational complexity for DMD compensation. Compared with conventional single-carrier TDE, complexity reduction for 33.2-ns DMD compensation is achieved by a factor of 33. Furthermore, the world's first demonstration of long-haul DSMD transmission of 527-km with spatial multiplicity of 36, the highest yet reported, was performed by employing proposed parallel MIMO FDE, ring-core FM EDFA, and free-space optics MDL equalizers. Second is space-time coding scheme that intersperses the data stream both spatially and temporally by using orthogonal transformation. It was found experimentally that the scheme substantially improves MDL tolerance, thus enabling transmission reach to be increased by 20 %. The last is a sequential signal detection technique called unreplicated SIC (U-SIC) that significantly removes intermodal interferences under an MDL-impaired link. The advantage of U-SIC is that it can be applied to dispersive channel without channel estimation by modifying conventional SIC scheme. Experimental evaluation revealed that it provides MDL-tolerance improvement of 3.3 dB and OSNR gain of  $> 4.5$  dB even under 39ns-DMD FMF link.

Future work on SDM transmission systems investigated in Chapter 7 through Chapter 8 is expected as follows.

- Advanced MIMO detection architecture in which a detector and a decoder in each detection stage are used jointly with a cooperative structure needs to be developed, because the signal processing of decoding, nulling, and canceling was performed only in a sequential manner in the proposed U-SIC scheme.
- Further research on fiber nonlinearity effects in SDM fibers should be explored, which was neglected throughout Chapter 7 and Chapter 8.
- An optical MIMO-SDM transmission scheme enhancing transmission reliability rather than system throughput needs to be investigated. While it is well known that in MIMO systems fundamental trade-off between diversity and multiplexing generally exists [143], most optical MIMO-SDM transmission experiments have concentrated only on *fully-loaded* increasing total system capacity.



# Bibliography

- [1] Cisco Visual Networking Index, “Forecast and methodology, 2014–2019 white paper,” *Technical Report, Cisco, Tech. Rep.*, 2015.
- [2] Cisco Global Cloud Index, “Forecast and methodology, 2015–2020 white paper,” *Technical Report, Cisco, Tech. Rep.*, 2016.
- [3] K. Kao and G. A. Hockham, “Dielectric-fibre surface waveguides for optical frequencies,” in *Proceedings of the Institution of Electrical Engineers*, vol. 113, pp. 1151–1158, July 1966.
- [4] I. Hayashi, M. Panish, P. Foy, and S. Sumski, “Junction lasers which operate continuously at room temperature,” *Applied Physics Letters*, vol. 17, no. 3, pp. 109–111, Aug. 1970.
- [5] Z. I. Alferov, V. Andreev, E. Portnoi, and M. Trukan, “AlAs-GaAs heterojunction injection lasers with a low room-temperature threshold,” *Soviet Physics Semiconductors*, vol. 3, no. 9, pp. 1107–1110, Mar. 1970.
- [6] F. Kapron, D. Keck, and R. Maurer, “Radiation losses in glass optical waveguides,” *Applied Physics Letters*, vol. 17, no. 10, pp. 423–425, Nov. 1970.
- [7] C. E. Shannon, “A mathematical theory of communication,” *The Bell System Technical Journal*, vol. 27, pp. 623–656, Oct. 1948.
- [8] P. P. Mitra and J. B. Stark, “Nonlinear limits to the information capacity of optical fibre communications,” *Nature*, vol. 411, no. 6841, pp. 1027–1030, June 2001.
- [9] Y. Yu, Y. Lu, L. Liu, yuanda huang, X. Wang, and liangchuan li, “Experimental demonstration of single carrier 400G/500G in 50-GHz grid for 1000-km transmission,” in *40th Optical Fiber Communications Conference and Exhibition (OFC 2017)*, Tu2E.4, Los Angeles, CA, USA, Mar. 2017.
- [10] T. Morioka, “New generation optical infrastructure technologies: ‘EXAT initiative’ towards 2020 and beyond,” in *14th OptoElectronics and Communications Conference*

- (*OECC 2009*), FT4, Hong Kong, China, July 2009.
- [11] P. J. Winzer, “Spatial multiplexing: The next frontier in network capacity scaling,” in *39th European Conference and Exhibition on Optical Communication (ECOC 2013)*, We.1.D.1, London, UK, Sept. 2013.
- [12] R. Kashyap and K. J. Blow, “Observation of catastrophic self-propelled self-focusing in optical fibres,” *Electronics Letters*, vol. 24, no. 1, pp. 47–49, Jan. 1988.
- [13] Y. Sasaki, K. Takenaga, K. Aikawa, Y. Miyamoto, and T. Morioka, “Single-mode 37-core fiber with a cladding diameter of 248  $\mu\text{m}$ ,” in *40th Optical Fiber Communications Conference and Exhibition (OFC 2017)*, Th1H.2, Los Angeles, CA, USA, Mar. 2017.
- [14] N. K. Fontaine, R. Ryf, H. Chen, A. V. Benitez, J. E. A. Lopez, R. A. Correa, B. Guan, B. Ercan, R. P. Scott, S. J. B. Yoo, L. Grüner-Nielsen, Y. Sun, and R. J. Lingle, “30  $\times$  30 MIMO transmission over 15 spatial modes,” in *38th Optical Fiber Communications Conference and Exhibition (OFC 2015)*, Th5C.1, Los Angeles, CA, USA, Mar. 2015.
- [15] J. Sakaguchi, W. Klaus, J. M. D. Mendinueta, B. J. Puttnam, R. S. Luis, Y. Awaji, N. Wada, T. Hayashi, T. Nakanishi, T. Watanabe, Y. Kokubun, T. Takahata, and T. Kobayashi, “Realizing a 36-core, 3-mode fiber with 108 spatial channels,” in *38th Optical Fiber Communications Conference and Exhibition (OFC 2015)*, Th5C.2, Los Angeles, CA, USA, Mar. 2015.
- [16] K. Igarashi, D. Souma, Y. Wakayama, K. Takeshima, Y. Kawaguchi, T. Tsuritani, I. Morita, and M. Suzuki, “114 space-division-multiplexed transmission over 9.8-km weakly-coupled-6-mode uncoupled-19-core fibers,” in *38th Optical Fiber Communications Conference and Exhibition (OFC 2015)*, Th5C.4, Los Angeles, CA, USA, Mar. 2015.
- [17] T. Sakamoto, T. Matsui, K. Saitoh, S. Saitoh, K. Takenaga, T. Mizuno, Y. Abe, K. Shibahara, Y. Tobita, S. Matsuo, K. Aikawa, S. Aozasa, K. Nakajima, and Y. Miyamoto, “Low-loss and low-DMD few-mode multi-core fiber with highest core multiplicity factor,” in *39th Optical Fiber Communications Conference and Exhibition (OFC 2016)*, Th5A.2, Anaheim, CA, USA, Mar. 2016.
- [18] H. Takara, A. Sano, T. Kobayashi, H. Kubota, H. Kawakami, A. Matsuura, Y. Miyamoto, Y. Abe, H. Ono, K. Shikama, Y. Goto, K. Tsujikawa, Y. Sasaki, I. Ishida, K. Takenaga, S. Matsuo, K. Saitoh, M. Koshiba, and T. Morioka, “1.01-Pb/s (12

- SDM/222 WDM/456 Gb/s) crosstalk-managed transmission with 91.4-b/s/Hz aggregate spectral efficiency,” in *38th European Conference and Exhibition on Optical Communication (ECOC 2012)*, Th.3.C.1, Amsterdam, Netherlands, Sept. 2012.
- [19] B. J. Puttnam, R. S. Luis, W. Klaus, J. Sakaguchi, J. M. D. Mendinueta, Y. Awaji, N. Wada, Y. Tamura, T. Hayashi, M. Hirano, and J. Marciante, “2.15 Pb/s transmission using a 22 core homogeneous single-mode multi-core fiber and wideband optical comb,” in *41st European Conference on Optical Communication (ECOC 2015)*, PDP.3.1, Valencia, Spain, Sept. 2015.
- [20] D. Soma, K. Igarashi, Y. Wakayama, K. Takeshima, Y. Kawaguchi, N. Yoshikane, T. Tsuritani, I. Morita, and M. Suzuki, “2.05 Peta-bit/s super-nyquist-WDM SDM transmission using 9.8-km 6-mode 19-core fiber in full C band,” in *41st European Conference on Optical Communication (ECOC 2015)*, PDP.3.2, Valencia, Spain, Sept. 2015.
- [21] T. Kobayashi, M. Nakamura, F. Hamaoka, K. Shibahara, T. Mizuno, A. Sano, H. Kawakami, A. Isoda, M. Nagatani, H. Yamazaki, Y. Miyamoto, Y. Amma, Y. Sasaki, K. Takenaga, K. Aikawa, K. Saitoh, Y. Jung, D. J. Richardson, K. Pulverer, M. Bohn, M. Nooruzzaman, and T. Morioka, “1-Pb/s (32 SDM/46 WDM/768 Gb/s) C-band dense SDM transmission over 205.6-km of single-mode heterogeneous multi-core fiber using 96-Gbaud PDM-16QAM channels,” in *40th Optical Fiber Communications Conference and Exhibition (OFC 2017)*, Th5B.1, Los Angeles, CA, USA, Mar. 2017.
- [22] G. P. Agrawal, *Nonlinear fiber optics*. Academic press, 2007.
- [23] E. Ip and J. M. Kahn, “Compensation of dispersion and nonlinear impairments using digital backpropagation,” *Journal of Lightwave Technology*, vol. 26, no. 20, pp. 3416–3425, Oct. 2008.
- [24] X. Li, X. Chen, G. Goldfarb, E. Mateo, I. Kim, F. Yaman, and G. Li, “Electronic post-compensation of WDM transmission impairments using coherent detection and digital signal processing,” *Optics Express*, vol. 16, no. 2, pp. 880–888, Jan. 2008.
- [25] A. Goldsmith, *Wireless communications*. Cambridge University Press, 2005.
- [26] S. S. Haykin, *Adaptive filter theory*. Pearson Education India, 2008.
- [27] A. Viterbi, “Nonlinear estimation of PSK-modulated carrier phase with application to

- burst digital transmission,” *IEEE Transactions on Information Theory*, vol. 29, no. 4, pp. 543–551, July 1983.
- [28] D. Godard, “Self-recovering equalization and carrier tracking in two-dimensional data communication systems,” *IEEE transactions on communications*, vol. 28, no. 11, pp. 1867–1875, Nov. 1980.
- [29] M. Shtaif, “Performance degradation in coherent polarization multiplexed systems as a result of polarization dependent loss,” *Optics Express*, vol. 16, no. 18, pp. 13918–13932, Aug. 2008.
- [30] B. Xie, Y. L. Guan, Z. Li, and C. Lu, “FEC performance of optical communication systems with PMD and wavelength interleaving,” in *International Conference on Communications, Circuits and Systems*, vol. 1, pp. 665–669, Chengdu, China, June 2004.
- [31] S. Hadjifaradji, S. Yang, L. Chen, and X. Bao, “PMD-PDL emulator designs for low interchannel correlation,” *IEEE Photonics Technology Letters*, vol. 18, no. 22, pp. 2362–2364, Oct. 2006.
- [32] S. Savory, F. Payne, and A. Hadjifotiou, “Estimating outages due to polarization mode dispersion using extreme value statistics,” *Journal of Lightwave Technology*, vol. 24, no. 11, pp. 3907–3913, Nov. 2006.
- [33] R.-D. Reiss, M. Thomas, and R. Reiss, *Statistical analysis of extreme values*, vol. 2. Springer, 2007.
- [34] S. Gringeri, B. Basch, V. Shukla, R. Egorov, and T. J. Xia, “Flexible architectures for optical transport nodes and networks,” *IEEE Communications Magazine*, vol. 48, no. 7, pp. 40–50, Aug. 2010.
- [35] Y. Aoki, X. Wang, P. Palacharla, K. Sone, S. Oda, T. Hoshida, M. Sekiya, and J. C. Rasmussen, “Dynamic and flexible photonic node architecture with shared universal transceivers supporting hitless defragmentation,” in *38th European Conference and Exhibition on Optical Communications (ECOC 2012)*, We.3.D.2, Amsterdam, Netherlands, Sept. 2012.
- [36] S. Yamanaka, T. Kobayashi, A. Sano, A. Matsuura, Y. Miyamoto, M. Nagatani, and H. Nosaka, “Nyquist-WDM transmission of  $7 \times 192$  Gb/s PDM 16-QAM signals using high-speed DACs operating at 42 GS/s,” in *SPIE OPTO*, vol. 8646, pp. 864600–864600–7, San Francisco, CA, USA, Dec. 2012.

- [37] Y. X. Zhou and M. Huang, "8 × 114 Gbit/s, 25 GHz-spaced, PolMux-RZ-8QAM straight-line transmission over 800 km of SSMF," in *40th European Conference on Optical Communication (ECOC 2014)*, P.4.02, Cannes, France, Sept. 2014.
- [38] A. Carena, V. Curri, P. Poggiolini, G. Bosco, and F. Forghieri, "Maximum reach versus transmission capacity for terabit superchannels based on 27.75-GBaud PM-QPSK, PM-8QAM, or PM-16QAM," *IEEE Photonics Technology Letters*, vol. 22, no. 11, pp. 829–831, Mar. 2010.
- [39] G. Bosco, V. Curri, A. Carena, P. Poggiolini, and F. Forghieri, "On the performance of Nyquist-WDM terabit superchannels based on PM-BPSK, PM-QPSK, PM-8QAM or PM-16QAM subcarriers," *Journal of Lightwave Technology*, vol. 29, no. 1, pp. 53–61, Nov. 2011.
- [40] J. Rahn, S. Kumar, M. Mitchell, R. Malendevich, H. Sun, K. T. Wu, P. Mertz, K. Crousore, H. Wang, M. Kato, V. Lal, P. Evans, D. Lambert, H. S. Tsai, P. Samra, B. Taylor, A. Nilsson, S. Grubb, R. Nagarajan, F. Kish, and D. Welch, "250Gb/s real-time PIC-based super-channel transmission over a gridless 6000km terrestrial link," in *35th Optical Fiber Communications Conference and Exhibition (OFC 2012)*, PDP5D.5, Los Angeles, CA, USA, Mar, 2012.
- [41] T. J. Xia, G. A. Wellbrock, Y. K. Huang, E. Ip, M. F. Huang, Y. Shao, T. Wang, Y. Aono, T. Tajima, S. Murakami, and M. Cvijetic, "Field experiment with mixed line-rate transmission (112-Gb/s, 450-Gb/s, and 1.15-Tb/s) over 3,560 km of installed fiber using filterless coherent receiver and EDFAs only," in *34th Optical Fiber Communications Conference and Exhibition (OFC 2011)*, PDP.A.3, Los Angeles, CA, USA, Mar. 2011.
- [42] F. Buchali, K. Schuh, D. Roesener, E. Lach, R. Dischler, W. Idler, L. Schmalen, A. Leven, R.-P. Braun, A. Ehrhardt, C. Gerlach, and L. Schuerer, "512-Gb/s DP-16-QAM field trial over 734 km installed SSMF with co-propagating 10 Gb/s NRZ neighbors incorporating soft-FEC decoding," in *35th Optical Fiber Communication Conference (OFC 2012)*, OW4C.4, Los Angeles, CA, USA, Mar. 2012.
- [43] E. Torrenco, R. Cigliutti, G. Bosco, G. Gavioli, A. Alaimo, A. Carena, V. Curri, F. Forghieri, S. Piciaccia, M. Belmonte, A. Brinciotti, A. L. Porta, S. Abrate, and P. Poggiolini, "Transoceanic PM-QPSK terabit superchannel transmission experiments

- at baud-rate subcarrier spacing,” in *36th European Conference and Exhibition on Optical Communication (ECOC 2010)*, We.7.C.2, Torino, Italy, Sept. 2010.
- [44] Y. K. Huang, D. Qian, F. Yaman, T. Wang, E. Mateo, T. Inoue, Y. Inada, Y. Toyoda, T. Ogata, M. Sato, Y. Aono, and T. Tajima, “Real-time 400G superchannel transmission using 100-GbE based 37.5-GHz spaced subcarriers with optical Nyquist shaping over 3,600-km DMF link,” in *36th Optical Fiber Communications Conference and Exhibition (OFC 2013)*, NW4E.1, Anaheim, CA, USA, Mar. 2013.
- [45] F. Heismann, “System requirements for WSS filter shape in cascaded ROADMs networks,” in *33rd Optical Fiber Communications Conference and Exhibition (OFC 2010)*, OThR1, San Diego, CA, USA, Mar. 2010.
- [46] Y. Sakamaki, T. Kawai, T. Komukai, M. Fukutoku, and T. Kataoka, “Evaluation of optical filtering penalty in digital coherent detection system,” *IEICE Communications Express*, vol. 1, no. 2, pp. 54–59, July 2012.
- [47] S. Mumtaz, G. R.-B. Othman, and Y. Jaouën, “PDL mitigation in PolMux OFDM systems using golden and silver polarization-time codes,” in *33rd Optical Fiber Communications Conference and Exhibition (OFC 2010)*, JThA7, San Diego, CA, USA, Mar. 2010.
- [48] S. Mumtaz, G.-B. Othman, and Y. Jaouen, “Space-time codes for optical fiber communication with polarization multiplexing,” in *2010 IEEE International Conference on Communications*, pp. 1–5, Cape Town, South Africa, May 2010.
- [49] E. Meron, A. Andrusier, M. Feder, and M. Shtaif, “Use of space-time coding in coherent polarization-multiplexed systems suffering from polarization-dependent loss,” *Optics Letters*, vol. 35, no. 21, pp. 3547–3549, Nov. 2010.
- [50] A. Andrusier, E. Meron, M. Feder, and M. Shtaif, “Optical implementation of a space-time-trellis code for enhancing the tolerance of systems to polarization-dependent loss,” *Optics Letters*, vol. 38, no. 2, pp. 118–120, Jan. 2013.
- [51] E. N. Onggosanusi, A. G. Dabak, T. Schmidl, and T. Muharemovic, “Capacity analysis of frequency-selective MIMO channels with sub-optimal detectors,” in *2002 IEEE International Conference on Acoustics, Speech, and Signal Processing*, vol. 3, pp. III–2369–III–2372, Orlando, FL, USA, May 2002.
- [52] P. vanRooyen and F. Solms, “Maximum entropy investigation of the inter user interfer-

- ence distribution in a DS/SSMA system,” in *6th International Symposium on Personal, Indoor and Mobile Radio Communications*, vol. 3, p. 1308, Toronto, Ont., Canada,, Sept. 1995.
- [53] R. Kudo, T. Kobayashi, K. Ishihara, Y. Takatori, A. Sano, and Y. Miyamoto, “Coherent optical single carrier transmission using overlap frequency domain equalization for long-haul optical systems,” *Journal of Lightwave Technology*, vol. 27, no. 16, pp. 3721–3728, Aug. 2009.
- [54] K. Shibahara and K. Yonenaga, “Experimental demonstration of PDL penalty reduction by wavelength-interleaving transmission,” *Optics Express*, vol. 20, no. 26, pp. B479–B484, Dec. 2012.
- [55] M. Shahmohammadi and M. H. Kahaei, “A new dual-mode approach to blind equalization of QAM signals,” in *8th IEEE Symposium on Computers and Communications (ISCC 2003)*, pp. 277–281, Kemer-Antalya, Turkey, Sept. 2003.
- [56] P. J. Winzer and R.-J. Essiambre, “Advanced optical modulation formats,” *Proceedings of the IEEE*, vol. 94, no. 5, pp. 952–985, May 2006.
- [57] S. J. Savory, “Digital coherent optical receivers: Algorithms and subsystems,” *IEEE Journal of Selected Topics in Quantum Electronics*, vol. 16, no. 5, pp. 1164–1179, May 2010.
- [58] T. Kobayashi, A. Sano, A. Matsuura, M. Yoshida, T. Sakano, H. Kubota, Y. Miyamoto, K. Ishihara, M. Mizoguchi, and M. Nagatani, “45.2 Tb/s C-band WDM transmission over 240km using 538Gb/s PDM-64QAM single carrier FDM signal with digital pilot tone,” in *37th European Conference and Exhibition on Optical Communication (ECOC 2011)*, Th.13.C.6, Geneva, Switzerland, Sept. 2011.
- [59] C. Xie, “Suppression of inter-channel nonlinearities in WDM coherent PDM-QPSK systems using periodic-group-delay dispersion compensators,” in *35th European Conference and Exhibition on Optical Communication (ECOC 2009)*, P.4.08, Vienna, Austria, Sept. 2009.
- [60] D. Sperti, P. Serena, and A. Bononi, “A comparison of different options to improve PDM-QPSK resilience against cross-channel nonlinearities,” in *36th European Conference and Exhibition on Optical Communication (ECOC 2010)*, Th.9.A.1, Torino, Italy, Sept. 2010.

- [61] S. Oda, T. Tanimura, T. Hoshida, C. Ohshima, H. Nakashima, Z. Tao, and J. C. Rasmussen, "112 Gb/s DP-QPSK transmission using a novel nonlinear compensator in digital coherent receiver," in *32nd Optical Fiber Communications Conference and Exhibition (OFC 2009)*, OThR6, San Diego, CA, USA, Mar. 2009.
- [62] C. R. Menyuk and B. S. Marks, "Interaction of polarization mode dispersion and nonlinearity in optical fiber transmission systems," *Journal of Lightwave Technology*, vol. 24, no. 7, pp. 2806–2826, July 2006.
- [63] M. Winter, D. Kroushkov, and K. Petermann, "Polarization-multiplexed transmission system outage due to nonlinearity-induced depolarization," in *36th European Conference and Exhibition on Optical Communication (ECOC 2010)*, Th.10.E.3, Torino, Italy, Sept. 2010.
- [64] Z. Tao, W. Yan, L. Liu, L. Li, S. Oda, T. Hoshida, and J. C. Rasmussen, "Simple fiber model for determination of XPM effects," *Journal of Lightwave Technology*, vol. 29, no. 7, pp. 974–986, Feb. 2011.
- [65] L. Li, Z. Tao, L. Liu, W. Yan, S. Oda, T. Hoshida, and J. C. Rasmussen, "Nonlinear polarization crosstalk canceller for dual-polarization digital coherent receivers," in *33rd Optical Fiber Communications Conference and Exhibition (OFC 2010)*, OWE3, San Diego, CA, Mar. 2010.
- [66] P. Serena, A. Ghazisaeidi, and A. Bononi, "A new fast and blind cross-polarization modulation digital compensator," in *38th European Conference and Exhibition on Optical Communication (ECOC 2012)*, We.1.A.5, Amsterdam, Netherlands, Sept. 2012.
- [67] H. Zhang, Z. Tao, L. Liu, S. Oda, T. Hoshida, and J. Rasmussen, "Polarization demultiplexing based on independent component analysis in optical coherent receivers," in *34th European Conference on Optical Communication (ECOC 2008)*, Mo.3.D.5, Brussels, Belgium, Sept. 2008.
- [68] P. Johannisson, H. Wymeersch, M. Sjödin, A. S. Tan, E. Agrell, P. A. Andrekson, and M. Karlsson, "Convergence comparison of the CMA and ICA for blind polarization demultiplexing," *Journal of Optical Communications and Networking*, vol. 3, no. 6, pp. 493–501, May 2011.
- [69] A. Nafta, P. Johannisson, and M. Shtaif, "Blind equalization in optical communications using independent component analysis," *Journal of Lightwave Technology*, vol. 31,



- no. 12, pp. 2043–2049, May 2013.
- [70] E. Bingham and A. Hyvärinen, “A fast fixed-point algorithm for independent component analysis of complex valued signals,” *International Journal of Neural Systems*, vol. 10, no. 1, pp. 1–8, Feb. 2000.
- [71] K. Igarashi, T. Tsuritani, I. Morita, Y. Tsuchida, K. Maeda, M. Tadakuma, T. Saito, K. Watanabe, K. Imamura, R. Sugizaki, and M. Suzuki, “1.03-Exabit/skm Super-Nyquist-WDM transmission over 7,326-km seven-core fiber,” in *39th European Conference and Exhibition on Optical Communications (ECOC 2013)*, PD3.E.3, London, UK, Sept. 2013.
- [72] L. Poti, G. Meloni, G. Berrettini, F. Fresi, M. Secondini, T. Foggi, G. Colavolpe, E. Forestieri, A. D’Errico, F. Cavaliere, R. Sabella, and G. Prati, “Casting 1 Tb/s DP-QPSK communication into 200 GHz bandwidth,” in *38th European Conference and Exhibition on Optical Communications (ECOC 2012)*, P4.19, Amsterdam, Netherlands, Sept. 2012.
- [73] S. Yao, S. Fu, J. Li, M. Tang, P. Shum, and D. Liu, “Phase noise tolerant inter-carrier-interference cancellation for WDM superchannels with sub-Nyquist channel spacing,” *Optics Express*, vol. 21, no. 18, pp. 21569–21578, Sept. 2013.
- [74] J. Pan, C. Liu, T. Detwiler, A. J. Stark, Y. T. Hsueh, and S. E. Ralph, “Inter-channel crosstalk cancellation for Nyquist-WDM superchannel applications,” *Journal of Lightwave Technology*, vol. 30, no. 24, pp. 3993–3999, July 2012.
- [75] T. Sugiyama, H. Kazama, M. Morikura, S. Kubota, and S. Kato, “Burst mode interference cancellation for superposed transmission of SSMA-QPSK signals and TDMA-QPSK signals in nonlinear channels,” in *IEEE Global Telecommunications Conference (GLOBECOM’93)*, pp. 1612–1616, Houston, TX, USA, Dec. 1993.
- [76] G. Golden, C. Foschini, R. A. Valenzuela, and P. Wolniansky, “Detection algorithm and initial laboratory results using V-BLAST space-time communication architecture,” *Electronics Letters*, vol. 35, no. 1, pp. 14–16, Jan. 1999.
- [77] O. Vassilieva, T. Yamauchi, S. Oda, I. Kim, T. Hoshida, Y. Aoki, J. C. Rasmussen, and M. Sekiya, “Systematic analysis of intra-superchannel nonlinear crosstalk in flexible grid networks,” in *40th European Conference on Optical Communication (ECOC 2014)*, Mo.4.3.6, Cannes, France, Sept. 2014.

- [78] ETSI, “User guidelines for the second generation system for broadcasting, interactive services, news gathering and other broadband satellite applications (DVB-S2),” tech. rep., 102 376, Feb. 2015.
- [79] A. Sano, T. Kobayashi, S. Yamanaka, A. Matsuura, H. Kawakami, Y. Miyamoto, K. Ishihara, and H. Masuda, “102.3-Tb/s ( $224 \times 548$ -Gb/s) C-and extended L-band all-Raman transmission over 240 km using PDM-64QAM single carrier FDM with digital pilot tone,” in *35th Optical Fiber Communications Conference and Exhibition (OFC 2012)*, PDP5C.3, Los Angeles, CA, USA, Mar. 2012.
- [80] D. Qian, M.-F. Huang, E. Ip, Y.-K. Huang, Y. Shao, J. Hu, and T. Wang, “101.7-Tb/s ( $370 \times 294$ -Gb/s) PDM-128QAM-OFDM transmission over  $3 \times 55$ -km SSMF using pilot-based phase noise mitigation,” in *National Fiber Optic Engineers Conference*, PDPB5, Los Angeles, CA, Mar. 2011.
- [81] J. M. Kahn, K.-P. Ho, and M. B. Shemirani, “Mode coupling effects in multi-mode fibers,” in *35th Optical Fiber Communication Conference and Exhibition (OFC 2012)*, OW3D.3, Los Angeles, CA, USA, Mar. 2012.
- [82] A. R. Shah, R. C. J. Hsu, A. Tarighat, A. H. Sayed, and B. Jalali, “Coherent optical MIMO (COMIMO),” *Journal of Lightwave Technology*, vol. 23, no. 8, pp. 2410–2419, Aug. 2005.
- [83] T. Mizuno, H. Takara, K. Shibahara, Y. Miyamoto, M. Oguma, H. Ono, Y. Abe, T. Matsui, S. Matsuo, K. Saitoh, and Y. Kimura, “Mode dependent loss equaliser and impact of MDL on PDM-16QAM few-mode fibre transmission,” in *41st European Conference on Optical Communication (ECOC 2015)*, P5.9, Valencia, Spain, Sept. 2015.
- [84] E. Awwad, G. R.-B. Othman, and Y. Jaouën, “Space-time coding and optimal scrambling for mode multiplexed optical fiber systems,” in *IEEE International Conference on Communications (ICC)*, pp. 5228–5234, June 2015.
- [85] T. Mizuno, H. Takara, A. Sano, and Y. Miyamoto, “Dense space-division multiplexed transmission systems using multi-core and multi-mode fiber,” *Journal of Lightwave Technology*, vol. 34, no. 2, pp. 582–592, Jan. 2016.
- [86] H. Takara, T. Mizuno, H. Kawakami, Y. Miyamoto, H. Masuda, K. Kitamura, H. Ono, S. Asakawa, Y. Amma, K. Hirakawa, S. Matsuo, K. Tsujikawa, and M. Yamada, “120.7-Tb/s (7SDM / 180WDM / 95.8 Gb/s) MCF-ROPA unrepeatereed transmission

- of PDM-32QAM channels over 204 km,” in *40th European Conference on Optical Communication (ECOC2014)*, PD.3.1, Cannes, France, Sept. 2014.
- [87] A. Sano, H. Takara, T. Kobayashi, H. Kawakami, H. Kishikawa, T. Nakagawa, Y. Miyamoto, Y. Abe, H. Ono, K. Shikama, M. Nagatani, T. Mori, Y. Sasaki, I. Ishida, K. Takenaga, S. Matsuo, K. Saitoh, M. Koshihara, M. Yamada, H. Masuda, and T. Morioka, “409-Tb/s+ 409-Tb/s crosstalk suppressed bidirectional MCF transmission over 450 km using propagation-direction interleaving,” *Optics Express*, vol. 21, no. 14, pp. 16777–16783, July 2013.
- [88] T. Kobayashi, H. Takara, A. Sano, T. Mizuno, H. Kawakami, Y. Miyamoto, K. Hiraga, Y. Abe, H. Ono, M. Wada, Y. Sasaki, I. Ishida, K. Takenaga, S. Matsuo, K. Saitoh, M. Yamada, H. Masuda, and T. Morioka, “ $2 \times 344$  Tb/s propagation-direction interleaved transmission over 1500-km MCF enhanced by multicarrier full electric-field digital back-propagation,” in *39th European Conference and Exhibition on Optical Communication (ECOC 2013)*, PD3.E.4, London, UK, Sept. 2013.
- [89] T. Mizuno, K. Shibahara, H. Ono, Y. Abe, Y. Miyamoto, F. Ye, T. Morioka, Y. Sasaki, Y. Amma, K. Takenaga, S. Matsuo, K. Aikawa, K. Saitoh, Y. Jung, D. J. Richardson, K. Pulverer, M. Bohn, and M. Yamada, “32-core dense SDM unidirectional transmission of PDM-16QAM signals over 1600 km using crosstalk-managed single-mode heterogeneous multicore transmission line,” in *Optical Fiber Communication Conference*, Th5C.3, Anaheim, CA, USA, Mar. 2016.
- [90] J. Sakaguchi, B. J. Puttnam, W. Klaus, Y. Awaji, N. Wada, A. Kanno, T. Kawanishi, K. Imamura, H. Inaba, K. Mukasa, R. Sugizaki, T. Kobayashi, and M. Watanabe, “305 Tb/s space division multiplexed transmission using homogeneous 19-core fiber,” *Journal of Lightwave Technology*, vol. 31, no. 4, pp. 554–562, Feb. 2013.
- [91] A. Turukhin, O. V. Sinkin, H. G. Batshon, H. Zhang, Y. Sun, M. Mazurczyk, C. R. Davidson, J. X. Cai, M. A. Bolshtyansky, D. G. Foursa, and A. Pilipetskii, “105.1 Tb/s power-efficient transmission over 14,350 km using a 12-core fiber,” in *39th Optical Fiber Communications Conference and Exhibition (OFC 2016)*, Th4C.1, Anaheim, CA, USA, Mar. 2016.
- [92] D. Gloge, “Weakly guiding fibers,” *Applied Optics*, vol. 10, no. 10, pp. 2252–2258, Oct. 1971.

- [93] V. Sleiffer, Y. Jung, V. Veljanovski, R. van Uden, M. Kuschnerov, H. Chen, B. Inan, L. G. Nielsen, Y. Sun, D. Richardson, S. Alam, F. Poletti, J. Sahu, A. Dhar, A. Koonen, B. Corbett, R. Winfield, A. Ellis, and H. de Waardt, "73.7 Tb/s ( $96 \times 3 \times 256$ -Gb/s) mode-division-multiplexed DP-16QAM transmission with inline MM-EDFA," *Optics Express*, vol. 20, no. 26, pp. B428–B438, Nov. 2012.
- [94] E. Ip, M. J. Li, K. Bennett, Y. K. Huang, A. Tanaka, A. Korolev, K. Koreshkov, W. Wood, E. Mateo, J. Hu, and Y. Yano, " $146\lambda \times 6 \times 19$ -Gbaud wavelength-and mode-division multiplexed transmission over  $10 \times 50$ -km spans of few-mode fiber with a gain-equalized few-mode EDFA," *Journal of Lightwave Technology*, vol. 32, no. 4, pp. 790–797, Nov. 2014.
- [95] R. Ryf, N. K. Fontaine, M. Montoliu, S. Randel, B. Ercan, H. Chen, S. Chandrasekhar, A. H. Gnauck, S. G. Leon-Saval, J. Bland-Hawthorn, J. R. Salazar-Gil, Y. Sun, and R. Lingle, "Photonic-lantern-based mode multiplexers for few-mode-fiber transmission," in *37th Optical Fiber Communications Conference and Exhibition (OFC 2014)*, W4J.2, San Francisco, CA, USA, Mar. 2014.
- [96] R. Ryf, M. Esmaelpour, N. K. Fontaine, H. Chen, A. H. Gnauck, R. J. Essiambre, J. Toulouse, Y. Sun, and R. Lingle, "Distributed Raman amplification based transmission over 1050-km few-mode fiber," in *41st European Conference on Optical Communication (ECOC 2015)*, Tu.3.2.3, Valencia, Spain, Sept. 2015.
- [97] R. Ryf, H. Chen, N. K. Fontaine, A. M. Velazquez-Benitez, J. Antonio-Lopez, C. Jin, B. Huang, M. Bigot-Astruc, D. Molin, F. Achten, P. Sillard, and R. Amezcua-Correa, "10-mode mode-multiplexed transmission over 125-km single-span multimode fiber," in *41st European Conference on Optical Communication (ECOC 2015)*, PDP.3.3, Valencia, Spain, Sept. 2015.
- [98] R. Ryf, J. C. Alvarado, B. Huang, J. Antonio-Lopez, S. H. Chang, N. K. Fontaine, H. Chen, R. J. Essiambre, E. Burrows, R. Amezcua-Correa, T. Hayashi, Y. Tamura, T. Hasegawa, and T. Taru, "Long-distance transmission over coupled-core multi-core fiber," in *42nd European Conference on Optical Communication (ECOC 2016)*, Th.3.C.3, Dusseldorf, Germany, Sept. 2016.
- [99] R. Ryf, R. J. Essiambre, A. H. Gnauck, S. Randel, M. A. Mestre, C. Schmidt, P. J. Winzer, R. Delbue, P. Pupalakis, A. Sureka, T. Hayashi, T. Taru, and T. Sasaki,

- “Space-division multiplexed transmission over 4200 km 3-core microstructured fiber,” in *35th Optical Fiber Communications Conference and Exhibition (OFC 2012)*, PDP5C.2, Los Angeles, CA, USA, Mar. 2012.
- [100] N. Kishi and E. Yamashita, “A simple coupled-mode analysis method for multiple-core optical fiber and coupled dielectric waveguide structures,” *IEEE Transactions on Microwave Theory and Techniques*, vol. 36, no. 12, pp. 1861–1868, Dec. 1988.
- [101] C. Xia, N. Bai, I. Ozdur, X. Zhou, and G. Li, “Supermodes for optical transmission,” *Optics Express*, vol. 19, no. 17, pp. 16653–16664, Aug. 2011.
- [102] K.-P. Ho and J. M. Kahn, “Frequency diversity in mode-division multiplexing systems,” *Journal of Lightwave Technology*, vol. 29, no. 24, pp. 3719–3726, Oct. 2011.
- [103] R. Ryf, N. K. Fontaine, B. Guan, R. J. Essiambre, S. Randel, A. H. Gnauck, S. Chandrasekhar, A. Adamiecki, G. Raybon, B. Ercan, R. P. Scott, S. J. B. Yoo, T. Hayashi, T. Nagashima, and T. Sasaki, “1705-km transmission over coupled-core fibre supporting 6 spatial modes,” in *40th European Conference on Optical Communication (ECOC2014)*, PD.3.2, Cannes, France, Sept. 2014.
- [104] T. Sakamoto, S. Aozasa, T. Mori, M. Wada, T. Yamamoto, S. Nozoe, Y. Sagae, K. Tsujikawa, and K. Nakajima, “Randomly-coupled single-mode 12-core fiber with highest core density,” in *40th Optical Fiber Communications Conference and Exhibition (OFC 2017)*, Th1H.1, Los Angeles, CA, USA, Mar. 2017.
- [105] Mizuno, T. Kobayashi, H. Takara, A. Sano, H. Kawakami, T. Nakagawa, Y. Miyamoto, Y. Abe, T. Goh, M. Oguma, T. Sakamoto, Y. Sasaki, I. Ishida, K. Takenaga, S. Matsuo, K. Saitoh, and T. Morioka, “12-core  $\times$  3-mode dense space division multiplexed transmission over 40 km employing multi-carrier signals with parallel MIMO equalization,” in *37th Optical Fiber Communications Conference and Exhibition (OFC 2014)*, Th5B.2, San Francisco, CA, USA, Mar. 2014.
- [106] D. Soma, Y. Wakayama, S. Beppu, K. Igarashi, T. Tsuritani, H. Taga, I. Morita, and M. Suzuki, “665 and 947b/s/Hz ultra-highly aggregate-spectral-efficient SDM/WDM transmission over 6-Mode 19-Core Fibre using DP-16QAM/64QAM signals,” in *42nd European Conference on Optical Communication (ECOC 2016)*, Th.3.C.2, Dusseldorf, Germany, Sept. 2016.
- [107] K. Shibahara, D. Lee, T. Kobayashi, T. Mizuno, H. Takara, A. Sano, H. Kawakami,

- Y. Miyamoto, H. Ono, M. Oguma, Y. Abe, T. Matsui, R. Fukumoto, Y. Amma, T. Hosokawa, S. Matsuo, K. Saitoh, M. Yamada, and T. Morioka, "Dense SDM (12-core  $\times$  3-mode) transmission over 527 km with 33.2-ns mode-dispersion employing low-complexity parallel MIMO frequency-domain equalization," *Journal of Lightwave Technology*, vol. 34, no. 1, pp. 196–204, Jan. 2016.
- [108] R. Ryf, S. Randel, N. K. Fontaine, X. Palou, E. Burrows, S. Corteselli, S. Chandrasekhar, A. H. Gnauck, C. Xie, R. J. Essiambre, P. J. Winzer, R. Delbue, P. Pupalais, A. Sureka, Y. Sun, L. Gruner-Nielsen, R. V. Jensen, and R. Lingle, "708-km combined WDM/SDM transmission over few-mode fiber supporting 12 spatial and polarization modes," in *39th European Conference and Exhibition on Optical Communication (ECOC 2013)*, We.2.D.1, London, UK, Sept. 2013.
- [109] H. Chen, R. Ryf, N. K. Fontaine, A. M. Velazquez-Benitez, J. Antonio-Lopez, C. Jin, B. Huang, M. Bigot-Astruc, D. Molin, F. Achten, P. Sillard, and R. Amezcua-Correa, "High spectral efficiency mode-multiplexed transmission over 87-km 10-mode fiber," in *39th Optical Fiber Communications Conference and Exhibition (OFC 2016)*, Th4C.2, Anaheim, CA, USA, Mar. 2016.
- [110] A. Turukhin, H. G. Batshon, M. Mazurczyk, Y. Sun, C. R. Davidson, J. X. Chai, O. V. Sinkin, W. Patterson, G. Wolter, M. A. Bolshtyansky, D. G. Foursa, and A. Pilipetskii, "Demonstration of 0.52 Pb/s potential transmission capacity over 8,830 km using multicore fiber," in *42nd European Conference on Optical Communication (ECOC 2016)*, Tu.1.D.3, Dusseldorf, Germany, Sept. 2016.
- [111] T. Sakamoto, T. Mori, T. Yamamoto, and S. Tomita, "Differential mode delay managed transmission line for WDM-MIMO system using multi-step index fiber," *Journal of Lightwave Technology*, vol. 30, no. 17, pp. 2783–2787, July 2012.
- [112] E. Ip, G. Milione, M.-J. Li, N. Cvijetic, K. Kanonakis, J. Stone, G. Peng, X. Prieto, C. Montero, V. Moreno, and J. L. nares, "SDM transmission of real-time 10GbE traffic using commercial SFP+ transceivers over 0.5 km elliptical-core few-mode fiber," *Optics Express*, vol. 23, no. 13, pp. 17120–17126, June 2015.
- [113] I. E. Telatar, "Capacity of multi-antenna Gaussian channels," *EUROPEAN TRANSACTIONS ON TELECOMMUNICATIONS*, vol. 10, pp. 585–595, Nov. 1999.
- [114] M. Jankiraman, *Space-Time Codes and MIMO Systems*. Norwood, MA, USA: Artech

- House, Inc., 2004.
- [115] H. Ono, T. Hosokawa, K. Ichii, S. Matsuo, and M. Yamada, "Improvement of differential modal gain in few-mode fibre amplifier by employing ring-core erbium-doped fibre," *Electronics Letters*, vol. 51, no. 2, pp. 172–173, Jan. 2015.
- [116] A. Lobato, F. Ferreira, J. Rabe, M. Kuschnerov, B. Spinnler, and B. Lankl, "Mode scramblers and reduced-search maximum-likelihood detection for mode-dependent-loss-impaired transmission," in *39th European Conference and Exhibition on Optical Communication (ECOC 2013)*, Th.2.C.3, London, UK, Sept. 2013.
- [117] E. Ip, G. Milione, Y.-K. Huang, and T. Wang, "Impact of mode-dependent loss on long-haul transmission systems using few-mode fibers," in *39th Optical Fiber Communications Conference and Exhibition (OFC 2016)*, W4I.4, Anaheim, CA, USA, Mar. 2016.
- [118] K. Shibahara, T. Mizuno, H. Takara, H. Kawakami, D. Lee, Y. Miyamoto, S. Matsuo, K. Saitoh, and M. Yamada, "Space-time coding-assisted transmission for mitigation of MDL impact on mode-division multiplexed signals," in *39th Optical Fiber Communications Conference and Exhibition (OFC 2016)*, Th4C.4, Anaheim, CA, USA, Mar. 2016.
- [119] J. van Weerdenburg, A. Velázquez-Benitez, R. van Uden, P. Sillard, D. Molin, A. Amezcua-Correa, E. Antonio-Lopez, M. Kuschnerov, F. Huijskens, H. de Waardt, T. Koonen, R. Amezcua-Correa, and C. Okonkwo, "10 Spatial mode transmission using low differential mode delay 6-LP fiber using all-fiber photonic lanterns," *Optics Express*, vol. 23, no. 19, pp. 24759–24769, Sept. 2015.
- [120] D. Lee, K. Shibahara, T. Kobayashi, T. Mizuno, H. Takara, A. Sano, H. Kawakami, T. Nakagawa, and Y. Miyamoto, "Adaptive MIMO equalization for few-mode fiber transmission with various differential mode delays," in *41st European Conference on Optical Communication (ECOC 2015)*, Th.1.6.3, Valencia, Spain, Sept. 2015.
- [121] G. Ginis and J. M. Cioffi, "On the relation between V-BLAST and the GDFE," *IEEE Communications Letters*, vol. 5, no. 9, pp. 364–366, Sept. 2001.
- [122] K. Raoof and H. Zhou, *Advanced MIMO systems*. ScientificResearchPublishing, 2009.
- [123] B. Hassibi, "An efficient square-root algorithm for BLAST," in *2000 IEEE International Conference on Acoustics, Speech, and Signal Processing. Proceedings*, vol. 2,

- pp. II737–II740, June 2000.
- [124] E. Viterbo and J. Boutros, “A universal lattice code decoder for fading channels,” *IEEE Transactions on Information Theory*, vol. 45, no. 5, pp. 1639–1642, July 1999.
- [125] K. J. Kim and J. Yue, “Joint channel estimation and data detection algorithms for MIMO-OFDM systems,” in *36th Asilomar Conference on Signals, Systems and Computers*, vol. 2, pp. 1857–1861, Nov. 2002.
- [126] R. van Nee, A. van Zelst, and G. Awater, “Maximum likelihood decoding in a space division multiplexing system,” in *Vehicular Technology Conference Proceedings*, vol. 1, pp. 6–10, May 2000.
- [127] Y. Jiang, X. Zheng, and J. Li, “Asymptotic performance analysis of V-BLAST,” in *GLOBECOM’05. IEEE Global Telecommunications Conference*, vol. 6, pp. 3882–3886, Dec. 2005.
- [128] S. Loyka and F. Gagnon, “Performance analysis of the V-BLAST algorithm: an analytical approach,” *IEEE Transactions on Wireless Communications*, vol. 3, no. 4, pp. 1326–1337, July 2004.
- [129] X. Chen, J. He, A. Li, J. Ye, and W. Shieh, “Characterization and analysis of few-mode fiber channel dynamics,” *IEEE Photonics Technology Letters*, vol. 25, no. 18, pp. 1819–1822, Sept. 2013.
- [130] J. Sakaguchi, B. J. Puttnam, W. Klaus, Y. Awaji, N. Wada, A. Kanno, T. Kawanishi, K. Imamura, H. Inaba, K. Mukasa, R. Sugizaki, T. Kobayashi, and M. Watanabe, “19-core transmission of  $19 \times 100 \times 172$ -Gb/s SDM-WDM-PDM-QPSK signals at 305Tb/s,” in *35th Optical Fiber Communications Conference and Exhibition (OFC 2012)*, PDP5C.1, Los Angeles, CA, USA, Mar. 2012.
- [131] R. Ryf, S. Randel, N. K. Fontaine, M. Montoliu, E. Burrows, S. Corteselli, S. Chandrasekhar, A. H. Gnauck, C. Xie, R. J. Essiambre, P. J. Winzer, R. Delbue, P. Pupalakis, A. Sureka, Y. Sun, L. Gruner-Nielsen, R. V. Jensen, and R. Lingle, “32-bit/s/Hz spectral efficiency WDM transmission over 177-km few-mode fiber,” in *36th Optical Fiber Communications Conference and Exhibition (OFC 2013)*, PDP5A.1, Anaheim, CA, USA, Mar. 2013.
- [132] R. Ryf, N. K. Fontaine, B. Guan, B. Huang, M. Esmaelpour, S. Randel, A. H. Gnauck, S. Chandrasekhar, A. Adamiecki, G. Raybon, R. W. Tkach, R. Shubochkin, Y. Sun, and



- R. Lingle, "305-km combined wavelength and mode-multiplexed transmission over conventional graded-index multimode fibre," in *40th European Conference on Optical Communication (ECOC 2014)*, PD.3.5, Cannes, France, Sept. 2014.
- [133] M. S. Faruk and K. Kikuchi, "Adaptive frequency-domain equalization in digital coherent optical receivers," *Optics Express*, vol. 19, no. 13, pp. 12789–12798, June 2011.
- [134] N. Bai and G. Li, "Adaptive frequency-domain equalization for mode-division multiplexed transmission," *IEEE Photonics Technology Letters*, vol. 24, no. 21, pp. 1918–1921, Nov. 2012.
- [135] K. Ishihara, R. Kudo, T. Kobayashi, A. Sano, Y. Takatori, T. Nakagawa, and Y. Miyamoto, "Frequency-domain equalization for coherent optical transmission systems," in *34th Optical Fiber Communications Conference and Exhibition (OFC 2011)*, IEEE, OWW4, Los Angeles, CA, USA, Mar. 2011.
- [136] J. J. Shynk, "Frequency-domain and multirate adaptive filtering," *IEEE Signal Processing Magazine*, vol. 9, no. 1, pp. 14–37, Jan. 1992.
- [137] P. Duhamel, "Implementation of 'Split-radix' FFT algorithms for complex, real, and real-symmetric data," *IEEE Transactions on Acoustics, Speech, and Signal Processing*, vol. 34, no. 2, pp. 285–295, Apr. 1986.
- [138] D. Chang, F. Yu, Z. Xiao, N. Stojanovic, F. N. Hauske, Y. Cai, C. Xie, L. Li, X. Xu, and Q. Xiong, "LDPC convolutional codes using layered decoding algorithm for high speed coherent optical transmission," in *35th Optical Fiber Communication Conference (OFC 2012)*, OW1H.4, Los Angeles, CA, USA, Mar. 2012.
- [139] A. Lobato, F. Ferreira, B. Inan, S. Adhikari, M. Kuschnerov, A. Napoli, B. Spinnler, and B. Lankl, "Maximum-likelihood detection in few-mode fiber transmission with mode-dependent loss," *IEEE Photonics Technology Letters*, vol. 25, no. 12, pp. 1095–1098, Apr. 2013.
- [140] K. Shibahara, A. Masuda, H. Kishikawa, S. Kawai, and M. Fukutoku, "Filtering-tolerant transmission by the Walsh-Hadamard transform for super-channel beyond 100 Gb/s," *Optics Express*, vol. 23, no. 10, pp. 13245–13254, Apr. 2015.
- [141] K. Sugihara, Y. Miyata, T. Sugihara, K. Kubo, H. Yoshida, W. Matsumoto, and T. Mizuoichi, "A spatially-coupled type LDPC code with an NCG of 12 dB for optical transmission beyond 100 Gb/s," in *36th Optical Fiber Communications Conference*

*and Exhibition (OFC 2013)*, OM2B.4, Anaheim, CA, USA, Mar. 2013.

- [142] X. Chen, J. Ye, Y. Xiao, A. Li, J. He, Q. Hu, and W. Shieh, "Equalization of two-mode fiber based MIMO signals with larger receiver sets," *Optics Express*, vol. 20, no. 26, pp. B413–B418, Dec. 2012.
- [143] L. Zheng and D. N. C. Tse, "Diversity and multiplexing: a fundamental tradeoff in multiple-antenna channels," *IEEE Transactions on Information Theory*, vol. 49, no. 5, pp. 1073–1096, May 2003.

# Author's Publication List

## Peer-Reviewed Publications on Journal Paper and Letter

1. K. Shibahara, and Y. Kazushige, "Experimental demonstration of PDL penalty reduction by wavelength-interleaving transmission," *Optics Express*, vol. 20, no. 26, pp. B479-B484, Dec. 2012.
2. K. Shibahara, A. Masuda, H. Kishikawa, S. Kawai, and M. Fukutoku, "Filtering-tolerant transmission by the Walsh-Hadamard transform for super-channel beyond 100 Gb/s," *Optics Express*, vol. 23, no. 10, pp. 13245-13254, May 2015.
3. K. Shibahara, T. Mizuno, H. Takara, A. Sano, H. Kawakami, D. Lee, Y. Miyamoto, H. Ono, M. Oguma, Y. Abe, T. Kobayashi, T. Matsui, R. Fukumoto, Y. Amma, T. Hosokawa, S. Matsuo, K. Saito, M. Yamada, and T. Morioka, "Dense SDM (12-core  $\times$  3-mode) transmission over 527 km with 33.2-ns mode-dispersion employing low-complexity parallel MIMO frequency-domain equalization," *Journal of Lightwave Technology*, vol. 34, no. 1, pp. 196-204, July 2015.
4. K. Shibahara, M. Nosé, T. A. Fritz, and J. Niehof, "A new generation mechanism of butterfly pitch angle distributions of energetic ions: Multiple pitch angle scattering in the stretched magnetic field," *Journal of Geophysical Research: Space Physics*, vol. 115, no. A7, A07229, July 2010.

## Peer-Reviewed/Invited Conference Proceedings

1. K. Shibahara, and K. Yonenaga, "Experimental demonstration of PDL penalty reduction by wavelength-interleaving transmission," in *38th European Conference and Exhibition on Optical Communication (ECOC 2012)*, Th.2.A.4, Amsterdam,

- Netherlands, Sept. 2012.
2. K. Shibahara, Y. Sakamaki, T. Kawai, H. Kishikawa, and M. Fukutoku, "Improving nonlinear degradation by combining optical and digital compensation techniques," in *18th OptoElectronics and Communications Conference / Photonics in Switching (OECC/PS 2013)*, WR4-6, Kyoto, Japan, June 2013.
  3. K. Shibahara and M. Fukutoku, "Novel digital equalizer for XPM-induced polarization crosstalk using overlapped fast independent component analysis," in *39th European Conference and Exhibition on Optical Communication (ECOC 2013)*, Mo.3.D.1, London, UK, Sept. 2013.
  4. K. Shibahara, A. Masuda, S. Kawai, and M. Fukutoku, "Multi-stage successive interference cancellation for spectrally-efficient super-Nyquist transmission," in *41st European Conference and Exhibition on Optical Communication (ECOC 2015)*, Th.1.6.4, Valencia, Spain, Sept. 2015.
  5. K. Shibahara, T. Mizuno, H. Takara, A. Sano, H. Kawakami, D. Lee, Y. Miyamoto, H. Ono, M. Oguma, Y. Abe, T. Kobayashi, T. Matsui, R. Fukumoto, Y. Amma, T. Hosokawa, S. Matsuo, K. Saito, H. Nasu, and T. Morioka, "Dense SDM (12-core  $\times$  3-mode) transmission over 527 km with 33.2-ns mode-dispersion employing low-complexity parallel MIMO frequency-domain equalization," in *38th Optical Fiber Communications Conference and Exhibition (OFC 2015)*, Th5C-3, Los Angeles, CA, USA, Mar. 2015.
  6. K. Shibahara, T. Mizuno, H. Takara, H. Kawakami, D. Lee, Y. Miyamoto, S. Matsuo, K. Saitoh, and M. Yamada, "Space-time coding-assisted transmission for mitigation of MDL impact on mode-division multiplexed signals," in *39th Optical Fiber Communications Conference and Exhibition (OFC 2016)*, Th4C.4, Anaheim, CA, USA, Mar. 2016.
  7. (*Invited*) K. Shibahara, T. Mizuno, D. Lee, and Miyamoto, "Advanced MIMO signal processing for dense SDM transmission using multi-core few-mode fibers" in *21st OptoElectronics and Communications Conference / Photonics in Switching (OECC/PS 2016)*, S2-6, Niigata, Japan, June 2016.
  8. (*Invited*) K. Shibahara, T. Mizuno, D. Lee, and Miyamoto, "Dense SDM transmission employing advanced MIMO signal processing" in *2016 IEEE Photonics*

*Society Summer Topical Meeting Series*, TuE2.3, Newport Beach, CA, USA, July 2016.

9. (Invited) K. Shibahara, T. Mizuno, D. Lee, and Miyamoto, "Signal processing techniques for DMD and MDL mitigation in dense SDM transmissions" in *40th Optical Fiber Communication Conference (OFC 2017)*, M2D3, Los Angeles, CA, USA, Mar. 2017.
10. K. Shibahara, T. Mizuno, and Miyamoto, "LDPC-coded FMF transmission employing unreplicated successive interference cancellation for MDL-impact mitigation" in *43rd European Conference and Exhibition on Optical Communication (ECOC 2017)*, Th.1.D.4, Gothenburg, Sweden, Sept. 2017.

## Awards

1. 126<sup>th</sup> Student Presentation Award (Aurora Medal) from Society of Geomagnetism and Earth, Planetary and Space Sciences (SGEPSS) in 2009.
2. The Tingye Li Innovation Prize from Optical Society of America (OSA) in 2016.
3. Young Researchers' Award from The Institute of Electronics, Information and Communication Engineers (IEICE) in 2017.